



University
of Glasgow

Gibbings, Alison Lorraine (2014) Laser ablation for the deflection, exploration and exploitation of near Earth asteroids. PhD thesis.

<http://theses.gla.ac.uk/5219/>

Copyright and moral rights for this thesis are retained by the author

A copy can be downloaded for personal non-commercial research or study, without prior permission or charge

This thesis cannot be reproduced or quoted extensively from without first obtaining permission in writing from the Author

The content must not be changed in any way or sold commercially in any format or medium without the formal permission of the Author

When referring to this work, full bibliographic details including the author, title, awarding institution and date of the thesis must be given.



University
of Glasgow

**LASER ABLATION FOR THE DEFLECTION,
EXPLORATION AND EXPLOITATION OF
NEAR EARTH ASTEROIDS**

Alison Lorraine Gibbings MEng(hons)

College of Science and Engineering
School of Engineering
University of Glasgow
Glasgow, Scotland, UK

Submitted in Fulfilment of the Requirements
for the Degree of Doctor of Philosophy

© Gibbings, Alison: 2014

Alison Gibbings, *Laser Ablation for the Deflection, Exploration and Exploitation of Near Earth Asteroids*, Doctor of Philosophy, College of Science and Engineering, School of Engineering, University of Glasgow, Scotland, UK, © 2014

ADVISORS:

Professor Massimiliano Vasile, Advanced Space Concepts Laboratory, Department of Mechanical & Aerospace Engineering, University of Strathclyde, Scotland, UK

Dr Ian Watson, Systems, Power and Energy Research Division, School of Engineering, University of Glasgow, Scotland, UK

EXAMINERS:

Professor Chris Chatwin, Chair of Engineering, University of Sussex, UK

Dr Patrick Harkness, Systems, Power and Energy Research Division, School of Engineering, University of Glasgow, Scotland, UK

CONVENER:

Professor Margaret Lucas, Systems, Power and Energy Research Division, School of Engineering, University of Glasgow, Scotland, UK

LOCATION:

School of Engineering, University of Glasgow, Scotland, UK

EXAM DATE:

28/02/2014

Abstract

Laser ablation has been investigated as a possible technique for the contactless deflection of Near Earth Asteroids. It is achieved by irradiating the surface of an asteroid with a laser light source. The absorbed heat from the laser beam sublimates the surface, transforming the illuminated material directly from a solid to a gas. The ablated material then forms into a plume of ejecta. This acts against the asteroid, providing a controllable low thrust, which pushes the asteroid away from an Earth-threatening trajectory.

The potential of laser ablation is dependent on understanding the physical and chemical properties of the ablation process. The ablation model is based on the energy balance of sublimation and was developed from three fundamental assumptions. Experimental verification was used to assess the viability of the ablation model and its performance in inducing a deflection action. It was achieved by ablating a magnesium-iron silicate rock, under vacuum, with a 90 W continuous wave laser. The laser operated at a wavelength of 808 nm and provided intensities that were below the threshold of plasma formation. The experiment measured the average mass flow rate, divergence geometry and temperature of the ejecta plume and the contaminating effects - absorptivity, height and density - of the deposited ejecta. Results were used to improve the ablation model. A critical discrepancy was in the variation between the previously predicted and experimentally measured mass flow rate of the ablated ejecta. Other improvements have also included the energy absorption within the Knudsen layer, the variation of sublimation temperature with local pressure, the temperature of the target material and the partial re-condensation of the ablated material. These improvements have enabled the performance of the ablation process and the specifications of the laser to be revised. Performance exceeded other forms of electric propulsion that provided an alternative contactless, low thrust deflection method.

The experimental results also demonstrated the opportunistic potential of laser ablation. Using existing technologies, with a high technology readiness level, a small and low-cost mission design could demonstrate the technologies, approaches and synergies of a laser ablation mission. The performance of the spacecraft was evaluated by its ability to deflect a small and irregular 4 m diameter asteroid by at least 1 m/s. It was found to be an achievable and measurable objective. The laser ablation system could be successfully sized and integrated into a conventional solar-power spacecraft. Mission mass and complexity is saved by the direct ablation of the asteroid's surface. It also avoids any complex landing and surface operations. Analysis therefore supports the general diversity and durability of using space-based lasers and the applicability of the model's experimental verification.

Table of Contents

List of Figures	VII
List of Tables	IX
Nomenclature	X
Acknowledgements	XVI
Dedication	XVIII
Declaration	XIX
Publications	XX
1 Introductory Scope	1
2 Asteroids	5
2.1 Introduction	5
2.2 The Characterisation of Asteroids	7
2.3 Missions to Asteroids	9
3 Deflection Techniques	16
3.1 Introduction	16
3.2 Impulsive Methods	17
3.3 Low Thrust Methods	19
3.4 Passive Methods	22
3.5 Comparative Analysis	23
4 Applications of Laser Ablation	24
4.1 Introduction	24
4.2 Launching and Controlling Vehicles in Space	24
4.3 De-orbiting of Space Debris	29
4.4 Deflection of Asteroids	32
5 Laser Ablation Model	38
5.1 Introduction	38
5.2 Sublimation Model	39
5.2.1 Mission Simulations	52
5.2.2 Outstanding Issues	55

5.3	Momentum Coupling and Energy Efficiency	56
5.4	Improved Ablation Model	58
6	Experiment Design and Results	65
6.1	Introduction	65
6.2	Laser	66
6.3	Target Material	67
6.4	Cameras and the Spectrometer	68
6.5	Collection Plates	73
6.6	Rock Analysis	90
6.7	Momentum Coupling and Mass Flow Rate	94
7	Performance Analysis	98
7.1	Introduction	98
7.2	Revised Absorptivity as a Contamination Factor	98
7.3	Momentum Coupling Analysis	99
7.4	Δv for Different Operational Conditions	102
7.5	Deflection System Mass	103
8	Technology Demonstration Mission	107
8.1	Introduction	107
8.2	Mission Architecture	108
8.3	Spacecraft Design	110
8.3.1	Laser	110
8.3.2	Impact Sensor	112
8.3.3	Raman/Laser Induced Breakdown Spectrometer	113
8.3.4	Spacecraft Configuration	115
8.4	Opportunistic Potential	120
9	Conclusions and Future Work	126
	Bibliography	129
A	Manufacture of the Composite Sample	159
A1	Introduction	159
A2	Manufacturing Process	159
A3	Note on Porosity	160
B	Tested Equipment and Proposed Methodologies	161
B1	Introduction	161
B2	Selection and Testing of the Target Material	161
B3	Quality and Selection of the Collection Plates	163
B4	Ongoing Maintenance of the Experiment	163
B5	Development of the Experimental Procedures	164
B6	Preliminary Development of Additional Experimental Techniques	165
C	Health and Safety of Operating the Laser	171

D Operations of the LIMO Fibre-Coupled Diode Laser	173
D1 Turn-on Procedure	173
D2 Turn-off Procedure	173
E Images of the Optical Bench	175
F Holder for the Collection Plates	176
G SEM Analysis of the Pre-ablated Olivine Sample	177
H SEM Analysis of the Recrystallised Ablation Rim	179
I Error Analysis	181
J Scatter Factor	182
K Roughing and Diffusion Pump	183
L Operating Procedures - Vacuum Chamber and Pump	187
L1 Starting Up	187
L2 Venting the System to Atmosphere	187
L3 Pumping the System from Atmosphere	188
L4 Shutting Down	188

List of Figures

Figure 2.1	Orbital Locations of Near Earth Asteroids - Drawn from Morrison [2007]; Belton et al. [2004]	8
Figure 3.1	Illustration of a Gravity Tractor taken from Lu and Love [2005]; Schweickart et al. [2006]	19
Figure 3.2	Illustration of the Ion Beam Shepherd taken from Bombardelli and Pelaez [2011b]	20
Figure 3.3	Smart Cloud - Initial Release and Impact Geometry	21
Figure 3.4	Mass Driver Mission Concept taken from SpaceWorks	22
Figure 4.1	Artist Impression and Cross-Sectional View of the LTD Vehicle taken from Richard and Myrabo [2005a,b]; Myrabo [1989]	26
Figure 4.2	Vertical Laser-Driven, In-tube Accelerator Demonstration taken from Sasoh [2011]; Yabe et al. [2003]	27
Figure 4.3	Principles of the Micro Laser Plasma Thruster - Combined from Phipps et al. [2004a,b]; Phipps [2002]; Phipps and Luke [2002]	28
Figure 4.4	Saturation of Orbital Space Debris <i>Credits ESA</i>	29
Figure 4.5	ORION Concept for the De-orbiting of Space Debris with Lasers. Image taken from Phipps [2011b]	30
Figure 4.6	Principles of the Solar Concentrator taken from Gritzner et al. [2002]	32
Figure 4.7	Solar Concentrator Deflection System: Dual Mirror System taken from Melosh et al. [1994]	33
Figure 4.8	Artistic Impression of the MIRROR BEES Deflection Technique	34
Figure 4.9	Spacecraft Design for an Indirect Pumped Laser System	37
Figure 5.1	Local Reference Frame and Geometry of the Ejecta Plume	43
Figure 5.2	Expected Scatter Factor, Velocity and Density Direction of the Ejecta Plume	44
Figure 5.3	Structural Classification of Asteroids taken from Richardson et al. [2004]	45
Figure 5.4	Reconstructed Shape Models of Asteroids	47
Figure 5.5	Spin Limit - Rotational Rate vs Body Size for Asteroids and Comets taken from Pravec et al. [2002]	48
Figure 5.6	Deflection Distance (measured in kilometers) of a 250 m diameter, $2.7 \cdot 10^{10}$ kg (based on Apophis) Asteroid: Without Contamination.	54
Figure 5.7	Deflection Distance (measured in kilometers) of a 250 m diameter, $2.7 \cdot 10^{10}$ kg (based on Apophis) Asteroid: With Contamination.	54

Figure 5.8	Experiment Data of the Mechanical Coupling of a KrF Laser to Nylon ($\lambda_b = 248$ nm, $\tau_b = 22$ ns, $I_{max} = 10^8$ W/cm ²). Data gained from Phipps et al. [1988]	58
Figure 5.9	Thrust Sensitivity to the Recondensation Ratio	62
Figure 5.10	Reflective Spectrum of Four Different Classes of Asteroids. All spectral data is available at http://smass.mit.edu/catalog.php [Bus and Binzel, 2002]	63
Figure 6.1	Illustration of the Laser Beam and Experiment Set-up	66
Figure 6.2	External Arrangement of the Test Chamber	68
Figure 6.3	Formation of the Ejecta Plume	69
Figure 6.4	Time-averaged Ejection of the Solid Ejecta	70
Figure 6.5	Alignment of the Spectrometer - Showing the Operational Wavelength of the Laser Beam	71
Figure 6.6	Data Recorded by the Spectrometer - Olivine Sample Under Vacuum	72
Figure 6.7	Solution of the Heat Diffusion Equation	73
Figure 6.8	Arrangement of the Collection Plates	74
Figure 6.9	Collection of the Deposited Ejecta - 3 cm from the Spot Location .	75
Figure 6.10	Collection of the Deposited Ejecta - 7 cm from the Spot Location .	75
Figure 6.11	Collection of the Deposited Ejecta - 10 cm from the Spot Location	75
Figure 6.12	Sample Points on the Collection Plate	76
Figure 6.13	Height of the Deposited Ejecta on the Collection Plate - Comparison between the Experimental Measurements and Improved Simulation. Results at 3 cm from the Spot	77
Figure 6.14	Height of the Deposited Ejecta on the Collection Plate - Comparison between the Experimental Measurements and Improved Simulation. Results at 7 cm from the spot	77
Figure 6.15	Height of the Deposited Ejecta on the Collection Plate - Comparison between the Experimental Measurements and Improved Simulation. Results at 10 cm from the Spot	78
Figure 6.16	Microscopic Imagery of Ejecta Deposited on the Collection Plates	79
Figure 6.17	Measuring the Transmittance and Absorbance Effects of the Deposited Ejecta	80
Figure 6.18	Measured Transmittance of the Collection Plates	81
Figure 6.19	Degradation Factor: Comparison between the Experimental Results and Improved Model Prediction at 3 cm from the Spot	84
Figure 6.20	Degradation Factor: Comparison between the Experimental Results and Improved Model Prediction at 7 cm from the Spot	84
Figure 6.21	Degradation Factor: Comparison between the Experimental Results and Improved Model Prediction at 10 cm from the Spot	85
Figure 6.22	Spontaneous Peeling of the Deposited Ejecta on the Central Collection Plate, 3 cm from the Spot	87
Figure 6.23	Deposited Mass per Unit Area: Experimental Results vs Improved Model Prediction at 3 cm from the Spot	89

Figure 6.24	Deposited Mass per Unit Area: Experimental Results vs Improved Model Prediction at 7 cm from the Spot	89
Figure 6.25	Deposited Mass per Unit Area: Experimental Results vs Improved Model Prediction at 10 cm from the Spot	90
Figure 6.26	Determining the Shape Profile of the Ablation Hole	91
Figure 6.27	Ablation Response at the Rim	91
Figure 6.28	SEM Image of Recrystallisation at the Ablation Rim	92
Figure 6.29	Enthalpy Change of MgSiO_3 - Adapted from O'Keefe and Ahrens [1971]	94
Figure 6.30	Predicted Mass Flow Rate vs the Measured Mass Flow Rate for Two Different Estimated Spot Diameters and Different Recondensation Factors	95
Figure 7.1	Revised Deflection Distance of a 250 m Diameter, $2.7 \cdot 10^{10}$ kg (based on Apophis) Asteroid: With the Experimentally Measured Degradation Factor	99
Figure 7.2	Momentum Coupling for Different Spot Sizes (Laser Efficiency 55 %)	101
Figure 7.3	Input Power and Spot Size Radius as a function of Momentum Coupling and Thrust Level	101
Figure 7.4	Imparted Δv as a Function of Spot Size and Input Power to the Laser	102
Figure 7.5	RIT System - Total Deflection System Mass as a Function of Δv .	105
Figure 7.6	PPS1350G - Total Deflection System Mass as a Function of Δv .	105
Figure 7.7	Imparted Δv - Function of the Asteroid Mass and Deflection System Mass	106
Figure 8.1	Thrusting Time to Achieve a Δv of 1 m/s - 20 and 30 m Shooting Distance. Reproduced from Vasile et al. [2013a]	109
Figure 8.2	Thrusting Time to Achieve a Δv of 1 m/s - 40 and 50 m Shooting Distance. Reproduced from Vasile et al. [2013a]	109
Figure 8.3	Schematic of the Laser System and Telescope Beam Expander. Image reproduced from Vasile et al. [2013a]	111
Figure 8.4	Beam Behaviour of a 1070 nm Fibre and a $f = 50$ m Optic. Data reproduced from Vasile et al. [2013a]	112
Figure 8.5	Parameters of the Laser beam	112
Figure 8.6	Deployed Configuration of AdAM in the Trailing Configuration - All Externally Mounted Instruments and Units	115
Figure 8.7	Deployed Configuration of AdAM in the Radial Configuration - All Externally Mounted Instruments and Units	116
Figure 8.8	Thrust Level and Δv for a Reduced 480 W Laser Input	120
Figure A.1	Component Parts of the High Porous Composite Mixture	159
Figure B.1	Range of Tested Material	162
Figure B.2	Initial Limestone Ablation	162

Figure B.3	Initial Sandstone Ablation	162
Figure B.4	Initial Shale Ablation	162
Figure B.5	Initial Marl Ablation	162
Figure B.6	Initial Shale Ablation	162
Figure B.7	Initial Development and Testing of a Torsion Pendulum	163
Figure B.8	Preliminary Testing of the WM25-SH Analytical Mass Balance	166
Figure B.9	Proposed Test Configuration	168
Figure B.10	Ellipsoidal Shape Model	169
Figure B.11	Photos of the Pre-selected Meteorites	170
Figure E.1	Laser Head	175
Figure E.2	Optical Bench	175
Figure F.1	Orientation of the Collection Plate Holder	176
Figure G.1	Elemental Analysis of the Olivine Target Material	177
Figure G.2	Rock Sample for Compositional Analysis	177
Figure G.3	Presence of Silicon	178
Figure G.4	Presence of Magnesium	178
Figure G.5	Presence of Oxygen	178
Figure G.6	Presence of Iron	178
Figure G.7	Presence of Carbon	178
Figure G.8	Presence of Calcium	178
Figure G.9	Presence of Aluminium	178
Figure G.10	Presence of Sodium	178
Figure H.1	Assessed Section	179
Figure H.2	Recrystallised Silicon	179
Figure H.3	Recrystallised Magnesium	179
Figure H.4	Recrystallised Oxygen	179
Figure H.5	Recrystallised Calcium	180
Figure H.6	Recrystallised Aluminium	180
Figure H.7	Recrystallised Iron	180
Figure H.8	Recrystallised Carbon	180
Figure I.1	Error Bar Analysis	181
Figure J.1	Definition of the Scatter Factor	182
Figure K.1	Configuration of the Test Chamber, Roughing Pump and Diffusion Pump	184
Figure K.2	Cross Sectional View of the Diffusion Pump and Cooling System	185

List of Tables

Table 2.1	Summary of the Impact Effects Caused by an Impacting Asteroid	6
Table 2.2	Asteroid Class relative to Surface Mineralogy and Albedo	9
Table 6.1	Material Characteristics of Olivine	67
Table 6.2	Recorded and Inferred Results from the Spectrometer	72
Table 6.3	3 cm from the Spot (Test 1): Measured Transmittance and Absorbance Effects	81
Table 6.4	3 cm from the Spot (Test 2): Measured Transmittance and Absorbance Effects	81
Table 6.5	3 cm from the Spot (Test 3): Measured Transmittance and Absorbance Effects	82
Table 6.6	7 cm from the Spot (Test 1): Measured Transmittance and Absorbance Effects	82
Table 6.7	7 cm from the Spot (Test 2): Measured Transmittance and Absorbance Effects	82
Table 6.8	7 cm from the Spot (Test 3): Measured Transmittance and Absorbance Effects	82
Table 6.9	10 cm from the Spot (Test 2): Measured Transmittance and Absorbance Effects	83
Table 6.10	10 cm from the Spot (Test 3): Measured Transmittance and Absorbance Effects	83
Table 6.11	10 cm from the Spot (Test 2): Absorptivity Results	86
Table 6.12	10 cm from the Spot (Test 3): Absorptivity Results	86
Table 6.13	7 cm from the Spot (Test 1): Absorptivity Results	86
Table 6.14	7 cm from the Spot (Test 2): Absorptivity Results	86
Table 6.15	7 cm from the Spot (Test 3): Absorptivity Results	86
Table 6.16	Vaporisation Products and Reactions	93
Table 8.1	Mass Budget for the 860 W Laser - PSLV XL GTO	118
Table 8.2	Mass Budget for the Revised 480 W Laser - PSLV XL GTO	119
Table 8.3	Critical TRL Components of the AdAM Spacecraft	123
Table 9.1	Comparison of Different Methods for Accessing Microgravity. The mass is defined as the experiment mass per payload, with possibly multiple payloads per flight opportunity.	129
Table B.1	Classification of the Pre-selected Meteorites	169

Table C.1 Hazard Classes for Laser Beams 171

Nomenclature

Acronyms

AdAM	Asteroid Ablation Mission
AIDA	Asteroid Impact & Deflection Assessment
AIM	Asteroid Impact Monitoring
APL	Applied Physics Laboratory
ATV	Automated Transfer Vehicle
AU	Astronomical Units
DART	Double Asteroid Redirection Test
EP	Electric Propulsion
ESA	European Space Agency
FP7	7 th Framework Programme
GDS	Grain Detection System
GIADA	Grain Impact Analyser & Dust Accumulator
GNC	Guidance, Navigation and Control
IMU	Inertia Measurement Unit
ISIS	Impactor for Surface and Interior Science
ISS	International Space Station
JAXA	Japanese Aerospace Exploration Agency
LEO	Low Earth Orbit
LIBS	Laser Induced Breakdown Spectrometer
LTD	Light-craft Technology Demonstrator
MLI	Multi-layering Insulation
MOID	Minimum Orbit Interception Distance
NAC	Narrow Angle Camera
NASA	National Aeronautics and Space Administration

NEA Near Earth Asteroid

NEAR Near Earth Asteroid Rendezvous mission

OSIRIS-Rex Origins, Spectra, Interpretations, Resource Identification, Security & Regolith Explorer

PCDU Power Control and Distribution Unit

PHA Potentially Hazardous Asteroids

PZT Piezoelectric Transducers

QCM Quartz-crystal Micro-balance

SE Standard Error of the Mean

SEM Scanning Electron Microscope

SD Standard Deviation

TRL Technology Readiness Level

UV Ultra-violet

WAC Wide Angle Camera

WISE Wide-Field Infrared Survey Explorer

Mathematical Terms

All base and derived terms are defined by the International System of Units (SI)

a Acceleration imparted onto the asteroid

A Area

A_f Frequency factor of the colliding molecules

A_R Area of the radiators

A_{SA} Area of the solar arrays

A_{SPOT} Area of illumination by the laser beam on the surface of the asteroid

c_A Heat capacity of the asteroid

c_R Concentration ratio

C_P Specific heat capacity of the ablated gaseous ejecta at constant pressure

C_V Specific heat capacity of the asteroid at constant volume

C_m Momentum coupling

C_{max} Maximum momentum coupling

d_A Estimated diameter of the asteroid, based on the observed magnitude

d_{SPOT} Surface spot diameter of the laser beam
 e Euler's number, Base of the Natural Logarithms
 e_I Coefficient of restitution
 E Energy
 E_a Activation Energy
 E_v Sublimation enthalpy
 E_v^* Augmented enthalpy
 F_{EP} Force applied by a single engine via electric propulsion
 F_{SUB} Force acting on the asteroid
 g_0 Standard acceleration due to free fall
 h_{EXP} Measured height of the deposited ejecta from the experiment
 I_{max} Maximum laser intensity
 h_{layer} Accumulated thickness of the deposited ejecta
 I_{SP} Specific impulse of an engine
 k Fraction of molecules that re-condense at the interphase
 k_A Heat conductivity of the asteroid
 k_b Boltzmann's constant
 k_I Adiabatic index
 k_P Jet constant
 k_s Reaction rate coefficient
 L Path length through the asteroid
 L_a Measured angle length of the ablation hole from the experiment
 L_v Measured vertical length of the ablation hole from the experiment
 m Initial mass of the asteroid
 m_a Mass of the asteroid
 m_e Mass of an engine
 m_{EP} Mass of the electric propulsion system
 m_L Mass of the laser
 m_{LS} Mass of the laser system (including optics)
 m_p Mass of the propellant
 m_a Molar mass of the ablated gaseous material
 \dot{m}_{SUB} Mass flow rate of the ablated material

n Number of values in the sample population
 p_{ref} Pressure corresponding to the reference temperature T_{ref}
 p_s Pressure corresponding to the temperature T_{SUB}
P Power transmittance through the collection plate
 P_{1AU} Solar constant at 1 AU
 P_{EP} Input power for the electric propulsion system
 P_I Absorbed laser power per unit area
 P_{IN} Absorbed input power at the spot location of the laser beam
 P_{INEXP} Absorbed laser input power at the spot location during the experiment
 P_L Input power of the laser
 P_o Initial power
 Q^* Energy required to ablated each kilogram of material
 Q_C Heat loss, per unit area, through conduction
 Q_{laser} Radiating power of the laser
 Q_R Heat loss, per unit area, through radiation
r Distance from the known spot location of the laser beam
R Universal gas constant
 R_{AU} Distance from the Sun in AU
 R_S Specific gas constant
t Illumination time of the laser beam
 t_o Oscillation period of surface molecules
 t_r Average resident time
T Experimentally derived degradation factor
 T_m Transmittance
 T_{AMB} Ambient surrounding temperature
 T_{gas} Temperature of the gaseous ejecta
 T_R Operating temperature of the radiators
 T_{ref} Reference temperature
 T_s Temperature of the substrate
 T_{sys} Temperature of the system
 T_o Temperature at the centre of the asteroid
 T_{SUB} Sublimation temperature of the asteroid

\bar{v} Average velocity of the ejecta plume
 \bar{v}_{EXP} Calculated velocity of the ejecta plume from the experiment
 V_{rot} Velocity of rotation on the surface of the asteroid
 w_o Beam waist of the laser beam
 \mathbf{y} Location of the laser beam
 Z_R Rayleigh Range

 α Internal angle of the ablation hole
 α_b Absorbance of the collection plate
 α_M Absorption at the spot
 α_P Mass per unit power of the power system
 α_s Albedo of the asteroid
 γ Sticky coefficient
 Δ Change in value
 Δt_{thrust} Thrust time of a single engine via electric propulsion
 $\Delta \mathbf{v}$ Change in velocity
 ε Black body emissivity
 ε_a Reflectivity of the asteroid at the wavelength of the laser beam
 ε_R Emissivity of the radiators
 η Absorptivity of the deposited ejecta
 η_{AB} Efficiency of the ablation process
 η_{EP} Efficiency of the electric propulsion system
 η_{EXP} Calculated absorptivity of the deposited ejecta from the experiment
 η_L Efficiency of the laser system
 η_P Efficiency of the output power system
 η_S Efficiency of the solar arrays
 θ Local elevation angle
 κ_A Thermal conductivity of the asteroid
 λ Scatter factor
 λ_b Wavelength of the laser beam
 λ_{PEAK} Peak wavelength of the emitted spectra
 $\dot{\mu}$ Mass flow rate per unit area of the sublimation material

ρ Density of the ejecta plume

ρ^* Density at the nozzle

ρ_A Density of the asteroid

ρ_{EXP} Calculated density of the deposited ejecta from the experiment

$\rho_{layer,EXP}$ Derived layer density of the deposited ejecta from the experiment

ρ_{layer} Layer density

ρ_R Specific mass of the radiators

σ_{SB} Stefan-Boltzmann constant

τ Degradation Factor

τ_b Pulse width duration

τ_g Absorption of the laser beam in the ejecta plume

ψ_{vf} Geometric view factor

Subscripts

$\mathbf{a}_I, \mathbf{b}_I, \mathbf{c}_I$ Three radii along the orthogonal axis

C Continuous wave laser beam

f Final value

i Initial value

in Enters illumination with the laser beam

out Exit illumination with the laser beam

MAX Maximum value

P Pulsed wave laser beam

Plates Data pertaining to the collection plates

Total Total value

Acknowledgements

The development of this thesis would not have been possible without the continued support of many different, but equally valuable people. My two supervisors, Professor Massimiliano Vasile from the Advanced Space Concepts Laboratory at the University of Strathclyde and Dr Ian Watson from the Systems, Power and Energy Research Division at the University of Glasgow have been instrumental in defining the initial scope and development of the project, but still giving me the manoeuvrability to develop my own ideas and direction. It included the acceptance of PEGGY the vacuum chamber, Jimmy the spectrometer and Maxine the laser. I am grateful for these three additional, yet temperamental members of the experiment team. Professor Vasile's stupidly high standards, enduring love affair with MATLAB and tough-love approach to research has undoubtedly raised the standard of my research and supported my development as a professional and creditable researcher. He has taken on various different aliases during the last four years, and I am, in part, grateful for each. Thanks must therefore be given to Maximus the Great Defender of the Thesis, the Task Generator and a few other, more colourful names! Thank you for holding my hand, so very tightly, during the final review stages. There were moments when I questioned whether or not this document would ever get finished. Max, please accept my sincere thanks and appreciation for your all your enduring support - and my apologies for all the grief.

The interdisciplinary nature of my research has also given me the opportunity to work with a pool of highly talented and incredibly friendly people. Dr John-Mark Hopkins and Dr David Burns from the Institute of Photonics at the University of Strathclyde were vital in the development of the experiment platform, the loan of the laser and the generation of the preliminary space-based laser system (including its optical control). The latter was developed through the 2012/13 SYSNova Challenge (supported by ESA, General Studies Programme). Thanks are therefore given to the entire 2012/13 LightTough² SYSNova study team. This was lead by Professor Vasile and included members from the Advanced Space Concepts Laboratory at the University of Strathclyde (Massimo Vertrisano, Daniel Garcia-Yarnoz, Dr Pau Sanchez and myself), Fraunhofer UK (Dr John-Mark Hopkins), EADS Astrium Ltd (Steven Eckersley & Alastair Wayman), GMV Portugal (Joal Branco) and the University of Southampton (Dr Camilla Colombo).

Professor Martin Lee, Peter Chang and John Gillece from the School of Geographical and Earth Sciences at the University of Glasgow provided a seemingly continuous supply of olivine, sample preparation facilities and sessions in the scanning electron microscope. Peter McKenna from the University of Glasgow spent hours imaging each collection plate. Thank you for your dedication to the cause. Brian Robb, Denis Kearns, Colin Roberts,

Bernie Hoey, Ewan Russell, Mark Dragsnes, Tim Montgomery and Bill Monaghan, all technicians from the School of Engineering at the University of Glasgow, were always able to find time for PEGGY. Thank you for your continued support, endless loan of equipment and coping with me when I entered my over-protective mother-hen-mode. I hope that I was not too much of a nag!

The thesis was funded by the James Watt Research Scholarship from the University of Glasgow, the IET Postgraduate award, The Planetary Society and the GU68 Engineers Trust Award. Thank you all. Conference travel was supported by The Planetary Society, the Royal Aeronautical Society, the Royal Academy of Engineering and the IET. In particular, the experiment itself was funded by members of The Planetary Society, including - Mark Bennett, Alistair Reid Bradley, Woody Carsky-Wilson, John Dunse, John E. Lamerson, Hakon Ljogodt, Alastair Robertson and John Swanson. Thanks are also given to Bill Nye, Dr Bruce Betts and Mat Kaplan, all from The Planetary Society. I am also incredibly grateful to the many open and endless discussions with Dr Claude Phipps (Photonic Associates), Dr Kevin Housen (Boeing), Daniel Mazanek (NASA Langley), Dr Mark Bentley (Institut fur Weltraumforschung), Dr Paul Miller (Lawrence Livermore National Laboratory), Dr Eric Herbold (Lawrence Livermore National Laboratory), Dr Damian Swift (Lawrence Livermore National Laboratory), Dr Hector Lorenzana (Lawrence Livermore National Laboratory), Dr Martin Elvis (Harvard University), Dr Donald Yeomans (JPL/Caltech), Professor Philip Lubin (UC Santa Barbara), Dr Steve Norman (SPI Lasers), Greg Thomas (SPI Lasers), Dr David Mitchell (Coherent Inc), Dr David Stothard (Fraunhofer UK) and Mohamed Sacranie (Mettler Toledo). These discussions pushed my existing boundaries of thought and increased the value of the research topic.

Outside the technical domain, sincere thanks is given to the most cherished, yet equally annoying member of my family. Without the never-ending and unconditional support of my twin sister, Sarah Gibbings, I may have fallen at the first hurdle of self doubt. Thank you for always believing in me and giving me the strength to see things through. She has always taught me that any obstacle can be overcome with hard-work, discipline and dedication. Sarah, you are the unsung hero of this thesis. Thanks are also given to my mother for her timely injection of cash and the continued supply of gluten free goodies, and to my own personal editor-in-chief, Mr Geoff Noble. His painstaking effort in proof reading and in dealing with my infinite supply of typos deserves a medal. A massive hug is also given to my life-long friend Victoria Lowe, all the instructors and members of British Military Fitness and my office mates at the University of Glasgow and Strathclyde. Thank you for always giving me the opportunity to vent my day's frustrations and sharing in the joys of success. The Saturday morning, post-running breakfast club is greatly missed. Happy Days!



Dedication

Without the cumulative support of my family, and so many friends and colleagues, I would not have been able to transfer the document-of-doom into the big and bad book of knowledge. It was built on a steady supply of Irn-Bru and a mountain of jelly beans (my thanks to Dr Rene Laufer for the latter). Together, I am incredibly proud of what we have been able to achieve. It therefore gives me great pride and satisfaction, with a little of sorrow, to dedicate this document in the memory of my father Mr David Gibbings (1952-1993) and my dearest grandfather Mr Kenneth D. Ford (1928-2007). Gone but never forgotten.

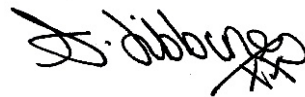
*Do not stand at my grave and weep
I am not there. I do not sleep
I am a thousand winds that blow
I am the diamond glints on snow
I am the sunlight on ripened grain
I am the gentle autumn rain
When you awaken in the morning's hush
I am the swift uplifting rush
Of quiet birds in circled flight
I am the soft stars that shine at night
Do not stand at my grave and cry
I am not there. I did not die*

Anonymous work of a fallen soldier

Declaration

I hereby declare that this submission is my own work and that, to the best of my knowledge and belief, it contains no material previously published or written by another person nor material which to a substantial extent has been accepted for the award of any other degree or diploma of the university or other institute of higher learning, except where due acknowledgement has been made in the text.

Glasgow, Scotland, UK, 2014

A handwritten signature in black ink, appearing to read 'A. L. Gibbings', with a stylized flourish at the end.

Alison L Gibbings

Publications

Some ideas and figures from this thesis have previously appeared, or will be appearing, in the following publications.

Journal Papers

- M Vasile, A Gibbings, J-M Hopkins, I Watson, Improved Laser Ablation Model for Asteroid Deflection, <http://dx.doi.org/10.1016/j.actaastro.2014.01.033i>, *Acta Astronautica*, 2014
- A Gibbings, M Vasile, I Watson, J-M Hopkins, Experimental Analysis of Laser Ablated Plume for Asteroid Deflection and Exploitation, *Acta Astronautica*, 90(1): 85-97, 2013
- A Gibbings, M Vasile, J-M Hopkins, D Burns, I Watson, Potential of Laser-induced Ablation for Future Space Applications *Space Policy: Assessing the Sustainability of Space Activities*, 28(3):149-153, 2012
- F Zuiani, M Vasile, A Gibbings, Evidence-based Robust Design of Deflection Actions of Near Earth Objects, *Celestial Mechanics and Dynamical Astronomy*, 114(1):107-136, 2012

Conferences

- A Gibbings, M Vasile, J-M Hopkins, I Watson, A Space-based Laser System for the Deflection and Manipulation of Asteroids, International High Power Laser Ablation and Beam Energy Propulsion Symposium, Santa Fe, USA, 2014
- M Vasile, M Vertisano, A Gibbings, D Yarnoz, J-P Sanchez, J-M Hopkins, D Burns, C McInnes, C Colombo, J Branco, A Wayman, S Eckersley, Light-Touch²: A Laser-Based Solution for the Deflection, Manipulation and Exploitation of Small Asteroids, Planetary Defense Conference: Gathering for Impact, Session 4: Mitigation Techniques and Missions, IAA-PDC13-04-22, Flagstaff, USA, 2013
- A Gibbings, M Vasile, J-M Hopkins, D Burns, I Watson, Experimental Characterization of the Thrust Induced by Laser Ablation onto an Asteroid, Planetary Defense Conference: Gathering for Impact, Session 4: Mitigation Techniques and Missions, IAA-PDC13-04-22, Flagstaff, USA, 2013 *Awarded 2nd prize in the student paper competition*

-
- A Gibbings, M Vasile, I Watson, J-M Hopkins, D Burns, Laser Ablation for the Effective Deflection, Exploration and Exploitation of Asteroids, Astrobiology Science Conference - Exploring Life: Past and Present, Near and Far, Atlanta, USA, 2012
 - A Gibbings, M Vasile, Smart Cloud - A Novel Method for the Deflection and Mitigation of Asteroids, Astrobiology Science Conference - Exploring Life: Past and Present, Near and Far, Atlanta, USA, 2012
 - A Gibbings, M Vasile, A Smart Cloud Approach to Asteroid Deflection, 62nd International Astronautical Congress, IAC-11-A3.4, Cape Town, South Africa, 2011
 - A Gibbings, M Vasile, A Smart Cloud Approach to Asteroid Deflection, Space Generation Congress, Cape Town, South Africa, 2011 *Winner of the Space Generation Advisory Council, Move an Asteroid Competition*
 - A Gibbings, E Komninou, M Vasile, Investigation and Modelling of Large scale Cratering Events - Lessons Learnt from Experimental Analysis, 62nd International Astronautical Congress, IAC-11-E1, Cape Town, South Africa, 2011
 - A Gibbings, J-M Hopkins, D Burns, M Vasile, I Watson, Exploring and Exploiting Asteroids with Laser Ablation, UK Space Conference, University of Warwick, Coventry, UK, 2011 *Short-listed for the 2011 Sir Arthur Clarke Award for Student Achievement; Advanced Space Concepts Laboratory, University of Strathclyde was awarded the 2011 Sir Arthur Clarke Award for its outstanding achievements in space research*
 - F Zuiani, M Vasile, A Gibbings, Robust Design of Deflection Actions for Non-Cooperative Targets, New Trends in Astrodynamics and Applications VI, Courant Institute of Mathematical Sciences, New York University, New York, USA, 2011
 - A Gibbings, J-M Hopkins, D Burns, M Vasile, I Watson, On Testing Laser Ablation Processes for Asteroid Deflection, IAA Planetary Defense Conference, Bucharest, Romania, 2011 *Awarded 1st prize in the student paper competition*
 - A Gibbings, M Vasile, Impact Cratering Experiments into Highly Porous Bodies, IAA Planetary Defense Conference, Bucharest, Romania, 2011 *Awarded 2nd prize in the student paper competition*
 - A Gibbings, E Komninou, M Vasile, Kinematic Impactors - Improved Modelling of Asteroid Deflection from an Experimental and Numerical Approach, European Planetary Science Congress, Rome, Italy, 2010

Technical Reports

- M Vasile, M Vetrivano, A Gibbings, D Yarnoz-Garcia, J-P Sanchez, D Burns, J-M Hopkins, C Colombo, J Branco, A Wayman, S Eckersley, C McInness, Light Touch²: Effective Solutions to Asteroid Manipulation, Final Report and Presentation - ESA SYSNova Challenge Opportunity Space Concept Competition:

To Compare Solutions to Given Space Mission Challenges, ESA/ESTEC, Noordwijk, The Netherlands, 2013 *Short-listed for the 2013 Sir Arthur Clarke Award for Student Achievement*

- A Gibbings, M Vasile, I Watson, J-M Hopkins, D Burns, LASER BEES - A Concept for Asteroid Deflection and Hazard Mitigation, Final Report and Presentation, The Planetary Society, Pasadena, USA, 2012
- A Gibbings, E Komninou, M Vasile, Large Scale Impact Cratering onto Highly Porous Asteroidal Bodies (Team No 1294), Final Experiment Report, ESA Education Office - Spin Your Thesis Campaign, 2010

External Presentations

- A Gibbings, M Vasile, I Watson, J-M Hopkins, An Introduction to Laser Ablation for the Deflection and Exploration of Asteroids, Equation of State Weekly Meeting, Lawrence Livermore National Laboratory, California, USA, 2013
- A Gibbings, M Vasile, I Watson, J-M Hopkins, M Vertisano, D Yarnoz, J-P Sanchez, C McInnes, C Colombo, J Branco, A Wayman, S Eckersley, D Burns, Using a Space-based Laser System for the Deflection and Exploration of Asteroids, International Graduate Summer School in Aeronautics and Astronautics, Beihang University, Beijing, China, 2013
- A Gibbings, M Vasile, I Watson, Deflecting, Exploring and Exploiting Asteroids with Lasers, International Space University Alumni Conference and Reunion, Strasbourg, France, 2013
- M Vertisano, A Gibbings, LightTough²: Autonomous Guidance Navigation & Control for Asteroid Deflection and Attitude Control via Laser Ablation, British Interplanetary Society, London, UK, 2013 *Short-listed (co-author), British Interplanetary Student Competition for UK representation at the 2013 International Astronautical Congress, Beijing, China*
- A Gibbings, M Vetrisano, Exploring and Deflecting Asteroids with Lasers, SET for Britain, House of Commons, Westminster, UK, 2013 *Finalist in exhibiting at the poster competition*
- M Vetrisano, A Gibbings, Deflecting Small Asteroids using Laser Ablation: Deep Space Navigation and Asteroid Orbit Control, SET for Britain, House of Commons, Westminster, UK, 2013 *Finalist in exhibiting at the poster competition*
- M Vasile, M Vetrisano, A Gibbings, D Yarnoz-Garcia, J-P Sanchez, D Burns, J-M Hopkins, C Colombo, J Branco, A Wayman, S Eckersley, C McInness, Light Touch²: Effective Solutions to Asteroid Manipulation, Final Review and Presentation - ESA SYSNova Challenge Opportunity Space Concept Competition: To Compare Solutions to Given Space Mission Challenges, SYSNova Workshop, 3rd Session: Contactless Asteroid Orbit Modification, ESA/ESTEC, Noordwijk, The Netherlands, 2013

-
- A Gibbings, Experimental Analysis of Laser Ablation for Asteroid Deflection and Exploitation, SET for Britain, House of Commons, Westminster, UK, 2012 *Finalist in exhibiting at the poster competition*
 - A Gibbings, M Vasile, I Watson, J-M Hopkins, D Burns, LASER BEES - A Concept for Asteroid Deflection and Hazard Mitigation, Final Presentation, The Planetary Society, Pasadena, USA, 2012
 - A Gibbings, F Zuiani, M Vasile, J-M Hopkins, D Burns, Asteroid Ablation: Experimental Investigation of Laser Momentum Coupling and Ejecta Plume Formation, Fly Your Thesis! Selection Workshop, ESA/ESTEC, Noordwijk, The Netherlands, 2011

Magazine Articles

- A Gibbings, LASER BEES - A Swarm of Solar Powered Lasers for Asteroid Deflection and Exploration, *Spaceflight*, 1(8):307-311, 2012
- Gibbings A, Vasile M, Smart Cloud to Deflect Killer Asteroids, *New Scientist*, 2863(1):14, 2012

Outreach Presentations

- M Vertisano, A Gibbings, M Vasile, Exploring and Deflecting Asteroids with Space-based Lasers, UK Space Conference Exhibition, Scottish Exhibition & Conference Centre, Glasgow, UK, 2013
- A Gibbings, M Vasile, I Watson, Using Lasers to Deflect and Explore Asteroids, Will We Be Next? - Tunguska 105, Association with Scotland Research into Astronautics and the Space Settler's Society, Mitchell Library, Glasgow, UK, 2013
- G Notkin, E Ryan, L Benner, D Trilling, A Mainzer, D Koshchyn, J Melosh, S Camacho, A Gibbings, A Harris, B Barbee, D Mazanek, Planetary Defense: 2013 Planetary Defense Conference, NASA Edge TV, 2013
- A Gibbings, Exploring and Deflecting Asteroids with Laser Systems, IMechE Speak Out for Engineering Competition, Glasgow, UK, 2013 *Winner of the Glasgow Heat*
- A Gibbings, M Vasile, I Watson, Deflecting and Exploring Asteroids with Lasers, University of Strathclyde Research Day, Glasgow, UK, 2013
- A Gibbings, Kindred Spirits: Alison Gibbings and Carolyn Shoemaker at the Planetary Defense Conference: Gathering for Impact, Planetary Radio Show, Flagstaff, USA, 2013
- A Gibbings, Tracking a Space Rock's Streak Past Earth, Science Friday, National Public Radio, USA, 2013
- A Gibbings, M Vasile, I Watson, Using Lasers for the Deflection and Exploration of Asteroids, College of Science and Engineering - Industry Day, University of Glasgow, Glasgow, UK, 2013

-
- A Gibbings, Laser Ablation for the Effective Deflection, Exploration and Exploitation of Asteroids - the Opportunity and the Risk, IMechE Speak Out for Engineering Competition, Glasgow, UK, 2012 *Awarded 2nd prize in the Glasgow heat*
 - A Gibbings, Can Laser Bees Save Earth? Exploring Asteroid Deflection, Planetary Radio Show, Pasadena, USA, 2012
 - A Gibbings, Smart Cloud - Move an Asteroid Competition May Help Protect Planet, Science Friday, National Public Radio, USA, 2011

Introductory Scope

The purpose of this doctoral dissertation is to investigate the potential of laser ablation as a contactless method of asteroid deflection. Any Earth-impacting asteroid event could cause extensive damage, tsunamis and even the mass extinction of life. It has happened before and it will happen again. However, technologies and approaches are being investigated to mitigate the risk and to provide a suitable deflection action. Laser ablation could be a possible solution. It is achieved by illuminating any surface with a laser light source. The heat from the laser beam is absorbed into the exposed material, enabling it to sublimate directly from a solid to a gas. The sublimated material then forms into a plume of ablated material. Similar to a rocket exhaust, the flow of ablated material produces a continuously controlled low thrust. This low thrust can modify the trajectory and tumbling motion of an asteroid.

Previous analysis performed by Sanchez et al. [2009] demonstrated the theoretical capability of surface ablation. With a relatively low mass into space, and a short warning time, ablation can provide a controllable deflection action. Here, the energy input is provided by concentrated solar energy. A large space-based solar concentrator can collect, focus and sublimate a small portion of the asteroid's surface [Melosh and Nemchinov, 1993; Melosh et al., 1994]. However launching and operating a single and large spacecraft is a significant technological challenge. The solar concentrator needs to be manoeuvred at close proximity to the asteroid, under the asteroid's irregular gravity field. The contaminating effects of the ejecta plume are also unknown.

A simpler and more adaptable solution could be to split the single spacecraft into multiple units. A swarm of small scale, low power spacecraft could fly in formation with the asteroid. Their overlapping beams of light would be used to increase the surface power density, enabling its sublimation [Vasile et al., 2009a; Maddock et al., 2009, 2007]. This provides a far more flexible solution that can be easily scaled. The number of spacecraft would depend on the size and composition of the asteroid and the warning time before impact. Multiple spacecraft also permit the delivery of a much more powerful system. This reduces the required time needed to achieve a suitable deflection distance and the occurrence of any single point failure.

Alternatively a collimated or focused laser beam could be used to increase the operating distance between the asteroid and the spacecraft. Lasers provide a convenient, versatile and predictable method of transporting energy. Each spacecraft could be equipped with an identical kilo-watt class, solar powered laser [Vasile et al., 2009b]. The swarm would be less affected by the asteroid's irregular gravity field and the contaminating

effects of the ejecta plume. Larger mega-watt or giga-watt space-based lasers could also be used. Powered by a nuclear reactor, the laser could be mounted onto a single spacecraft, the International Space Station (ISS) or the Moon [Park and Mazanek, 2005b; Yoo et al., 2009; Song et al., 2009; Ivashkin, 2004; Mazanek, 2005]. This however would require developing a high-power, space-based laser system and overcoming the significant political ramifications of launching, controlling and operating a nuclear reactor in space. A swarm of low power, but highly efficient space-based lasers, powered by conventional solar arrays is therefore a far more attractive solution.

More research is still required to advance the current understanding of laser ablation as an asteroid deflection method. The initial ablation model was based on an energy balance. Proposed by Kahle et al. [2006] and expanded by Sanchez et al. [2009], it combined the absorption of the laser beam, the sublimation enthalpy of the asteroid, and the heat loss through conduction and radiation respectively. The model was also developed from three fundamental assumptions. It defined the physical formation of the ejecta plume, the composition of a dense and homogeneous target asteroid with a one-dimensional transfer of heat, and the potential of the ejecta plume to contaminate any exposed surface. The formation of the ejecta plume was therefore expected to be similar to the rocket exhaust in standard methods of rocket propulsion. The ejecta plume is limited to the generation of a mono-energetic, friction-free compressible gas without any ionisation. Degradation, caused by the deposition of the ejecta plume, is assumed to follow the Beer-Lambert-Bouguer law. Any particle of ejecta will immediately re-condense and stick onto any exposed surface. A thin layer of permanently attached material will form. Degradation is expected to be dependent on the absorptive properties - absorptivity, height and density - of the deposited ejecta. Affected surfaces include solar cells, radiators, multi-layering insulation (MLI) and any optical surface or device.

To examine the viability of these assumptions and the general applicability of the ablation and contamination models, a series of laser ablation experiments were performed. In vacuum, a 90 W continuous wave laser beam has been used to re-create the laser-asteroid ablation event. Operating at a wavelength of 808 nm, a rocky magnesium silicate based material (olivine) was ablated. Olivine was used to represent a rocky and solid asteroidal body. Assessed parameters included the average mass flow rate, dispersion, temperature and velocity of the ejecta plume and the height, density and absorptivity of the deposited ejecta. Degradation caused by the deposited ejecta is a critical factor. It will affect the performance of the laser beam, its operational lifetime and the overall endurance of the ablation technique. The system performance of the spacecraft will also be affected. The ejection of material will affect the stability and directionality of the resultant thrust vector.

Results gained from the experiment have enabled the ablation model to be updated and the performance of a laser ablation deflection mission to be reassessed. A critical discrepancy was in the variation between the previously predicted and experimentally measured mass flow rate of the ablated material. This may lead to an overestimation in the thrust generation ability of the laser ablation process. Other improvements to the ablation model also included the energy absorption within the Knudsen layer, the

variation of sublimation temperature with local pressure, the temperature dependent thermal conductivity of the target material and the partial re-condensation of the ablated material. An analytical expression was also derived that compared the deflection system mass of the laser ablation system to produce a given Δv to other forms of electric propulsion. Ion beaming and the gravity tractor, for example, could provide an alternative low thrust, contactless deflection technique. Other assessed performance parameters also included a revised contamination factor, achievable momentum coupling, input power to the laser, spot size radius and the operating distance from the asteroid. These factors define the mission performance of the ablation process and the operational conditions of the laser system. The impact of a laser ablation system on the design - mission architecture, spacecraft design and subsystem analysis - of a deflection mission have also be considered. It demonstrated the technological capabilities of laser ablation in providing a sufficiently high and measurable deflection action. Results will show that laser ablation is always more advantageous in the deflection of small and medium size asteroids. The same technique can also be applied to the de-orbiting of space debris [Vasile et al., 2010a,b].

The thesis is structured in the following - Chapter 2 introduces the reader to the risk posed by asteroids. Past impact events are used to demonstrate their destructive potential. Close planetary encounters highlight their ongoing risk. The asteroid population is also presented and further divided by their orbital characteristics, diameter and inferred material composition. Past, current and planned missions demonstrate the pertinent interest in the exploration of asteroids. It includes closes planetary flybys, remote sensing, in-situ and sample return missions, a range of ground based telescopic platforms and near-Earth orbiting platforms. European capabilities are also being developed through large framework programmes. Chapter 3 presents the different impulsive, low thrust and passive methods of deflection. The common objective is to increase the minimum orbit interception distance between the Earth and the asteroid. Results from a comparative analysis are presented. This suggests the theoretical benefits of a surface ablation event. Chapter 4 shows how the strategic development of lasers and optical technology has expanded the commercial and scientific capability of laser ablation. Three main space-based applications are presented. This includes launching and controlling vehicles in space, the de-orbiting of space debris and the deflection of Earth approaching asteroids. It includes both ground and space-based systems. The input energy can be collected solar radiation or a laser beam.

Chapter 5 details the initial and improved ablation model. Initially developed by Kahle et al. [2006] and expanded on by Sanchez et al. [2009], it combines the energy balance of sublimation with the data gained from the experimental results. Modelled parameters include the mass flow rate, velocity and density distribution of the ejecta plume, the contamination caused by the deposited ejecta, and the momentum coupling between the asteroid and the laser beam. Chapter 6 details the experiment platform and results. It includes the design of the laser system, the selection of the target material and all of the diagnostic procedures. The experiment measured the divergence, average mass flow rate and temperature of the ejecta plume and the composition, absorptivity, height and density of the deposited ejecta. The momentum coupling is

also inferred. Chapter 7 shows how the improved ablation model can be used to revise the performance of laser ablation in providing a deflection action. Assessed parameters included a revised contamination factor based on the absorptivity of the deposited ejecta, momentum coupling, Δv and the deflection system mass. To exceed the performance of other methods of low thrust, contactless deflection, the laser system must surpass a minimum input power and momentum coupling. These factors govern the surface spot radius, operating distance (and therefore its optical control) and the expected level of contamination. Chapter 8 demonstrates how a relatively simple, laser ablation system could be implemented, and considers the design and integration of a viable spacecraft design.

The concluding remarks and discussions of the future work are presented in Chapter 9. The thesis is supported by ten appendices. Appendix A provides instruction on the manufacture of a highly porous, composite material. Appendix B reviews all the test equipment and proposed methodologies that were developed for the experiment. The health and safety issues of operating the laser are addressed in Appendix C. Appendix D details the operational procedures of the laser system. Appendices E and F provide additional information on the layout - optical bench and collection plate holder - of the experiment. Data from the Scanning Electron Microscope (SEM) are presented in Appendices G and H. Appendix I provides an example of the error bar analysis. The scatter factor is derived in Appendix J. A scatter factor is used throughout the ablation model. Appendices K and L provide a technical description of the combined roughing and diffusion pump, and its operational procedure.

Asteroids

2.1 Introduction

Asteroids, the rocky remains from planetary accretion, represent both an opportunity and a risk. Their pristine environment captures the early impact evolution of the solar system, while their inherent impact potential with Earth could result in the mass extinction of life. Data combined from astronomical telescopes, space surveys and deep space radar suggest that there are at least 2,000 to 20,000 objects - asteroids and comets - that could impact the Earth [Morrison, 2007; Campbell et al., 2002; Canavan, 1996].

On average an asteroid with a diameter greater than 100 m impacts the Earth once every 10,000 years [Morrison et al., 2004]. This can cause extensive land damage, earthquakes and tsunamis [Campbell et al., 2002]. Smaller objects are more frequent, but are far less dangerous. Most will break-up in the atmosphere as meteorites. Larger objects, asteroids greater than 1 km in diameter are considered to be global killers. This could catastrophically annihilate 90 % of all life [Ahrens and Harris, 1994; Campbell et al., 2002]. Global climate change would be caused by extensive firestorms, land damage and the destruction of the ozone. The Earth would have little chance of near-term recovery. An example of global annihilation occurred approximately 65 million years ago with the Cretaceous-Tertiary mass extinction of the dinosaurs and numerous other species [Alvarez et al., 1980; Sharpton and Ward, 1990]. The impact site is believed to be in Mexico, just off the Yucatan Peninsula [Alvarez et al., 1980]. Although the risk of such an impact is relatively low, approximately once every 100,000 years, the corresponding destruction is immense [Canavan, 1996]. The range of catastrophic consequences cannot be ignored.

The Earth has been, and will continue to be the subject of many different ground and air impacting events. It is just a matter of time. Asteroids are responsible for the formation of at least 170 impact craters on the Earth and almost all the craters on the Moon [Ahrens and Harris, 1994; Grieve and Shoemaker, 1994]. The magnitude of damage is dependent on the asteroid's size, composition and structure, relative velocity and impact location [Ahrens and Harris, 1992; Gritzner and Kahle, 2004; Grieve and Shoemaker, 1994]. Table 2.1 summarises this affect [Morrison et al., 1994].

In 1908 an aerial explosion of a 60-100 m diameter asteroid, known as the Tunguska fireball, in Siberia, Russia resulted in the wide spread deviation of over 2,000 km² of isolated forest. It was equivalent to the release of 5 mega-tonnes of TNT. If this had occurred over a densely populated area, then the consequences would of been devastating

Asteroid Diameter	Energy Yield (MT)	Consequence
< 50 m	< 10	High, upper atmosphere break-up of asteroids and comets
50 - 300 m	10^1 - 10^3	Tunguska class event produces a large impact crater or air burst that destroys large local areas of land.
300 m - 2 km	10^3 - 10^5	Sub-global impacts event on either land or ocean causes significant land damage and tsunamis.
1 - 3 km	10^5 - 10^6	Threshold for global catastrophes caused by both land and ocean impacts. This results in the global destruction of the ozone and hemispheric scale tsunamis. Land damage is comparable to a large state or country
> 4 km	$>10^7$	Mass extinction event that threatens the survivals of all advanced forms of life. Destruction occurs on a continental scale, with prolonged climate effects and global conflagration.

Table 2.1: Summary of the Impact Effects Caused by an Impacting Asteroid

[Ahrens and Harris, 1994]. Another more pressing example is asteroid 99942 Apophis. Apophis is a 325 m diameter asteroid that was considered to pose a non-negligible impact risk of occurring in 2036 [Chesley, 2006]. Uncertainty was based on inaccuracies in the asteroid's observational data. The impact potential was also dependent on the asteroid passing and interacting with Earth's gravity. This could occur on its earlier terrestrial flyby in 2029 where Apophis will pass $\sim 36,000$ km from the centre of the Earth, travelling inside the orbit of geostationary satellites. The interaction with Earth's gravity could be enough to shift its orbit into one that would collide with Earth on its later 2036 approach [Valsecchi et al., 2003; Milani et al., 2004]. Apophis's impact would be equivalent to the release of 875 mega-tonnes of TNT [Yeomans et al., 2009]. This would cause catastrophic damage over an area equal in size to Tokyo, Paris or Washington [Morrison et al., 1994]. However, new, more recent observations have further refined the asteroid's orbital parameters and estimated impact risk. Data gained from optical telescopes and deep space radar have ruled out the possibility of a direct impact event. Apophis is still classified as a hazardous object, but the emphasis is now on its scientific investigation. It is however still considered to be a good candidate for further analysis and research.

The Earth could still be subjected to other near-miss or direct impact events. It could be caused by, but is not limited to, asteroid 1997 XF11, 1999 RQ36, 2005 YU55, 2007

PA8, 2011 AG5, 2012 DA14, 2012 BX32, 2012 NT7, 4179 Toutatis (1989 AC), 2012 YQ1, 2013 TV135 and 2013 GM3. On the 15th February 2013, the small, rocky asteroid 2012 DA14 passed within 27,000 km of the Earth. Its trajectory was inside the orbit of geostationary satellites. On the same day Russia suffered from a small, yet previously undetected, meteorite explosion. This occurred over the Ural mountains, above the city of Chelyabinsk. The resulting shock-wave shattered windows, caused 1,200 related injuries and \$33 million-worth of damage. It was unrelated to the close approach of 2012 DA14. The probability of both events happening at the same time was estimated to be 10^{-4} - 10^{-9} .

2.2 The Characterisation of Asteroids

To fully assess the impact potential of asteroids, research has been conducted to discover, track and examine any potentially threatening object. It includes ground based surveys performed by the international Spaceguard Survey, the radar facilities at Arecibo and Goldstone, and the European Space Situational Awareness Preparatory Programme [Ostro and Giorgini, 2002]. Other telescopic platforms also include the Lincoln Near Earth Asteroid Research programme and the Near Earth Asteroid Tracking programme [Morrison, 2007, 1992]. More recent tracking programmes include the Panoramic Survey Telescope and Rapid Response System, the Large Synoptic Survey Telescope, the La Sagra Sky Survey and the Catalina Sky Survey [Chesley and Spahr, 2004]. These programmes have provided essential information on the size, density, spin rate and shape of asteroids [Huebner and Greenberb, 2000; Fork, 2007; Chesley and Spahr, 2004]. The University of Hawaii is also developing the Asteroid Terrestrial-Impact Last Alert System. This would be used as a rapid response warning system of an impending impact event. Other proposed space-based detection systems include the NASA Near Earth Object Camera space telescope and the B612 Foundation's privately owned and operated infrared space telescope.

The majority of asteroids are located within the main asteroid belt, between the orbit of Mars and Jupiter. These objects are known as main belt asteroids, but have the potential to be classified as Near Earth Asteroids (NEAs). Changes in an asteroid's orbital characteristics can be enough to shift the asteroid onto a close proximity trajectory with the Earth. This can be caused by planetary encounters, orbital precession, collisions and a periodic variation in the asteroid's orbital elements [Ahrens and Harris, 1994; O'Brien and Greenberg, 2005; Binzel et al., 2004a]. NEAs can be further divided into three main categories. This includes Apollo, Amor and Aten type asteroids [Shoemaker et al., 1979; Binzel et al., 2004a]. The division between each category is based, with respect to Earth, on their orbital characteristics. This is illustrated further in Figure 2.1 [Morrison, 2007; Belton et al., 2004].

Apollo and Aten type asteroids are classified with an Earth-crossing orbit. They currently account for 90 % of all NEAs and are relatively equal in number. A minor subgroup of the Atens type asteroids are the Atiras. These are asteroids whose orbital elements are contained within the orbit of the Earth. They are limited in number, with only

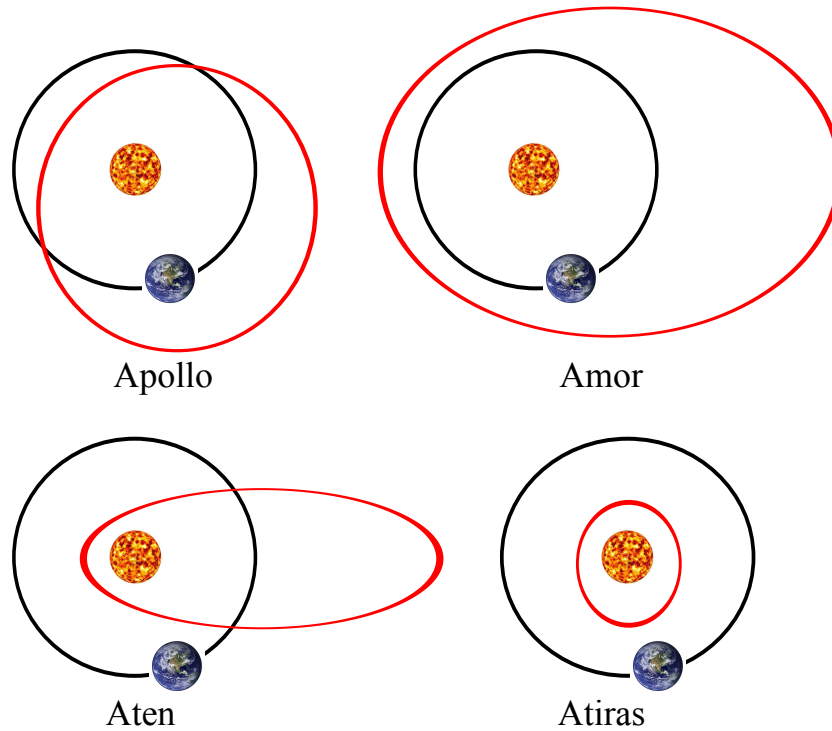


Figure 2.1: Orbital Locations of Near Earth Asteroids - Drawn from Morrison [2007]; Belton et al. [2004]

twelve recorded observations. The majority of their orbital passes occur in Earth's daytime sky, this makes them rather difficult to detect and observe with ground-based observations. There may be more in existence. Amor type asteroids exist just outside Earth's orbit. They can (together with the Atiras type) however be perturbed into an Earth-crossing trajectory. They are smaller in population, accounting for only 8 % of the NEA population. The remaining 2 % include short period comets [Binzel et al., 2004a].

Potentially Hazardous Asteroids (PHAs) are those objects characterised with a diameter greater than 100-150 m and a minimum orbital interception distance with the Earth of 0.05 AU or less (~ 7.5 million km) [Gritzner and Kahle, 2004; Ostro and Giorgini, 2002]. The minimum diameter of the asteroid is based on its observable absolute magnitude and albedo. It is however the size, not the colour, of the asteroid that makes it dangerous. A close approach of any PHA does not necessarily indicate that it will impact the Earth. It is merely the possibility and threat that an impact event might occur.

Asteroids can also be classified by their spectral characteristics and albedo. These factors are then related to a taxonomic classification which is used to infer the asteroid's surface mineralogy [Bowell et al., 1987]. The four main categories include S, C, M and E class asteroids. It is defined further in Table 2.2 [Harris, 2004; Rivkin et al., 2000; Gaffey et al., 2004; Clark et al., 2004; Pieters and McFadden, 1994; Remo, 1994]. S and C class asteroids are the most common classification within the NEA population.

There is also a suggestive generic link between the meteorites found on Earth and the asteroid population. A meteorite is a fragmented piece of a much larger NEA. It has survived its passage through the Earth's atmosphere without being completely vaporised

Asteroid Class	Suggested Surface Mineralogy	Range of Albedo
S	Silicates (olivine, pyroxene) and metals	10-30 %
C	Carbon, organics and hydrated silicates	3-10 %
M	Highly metallic with possible traces of silicate	10-20 %
E	Enstatite and/or other iron free silicates	30-60 %

Table 2.2: Asteroid Class relative to Surface Mineralogy and Albedo

[Pieters and McFadden, 1994]. Although not conclusive and representative within the entire asteroid population, a few unambiguous spectral and mineralogical associations have been established [Remo, 1993; Harris, 2004; O'Brien and Greenberg, 2005; Remo, 1994; Price, 2004]. S, C and E class asteroids are considered to be mineralogical similar to ordinary chondrite, primitive carbonaceous chondrite and enstatite chondrite meteorites respectively [Harris, 2004; O'Brien and Greenberg, 2005; Remo, 1994; Chapman, 1996]. These are known as non-differentiated structures that still reflect the composition of their parent body. M class asteroids are linked to stony iron meteorites and enstatite chondrite [Rivkin et al., 2000]. Iron meteorites are highly processed bodies that have undergone extensive interior melting, melt migration and fractional crystallisation [Remo, 1993; Burbine et al., 2004; Perron and Zanda, 2005]. Differentiation would have caused the initially homogeneous body to separate into different layers of composition. No single sample is therefore representative of the entire parent body [Perron and Zanda, 2005].

The vast majority of meteorites are collected from Antarctica and the dry deserts of Africa and Australia [Weisberg et al., 2006]. Ordinary chondrites are by far the most common meteorite group, accounting for 80 % of the meteorite collection [Remo, 1993; Britt et al., 1992; Weisberg et al., 2006]. They also provide the best spectral match to the NEA population. Ordinary chondrites can be further divided into three main groups. Based on their iron content this includes: H (a high iron content greater than 50 %), L (a low iron content) and LL (a low iron content where most of the material has been oxidised) [Burbine et al., 2004; Pieters and McFadden, 1994; Perron and Zanda, 2005]. Carbonaceous chondrites are the rarest group within the meteorite collection. This is due to their low mechanical weakness and inability to survive the passage through the Earth's atmosphere.

2.3 Missions to Asteroids

National and international space agencies have sent many different, yet scientifically orientated space missions to investigate the physical and chemical properties of asteroids and comets. It has included close proximity flybys, rendezvous, in-situ analysis and sample return missions [Morrison, 2007; Cheng, 2004; Muller et al., 2007]. The first three are directly applicable to any deflection based mission, while the fourth is more relevant to scientific and exploration based activities. These exploration missions have,

and continue to include:

Past Missions

- **Soviet Union Vega spacecraft (1984-1986)** Two identical spacecraft, VEGA-1 and VEGA-2 intercepted comet P/Halley on a flyby mission. This was part of an international exploration fleet that encountered the comet.
- **ESA GIOTTO (1985-1992).** GIOTTO was ESA's first deep space mission. It captured the first close-up images of comet P/Halley and studied comet P/Grigg-Skjellerup during its extended mission.
- **NASA Galileo (1989-2003)** The Galileo mission to Jupiter consisted of two spacecraft; an Orbiter and an atmospheric probe. The mission objective was for the Orbiter to study Jupiter, its satellites and its magnetosphere for two years, and to send a probe into Jupiter's atmosphere. En-route to Jupiter the spacecraft passed through the main asteroid belt. This enabled flyby analysis of asteroids 951 Gaspra and 243 Ida (and Dactyl). It also observed the fragmented impact of comet Shoemaker-Levy into Jupiter.
- **NASA Clementine mission (1994)** Primarily a Moon mission, Clementine performed remote sensing observations of the lunar surface, with the intention of performing flyby analysis of asteroid 1620 Geographos. However the spacecraft experienced an onboard computer failure. This caused one of its attitude control thrusters to burn all the remaining fuel. The flyby was no longer possible. Instead the spacecraft was placed into a geocentric orbit, passing through the Van Allen radiation belt.
- **NASA/APL Near Earth Asteroid Rendezvous (NEAR) Shoemaker mission (1996-2001)** The NEAR spacecraft performed flyby analysis of asteroid 433 Eros, 951 Gaspra, 243 Ida and 253 Mathilde. The mission terminated by touching down on Eros a year later. Eros, Gaspra and Ida are S class asteroids. Mathilde is a highly porous C class asteroid. The mission was funded by NASA, but managed by the Johns Hopkins University Applied Physics Laboratory (APL). The spacecraft was also designed and built at APL.
- **NASA Deep Space 1 mission (1998-2000)** This was a technology demonstration probe that performed a flyby mission of asteroid 9969 Braille and the comet Borrelly.
- **NASA Stardust mission (1999-2006)** This mission performed flyby analysis of asteroid 5535 Annefrank and returned samples to Earth from comet Wild2. Its primary mission objective was to collect interstellar dust particles from the comet's coma. This was achieved with an aerogel collection device that was externally mounted onto the spacecraft. During the spacecraft's return the mission was extended to include an encounter with Temple 1. Temple 1 had been previously impacted by the NASA Deep Impact mission.
- **NASA Comet Nucleus Tour mission (2002)** This mission intended to visit two comets; Encke and Schwassmann-Wachmann-3. The mission failed six weeks

after launch during a planned inter-planetary burn manoeuvre.

- **China Space Probe Chang'e-2 (2003-2011)** This mission performed a close flyby of asteroid 4179 Toutatuis. It was part of a much larger, three-phase lunar exploration activity. It demonstrated China's operational capability for interplanetary navigation and flight.
- **NASA Deep Impact mission (2005-2013)** This mission collided a 366 kg spacecraft-impactor into the nucleus of a 6 km diameter comet, 9P/Tempel 1. The impact event was observed by an accompanying spacecraft. The mission was extended to perform a flyby of comet Hartley2 and remote distant imaging observations of comet C/2009 PI (Garrado) and ISON.

Current Missions

- **NASA/ESA Cassini-Huygens mission (1997+)**. This joint mission consists of the Cassini Orbiter and a smaller planetary probe. The mission objective was to orbit Saturn, performing structural and compositional analysis of the planet, and to deliver the Huygens probe onto the surface of Titan. During its orbital transfer to Saturn, the Orbiter-spacecraft flew through the main asteroid belt, performing flyby analysis.
- **ESA Rosetta mission (2004-2014+)**. The Rosetta spacecraft is due to rendezvous with comet 67/P Churyumov/Gerasimenko in 2014. It will release a small lander that will attach itself onto the surface of the comet performing in-situ analysis. The spacecraft will also perform remote sensing measurements of the comet. En-route to the comet the spacecraft has performed flyby analysis of asteroid 21 Luteita and 2867 Steins. Luteita and Steins are M and E class asteroids respectively.
- **JAXA Hayabusa Sample-Return Mission Series (2003-2020+)**. The first Hayabusa spacecraft, launched by the Japanese Aerospace Exploration Agency (JAXA), successfully rendezvoused with asteroid 25142 Itokawa (S class asteroid). It performed two touch down manoeuvres, released (unsuccessfully) a small micro rover and retrieved a small milligram sample of dusty regolith from the asteroid's surface [Kawaguch et al., 2003].

The spacecraft suffered from several different equipment failures. It included two-of-the-three reaction wheels, the ion-engines, the batteries, a fuel leak and a periodic loss of communication with the Earth [Fujiwara et al., 2006]. These problems caused a malfunction in the attitude and orientation of the spacecraft. It also prevented the collection of any other samples. Despite this, Hayabusa returned to Earth in June 2010.

Hayabusa-2 is due to be launched in 2014/15 and will arrive at asteroid 1999 JU34 (C class asteroid) in 2018. The spacecraft's design philosophy is based on the first Hayabusa spacecraft (for example, heritage, lessons learnt). It has enabled the rapid development of the design, production and testing of the spacecraft. It also permitted engineers and scientists to obtain a higher level of system reliability and

scientific capability. Almost all of the spacecraft components have been replaced or updated with state-of-the-art alternatives [Tsuda et al., 2012]. Hayabusa-2 aims to return samples of the asteroid's subsurface material. A high speed impactor will be released by the spacecraft and create a 2 m diameter crater. The ejected fragments will be collected and the newly exposed subsurface material will be sampled. The spacecraft is also equipped with a lander, three small rovers and a range of remote sensing instruments [Tsuda et al., 2012].

- **NASA DAWN mission (2007-2015+)** This is a deep space remote sensing asteroid mission. It has performed extensive geological and geochemical observations of Vesta, the second most massive object in the main asteroid belt. Over a year of observations has led to several scientific discoveries. This includes extensive scarring of two colossal impact events, deep impact basins, equatorial troughs and complex cratering [Russell et al., 2012]. Vesta is believed to be a protoplanet with a differentiated, dense iron-nickel core, mantle and crust. More recently, the spacecraft (as of the date of writing) embarked on a two-and-a-half year journey to the dwarf planet Ceres, also located in the main asteroid belt (arriving in early 2015). Here, the spacecraft will perform a detailed, five month study, on Ceres's structure and composition.
- **NASA NEOWISE (2009-2011)** This is an extension of the NASA Wide-Field Infrared Survey Explorer (WISE) telescope. Positioned in a nearly polar orbit, with a 40 cm diameter aperture and infrared camera, the telescope has performed a global assessment and prediction of the entire solar system population of PHAs, main belt asteroids and comets. Results have revealed new, creditable estimations, on the number, size, danger and origins of PHAs. In late 2013, after a two year hibernation period, NEOWISE is continuing its detection and identification of NEAs. It supports the target selection of a new NASA asteroid initiative programme.

Other proposed robotic concept missions have included, but are not limited to, Marco Polo(-R), Don Quijote, OSIRIS-REx and AIDA. Marco Polo, under the ESA Cosmic Vision programme, was first conceived as an asteroid sample return mission. This was later adapted into an in-situ remote sensing mission and is now being considered as a smaller, low-cost (medium class, 470M Euros) sample return mission. Launched between 2020-2024 Marco Polo-R aims to investigate asteroid 2008 EV5 (1996 FG3 as the back-up), returning 30-100 g of material to Earth for further analysis. 2008 EV5 is a primitive, C class asteroid [Barucci et al., 2012, 2013]. The mission has the potential to revolutionise the current understanding of primitive solar system bodies, the primordial conditions responsible for planet formation and the emergence of life. Key technological and strategic mission development can also be applied to protect the Earth from any incoming asteroid impact event. Don Quijote was developed as an asteroid deflection technology demonstrator mission [Milani et al., 2003]. It included two spacecraft - an Orbiter and an impactor - that would rendezvous with a given asteroid. Each spacecraft would be launched into a separate interplanetary trajectory. The impactor would be used to impact the asteroid. This would enable the Orbiter to measure the resulting transfer of

momentum, variation in orbital parameters and rotational state of the impacted asteroid. The Orbiter would also perform assessment of the asteroid's composition, size and surface parameters [Milani et al., 2003].

OSIRIS-REx (Origins, Spectra, Interpretations, Resource Identification, Security & Regolith Explorer) is an asteroid sample return mission. Intended to be launched in 2016, it will arrive at the C class asteroid 1999 RQ36 in 2018. Here, it will perform precise measurement on the Yarkovsky effect. It will also perform detailed mapping of the asteroid's surface and collect samples of the surface regolith. More than 60 g of material will be retrieved through a touch-and-go manoeuvre. Samples will be returned to Earth in 2023 [Mink et al., 2013; Russell et al., 2013]. The scientific objectives of the OSIRIS-REx mission will also be supported with the complementary operations of a small, independent and autonomous impactor-spacecraft. The Impactor for Surface and Interior Science (ISIS) intends to arrive after the OSIRIS-REx mission and will guide itself to perform a high-velocity impact event with asteroid 1999 RQ36. The collision will be observed by the awaiting OSIRIS-REx spacecraft. OSIRIS-REx will also perform a series of slow flybys taking images and spectra measurements of the impact site. ISIS is a secondary payload on the NASA Discovery programme InSight mission. It was designed to leverage NASA's investment in the OSIRIS-REx mission and the InSight launch opportunity. The mission will address Discovery-level science themes, the strategic knowledge gaps for human exploration and demonstrate an asteroid impact mitigation technology [Chesley et al., 2013]. NASA is also planning a possible crewed mission to an asteroid by 2025.

ESA is also appealing for research ideas to help guide the development of the Asteroid Impact & Deflection Assessment (AIDA) study. AIDA is a joint international (USA and European led) asteroid impact mission. It aims to characterise the orbital, physical (for example, size, mass, surface features) and rotational state of the binary asteroid system Didymos. Two independent, but mutually supporting mission concepts are being evaluated. It includes the Double Asteroid Redirection Test (DART) and the Asteroid Impact Monitoring mission (AIM). The DART mission will use a single spacecraft to impact the smaller, 150 m diameter member of the binary system. It will produce an orbital deflection that is larger and easier to measure than an impact into a typical, single NEA. The DART impact will be observable by ground-based radar and optical telescopes. This will be used to record the deflection event. Data will also be gained on the target body's geology and surface features. AIM is a rendezvous mission and will examine the physical and dynamic characteristics of the binary asteroid. It will also observe the DART-induced impact crater and derive the collision and impact properties. To support this mission concept, ESA is inviting all international institutions to submit experimental research ideas relating to impact and collision physics, applied planetary science, planetary defence, human exploration and technology innovation in spacecraft operations and navigation. The call will assist ESA to map the global interests of asteroid assessment, hypervelocity impacts and debris, and detector technology. Concepts are being sought for both ground and space-based investigation.

The European Commission have also invested in two asteroid deflection, technology

programmes - NEOShield and Stardust. These programmes, once again, underlines the importance of understanding the current impact threat posed by asteroids, and how to best organise, prepare and implement any mitigation strategy [Harris, 2011].

NEOShield is a 3.5 year, 5.8M Euros project. It was proposed as part of the 2011 European Union's 7th Framework Programme (FP7) for Research and Technological development. The FP7 programme aims to strengthen the scientific and technological base of European industry and to encourage Europe's international competitiveness. It is achieved by co-funding transnational research and technological development that supports EU policies and adds European value. NEOShield was funded through the call category for the *Prevention of Impacts from Near-Earth Objects on our Planet*. The project brings an international team together to address the global issues of preventing a hazardous asteroid impact event [Harris et al., 2013; Saks et al., 2011]. It will investigate the scientific, technological and programmatic feasibility of three different deflection techniques. This includes kinetic impactors, blast deflection and gravity tractors [Harris et al., 2013]. Blast deflection includes the detonation of either a stand-off or subsurface nuclear or non-nuclear device. Other combined deflection methods also include, but are not limited to, multiple kinetic impactors, a kinetic impactor with a non-nuclear blast, a kinetic impactor with an ion-beam shepherd and a kinetic impactor with electrostatic repulsion. Combined techniques can capitalise on the relative benefits of the different, overlapping approaches to asteroid deflection. Initially, a significant deflection action can first be imparted by the kinetic impactor. This is followed by a more controlled, secondary technique, which would be used to slowly push and trim the trajectory of the threatening asteroid. Key trade-off criteria include the achievable and controllable deflection action, mission risk, warning time and overall mission technology readiness level (TRL). Analysis also includes both laboratory and theoretical modelling. It is critical to understand the behaviour of the NEA during its deflection event and to develop the necessary technological skills and expertise for a rapid test or deflection mission. NEOShield will also assess and formulate the implementation of a decision making tool-box. This will be used to prepare an international response strategy and technology roadmap for any Earth-impacting or threatening asteroid [Harris et al., 2013]. It will enable decision makers to rapidly assess the threat, plan and implementation of an appropriate deflection strategy.

Stardust, funded by a 2012 FP7 Marie Curie Initial Training Network, will develop European capabilities to address the risk posed by asteroids and space debris. Both objects share a number of commonalities. They are uncontrolled objects with an irregular shape and inhomogeneous structure, whose uncertain orbital motion is deeply affected by a range of gravitational and non-gravitational interactions. Stardust will therefore develop the technologies and approaches needed to mitigate the risk offered by asteroids and space debris. It is a four year, 4M Euros project that consists of fourteen academic and industrial partners across Europe. Areas of investigation include: [1] the observation, orbital determination and state estimation required to discover, identify and track both objects, [2] the active removal and deflection of uncooperative targets and [3] the impact prediction that is required to inform decision makers on how to derive the necessary actions and requirements.

Future funding opportunities may also be achieved through the European Union Horizon 2020 programme. This aims to strengthen European competitiveness and innovation within the space sector, provide advances in space technology, enable the exploitation of space data and support international partnerships. This could be achieved by developing European capabilities in the on-going and follow-up observations of NEAs and collision-based deflection strategies. It is a topic that would address one of the seven strategic research clusters. Other areas of consideration also include debris mitigation and removal, the next generation of Earth observation and navigation systems, and the development of advanced space exploration technologies and mission concepts.

These missions and programmes continue to increase humanity's understanding of comets and asteroids. Data gained from ground based facilities, space-based surveys and deep space missions have also been used to dramatically redefine and confirm the occurrence of a possible impacting, or close approach, asteroid event. It includes the warning time, the probability of impact and the expected level of damage. Technologies are also being developed in an ongoing attempt to mitigate the risk and to deflect any threatening NEA.

Deflection Techniques

3.1 Introduction

To address the asteroid-to-Earth impact risk, numerous methods of asteroid mitigation and deflection have been considered by various authors, research groups and establishments. These deflection techniques can be divided into three main categories, including, impulsive, low thrust and passive methods of deflection.

The common objective for all deflection techniques is to increase the Minimum Orbit Interception Distance (MOID) between the Earth and the asteroid [Bonanno, 2000; Milani et al., 2004; Valsechi et al., 2003]. The MOID is a measure of the separation distance between the orbit of the asteroid and the orbit of the Earth. The MOID will always vary with time. This is caused by long-term secular perturbations and shorter periodic variations caused by close planetary encounters [Gronchi and Milani, 2001; Milani et al., 2004]. An impact event will therefore only occur when the MOID is small and the orbit of the asteroid and the Earth are correctly phased [Milani et al., 2004].

The MOID can be maximised by applying a deflection action at a certain time before impact. This is known as the warning time. It is the time from the start of the deflection action to the expected impact with the Earth. Any deflection action will change the velocity (Δv) of the asteroid. This acts as a perturbation on the asteroid's original orbit. It creates a new orbital configuration that is proximal to the original, unperturbed orbit [Vasile and Colombo, 2008; Colombo et al., 2009]. To achieve an impact probability of less than 10^{-6} then, at the point of collision with Earth, the asteroid must be deflected by at least one Earth's radius (~ 6400 km) [Morrison, 2007]. It is always assumed that any impact event will occur at the centre point of the Earth. The miss distance is therefore the distance from the Earth to the intercept of the asteroid's deflected orbit. It is considered to be a good approximation of the MOID [Milani et al., 2004; Yeomans et al., 2009]. For any given deflection technique, the greater the increase in the deflection distance the more effective the technique becomes. It is the increase in the deflection distance that is used to prevent the occurrence of an Earth-impacting event.

The success of any deflection technique is dependent on the asteroid's warning time, orbital elements, size and composition, and the method in which the Δv is applied [Park and Mazanek, 2005a,b]. An effective way to deflect an asteroid, or any orbiting body, is to apply the Δv along the object's orbital path, aligned with the velocity vector. This should occur at the earliest possible time [Conway, 2001; Carusi et al., 2002]. A larger deflection distance can be obtained with a longer warning time, where less Δv is required

to alter the asteroid's trajectory [Campbell et al., 2002; Melosh et al., 1994; Park and Ross, 1999; Vasile and Colombo, 2008]. It is also favourable to apply any deflection manoeuvre at, or close to, the asteroid's centre of mass. The centre of mass defines the stability of the asteroid. Energy and momentum could otherwise be wasted in spinning, rather than deflecting the asteroid. Error could also be created by the dispersion of the asteroid's orbital elements, uncertainty in the asteroid's size and composition and in the transfer method of the deflecting spacecraft [Bonanno, 2000]. Ideal deflection conditions can not always be achieved. Adequate margin must therefore be included in the design of any generic deflection mission and strategy.

3.2 Impulsive Methods

Impulsive methods of deflection include kinetic impactors and nuclear detonation. Deflection by a kinetic impactor is achieved by the release and subsequent impact of a high velocity projectile. Momentum is initially imparted by the initial impact of the projectile, but is greatly enhanced by the additional momentum carried away by the ejected particles [Lawrence, 1990; Koenig and Chyba, 2007; McInnes, 2004; Shafer et al., 1997]. The latter is known as the momentum enhancement factor. Kinetic impactors are amongst the simplest deflection techniques, with the highest TRL [Walker and Chocron, 2008; Izzo et al., 2006]. However the technique is heavily dependent on the overall efficiency of the projectile, the impact geometry and the composition of the asteroid [Walker and Chocron, 2011; Izzo et al., 2005]. Factors include the porosity, elasticity, density and yield strength of the surface and subsurface material.

Deflecting a small rocky monolithic asteroid is very different from deflecting a larger, porous, rubble pile asteroid. The momentum enhancement factor varies a lot between the ejecta created from a hard (~ 2) and soft rock (~ 3.8) and a porous (~ 1.16) and non-porous (~ 4) rock [Housen and Holsapple, 2013; Ahrens and Harris, 1994; Holsapple, 2004; Fujiwara et al., 2006]. The additional momentum transfer decreases with increasing porosity. Highly porous impacts are dominated by the compression, rather than the large-scale evacuation, of its target material [Housen and Holsapple, 1999; Michukami et al., 2007]. Compaction permanently deforms and compresses much of the target material, consuming the initial energy of the impact event. Little ejecta is able to escape the rim. Experiments using a large diameter centrifuge demonstrated that the majority of ejecta are re-deposited within, or at close proximity to the crater bowl [Gibbings and Vasile, 2011; Gibbings et al., 2010]. This reduces the overall contribution to the momentum exchange. Little remaining energy is available for particle ejection. However further work is still required. When two or more bodies collide there is an immense spectrum of possible outcomes. It ranges from the re-adjustment of shape, size, external surfaces and rotational states. These factors will ultimately influence the overall efficiency and performance margin of any kinetic deflection event.

Asteroid deflection can also be achieved through the surface, subsurface or stand-off detonation of a nuclear warhead [Shafer et al., 1997; Barbee et al., 2006; Ahrens and Harris, 1994]. From the initial focus point, deflection by surface and subsurface

detonation is achieved by the explosion and expansion of gas and ejecta. It therefore necessitates the delivery and placement of an optimally buried or surface warhead. This adds complexity, development and operational risk into the mission design, which is further coupled with the unknown physical properties of the asteroid. Factors include the strength, density and the structural composition of the asteroid. Therefore a stand-off nuclear detonation, at a fixed and optimally positioned point from the asteroid is considered to be a far more favourable approach.

Deflection could be achieved by only knowing the orbit and approximate mass of the asteroid. It also eliminates the requirement for any extensive in-orbit operations. Instead of a focused detonation, momentum is induced by a stand-off blast wave hitting and interacting with the surface of the asteroid. The blast wave penetrates the surface of the asteroid, super-heating the exposed material. Vapour and ejecta blow-off is created. More material will be mobilised for a thicker penetration depth. This increases the transfer of momentum that is initially induced by the blast wave. However the technique is still dependent on the height and yield of detonation and the shape, structure & composition of the asteroid [Hammerling and Remo, 1995]. Factors include the vaporisation efficiency, the heat capacity and the radiation absorption properties of the asteroid. The legal and political ramifications of launching and operating a nuclear warhead in space also needs to be addressed [Gritzner and Kahle, 2004]. This will increase the warning time needed for any nuclear-based deflection technique.

For any impulsive technique the creation of ejecta adds significantly to the total transfer of momentum. However, understanding the velocity, volume and size of the emitted ejecta is extremely complex. It depends on the structure and composition of the given asteroid. The risk of fragmentation, with or without the re-aggregation of the parent body, can also not be ignored [Michel and Jutzi, 2009; Sanchez et al., 2010]. Re-aggregation occurs when the ejected fragments are not imparted with a high enough velocity to fully disperse. Instead they reform and re-accumulate into a smaller loose fitting rubble pile asteroid, held together by self-gravity [Richardson et al., 2004; Fujiwara et al., 2006]. This can make any subsequent orbit shaping more difficult [Campbell et al., 2002]. For a much larger impact velocity, fragmentation without re-aggregation can also occur. It results in the separation of the original asteroid into a number of larger pieces. These larger pieces could still impact the Earth [Remo, 1994; Melosh et al., 1994]. The impact of multiple bodies may cause more cumulative damage than that of the original asteroid [Lunan, 1992a; Melosh et al., 1994].

Any form of fragmentation, with or without re-aggregation represents a risk within the deflection event. It may be extremely difficult, or impossible, to deflect multiple fragmented bodies on a second and third deflection attempt. Uncertainty is caused by the unpredictable, orbital motions of the fragmented bodies. The tracking and interception of multiple bodies at short notice would also be difficult. Once any impulsive technique has been initially released or activated, there is an inherent uncertainty in its outcome. Nor is there any practical means of control. This includes both the deflection method and its dynamic response in producing the final adjusted orbit.

3.3 Low Thrust Methods

Gravity tractors, ion beaming, the smart cloud, surface ablation, low thrust propulsion and mass drivers all provide deflection by creating a low thrust action over an extended period of time. This is advantageous as it avoids the fragmentation of the asteroid and provides a controllable, and often continuous and contactless method of deflection.

A gravity tractor provides deflection by exploiting the mutual gravitational attraction between an asteroid and an extremely large and heavy spacecraft (the gravity tractor itself). Illustrated in Figure 3.1, the gravitational attraction between the asteroid and the spacecraft can pull the asteroid away from its original threatening trajectory [Lu and Love, 2005; Schweickart et al., 2006]. Multiple gravity tractors could also be used to increase the deflection distance.

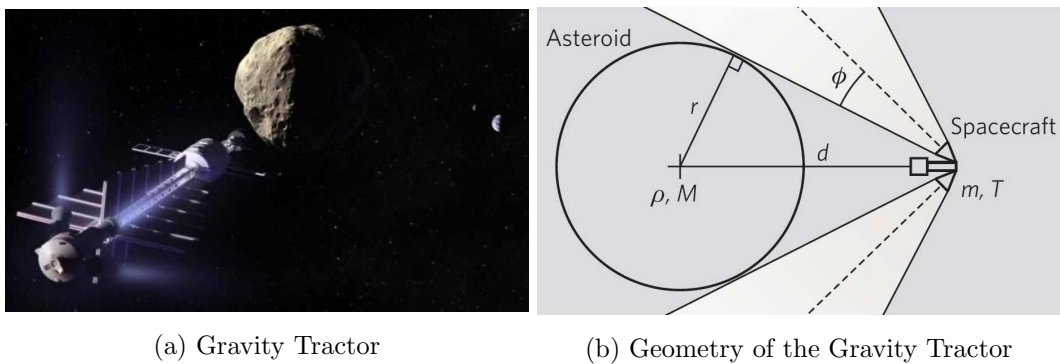


Figure 3.1: Illustration of a Gravity Tractor taken from Lu and Love [2005]; Schweickart et al. [2006]

The technique is however dependent on the masses of the asteroid and the spacecraft, the asteroid's centre of mass, the warning time and the spacecraft's ability to maintain a constant and controlled hover-distance from the surface of the asteroid [Schweickart et al., 2006]. Positioning would be achieved with the simultaneous operations of two low thrust engines. Each thruster would point outwards at a slant angle of at least 20 degs. This would prevent the engine exhaust from impinging onto the surface of the asteroid. In the study performed by Lu and Love [2005], the spacecraft's hover-distance also needs to be equal to half the asteroid's mean radius. The closer the spacecraft is to the asteroid, the higher the gravitational pull and the greater the deflection action becomes. This is however a demanding guidance, navigation and control (GNC) requirement. It also requires knowledge of the mass distribution, rotation and morphology of the target asteroid.

Shown in Figure 3.2, the Ion Beam Shepherd provides a deflection action by continuously impacting the asteroid with a high velocity (30-50 km/s), dense beam of plasma ions [Bombardelli and Pelaez, 2011b]. The concept was initially developed for the de-orbiting of space debris [Bombardelli and Pelaez, 2011a; Bombardelli et al., 2011a,b; Kitamura, 2010].

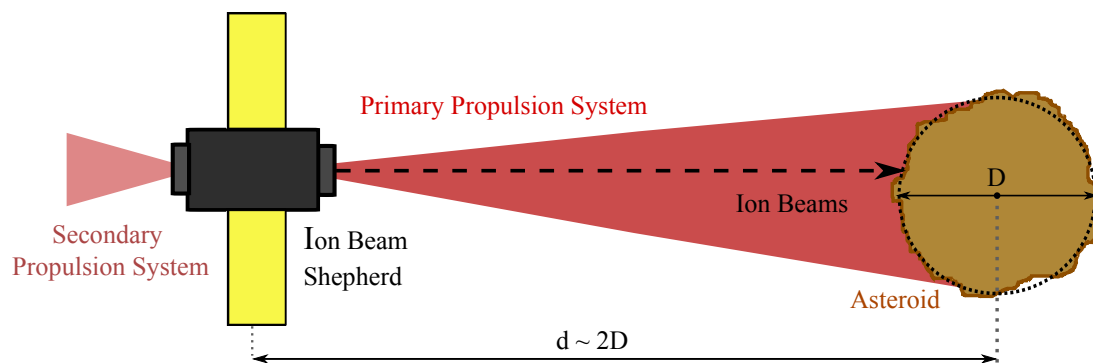


Figure 3.2: Illustration of the Ion Beam Shepherd taken from Bombardelli and Pelaez [2011b]

A low divergence, high specific impulse beam of ions would enable the spacecraft to operate at a greater distance from the asteroid [Merino et al., 2011; Bombardelli and Pelaez, 2011a; Bombardelli et al., 2011a]. Positioning would be achieved with two ion engines; one for releasing and accelerating the ions for deflection purposes and another for maintaining its position. The latter will always act in the opposing thrust direction. This will prevent the spacecraft from drifting away from the asteroid [Bombardelli and Pelaez, 2011b]. Any errors in beam pointing will reduce the fraction of ions that can intercept the asteroid. Ions could miss the target, reducing the total transfer of momentum [Merino et al., 2011; Bombardelli and Pelaez, 2011a]. The technique also requires a substantial and highly efficient onboard power source, particle acceleration unit and heat dissipation system. These units are needed to accelerate the ions and has yet to be addressed. The direct impingement and deposition of secondary, back-scattered ions will also degrade the performance of the spacecraft and the overall deflection technique. Ion interaction is complex and includes material sputtering, beam attenuation, thermal fluctuations and plasma instabilities [Brown et al., 2007]. These factors have not yet been included.

The Smart Cloud is another low thrust, contactless deflection technique. Shown in Figure 3.3, deflection is achieved with the release and impact of a high velocity (exceeding 50 km/s), dense cloud of low mass, small-size, smart particles [Gibbings and Vasile, 2012b,a]. Each smart particle is a small, passively operated silicon or gallium-arsenide spacecraft-on-a-chip [D.J Barnhart and Sweeting, 2007; Atchison and Peck, 2010]. Millions-and-billions of these small particles are contained within the cloud's geometry. Each particle has a mass of 7.5 mg, which based on state-of-the-art technology corresponds to an area of 1 cm² and a thickness of 2.5 micrometers. The thickness is dependent on different nano-fabrication technologies [Atchison and Peck, 2010]. Localised manoeuvring is achieved through solar radiation pressure [Colombo and McInnes, 2011].

Upon impact, each particle provides an maximum impact energy density of $8 \cdot 10^{-11}$ J/kg [Gibbings and Vasile, 2012b]. The impact energy density is significantly smaller than the fragmentation limit for both rocky and rubble pile asteroids. Sputtering might occur, but the asteroid will not fragment. The technique also avoids the need for the spacecraft to carry a mass consuming particle acceleration system. The impact velocity of the Smart Cloud is provided for free by gravity. It is a result of the Smart Cloud's and the asteroid's relative, collision course motion. Results have shown that the Smart

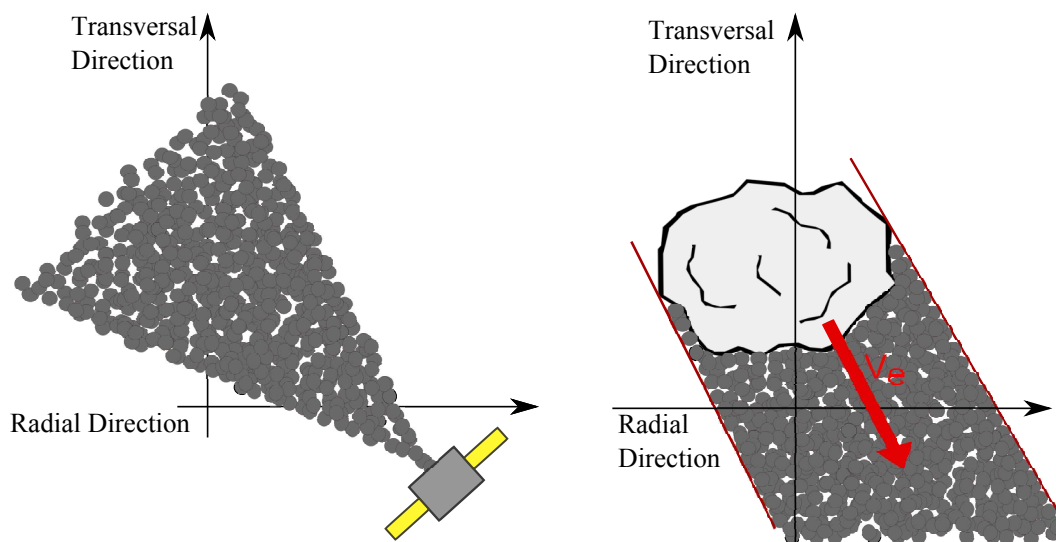


Figure 3.3: Smart Cloud - Initial Release and Impact Geometry

Cloud is highly effective for the deflection of deep crossing asteroids. A higher relative velocity results in a larger deflection distance [Gibbings and Vasile, 2012b].

However for the technique to be fully effective the swarm of smart particles would need to be successfully deployed and until impact maintain its shape geometry. It is currently assumed that the maximum diameter of the cloud coincides with the largest diameter of the asteroid. A more detailed understanding on the short-term and long-term evolution of the cloud is therefore required. The exact size of each smart particle will depend on the fragmentation limit and the physical response of the asteroid. Similar to the kinetic impactor approach, this is dependent on the composition and structure of the asteroid and on the impact velocity of the cloud. The impact area of the smart cloud also needs to be considered. Further experimental work could be conducted to verify the physical response of this deflection technique.

Deflection can also be achieved by the ablation of the asteroid's surface material. This can be accomplished by irradiating the asteroid with a light source. Power sources can include collected and focused solar radiation or a laser light source [Melosh and Nemchinov, 1993; Melosh et al., 1994; Phipps, 1992a; Kahle et al., 2006]. Surface heating sublimates the illuminated material, transforming it directly from a solid to a gas. The ablated material then forms into a plume of ejecta that exerts a small, yet continuous and controllable force onto the asteroid. Over an extended period of time this can push an asteroid away from its potentially threatening trajectory.

The low thrust tug and mass driver provides deflection by physically interacting with the asteroid. Here, a low thrust tug would land and attach a highly efficient and controllable deflection engine onto the surface of the asteroid [Scheeres and Schweickart, 2004; Schweickart et al., 2003]. The engine can be powered by nuclear, chemical or low thrust propulsion. When the direction of the engine is aligned to the asteroid's velocity vector, propellant is ejected. The ejection of propellant provides the deflection push. The technique is therefore susceptible to the rotational motion of the asteroid [Melosh et al., 1994]. This is rarely optimal and will affect the control and direction of the resultant

thrust vector. It will also prevent the technique from being continually operated. The technique also requires a large amount of deflection-only propellant. This adds wasteful mission mass and limits the lifetime of the mission. To alleviate these affects, the asteroid itself could first be excavated. Small pieces of the asteroid's subsurface mass could be mined and then be ejected at a high velocity [Olds et al., 2007; Melosh et al., 1994]. This is known as a mass driver and is illustrated further in Figure 3.4. Deflection would be provided by a series of small, yet controllable impulses over an extended period of time [Melosh et al., 1994].



Figure 3.4: Mass Driver Mission Concept taken from SpaceWorks

Both techniques require the landing, attachment and installation of extensive hardware. The mass driver also involves considerable in-situ construction. Surface features, such as regolith, unconsolidated rocks or boulders and roughness, can make stable attachment difficult. All activities will also have to be performed in an irregular and low gravity field.

3.4 Passive Methods

Passive methods of deflection include changing the thermo-optical properties (for example, absorptivity, reflectivity and emissivity) of the asteroid's surface [Spitale, 2002; Hall and Ross, 1997]. For example, coating the asteroid in a thin layer of paint would provide an enhancement of the Yarkovsky effect. For a rotating body thrust is created by the asteroid's absorption and emission of solar radiation as heat. The difference between the two directions yields a net force along the motion of the orbit. Proposed by Paek [2012] a number of small paint pellets could be used to coat the asteroid with a thin, micrometer layer of paint. Each pellet would be designed to explode on impact. The deflection force is provided through the initial nudge of the pellets, but is enhanced further by increasing the solar radiation pressure acting on the asteroid. The paint-ball concept was developed from the smart cloud design initially proposed in Gibbings and Vasile [2012b]. Deflection is also dependent on the asteroid's position relative to the Sun and its physical characteristics. Factors include the asteroid's thermal inertia and rotational state. Passive methods of deflection also suffer from a low level of technology readiness. Substantial research and development is therefore required. This would increase the

required warning time.

3.5 Comparative Analysis

To assess the effectiveness of the different deflection techniques, a multi-criteria, quantitative comparison was conducted by Sanchez et al. [2009]. It compared the kinetic impactor, nuclear detonation, mass driver, ablation, low thrust tug, and the gravity tractor. All passive methods were excluded from the analysis. This was due to their low technology readiness level, which would have resulted in an excessively long warning and development time. The analysis also included a wide range of realistic launch opportunities (over a 20 year period) and different classes of target asteroids. It was used to determine the optimality of a particular method.

Assessment was relative to the achievable miss distance at the Earth, the warning time, the total mass in orbit and the current TRL. For a particular method, the first three factors express quantitatively how easy it is to deflect a given asteroid and whether it can be implemented with current launch capabilities. TRL gives information on the reaction time of deflection [Sanchez et al., 2009]. It describes the stage of maturity in the development process from the observation of the basic principles, through to the final product operation. A low level of TRL would extend the warning time. Specific technological development would be needed to implement a given deflection strategy.

Results showed that ablation was theoretically one of the most effective and promising techniques. Controllable deflection can be achieved with a relatively low mass into space and a short warning time. Mission mass is saved as the spacecraft does not have to carry additional propellant for deflection-only purposes. The propellant mass is provided, for free, by the direct ablation of the asteroid's surface [Melosh, 2004; Melosh et al., 1994; Mazanek, 2005]. The technique could also be effective for a range of materials. This assumes that a minimum surface power density can be maintained [Yoo et al., 2009; Park and Mazanek, 2005b; Song et al., 2009; Mazanek et al., 2002]. It is also dependent on the density of the asteroid and the required Δv [Mazanek et al., 2002]. Ablation also eliminates the need for the spacecraft to physically land, attach or interact a system onto the surface of the asteroid [Park and Mazanek, 2005a,b; Melosh and Nemchinov, 1993; Song et al., 2009; Mazanek et al., 2002, 2003; Mazanek, 2005]. These factors reduce the overall complexity and risk of the deflection mission.

To date, no single research group, establishment or organisation has selected a definitive solution for the deflection of NEAs. There is no dedicated, nor intergrated planetary defense system. It is still considered to be an ongoing and open problem. Deflection by laser ablation could be a potential solution.

Applications of Laser Ablation

4.1 Introduction

The strategic development of lasers and optical technology has rapidly reduced the cost, size, mass and operational complexity of many laser-based systems. Key technological development includes increasing the efficiency of the semiconductor laser and the Yb:fibre sources in providing a coherent output power. Lasers are now available in a range of wavelengths, output power and efficiencies. It is a mature technology that can be easily incorporated into small commercial applications [Russo et al., 2002].

Advancement has enabled many terrestrial and space-based applications to be developed. Each application exploits the use of laser technology and matter interaction. Terrestrial applications include, but are not limited to, material processing & machining, the deposition of thin films, chemical analysis through mass and emission spectroscopy and in the ablation of bone and tissue [Plohli, 2005; Walsh et al., 1989; Nelson et al., 1988; Nuss et al., 1988; Dwivedi and Thareja, 1995; Fernandez et al., 1995]. Conventional space-based applications include long range wireless power transmission and communication, and LIDAR for remote Earth observation and sensing. Other, more novel concepts include the launch and in-orbit control of spacecraft, the vaporisation and removal of space structures and in the deflection of asteroids. ESA is also supporting the strategic development of space-based laser systems. It has been included within ESA's technology roadmap and recently open tenders have addressed several aspects of laser technology. The latter includes direct solar pumping, improved efficiency and enhanced beam quality. Considerable and ongoing investment is therefore being committed. There is a persistent interest in pushing laser technology beyond its current technological boundaries.

4.2 Launching and Controlling Vehicles in Space

Access to space, and in particular to Low Earth Orbit (LEO), has been, and is currently, dominated with the use of chemically-powered engines. These are energy inefficient, expensive and a polluting form of propulsion. They often need a significant amount of hardware and the continual storage of fuel. For a given launch vehicle, the thrust is achieved by igniting the propellant carried onboard. The availability of energy is limited by the chemical composition and quantity of the selected propellant [Sasoh, 2011].

Laser ablation, in theory and demonstrated at the small scale, could provide an alternative and novel access to LEO and beyond. Instead of burning propellant, previous proposals have suggested the use of a highly focused or collimated laser beam as a remote energy source [Phipps et al., 2010a; Kantrowitz, 1972]. Supplied by either a ground or space-based facility, a high power mega-to-giga watt laser system could transform the exposed propellant - either a solid or a liquid - directly into a gas [He et al., 2011; Phipps et al., 2010b, 2000; Uchida et al., 2005]. A small and extended plume of gaseous ejecta (vapour or plasma) would form. The plume of ejecta acts against the surface of the spacecraft. The resultant force is used to propel the spacecraft into space. The technique could also be used to perform LEO to geosynchronous transfers, re-boost or de-orbit the decay of LEO satellites and maintain station-keeping for geosynchronous satellites [Phipps, 1992c]. Laser ablation removes the requirement for an onboard ignition source, the additional volume of reactable compounds (for example, fuels plus oxidisers) and their associated hardware.

Thrust generation is dependent on the intensity of the laser beam. This is a function of wavelength, power, spot size and if a pulsed laser is used, the pulse duration, shape and energy [Schall et al., 2007]. A variable specific impulse can therefore be achieved by changing the laser intensity, and if using a pulsed laser, the pulse frequency and wavelength. It can provide an almost instantaneous demand of Δv [Phipps, 2002; Phipps et al., 2004a; Phipps and Luke, 2002]. Compared to standard methods of chemical propulsion, laser ablation can provide a much broader range of exhaust velocities [Yabe and Uchida, 2007; Phipps et al., 2010b]. For ordinary chemical rockets the maximum specific impulse is approximately 500 s. This is limited by the temperatures available in the chemical reactions and by inefficiencies inherent in the design of the engine [Phipps et al., 2000; Johnson and Holbrow, 1977; Phipps and Luke, 2002]. The Space Shuttle main engine provided an exhaust velocity of 4.56 km/s. This corresponds with a specific impulse of 456 s [Phipps et al., 2004a]. Larger values can only be achieved with laser ablation. Experiments with a 20 ns duration pulsed KrF laser have measured specific impulses up to 7600 s [Phipps and Michaelis, 1994].

Thrust can also be achieved by using a laser induced blast wave [Sasoh, 2001; Ageev et al., 1980]. Here, by illuminating sufficiently dense portions of the atmosphere, a highly focused laser beam can create a series of detonations. Sequentially these detonations, in theory and tested at the small scale within the laboratory, can propel a given spacecraft to an altitude of approximately 30 km [Ageev et al., 1980; Myrabo, 2001; Bohn, 2000; Myrabo, 1998]. Beyond this point the atmospheric pressure is not sufficiently dense enough to initiate the detonation process. The technique would have to be combined with a rocket motor [Bohn, 2000; Myrabo, 1998]. Additional in-orbit injection and stabilisation manoeuvres may also have to be performed [Richard et al., 2006]. Experiments conducted at the High Energy System Test Facility, White Sands Missile Range, USA, used a remote 10 kW pulsed laser to launch a small, 22-52 g lightcraft to an altitude of appropriately 30 m [Myrabo, 1998]. It supported the theoretical and experimental development of the Light-craft Technology Demonstrator (LTD) spacecraft. Illustrated in Figure 4.1 the LTD is a frisbee-like annular shroud [Richard and Myrabo, 2005a,b; Myrabo, 1989]. The bottom inner surface of the shroud is used as the impulse

generating surface [Richard and Myrabo, 2005b]. Air or a gaseous rocket fuel is passed over the surface and is ignited by a 100 MW class, ground based, pulsed laser. A parabolic mirror, mounted onboard the LTD, is used to reflect and concentrate the incoming incident laser radiation. Thrust is created by a series of laser generated blast waves. The blast waves expand over the length of the impulse generating surface [Richard and Myrabo, 2005a; Richard et al., 1988].

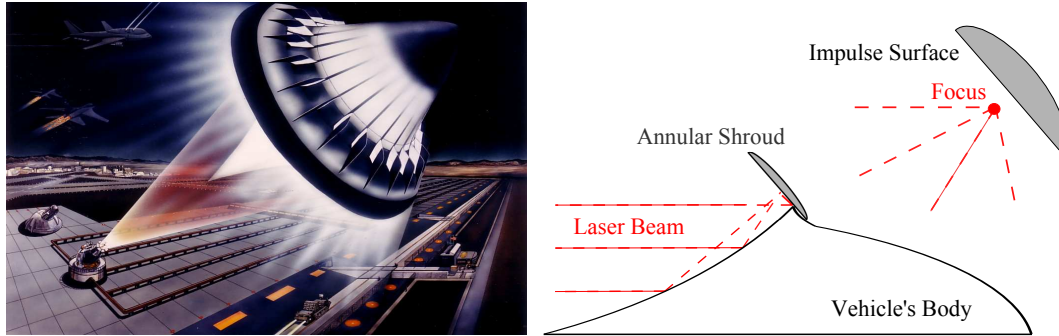


Figure 4.1: Artist Impression and Cross-Sectional View of the LTD Vehicle taken from Richard and Myrabo [2005a,b]; Myrabo [1989]

Performance of the LTD can be enhanced with the instantaneous variation of the laser beam's parameters. Factors include the pulse energy, shape, duration and repetition rate, or by first accelerating the LTD out of a compressed air cannon [Richard et al., 2006]. Beyond an altitude of 30 km the LTD would transition into a rocket engine [Richard and Myrabo, 2005a]. Onboard liquid propellant would be burnt, providing the final boost and insertion into LEO. A laser relay satellite could also be used [Richard et al., 2006; Bergstue and Fork, 2012]. It is advantageous in reducing the mass and cost of the receiving spacecraft. Although additional complications in the tracking, pointing and locking of the respective spacecrafts will need to be addressed. A LTD with a diameter of 1.4 m could provide a direct single-stage-to-orbit access for payloads up to 140 kg [Richard et al., 2006; Richard and Myrabo, 2005a,b; Richard et al., 1988].

The performance of atmospheric detonation can however also be improved by first confining the spacecraft within a launch tube [Hertzberg et al., 1988; Bruckner, 1998; Sasoh, 2001]. Prior to detonation, the inclusion of either a combustible gas mixture or an inert, monotonic gas, behind the spacecraft can increase the pressure and density within the launch tube [Hertzberg et al., 1988; Bruckner, 1998; Sasoh, 2000; Sasoh et al., 2002, 2003; Schall et al., 2007]. The gas acts as the propellant. Reflections of the blast wave against the walls of the launch tube increases the impulse acting on the spacecraft. This is known as the confinement effect and makes the technique far more effective and controllable. The requirement for trajectory tracking and altitude control is also removed [Sasoh, 2001; Sasoh et al., 2001, 2004; Schall et al., 2007]. Variation in the over pressure and the gas selection can create any favourable impulse performance. Thrust can also be enhanced by wall-propelled, in-tube ablation [Sasoh et al., 2008, 2009]. The performance of the LTD therefore depends on the chemical and physical formation of the laser-induced shock wave. It includes the state of detonation and the propagating wave structure. A demonstration of the vertical laser-driven, in-tube accelerator is given

in Figure 4.2 [Sasoh, 2011; Yabe et al., 2003].

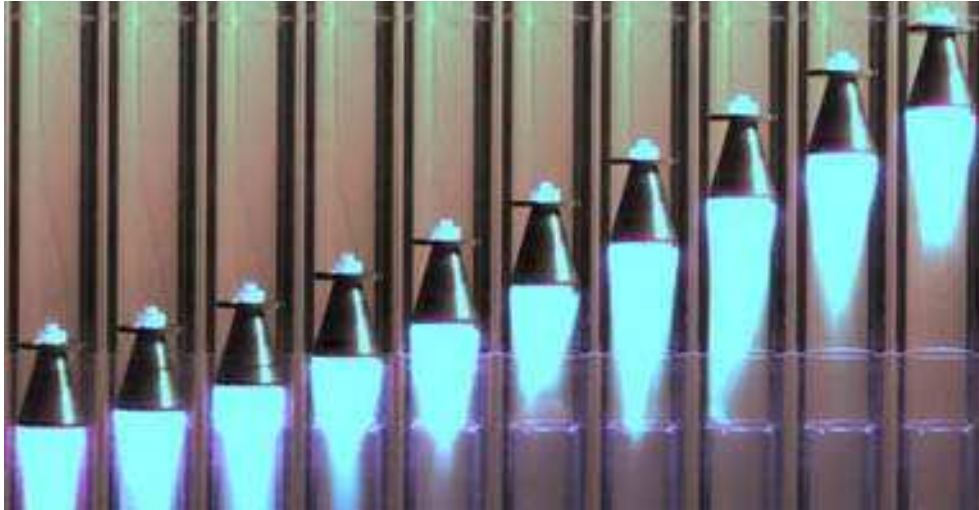


Figure 4.2: Vertical Laser-Driven, In-tube Accelerator Demonstration taken from Sasoh [2011]; Yabe et al. [2003]

Laser driven micro-planes have also been proposed. Small scale experiments conducted with a single pulsed 590 mJ/5ns YAG laser have already demonstrated its feasibility. A small, thin film structure (launch mass between 0.1 and 0.6 g) manufactured from aluminium and acrylic has been successfully launched. Micro-planes could provide rapid response telecommunications, exploration and Earth observations. However future work is required to control and track the micro-plane. This could be achieved by directly ablating the wing, or with the use of a shape memory alloy. A laser beam would be used to deform the structure by the deposition and transfer of heat, rather than in the direct ablation of its surface [Yabe et al., 2003].

These techniques are advantageous as it eliminates the requirement for the spacecraft to carry a dedicated propulsion system, removing the need for an onboard energy source [Yabe and Uchida, 2007; Bergstue and Fork, 2011]. It saves mass, allowing for a higher thrust to weight ratio to be maintained [Phipps et al., 2010a; Myrabo, 1998; Uchida et al., 2005]. More mass can therefore be dedicated to its payload capability. The launch cost is also reduced [Phipps, 2005; Richard et al., 1988].

However, more research is required to advance the perceived theoretical advantages into an achievable form of propulsion. This includes optimising the momentum coupling between the laser beam, and the spacecraft and the formation of the gaseous ejecta plume. Non-optimal conditions must also be considered. This includes the incomplete ablation of the propellant vapour, the sputtering of material, and the degrading products from the propulsion or attitude control system. Atmospheric absorption also needs to be accounted for. This includes the effects of beam excitation, scattering and spreading [He et al., 2011]. The control of the spacecraft's altitude during its ascent must also be controlled. Thrust is not just a matter of intensity, but is also governed by the direction and stability of the ablation event. If the latter two issues are solved, then laser ablation could provide localised attitude control and station keeping manoeuvres [Phipps and

Luke, 2002, 2003]. Instead of conventional thrusters, small and lightweight kilo-watt lasers, coupled with a reel of fuel tape could be integrated into a spacecraft's subsystem. These are known as micro laser plasma thrusters. They could provide attitude control (pointing and positioning) and propulsion for a 100 kg, or less spacecraft [Phipps et al., 2004a,b; Phipps, 2002; Phipps and Luke, 2002]. Each thruster would either operate in a transmission or reflection mode. This is illustrated further in Figure 4.3.

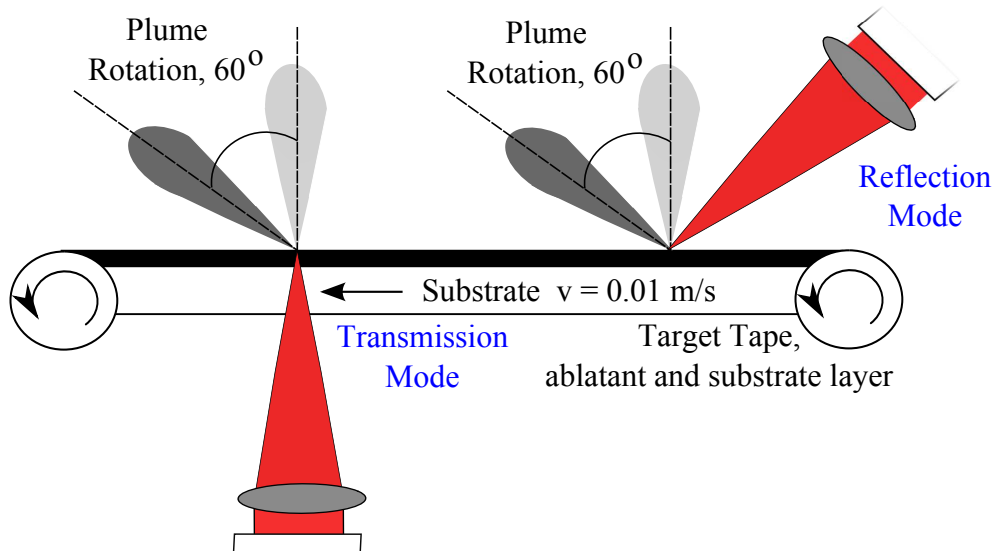


Figure 4.3: Principles of the Micro Laser Plasma Thruster - Combined from Phipps et al. [2004a,b]; Phipps [2002]; Phipps and Luke [2002]

Previous development and testing has shown that the reflection mode is far more effective than the transmission mode. Momentum coupling increased by 50 % [Phipps and Luke, 2002]. However as the laser and ablation jet is located on the same side of the real tape, the design becomes sensitive to the contaminating effects of the ablated ejecta. Awkward shielding is needed to prevent optical contamination and attenuation of the laser beam [Phipps and Luke, 2002]. Shielding is often difficult to accomplish within the tight size constraints of a small scale spacecraft. The transmission mode is therefore considered to be a better, more favourable approach. The laser beam would pass through an optically transparent substrate layer and illuminate a highly absorptive and damage-resistant film. Ablation would occur on the opposite side, away from any optical equipment and the laser beam.

Both modes of ablation are also affected by plume rotation. This is caused by the formation of a steady-state concavity within the fuel tape [Phipps and Luke, 2002]. Tested prototypes used a 0.5 m long, 2.54 cm wide, continuous loop of tape, which moved at 0.01 m/s. The movement, together with the concavity steered the plume in the direction of the tape. Illustrated in Figure 4.3, relative to the incoming laser beam, rotation is ~ 60 degs [Phipps and Luke, 2002]. Plume rotation could however be used to protect the optical elements in the transmission mode. Other recent advancements have also proposed a hybrid laser-electric thruster system [Horisawal et al., 2010; Zhang et al., 2012]. The products of ablation are accelerated by a locally induced electromagnetic field.

4.3 De-orbiting of Space Debris

Over the last 51 years of space activity approximately 5800 tonnes of obsolete material have been left to accumulate in both LEO and geostationary orbits. Waste material includes expendable rockets, non-operational spacecraft and fragmented pieces of technogenic material [Kessler and Cour-Palais, 1978; Kessler, 1989]. In-orbit space debris can also be created by object collision, explosions and deliberate anti-satellite weapons firing [Johnson, 1989]. The continual accumulation of waste material has now reached the limit of the runaway Kessler syndrome [Kessler and Cour-Palais, 1978]. The creation rate of debris exceeds the ambient decay rate of any orbiting structure. Object-to-object collisions now dominate the debris-generating mechanisms [Phipps et al., 2011]. Any impact event can create hundreds, if not thousands, of new, small scale and fragmented structures. The formation of a debris belt is an inevitable consequence [Kessler and Cour-Palais, 1978; Liou and Johnson, 2008, 2009]. The density of material in the two orbital zones is further illustrated in Figure 4.4.

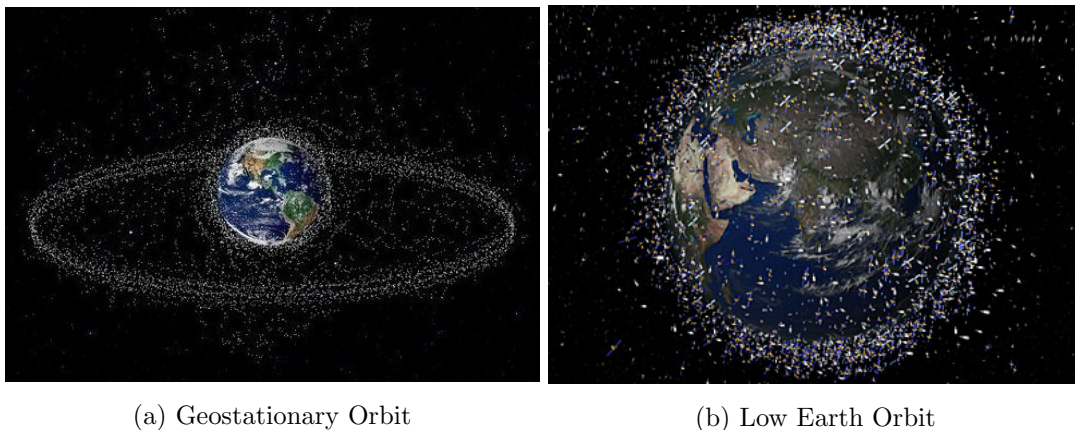


Figure 4.4: Saturation of Orbital Space Debris *Credits ESA*

The continual accumulation of space debris can render orbits unusable and significantly increase the risk of any form of space-based activity. To stabilise this growth, it has been estimated that between five and ten large size objects will need to be de-orbited per year [Liou, 2011, 2010; Lewis et al., 2011]. The active removal and disposal of space debris is therefore one of the most challenging, yet compelling problems facing the international space community. It demands an immediate solution to avoid the catastrophic loss of vital and expensive space assets. The space environment must be protected for essential telecommunications, navigation and Earth observation services. Laser ablation could be a potential solution.

A laser beam can illuminate and ablate the surface of any obsolete spacecraft or structure [Campbell, 2000; Phipps et al., 1996; Phipps and Michaelis, 1995; Phipps et al., 2011; Campbell, 1996]. This would impart a small de-orbiting force onto the spacecraft that would lead to its eventual re-entry and disintegration into Earth's atmosphere [Schall, 1991]. The ablated surface could include, but is not limited to, aluminium, carbon fibre, MLI and second surface mirrors [Vasile et al., 2010a; Schall, 1998; Campbell, 1996]. Material selection is dependent on the construction method of the original spacecraft.

It may not be possible to ablate all parts of the spacecraft.

For small fragmented structures, 1-10 cm in diameter, a ground-based laser system could be used. A study validated by NASA, known as the ORION concept, proposed the use of a 20 kW average-power repetitive pulsed laser [Phipps et al., 1996; Bekey, 1997; Phipps and Sinko, 2010]. A pulsed laser system allows for variation in intensity, wavelength and pulse length duration [Phipps et al., 1996; Phipps and Michaelis, 1995]. Combined with state-of-the-art detection capabilities, all small-size hazardous objects could be removed from near-Earth space ($h \leq 1000$ km) in two years. All objects larger than 1 cm, but less massive than 100 kg could be removed in four years [Phipps et al., 1996; Phipps, 1995a,b; Phipps and Michaelis, 1995]. LEO is widely acknowledged to be the worst region for space debris. The ORION concept is illustrated further in Figure 4.5.

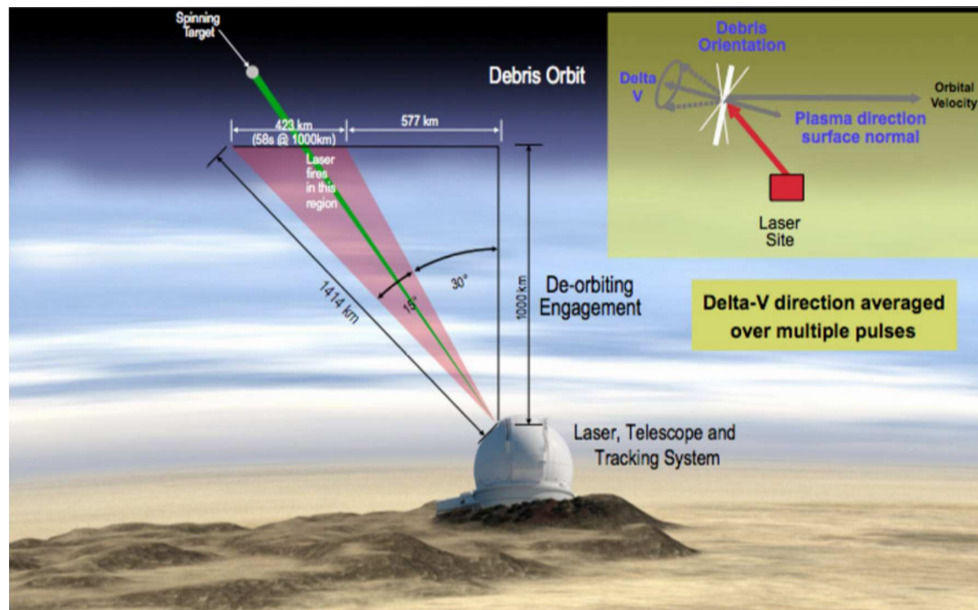


Figure 4.5: ORION Concept for the De-orbiting of Space Debris with Lasers. Image taken from Phipps [2011b]

Ideally the laser would be located on a high, flat-topped equatorial mountain. This would minimise the effects of atmospheric turbulence and the absorption of the laser beam. Acquisition and tracking would be provided by an astronomical observatory-style beam director [Phipps et al., 1996; Schall, 1998; Phipps and Michaelis, 1995]. The Mount Stromlo facility, operated by Electro Optics, Australia, for example, is able to acquire and track 5 cm size objects over a range of 3000 km [Mason et al., 2011].

Illumination, and therefore ablation, of any piece of space debris would occur when the object passes over-head of the laser facility. From the local ascending zenith the illuminated field-of-view would be accessible between 30-45 degs [Phipps, 1997]. The laser beam provides an assumed surface spot diameter of 40 cm [Phipps, 1997; Phipps and Michaelis, 1995]. This is provided by a 6 m aperture observing telescope at a maximum slant range of 1400 m [Phipps, 1997; Phipps and Michaelis, 1995]. The intercepting laser beam is much larger than the de-orbiting object. Energy is wasted in illuminating the surrounding space. Progressively more energy is wasted in the ablation of smaller objects [Phipps et al., 1996; Schall, 1998]. However this overspill does relax the pointing

and steering requirements of the laser beam [Phipps, 1997].

Adaptive optics would be needed to overcome the attenuation of the laser beam caused by atmospheric scattering and beam fragmentation [Early et al., 2004; Campbell et al., 2002; Campbell, 2000; Mason et al., 2011; Phipps et al., 1996]. It is provided by a deformable, phase plate mirror, that is controlled by piezoelectric actuators. Moment-by-moment this is used to compensate for any phase distortions within the atmosphere. It occurs ahead of the laser input phase at a bandwidth of approximately 1 kHz [Beckers, 1993]. Adaptive optics can also improve the beam pointing, stability and the occurrence of any focusing errors [Phipps et al., 1996; Bekey, 1997]. A reliable method of optical control is critical. Depending on the size and orientation of the space debris, the de-orbiting procedure can be repeated many times. This can occur over multiple overhead passes, until atmospheric re-entry is achieved [Phipps, 1997]. Rapid re-targeting would also enable multiple objects to be illuminated [Phipps and Michaelis, 1995]. However care must be taken to track, direct and assign each piece of debris. Multiple ground stations, distributed across the globe are therefore preferable [Schall, 1998].

De-orbiting larger structures would require the use of a space-based laser system. This is beneficial as the laser beam is not degraded by atmospheric interference and can be operational for extended periods of time, along the spacecraft's orbital track. It offers improved visibility and access angles. Previous proposals envisaged by Vasile et al. [2010a,b] suggest the use of a small, agile spacecraft, mounted with a kilo-watt space-borne laser. Another proposal suggests the use of a much higher mega-watt class laser [Schall, 1991]. In either case, the spacecraft would rendezvous and fly in formation with the given piece of debris; operating in a fetch and de-orbiting fashion. Once the required de-orbiting manoeuvre is achieved the spacecraft would move onto the next, only de-orbiting one piece at a time. The concept could also be adapted via the use of fuel foams, with a known and very low enthalpy of sublimation. Prior to the ablation event, foam would be attached to the given piece of debris. The laser beam would then ablate the foam and not the spacecraft structure [Vasile et al., 2010b]. It would guarantee a minimum level of ablation and associated thrust.

These techniques are advantageous as they avoid the need to physically dock with potentially non-cooperative (tumbling or spinning) and poorly known targets. However it is reliant on the spacecraft's ability to ablate enough of the debris's structural mass. The direction of the de-orbiting manoeuvre is dependent on the direction and orientation of the exposure spacecraft [Yabe and Uchida, 2007]. The ablation of an irregular shaped, spinning piece of debris could easily alter its spin frequency and orientation of its spin vector. A torque could be created around the spacecraft's centre of mass. This would complicate any future targeting and re-acquisition procedure [David et al., 1997]. The issues relating to shape irregularity needs to be addressed. It is also critical that the ablation process does not contribute further to the space debris problem. The effect of ablation on a multi-layer, inhomogeneous material or structure also needs to be considered. Experimental work is therefore required to validate the concept and any proposed acquisition and targeting strategies.

4.4 Deflection of Asteroids

The deflection of an Earth approaching asteroid could be achieved by either a ground or space-based ablation system. A ground based system would use a laser beam as the illuminating light source. Lasers are advantageous as they can propagate over an extended distance, with very little loss of energy, dispersion and beam quality [Vertes et al., 1993; Park and Mazanek, 2005b; Melosh et al., 1994; Canavan, 1996; Pakhomov et al., 2003; Bergstue and Fork, 2011]. It is a convenient, versatile and predictable method of transporting energy. They do however require a substantial investment in infrastructure and resources [Canavan, 1996]. The deflection of a small 40-80 m diameter asteroid would require a giga-watt average power laser system [Phipps, 1992b]. The laser beam would illuminate the hemisphere of the asteroid. Beam steering would be provided by a 30 to 30,000 m ground-based mirror. The exact number is dependent on the wavelength of the laser and the Earth-to-asteroid distance [Phipps, 1998, 1993]. A large mirror could be constructed by synthesising an aperture from an array of segmented mirrors [Canavan, 1996; Phipps, 1998]. This would provide a surface spot diameter between 100 and 10,000 m [Phipps, 1993]. For a small asteroid, considerable energy would therefore be wasted in illuminating the surrounding space. The laser beam will also be attenuated by the atmosphere of the Earth and be subjected to errors in pointing accuracy and control.

Other studies have proposed the use of a space-based ablation system. Here, a large rendezvousing spacecraft would deploy a pre-mounted mirror. This is known as the solar concentrator. The solar concentrator would be used to collect, direct and concentrate solar radiation onto a small area of the asteroid's surface [Melosh and Nemchinov, 1993; Melosh et al., 1994; Lunan, 1992a,b]. Ablation would follow. The initial concept is further illustrated in Figure 4.6 [Gritzner et al., 2002].

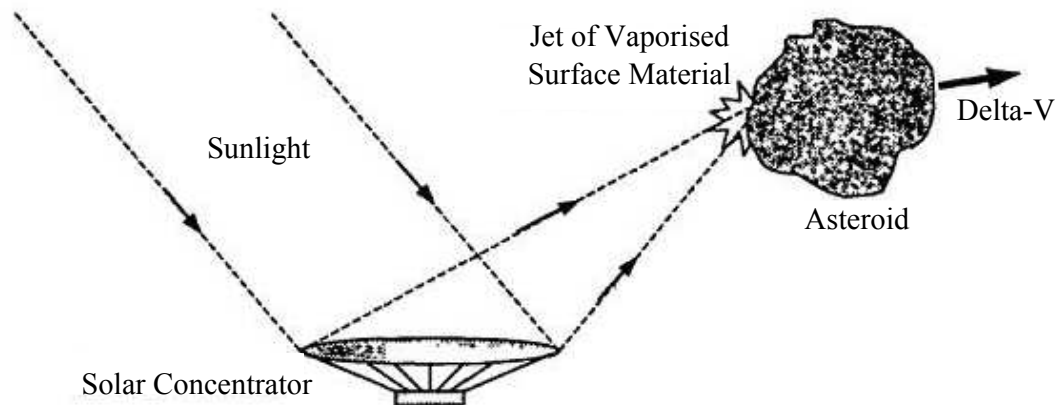


Figure 4.6: Principles of the Solar Concentrator taken from Gritzner et al. [2002]

Analysis suggests that the solar concentrator would need to be between 0.5 and 10 km in diameter. This corresponds with a solar concentrator mass of between one and four tonnes [Melosh and Nemchinov, 1993; Melosh et al., 1994]. The exact number is dependent on the size of the asteroid, the warning time and the distance between the spacecraft and the asteroid. Operating and manoeuvring such a large, heavy structure is

technologically challenging and difficult. To date, the largest deployable space structure was the 41 m diameter Echo 2 balloon [Leonard, 1961]. It was launched as the first passive communication satellite experiment. More recently, JAXA successfully launched the 20 m (measured across the diagonal) IKAROS solar sail. It was launched as part of the 2010 JAXA interplanetary demonstrator mission.

The solar concentrator would also have to be positioned at close proximity to the asteroid, under the asteroid's irregular gravity field [Melosh et al., 1994]. It would therefore become susceptible to the deposition and contaminating effects of the ablated ejecta. Ejecta deposition would rapidly reduce the reflectivity of the concentrator and ultimately bring the sublimation process to a halt. To alleviate this affect, Melosh et al. [1994] proposed a dual mirror system. An extended focus length would increase the asteroid-to-spacecraft distance, reducing the risk of ejecta contamination [Melosh and Nemchinov, 1993; Melosh et al., 1994]. Illustrated in Figure 4.7, this system would use a primary concentrator to initially collect the incoming solar radiation [Melosh et al., 1994]. The solar radiation would then be reflected onto a smaller secondary concentrator. The secondary concentrator would direct the solar radiation onto the surface of the asteroid.

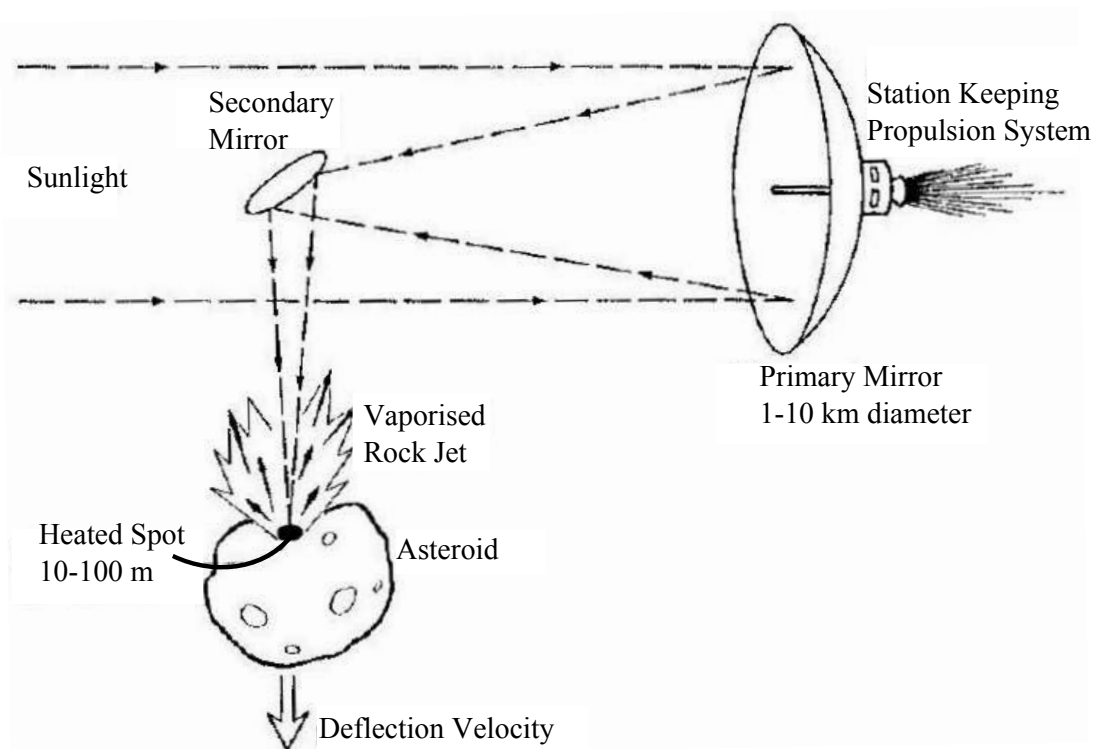


Figure 4.7: Solar Concentrator Deflection System: Dual Mirror System taken from Melosh et al. [1994]

Increasing the distance also increases the size and mass of the solar concentrator. Manoeuvrability becomes difficult. The accumulation of light pressure would require constant orbital control. The smaller, secondary concentrator would still be affected by the contaminating ejecta. It would have to be periodically replaced [Gritzner et al., 2002]. Depending on the size, several secondary, replacement concentrators could be carried onboard by the deflecting spacecraft [Kahle et al., 2006]. However the exact replacement mechanism has yet to be developed and would demand a high level of

complexity and control. Another possible approach of protection is to place a number of light, permeable foils in front of the solar concentrator [Kahle et al., 2006]. Once a certain transmittance decrease is achieved the outermost foil would be removed. This again adds to the overall complexity and mass of the mission, and would limit the overall lifetime of the mission.

To address these limitations an alternative proposal was suggested. Instead of using a single, large solar concentrator, a number of smaller structures was proposed. Each structure would be an identical, small scale spacecraft that would be mounted with a much smaller solar concentrator [Maddock et al., 2009, 2007]. The concept is known as MIRROR BEES and is illustrated further in Figure 4.8. It is an example of a fractionated spacecraft.

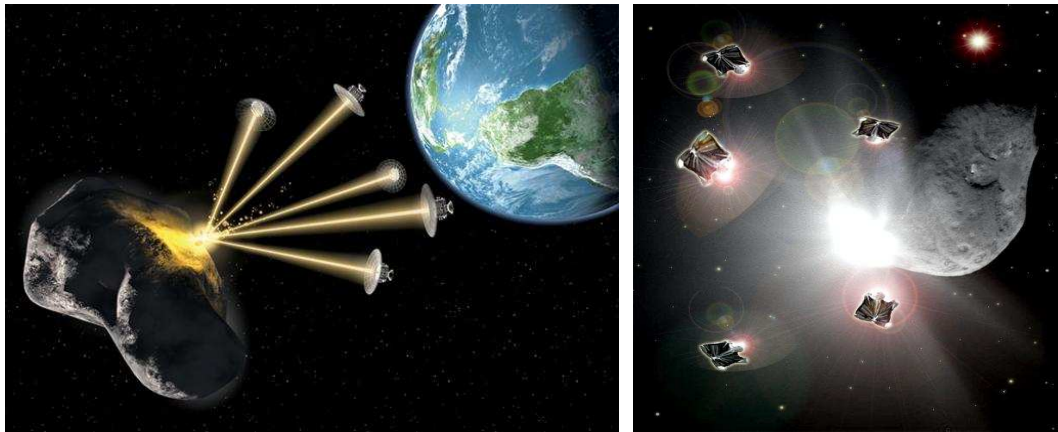


Figure 4.8: Artistic Impression of the MIRROR BEES Deflection Technique

Together each spacecraft would form into a swarm. The swarm would orbit in formation with the asteroid [Vasile et al., 2009a]. Each solar-concentrator- spacecraft would be used to collect and focus a beam of light onto the surface of the asteroid. By superimposing multiple beams the cumulative surface power density would be high enough to initiate the ablation process. The potential for deflection is therefore dependent on the number of spacecraft in formation with the asteroid, the available surface power density, the material properties of the asteroid and the contaminating effects of the ablated ejecta. The surface power density is affected by the quality and intensity of the incoming solar radiation, and in the size of the illuminated area. This approach is only possible due to recent advances in the design and fabrication of low cost, low mass, modular mirrors [Phipps et al., 2011]. It is also dependent on the spacecraft's ability to maintain and track their position within the swarm. This is relative to the Sun, the asteroid's surface and the other spacecraft. The co-ordination of multiple spacecraft is critical [Vasile et al., 2009a].

The multi-mirror approach is conceptually similar to Melosh et al. [1994]; Melosh and Nemchinov [1993], but has a number of significant advantages [Maddock et al., 2009; Bergstue and Fork, 2011; Phipps, 1997; Vasile et al., 2009a]. This includes:

- The increased redundancy, flexibility and scalability of the mission design. As required, on a case-by-case basis, more or less spacecraft can be added or removed from the existing orbital configuration.

- Multiple spacecraft illuminating a constant spot area permits the surface delivery of a much more powerful system [Vasile et al., 2009b]. It can reduce the time to achieve a suitable deflection distance. The thrust time, which defines how long the ablation process is induced for, can be decreased by increasing the number of spacecraft.
- The mission design can be adapted to include multiple ablation sites or repeated and reused for different deflection scenarios. It improves the adaptability and endurance of the system. Multiple systems also reduce the risk of any single point failure. Each spacecraft can be easily replaced by an awaiting unit. A highly redundant mission scenario is preferable as it accounts for large observational uncertainties in the asteroid's material and structural composition, and in the mission design parameters [Zuaini et al., 2012].
- The use of identical units avoids the need to design and develop new spacecraft structures. This lends itself to the rapid deployment of prepared units.
- Each spacecraft is comparatively smaller and lighter. It improves the deployment, control and manoeuvrability of each spacecraft. The solar pressure acting on the spacecraft is significantly reduced. This improves the overall agility of the system. The need for station keep is therefore reduced. A smaller, more compact spacecraft will also be less susceptible to the degrading effects of the deposited ejecta.

A collimated or focused laser beam could also be used as the ablating light source. Each spacecraft can be positioned further way from the asteroid. Here, it would be less affected by the asteroid's irregular, inhomogeneous gravity field and contaminating ejecta. The second concept is called LASER BEES and would use superimposing laser beams to initiate the ablation process [Vasile et al., 2009b]. Each spacecraft would be equipped with an identical, low power, kilo-watt solar-pumped laser.

Previous proposals for space-based ablation have suggested the use of a large, high power mega or giga-watt laser. The laser could be mounted onto a rendezvousing spacecraft, the ISS or the Moon and would be powered by a nuclear reactor [Park and Mazanek, 2005b; Yoo et al., 2009; Song et al., 2009; Melosh and Nemchinov, 1993; Ivashkin, 2004; Mazanek, 2005]. However there are significant legal and political ramifications of launching and operating a nuclear reactor in space. This is coupled with the design and development required to initiate a nuclear power source and a high power, highly efficient space-based laser. Manoeuvring and operating a large space structure is also difficult. A swarm of low power, but highly efficient LASER BEES is therefore a more attractive option.

Within the swarm each laser spacecraft would be powered by the Sun, either directly or indirectly. For direct solar pumping the solar radiation would be collected and concentrated directly onto the laser's gain medium [Landis, 1994]. Nd:YAG and Nd:CR solar pumped lasers have been successfully demonstrated [Weksler and Schwartz, 1988]. However direct solar pumping suffers from a seriously low level of energy conversion. A Nd:YAG laser can only currently provide a direct power-to-electrical conversion efficiency of between 2-36 %. The latter is the future, theoretically possible expectation [Landis,

1994]. This inefficiency is further coupled with the mismatch between the wide emission band of the Sun and the relatively narrow absorption band of the laser's gain medium. The overlap for the Nd:YAG laser is approximately 0.4 [Weksler and Schwartz, 1988]. Considerable solar energy is therefore lost in the conversion process. This also reduces the overall system efficiency. It makes the technique susceptible to even a low level of optical contamination [Melosh et al., 1994].

For indirect solar pumping the incoming solar radiation is first focused onto a set of highly efficient photovoltaic solar cells. This intermediate step is used to convert the incoming radiation into electrical energy that is then used to power the laser and the remaining spacecraft. While the inclusion of solar cells as an electrical power generator adds mass, size and a power requirement into the mission design, it does, in comparison to direct pumping offer a more efficient transfer of energy [Vasile et al., 2010b]. An electrically pumped semiconductor laser has a proven plug-in efficiency of over 70 %. Optimally designed solar cells can provide a power-to-electrical conversion of up to 40 % [Landis, 1994; Dimroth et al., 2009; Phipps, 2002; nLIGHT Press Release, 2006]. Both units are commercially available, relatively inexpensive and are supported by continued research and development [Lando et al., 2003]. Enabling technologies include highly efficient semiconductor and fibre lasers, photovoltaic cells and power management units. These are also three fundamental technologies that will support the development of green renewable energy. Indirect pumping is therefore a superior method, providing a higher level of efficiency and technology readiness.

The current conceptual design for indirect pumping is shown in Figure 4.9. It envisages the use of two lightweight deployable mirrors, including a large primary and a smaller secondary structure. A primary, parabolic shaped mirror is used to collect the incoming solar radiation and then reflect it onto a smaller secondary mirror. The secondary mirror then reflects the light onto a solar array. The parabolic shape of the reflector minimises any optical aberration. This improves the beam quality [Bergstue and Fork, 2012]. The solar array, together with the laser is located within the shadow-cone of the primary mirror. This is used to control heat dissipation [Vasile et al., 2009a].

A similar architecture could also be used for direct pumping. The solar arrays would be removed and replaced with the laser's gain medium. This would allow direct illumination from the Sun's freely available solar radiation. For both cases the spacecraft would also need to be equipped with a beam steering device. In Figure 4.9 this is conceptualised as a steering mirror. It would be used to target the laser beam onto the surface of the asteroid. Large radiators are also needed to dissipate any excess heat, maintain the laser within its operational limit and cool the remaining spacecraft. For cooling purposes, the radiators are also located within the shadow-cone of the primary mirror. The durability of the laser system is dependent on the effectiveness of the spacecraft's thermal control system. This is dependent on the efficiency of the laser. Efficiency also governs the size, form and mass of the required power source.

Any exposed surface located in the ejecta's ablation volume will become subjected to its contaminating and degrading effects. Exposed surfaces include the solar cells, steering mirror, solar concentrators, radiators and MLI. It is currently assumed that once the

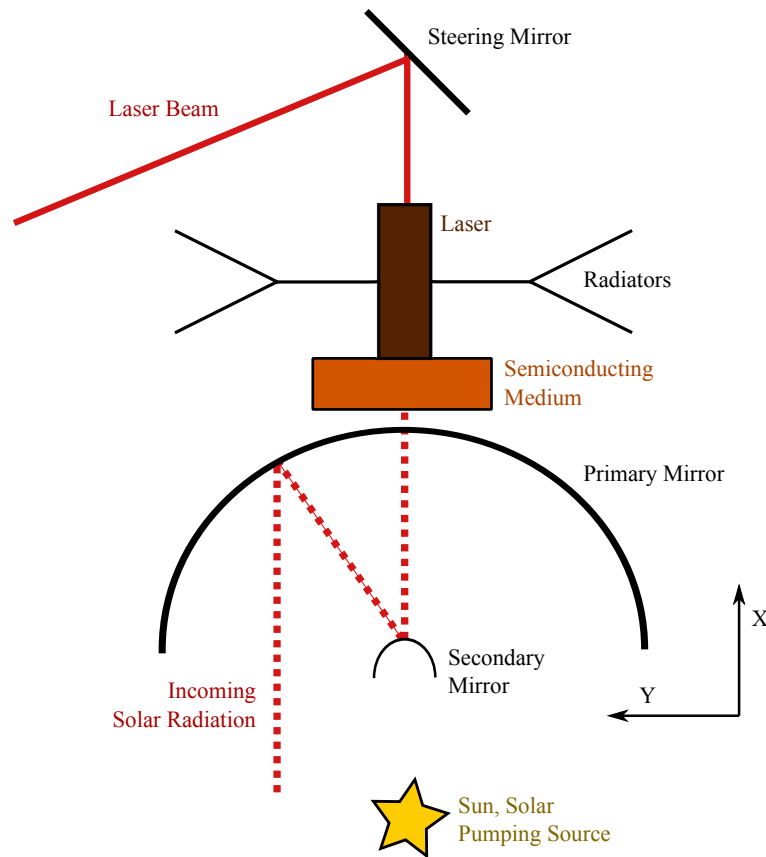


Figure 4.9: Spacecraft Design for an Indirect Pumped Laser System

ablated ejecta comes into contact with any surface, that the particles will immediately re-condense and stick. Degradation will follow the Beer-Lambert-Bouguer law and is dependent on the absorptive properties of the deposited ejecta [Kahle et al., 2006]. The continual accumulation of the ablated ejecta will decrease the transmittance and increase the absorbance of any exposed surface. It includes the reflectivity of the mirrors and the power generating ability of the solar arrays. The laser beam is also expected to be attenuated by the ejecta plume [Plohli, 2005]. Semi-opaque or opaque particles within the laser beam will scatter much of the incoming energy [Bergstue and Fork, 2011]. Degradation will therefore affect the intensity of the laser beam, its operational lifetime and the overall endurance of the ablation technique.

Laser Ablation Model

5.1 Introduction

The ablation model is based on the energy balance of sublimation. It was initially developed to model the deflection action induced by a solar concentrator. This was achieved by modelling the evaporation process of sublimation, the expansion of a gaseous ejecta plume and the contamination caused by the deposited ejecta [Kahle et al., 2006]. A critical parameter is the surface power density. This must be high enough to initiate the sublimation process. The model also combines the absorption of the laser beam, the latent heat of complete sublimation (also known as the sublimation enthalpy) and the heat loss through conduction and radiation respectively [Kahle et al., 2006; Sanchez et al., 2009]. The sublimation enthalpy is a measure of the volatility of the asteroid. It is a physical quantity that describes the easiness of vaporisation [Hashimoto, 1982]. Ideal sublimation occurs when there is no compound decomposition. Instead a single solid-to-gas phase change occurs. This is dependent on the thermodynamic properties of the asteroid [Harris, 2004].

In assuming a vapour-only flow regime, the sublimation model derived from solar sublimation can be applied to laser ablation. Instead of focused solar radiation, a low power and continuous wave laser beam can initiate the ablation process. Ablation occurs without any ionisation or the ejection of solid particles. The target asteroid is also assumed to be a dense, homogenous structure, which behaves as a black body with an infinite heat sink. The degradation caused by the ejecta plume is based on the Beer-Lambert-Bouguer law. These assumptions were used to develop the ablation model. However experimental verification was required to assess the viability of the model and its applicability in inducing a deflection action.

Verification was achieved by ablating a magnesium silicate rock with a 90 W continuous wave laser beam. Shown in Chapter 6, a number of inconsistencies existed between the model and the experimental results. Inconsistencies included the measured mass flow rate, the expected level of contamination and the additional absorption effects between the laser beam and the ejecta plume. These results enabled the ablation model to be updated and improved. The improved model combines the energy balance of sublimation with the energy absorption within the Knudsen layer, the variation of sublimation temperature with local pressure, the temperature dependent thermal conductivity of the target material and the partial re-condensation of the ablated material. It was developed from previous research papers on laser ablation for non-space applications

[Knight, 1979; Bulgakov and Bulgakov, 1999; Robbie et al., 1982; Ketren et al., 2010; O’Keefe and Ahrens, 1971]. The momentum coupling was derived from the work of Phipps [2011a, 1997]; Phipps et al. [2000, 1988].

5.2 Sublimation Model

During the sublimation process, for a static and non-rotating asteroid, the mass flow rate per unit area of the ablated material can be expressed as:

$$\dot{m} = \frac{1}{E_v} [P_I - Q_R - Q_C] \quad (5.1)$$

Equation (5.1) is based on the energy balance of the system. E_v is the latent heat of complete sublimation (also known as the sublimation enthalpy), P_I is the absorbed laser input power per unit area, Q_R is the heat loss per unit area through radiation and Q_C is the heat loss per unit area through conduction.

For a rotating body, the mass flow rate is found by integrating over the surface of the illuminated spot. It is then used to calculate the applied thrust (as defined in equation (5.6)). If the mass flow rate is negative then there is not enough energy available to initiate the ablation process. The laser beam is also assumed to be uniform in both space and time, and that ablation occurs instantaneously.

Therefore [Sanchez et al., 2009]:

$$\dot{m}_{SUB} = 2V_{rot} \int_{y_{min}}^{y_{max}} \int_{t_{in}}^{t_{out}} \frac{1}{E_v} [P_I - Q_R - Q_C] dt dy \quad (5.2)$$

The limits $[y_{min}, y_{max}]$ and $[t_{in}, t_{out}]$ define the location and duration for which the surface spot is illuminated respectively. $[y_{min}, y_{max}]$ is symmetric and is measured from the centre of the surface spot. This therefore defines the vertical components of the surface spot area. $[t_{in}, t_{out}]$ are the times at which the asteroid’s surface moves inside and out of the illuminated spot. V_{rot} is the velocity of rotation of the asteroid’s surface as it travels under the illuminated spot area.

The loss through radiation and conduction are given as:

$$Q_R = \sigma_{SB} \varepsilon (T_{SUB}^4 - T_{AMB}^4) \quad (5.3)$$

$$Q_C = (T_{SUB} - T_o) \sqrt{\frac{c_A \rho_A \kappa_A}{\pi t}} \quad (5.4)$$

The heat loss from radiation is described by the Stefan-Boltzmann law. It therefore assumes that the asteroid acts as a black-body. A hypothetical black body is an ideal absorber (and isotropic emitter) of electromagnetic radiation, where no reflection occurs. This is independent on the wavelength and angle of incidence of the incoming radiation and on the target body’s shape and composition. σ_{SB} is the Stefan-Boltzmann constant

$(5.6704 \cdot 10^{-8} \text{ W/m}^2\text{K}^4)$ and ε is the black body emissivity of the asteroid. Emissivity defines, at a given temperature, the ability of a surface to emit energy by radiation. An ideal black body would have an $\varepsilon = 1$. Any other object would have $\varepsilon < 1$. Emissivity is dependent on the characteristics of the target material (temperature, physical and chemical composition, surface roughness) and the angle and wavelength of the emitted radiation [Tribble, 1961]. T_{SUB} is the sublimation temperature of the asteroid. This is defined in vacuum conditions and occurs within the vapour-only regime. It excludes any ionisation. T_{AMB} is the ambient surrounding temperature.

The heat loss due to conduction is determined by the temperature at the centre of the asteroid T_o and the specific heat capacity c_A , density ρ_A and thermal conductivity κ_A of the asteroid. Each parameter is assumed to be constant and therefore independent of temperature and time [Chen, 1965]. The specific heat capacity is the amount of heat energy required to change a fixed mass by one unit of temperature. It is either measured at a constant temperature or pressure [Opeil et al., 2010; Ghost and McSween, 1999]. Thermal conductivity is also a fundamental parameter. It defines the asteroid's ability to conduct heat [Opeil et al., 2010]. During ablation the asteroid is assumed to behave as an infinite heat sink. It therefore maintains a constant internal temperature [Chen, 1965]. The model is one dimensional and does not account for thermal diffusivity within a three dimensional body.

Ablation will only occur when the temperature of the illuminated spot is equal to or greater than the temperature of sublimation. The energy from the laser beam must therefore be absorbed into the asteroid, increasing its local surface spot temperature. Absorption is a physical parameter. It provides the energy input for the kinetic ejection and expansion of the ejecta plume [Phipps et al., 1988; Lowndes, 1998]. It is therefore dependent on the material properties of the asteroid, and the duration and intensity of the laser beam [Mayboudi, 2008; Plohli, 2005].

Conduction provides the absorptive heat transfer [Spohn and Benkhoff, 1990]. It is assumed to be one dimensional, where the heat energy is transferred directly from the illuminated spot towards the centre of the asteroid [Marla et al., 2011]. According to the model developed by Clauser and Huenges [1995], heat is modelled without diffusion from the centre line of the asteroid. Given this, conduction was assumed to occur along an infinitely long, cylindrical shaped rod, which has a cross sectional area equal to the spot's [Sanchez et al., 2009]. The ablation hole will therefore remain constant and be equal to the initially illuminated spot size diameter. This is a conservative assumption. Material around the spot location might also heat-up and sublimate. For a lower energy input, it would increase the mass flow rate of the ablated material and the associated thrust level. Further experimental and numerical analysis is therefore required to fully assess this assumption.

The average velocity of the ejecta plume \bar{v} is calculated by assuming Maxwell's distribution of an ideal gas. It is defined by the sublimation temperature T_{SUB} , the molar mass of the ablated gaseous material M_a and Boltzmann's constant k_b . This is given by:

$$\bar{v} = \sqrt{\frac{8k_b T_{SUB}}{\pi M_a}} \quad (5.5)$$

The force F_{SUB} acting on the asteroid is therefore given by a product of the ejecta velocity and the mass flow rate of the ablated material. It is expressed as:

$$F_{SUB} = \lambda \bar{v} \dot{m}_{SUB} \quad (5.6)$$

The acceleration a imparted onto the asteroid is given by:

$$a = \frac{F_{SUB}}{m} \quad (5.7)$$

where m is the initial mass of the asteroid.

In equation (5.6) a constant scatter factor λ is used to account for the hemispheric, rather than the linear expansion of the ejecta plume. Hemisphere expansion is defined as the average of all the possible directions in which the ablated material can be randomly ejected. Linear expansion occurs when the material is directed in a single direction with a given velocity. Shown in Figure 5.1, the ablated ejecta is assumed to be distributed over a range of elevation angles θ , between $-\frac{\pi}{2}$ and $\frac{\pi}{2}$ [Sanchez et al., 2009; Vasile and Maddock, 2010]. The scatter factor, derived further in Appendix J, is determined from the integration of the cosine wave divided by the interval of integration [Lin and Pakhomov, 2005]. A constant scatter factor of $\frac{2}{\pi}$ therefore assumes that all of the ablated material expands uniformly over a half sphere [Vasile and Maddock, 2010; Brown et al., 2011]. This is a conservative worst-case assumption that requires quantitative assessment. A constrained cone of ejecta might be more plausible.

The scatter of the ablated ejecta not only affects the direction of the resultant thrust vector but also (as shown in equation (5.6)) the modulus of thrust. Since $\frac{2}{\pi} = 0.64$, then on average only 64 % of the ejected gas will contribute to the exchange of linear momentum, and therefore to the generation of thrust. Particles of gas may also be ejected in opposite directions, therefore their contribution to the change of linear momentum is zero. A scatter factor of one would imply that all the gaseous material is being ejected in a single direction.

Throughout the sublimation process the velocity of the ejecta plume is also assumed to be constant and independent of the local elevation angle. It has reached a free molecular flow rate. No molecular collisions occur [Kahle et al., 2006; Skorov et al., 1999]. The velocity, as previously defined in equation (5.5), is only dependent on the sublimation temperature of the asteroid. The sublimation temperature was assumed to be 1800 K (based on forsterite). Therefore the force is dependent on the product between the mass flow rate and velocity. A higher force can be created by increasing the mass flow rate, but will result in a faster contamination of any exposed surface [Vasile et al., 2009b]. The relative flow rate, velocity and dispersion of the ablated ejecta will ultimately define the modulus and direction of the imparted force exerted onto the asteroid.

Modelling of the sublimation process is also governed by three fundamental assumptions. This includes the formation of the ejecta plume, the shape, surface topography and composition of the asteroid, and the ejecta's potential for causing contamination [Kahle et al., 2006; Sanchez et al., 2009; Vasile et al., 2009b]. It includes:

ASSUMPTION ONE:

- **The formation of the ejecta plume is similar to the rocket exhaust in standard methods of rocket propulsion.**

This assumes the continuous expansion of a gaseous plume of ejecta. The gas expands from a reservoir, through a nozzle and into a vacuum [Kahle et al., 2006; Komle, 1990]. The same approach is used to model cometary sublimation [Kimura et al., 2002; Komle, 1990; Mohlmann, 1996; Crifo, 1995; Spohn and Benkhoff, 1990; Brown et al., 2011; Kahle et al., 2006]. A large reservoir of dirty ice is assumed to be located underneath the near-surface of each comet. The dirty ice consists of a conglomerate, volatile mixture of water-ice and refractory particles [Whipple, 1950, 1985; Keller, 1989; Grun et al., 1987]. Gaseous ejection is driven by the solar sublimation of H₂O, CO, CO₂, NH₃ and CH₄ [Espinasse et al., 1991; Seiferlin et al., 1995; Kossacki et al., 1997; Crifo, 1995]. Sublimation excludes the ejection of any solid particles and the ionisation of the ablated material. The flow is also assumed to be a mono-energetic, friction-free compressible gas [Phipps, 2002; Phipps et al., 2000]. The plume expands with a constant velocity, temperature and adiabatic index k_I [Kahle et al., 2006; Phipps and Michaelis, 1994]. Adiabatic expansion occurs without the exchange of heat or matter between the system and the surrounding. For diatomic molecules $k_I = 1.44$ [Legge and Boettcher, 1982]. The majority of chemical compounds will evaporate into diatomic molecules [Dwivedi and Thareja, 1995]. Each molecule is comprised of either two identical or different atoms. The jet constant k_P for diatomic molecules is 0.345 [Kahle et al., 2006]. It should be noted that these values are empirical and therefore require verification. The sublimation of an asteroid may differ significantly [Vasile et al., 2009a].

Accounting for these assumptions, the density of the ablated ejecta ρ can be expressed as [Kahle et al., 2006]:

$$\rho(r, \theta) = \rho^* k_P \frac{d_{SPOT}^2}{(2r + d_{SPOT})^2} \left[\cos \left(\frac{\pi \theta}{2\theta_{MAX}} \right) \right]^{\frac{2}{k_I - 1}} \quad (5.8)$$

where d_{SPOT} is the surface spot diameter.

The density at the nozzle (at the sublimation point) ρ^* is given by:

$$\rho^* = \frac{\dot{m}_{SUB}}{A_{SPOT} \bar{v}} \quad (5.9)$$

where A_{SPOT} is the area of illumination by the laser beam onto the surface of the asteroid.

Equation (5.8) is defined as a function of distance r from the known spot location and the local elevation angle θ . The elevation angle is measured from the surface normal. The local reference frame of the plume geometry is shown in Figure 5.1.

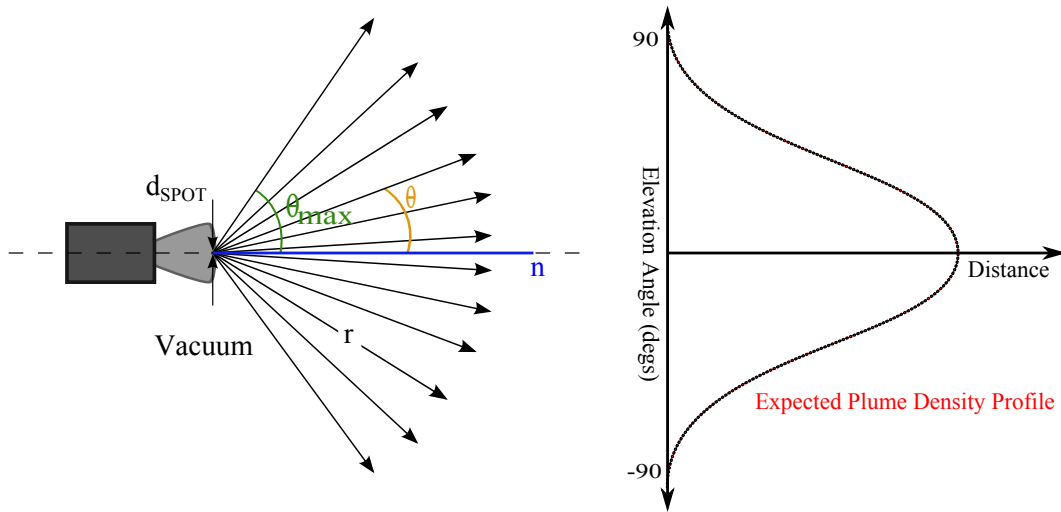


Figure 5.1: Local Reference Frame and Geometry of the Ejecta Plume

Shown in Figure 5.1 the cosine term in equation (5.8) defines the spatial distribution of the ejecta plume. It results in an axial-symmetric, Gaussian shape distribution which is elongated perpendicular to the surface of the asteroid [Gritzner et al., 2002; Harris, 2004; Schou et al., 2007; Kahle et al., 2006; Komle et al., 1990b,a]. The maximum density coincides with the centre line of the plume [Komle, 1990]. The density and distribution of the ejecta plume depends on the size of the ablation spot and the local elevation angle. The density decreases with an increasing distance from the asteroid. This distribution is different from the scatter factor distribution that is given in equation (5.6), which is expected to be less than 1 but greater than 0.64.

Analysis performed by Kahle et al. [2006] assumed that $\theta_{MAX} = 130.45$ degs, where by definition there is a backwards expansion of the ejecta plume. Backwards expansion occurs behind the spot location and envelopes the asteroid over a total angle of 260.9 degs [Legge and Boettcher, 1982]. It best describes the dispersion (in the far field), rather than the initial ejection, of the ejecta plume. The scatter factor, density and velocity direction can be expressed as:

Density Direction

$$\left[\cos \left(\frac{\pi \theta}{2\theta_{MAX}} \right) \right]^{\frac{2}{k_I - 1}} \quad (5.10)$$

Velocity Direction

$$\left[\cos \left(\frac{\pi \theta}{2\theta_{MAX}} \right) \right]^{\frac{k_I - 1}{2}} \quad (5.11)$$

Scatter Factor

$$\lambda = \frac{\int_{-\theta_{MAX}}^{\theta_{MAX}} \left[\cos \left(\frac{\pi \theta}{2\theta_{MAX}} \right) \right]^{\frac{k_I - 1}{2}} d\theta}{2\theta_{MAX}} \quad (5.12)$$

A better, more robust analysis would be to limit θ_{MAX} to ± 90 degs $[\pm \frac{\pi}{2}]$. This defines the initial expansion of the ejecta plume, which is the main contributor to the momentum

exchange, rather than its later dispersion. Taking this into account the scatter factor, density and velocity direction can be reduced to:

Density Direction

$$[\cos(\theta)]^{\frac{2}{k_I-1}} \quad (5.13)$$

Velocity Direction

$$[\cos(\theta)]^{\frac{k_I-1}{2}} \quad (5.14)$$

Scatter Factor

$$\lambda = \frac{\int_{-\frac{\pi}{2}}^{\frac{\pi}{2}} [\cos(\theta)]^{\frac{k_I-1}{2}} d\theta}{\pi} \quad (5.15)$$

The scatter factor, density and velocity direction for these two conditions are shown in Figure 5.2. Case 2 denotes the new imposed limits for θ_{MAX} . Analysis is expressed as a function of the local elevation angle and the direction contribution imparted by the gaseous ejecta plume. A direction contribution of one would result in the density and velocity being aligned in a single thrust direction. Both cases result in the same scatter factor value. Experiments are needed to validate which relationship is correct.

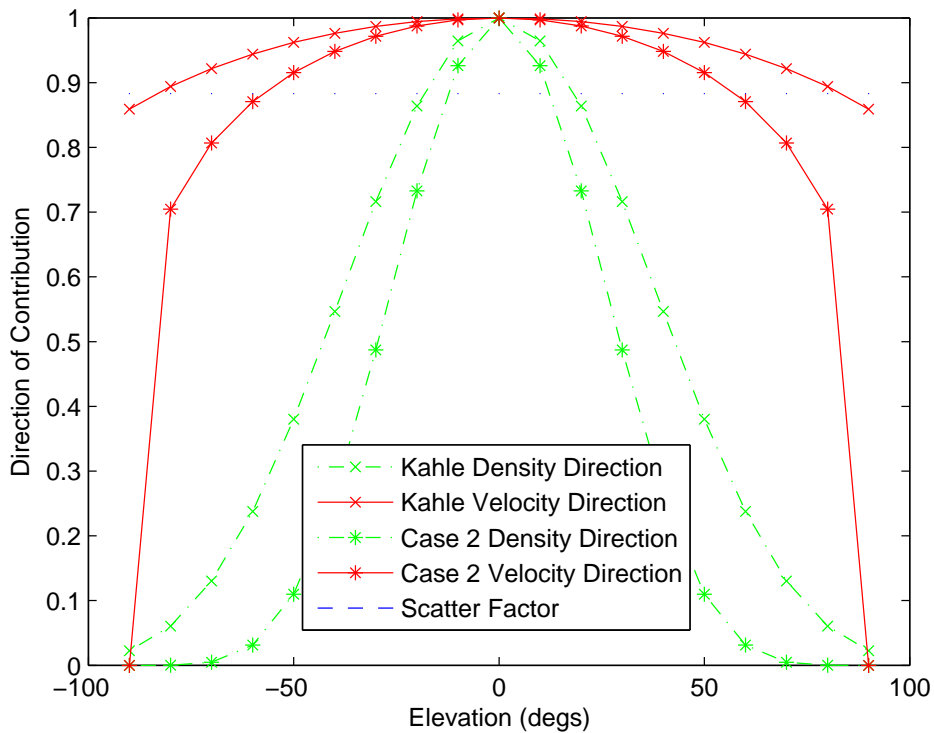


Figure 5.2: Expected Scatter Factor, Velocity and Density Direction of the Ejecta Plume

ASSUMPTION TWO

- **The asteroid is a dense, non-porous, homogeneous body.**

Forsterite (Mg_2SiO_4) is often used to represent the entire asteroid population. It is a compound of MgO and SiO_2 and is classified as the magnesium rich end-member of the olivine solid-solution series [Hashimoto, 1990]. The solid-solution exists between magnesium rich forsterite and iron rich fayalite (Fe_2SiO_4). For each case, iron and magnesium are substitutable for each other. Substitution does not cause any significant effect on the crystalline structure. Olivine is therefore expressed as $\text{Mg}_x, \text{Fe}_{1-x}\text{SiO}_4$, where x is between the limits of zero and one. Olivine rich surfaces occur throughout the solar system. It includes the Moon, several asteroids and meteorites.

However, asteroids exist over a diverse range of compositions, geometries and surface features. It includes loose re-accumulated rubble piles, monolithic structures, porous bodies and those that contain an inhomogeneous structure [Huebner and Greenberg, 2001; O'Brien and Greenberg, 2005]. The model must therefore be advanced to represent the diversity within the asteroid population. It includes realistic and representative shape models that are inclusive of complicated and irregular shape geometries. The variety within the asteroid population is shown in Figure 5.3 [Richardson et al., 2004]. Variation is assessed relative to the porosity and the relative tensile strength of the given asteroid. Porosity is a measure of void space. The tensile strength is defined as the maximum stress that the asteroid can withstand before fracture or rupture occurs. The relative tensile strength, as defined in Richardson et al. [2004] is therefore the tensile strength of the asteroid divided by the mean tensile strength of its components. In Richardson et al. [2004] both the porosity and relative tensile strength are dimensionless and vary from zero to one.

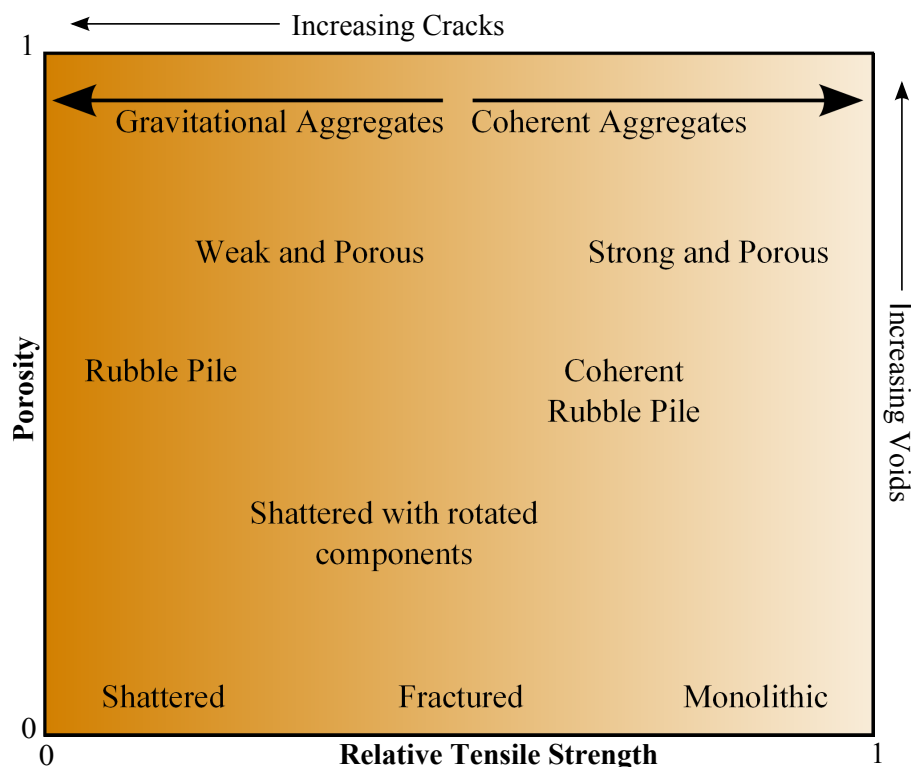


Figure 5.3: Structural Classification of Asteroids taken from Richardson et al. [2004]

Rubble pile asteroids are strengthless bodies without cohesive or tensile strength. They are formed from the collection and re-accumulation of small, individual aggregates that are held together by self-gravity [Korycansky and Asphaug, 2006; Richardson et al., 2004]. If the individual aggregates provide some cohesive strength (become attached or cemented to each other) then they are known as cohesive rubble piles. A monolithic structure is an individual, cohesive shard of a much larger, fragmented body [Harris and Pravec, 2006]. Fractured bodies are characterised with a large number of faults or joints. They are unable to resist any long-term disruption. Shattered bodies are dominated with joints and cracks and can be easily re-oriented. They are susceptible to significant amounts of disruption. This can contribute to a large rotational component [Richardson et al., 2004].

Data combined from spacecraft, ground based radar and meteorite analysis suggest that a large proportion of asteroids are highly porous [Britt et al., 2004; Fujiwara et al., 2006]. Of the surveyed bodies, 43 % have an estimated bulk density of less than 2.0 g/cm^3 and a further 22 % have a bulk density below 1.5 g/cm^3 [Britt et al., 2004]. This implies that much of their structural interior is occupied by void space. Asteroid 253 Mathilde, located in the main asteroid belt is the most widely accepted example of a highly porous body. Mathilde has been classified as a C class asteroid with an observed density of 1.35 g/cm^3 [Yeomans et al., 2006; Cheng, 2004; Veverka et al., 1999; Thomas et al., 1999]. The surprisingly low bulk density is associated with an implied internal porosity - compared with the typical densities of carbonaceous chondrite meteorites - to be in the order of 50 % [Cheng, 2004]. However this value, due to uncertainty in the observational data, has the potential to reach as high as 70 % [Korycansky and Asphaug, 2006].

For a highly porous asteroid the gaseous ejecta could expand inside the asteroid. This would significantly reduce the formation of the ejecta plume [Komle et al., 1990b]. A pressure wave created during the ablation process may also result in the lateral subsurface transport of the ablated gas. Penetration and permeability of the gas could occur through cracks, voids and interlocking pore space [Mohlmann, 1996]. Or alternatively, internal expansion and compaction could occur. This would create a very thin layer of material where surface ablation could occur. If the latter is true then laser ablation could be highly effective on porous asteroids. A similar mechanism may also occur in cometary sublimation. The KOSI experiments investigated the behaviour of a mineral-ice mixture under simulated space conditions (vacuum and low temperatures) with a solar-like spectrum light source [Grun et al., 1991]. Underneath the dust mantle a coherent crust of modified material was formed. This provided a thermal shield (due to its low thermal conductivity) to the underlying icy mixture [Grun et al., 1993; Kuhrt et al., 1995]. The magnitude of any ablation event is therefore dependent on the density and composition of the target material. Substantial experimental verification is therefore required.

Asteroids also exist over a range of rotational states and shapes. Shape is important as it defines the mass distribution, density and angular momentum of the asteroid. It is a result of the asteroid's evolution and formation - occurrence of impacts, catastrophic collision, geological activity and early planetesimal accretion - with other bodies throughout the solar system [Skoglov, 1999]. Data reconstructed from ground based

radar is shown in Figure 5.4. This illustrates the wide range of permissible and possible shapes. It can include, but is not limited to, simple spherical bodies, asymmetric structures, elongated bars and close or contact binaries [Taylor et al., 2012; Richardson et al., 2004]. No group dominates the asteroid population.

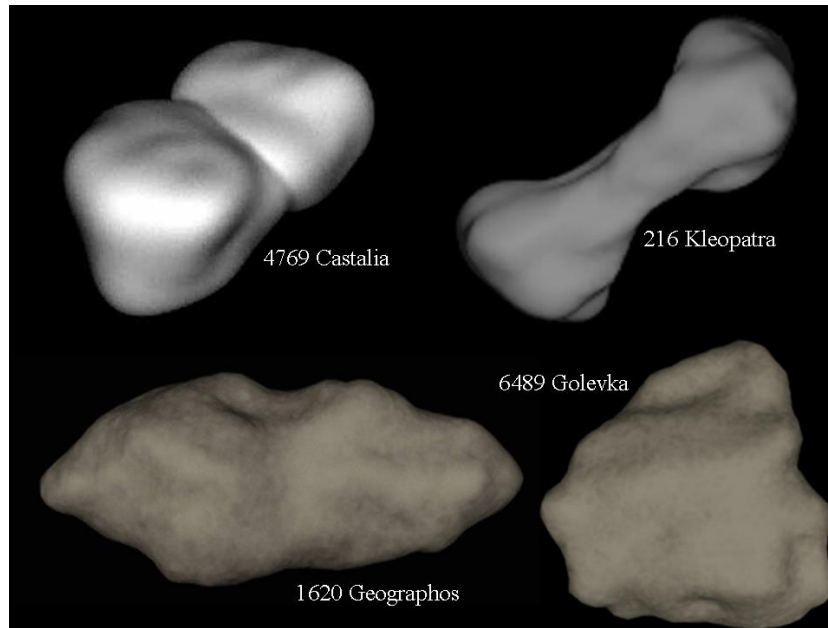


Figure 5.4: Reconstructed Shape Models of Asteroids

About their maximum moment of inertia, asteroids have a wide range of rotational characteristics and orientations. It includes fast and slow rotators, and bodies that tumble randomly in space [Scheeres and Schweickart, 2004; Pravec et al., 2002; Pravec and Harris, 2000]. Fast rotating asteroids tend to be small monolithic shards. They are characterised with a rotational period of less than 2 hours and a diameter (based on absolute magnitudes) less or equal to 150-200 m [Pravec et al., 2002; Whiteley et al., 2002]. Any loose material, initially held by self-gravity has been lost. A large centrifugal force has either transported material towards, or removed from, the equator of the asteroid [Harris, 1996; Harris et al., 2008]. The remaining structure is held together by cohesion and tension [Pravec et al., 2006; Harris and Pravec, 2006]. Observations suggest that asteroids larger than 150-200 m in diameter tend to be rubble pile asteroids. They have a minimum period of rotation of ~ 2 hours [Pravec et al., 2006]. This is known as the rubble pile limit and is shown further in Figure 5.5 [Pravec et al., 2002]. The vertical scale on the right indicates the period of the asteroid in hours. A light blue cross is for a NEA and a darker black cross is for a main belt asteroid (and some comets). The red, solid line indicates the rubble pile limit. Throughout the NEA population the average period of rotation is approximately 5 hours [Scheeres and Schweickart, 2004].

The rubble pile limit is for structures that have no cohesive or tensile strength. The maximum achievable spin rate is determined by self-gravity and spin stresses [Holsapple, 2007]. Their tensile strength is too low to withstand any large centrifugal acceleration [Pravec et al., 2006]. Larger asteroids, characterised with significant equatorial elongation tend to be slow rotating bodies [Pravec et al., 2006; Harris and Pravec, 2006]. They slowly

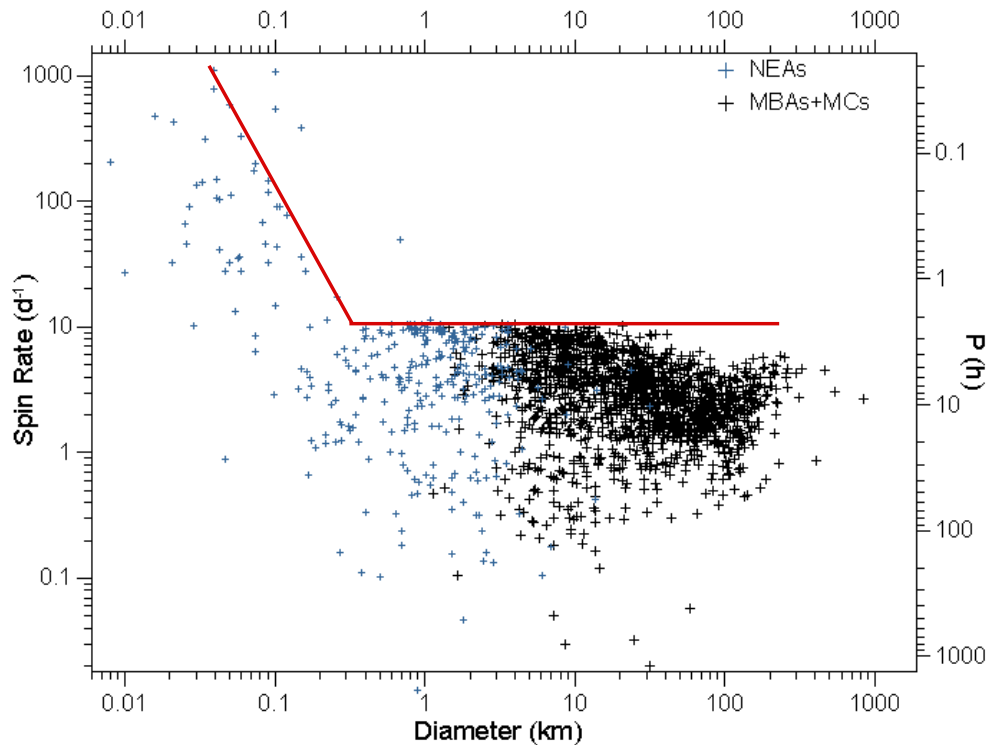


Figure 5.5: Spin Limit - Rotational Rate vs Body Size for Asteroids and Comets taken from Pravec et al. [2002]

tumble about their non-principal axis of rotation [Pravec and Harris, 2000]. Asteroid 253 Mathilde is a prime example. It has a diameter of about 50 km and a tumbling rotational period of ~ 17.4 days [Yanagisawa and Hasegawa, 2000; Richardson et al., 2004]. Mathilde is further characterised by at least four impact craters whose diameter is larger than the mean radius of the asteroid. The de-spinning of the asteroid is thought to be the result of a number of large scale, yet compressive impact events [Yanagisawa and Hasegawa, 2000].

Variation in shape, structure and rotational state must therefore be accounted for within the numerical model. It will affect the available illumination time of the laser beam, the supply of fresh pre-ablated virgin material and the direction of the thrust vector [Melosh and Nemchinov, 1993]. The illumination time is governed by the angular rotation of the asteroid and the size of the spot. The asteroid will always move under the laser beam. Therefore at any given location, the time taken for the asteroid to rotate through the laser beam must be less than the time taken to reach the minimum sublimation temperature. Analysis performed by Sanchez et al. [2009] has shown that as the rotation of the asteroid increases the achievable deflection distance decreases. An irregular, rough, three dimensional surface will also distort the projection of the laser beam onto the surface of the asteroid. This will affect the shape and directionality of the ejecta plume. A flat smooth surface will provide a highly directional plume, whereas a rough surface will produce a more dispersed plume [Farquhar and Rumble, 1998]. Error can also be created by the focusing mismatch on a rugged, or significantly elongated asteroid [Kahle et al., 2006]. Elongation of the surface spot can also be caused by a high elevation angle of the incoming laser beam. These cumulative effects can reduce the surface power

density and result in a variable, time dependent distance between the spacecraft and the surface spot diameter. Any misalignment of the focus point and initial beam diameter would reduce the performance of the ablation process. It may also, over an extended period of time, contribute to altering the asteroid's rotational state. This can be caused by the creation of an off-axial thrust.

ASSUMPTION THREE:

- **The ablated ejecta will immediately re-condense and stick to any exposed surface.**

Within the ablation volume a thin film of deposited material is assumed to form on any exposed surface. It is caused by the direct impingement and scattering of the ablated particles within the ejecta plume [Rantanen and Gordon, 1996]. Scattering can be caused by the collision of an ambient atmosphere or between the ejected particles.

The growth of this deposited material is given by [Kahle et al., 2006; Vasile and Maddock, 2010]:

$$\left[\frac{dh}{dt} \right]_{layer} = \frac{2\bar{v}\rho}{\rho_{layer}} \cos\Psi_{vf} \quad (5.16)$$

where h_{layer} is the accumulated thickness. Equation (5.16) is governed by the velocity and density of the ablated ejecta, the deposition time and the surface properties (roughness, temperature and stickiness) of the exposed surface [Tribble, 1961; Rantanen and Gordon, 1996; Dursch et al., 1995]. The denominator of equation (5.16) is the layer density. It is the expected density of the deposited material. Each deposited particle is assumed to be spherical and have an accumulative layer density of 1000 kg/m^3 [Tribble, 1961; Kahle et al., 2006; Rantanen and Gordon, 1996]. A factor of two in equation (5.16) accounts for the expansion of gas into a vacuum, as it will cause an increase in the expansion velocity. Ψ_{vf} is the geometric view factor. It is used to relate the fraction of material that is ejected and deposited onto a given surface. Ψ_{vf} therefore accounts for the physical geometry between the source and the affected surface [Tribble, 1961; Rantanen and Gordon, 1996]. It is measured as the angle between the normal of the exposed surface and the incoming flow of the ablated material. A view factor of one occurs when the flow is perpendicular to the affected surface. The same approach is used to model the contamination caused by the outgassing and off-gassing of particles [Rantanen and Gordon, 1996].

The deposited ejecta is also assumed to be permanently attached onto the exposed surface. This occurs when the particle's resident time exceeds the period of interest. The latter is often the life time of the mission. The particle enters a state of thermal equilibrium with the given surface. Particles will only escape if they acquire enough energy to overcome the electrical attraction of the surface. This has to be provided by an external force and varies widely with the particle shape, size and material characteristics. To account for this permeability a sticky coefficient γ of one is assumed throughout [Tribble, 1961; Matteson, 1988]. This is the worst case condition. However in practice it could vary between $0 < \gamma < 1$. The sticky coefficient defines the probability that

any given particle, colliding with a surface, will stay on the surface before thermal re-evaporation occurs [Tribble, 1961]. A more realistic, reduced value of the sticky coefficient would decrease the degrading effects of the deposited ejecta. The exact value is dependent on the physical properties of the exposed surface. This includes the local composition, morphology, available area and temperature.

A warmer surface will have a much lower sticky coefficient; its resident time is so small that particles can escape the surface. Defined in equation (5.17) the average resident time t_r of any particle is given as an exponential of surface temperature [Tribble, 1961; Smith, 1998]. This is defined as:

$$t_r(T) = t_o e^{\frac{E_a}{RT_s}} \quad (5.17)$$

where R is the universal gas constant, E_a is the activation energy, T_s is the temperature of the substrate and t_o is the oscillation period of the molecules on the surface [Chen et al., 1990]. Scialdone [1981] reported an average oscillation time as 10^{-13} s. This however varies in magnitude between 10^{-14} and 10^{-12} s. The activation energy is the thermal energy that is required to excite and remove any unexpected particle from a given surface. The expression $\frac{E_a}{RT_s}$ therefore accounts for the temperature variation effects on the overall volatility of the chemical reaction [Hashimoto, 1982]. Shown in equation (5.18) the activation energy is dependent on the temperature of the system T_{sys} , the reaction rate coefficient (the speed of the chemical reaction) k_s and the frequency factor A_f of the colliding molecules.

$$E_a = -RT_{sys} \ln \frac{k_s}{A_f} \quad (5.18)$$

Increasing the temperature increases the kinetic energy of the particles. It results in a faster reaction rate [Smith, 1998]. If the temperature of the substrate material is kept high enough, then most of the deposited particles with a low enough activation energy could successfully re-ablate.

One of the easiest methods of removal is to re-evaporate the deposited material from the affected surface. This can be achieved by connecting the contaminated surface to a heater or through thermal cycling. In space, a spacecraft can undergo thermal cycling by re-orientating the affected surface towards the general direction of the Sun [Rantanen and Gordon, 1996]. This will drive off much of the contaminated surface. Another method of removal is to gently vibrate the contaminated surface. The energy of the recoil force can dislodge the attached particles. However care must be taken not to damage the underlying surface and to leave any surface residual [Tribble, 1961; Rantanen and Gordon, 1996]. The chosen technique must also be effective on a wide range of surfaces and substances. The migration of the recently liberated contaminants must also be considered. Particles could potentially redeposit on a later orbital pass. This depends on the release angle and velocity of the re-evaporated particles.

The continual accumulation of the ablated ejecta will ultimately affect the behaviour of any exposed surface. For an optical surface located within the ablation volume it will

decrease the transmittance and increase of absorbance of the affected surface. More of the incoming radiation will be absorbed, but will be unable to penetrate to the surface below [Dursch et al., 1995]. Contamination can also alter the thermal emittance of any surface or structure. This becomes a critical factor in the design of thermal radiators and solar arrays. The energy absorbed into the ejecta layer will diffuse throughout and be conducted into the underlying surface. It can increase the thermal equilibrium temperature of any affected unit, and more importantly lead to critical components overheating [Hamberg and Tomlinson, 1971; Tribble, 1961]. Contamination also reduces the ability of solar arrays as a power generating mechanism.

Contamination of any optical component will affect the performance of the ablation event. This includes the design of the laser and spacecraft. The surface power density of the laser beam will be reduced and particle scattering will increase the occurrence of background noise. [Bousequet et al., 1981; Tribble, 1961]. Complete saturation of the solar concentrator and steering mirror will prevent any further ablation event from occurring. The laser will be unable to power, direct and supply the required power density onto the surface of the asteroid. The system's ability of generating thrust will cease completely. Other, optically sensitive payloads will also be affected. This includes, but is not limited to, LIDAR, star trackers, spectrometers and visible cameras. Ablated particles captured within the instruments' field-of-view or line-of-sight will obscure, scatter and reflect light. It will reduce the performance of each instrument [Rantanen and Gordon, 1996; Dursch et al., 1995]. Observations in the far-field will become obscured or degraded [Dursch et al., 1995]. Images will exhibit structural background and bright streaks will be caused by the transit of the ejected particles [Dursch et al., 1995]. This will also degrade the ability of the sensor to perform any of its acquisition, detection, imaging and track correction functions [Dursch et al., 1995]. It can result in inaccurate imaging and unreliable detection. Optical payloads are often the most contamination-sensitive surfaces. They frequently govern the contamination control process of the entire spacecraft and define the lifetime of the mission [Tribble, 1961]. System performance depends on the wavelength of the spectral band and the density of the ejecta layer [Dursch et al., 1995]. A suitably large margin of subsystem safety should always be accounted for within the mission design process. The success of any mission may depend on understanding the tolerance of the spacecraft and its subsystem design.

To account for these cumulative effects, a degradation factor τ is applied to the power density initially beamed onto the surface of the asteroid. τ is dependent on the thickness and, at the wavelength of the laser beam, the absorbance profile of the deposited ejecta [Tribble, 1961; Chen et al., 1987]. Based on the Beer-Lambert-Bouguer law, these factors vary exponentially and can be expressed as [Kahle et al., 2006]:

$$\tau = e^{-2\eta h_{layer}} \quad (5.19)$$

where η is the absorptivity of the deposited ejecta. It is the absorbance per unit length. Data derived from the mass absorption coefficient for forsterite often quotes an absorptivity value of $\eta = 10^4 \text{ cm}^{-1}$ (10^6 m^{-1}) [Demyk et al., 2000]. A factor of two

accounts for the double passing of photons within the ejecta layer. Photons will have to transverse the contaminated layer, be reflected and then transverse the ejecta layer for a second time [Kahle et al., 2006; Tribble, 1961]. It therefore defines the worst case, conservative conditions, where solar concentrators are used throughout.

Photochemical reactions of ultra-violet (UV) radiation can also accelerate the degrading effects of the deposited ejecta. Illumination of UV radiation darkens the deposited ejecta [Brunetto et al., 2006]. This provides a far more pessimistic absorbance profile [Stewart et al., 1989; Judeikis et al., 1993; Tribble, 1961; Rantanen and Gordon, 1996]. It also increases the resident time and sticky coefficient of the particles [Hall et al., 1985]. There is a synergistic interaction between UV radiation and molecular contamination.

5.2.1 Mission Simulations

Using the mathematical model described in Chapter 5.2, the achievable deflection distance induced by a laser ablation event can be determined. Figure 5.6 shows the deflection distance of a small 250 m diameter asteroid. This is given as a function of warning time and the number of spacecraft that fly in formation with the asteroid. The deflection distance is given in kilometers. It was computed using the deflection model developed in Vasile and Maddock [2010] and by excluding the degrading affects of the ejecta plume. Gauss planetary equations were used to compute how the ablation process will affect the orbit of the asteroid [Colombo et al., 2009]. From the start of the ablation process to the expected time of impact with the Earth, the Gauss planetary equations are propagated forward in time. The position and velocity of the deflected asteroid was computed at the expected time of impact with the Earth. It was also assumed that the force is always aligned to the velocity vector of the asteroid.

Each spacecraft, operating within a swarm, is assumed to be identical and is pumped indirectly by the Sun. Together each spacecraft simultaneous targets their laser beam onto the same overlapping spot on the surface of the asteroid. Indirect pumping is provided by a 10 m diameter primary mirror and a set of solar arrays. This system has been previously described in Figure 4.9. The solar arrays are assumed to have an efficiency η_S of 40 %. The conversion efficiency between the electrical-to-laser power system η_L was assumed to be 20 %. The laser itself has an assumed output power of 22 kW and a combined efficiency of 60 %. The power system operates at an efficiency η_P of 85 %. The efficiencies of the solar arrays, electrical-to-power conversion and the power unit defines the overall systems ability of the spacecraft.

On the surface of the asteroid the absorption at the spot α_M is assumed to be dependent on the albedo of the asteroid α_s . Discussed further in Chapter 5.4 (Figure 5.10), this is dependent on the wavelength of the laser beam and can be expressed as $\alpha_M = (1 - \alpha_{s\lambda})$. Shown in Table 2.2, for a S class asteroid the albedo is between 0.1 and 0.3. An average S class asteroid has a peak reflectance of about 1.2 between 0.72 and 0.76 μm (720-760 nm) [Bus and Binzel, 2002]. For a worst-case scenario, the expected expected absorption at the spot would vary between 64-88 %. A wavelength higher than 800 nm or lower than 700 nm would significantly increase the total energy absorption effects. Wavelength

also affects the ability of the laser beam to be focused over an extended distance.

The laser system is also assumed to provide a constant spot size diameter of approximately 8 cm. This corresponds to a concentration ratio C_R of 5,000. The concentration ratio is the ratio between the area of the solar concentrator and the area of the spot. It defines the amount of energy that is focused onto a particular surface spot location [Vasile et al., 2009a]. It is a key parameter in assessing the focusing capability of the system. The sublimation temperature is assumed to be 1800 K. This is based on the material properties of forsterite [Nagahara et al., 1994; Wang et al., 1999; Ranc, 1969].

Taking these parameters into account, the absorbed input power P_{IN} at the spot location, as given in equation (5.1) can be expressed as:

$$P_{IN} = \tau \alpha_M \eta_P \eta_L \eta_S C_R \frac{P_{1AU} A_{SA}}{R_{AU}^2} \quad (5.20)$$

where $P_{1AU} = 1378 \text{ W/m}^2$ and is the solar constant at 1 Astronomical Unit (AU). A_{SA} is the area of the solar arrays and R_{AU} is the distance from the Sun measured in AUs. τ is the degradation factor caused by the deposited ejecta.

Shown in Figure 5.6, under ideal conditions, a maximum deflection distance of 30,000 km can be achieved. This corresponds with nine spacecraft operating for ten years. To achieve deflection greater than one Earth's radius, then three to ten spacecraft are needed over an operational period of nine to four years respectively. However in accordance with the model developed by Kahle et al. [2006], taking into account the degrading effects of the ablated ejecta, then for the same spacecraft configuration the maximum deflection distance reduces to 4500 km. Shown in Figure 5.7, this results in a significant 85 % reduction in performance. The deflection distance also varies with a periodic trend with warning time. This is dependent on the start and end points of the ablation process. It is relative to the orbit of each spacecraft, and is reported further by Colombo et al. [2009].

It is this discrepancy between the optimal and worst-case conditions that needs to be investigated. The laser ablation process is currently subjected to a number of critical assumptions and phenomena that are not completely understood. It includes the formation of the ejecta plume, the physical composition and shape model of asteroids and the ejecta's potential to cause degradation.

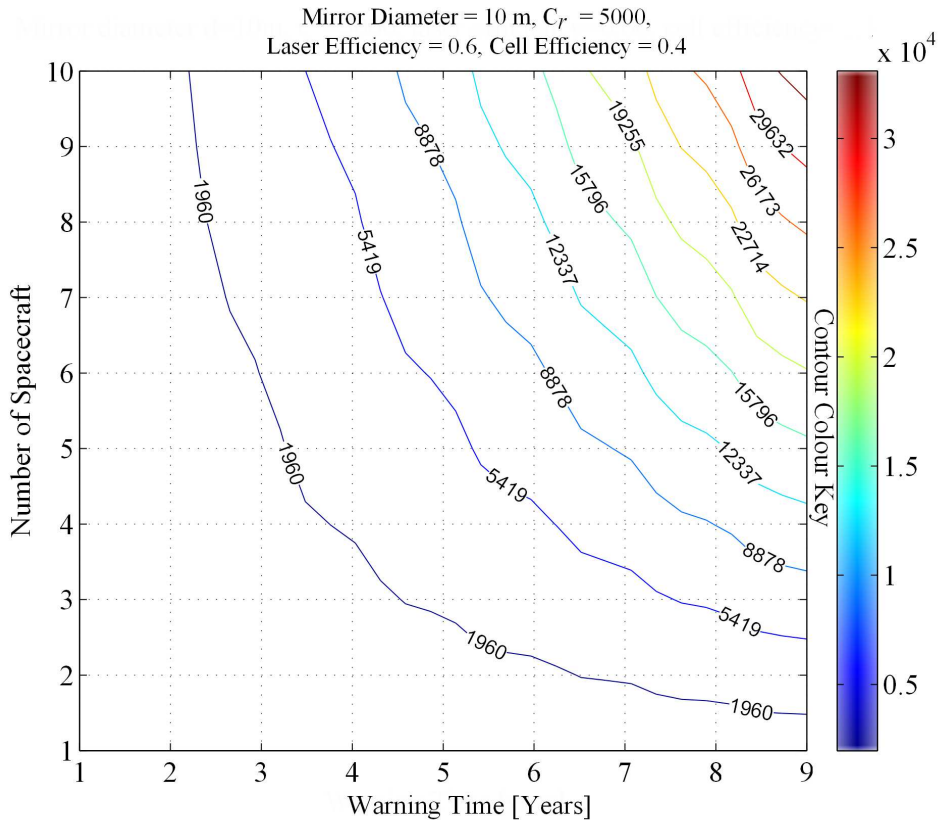


Figure 5.6: Deflection Distance (measured in kilometers) of a 250 m diameter, $2.7 \cdot 10^{10}$ kg (based on Apophis) Asteroid: Without Contamination.

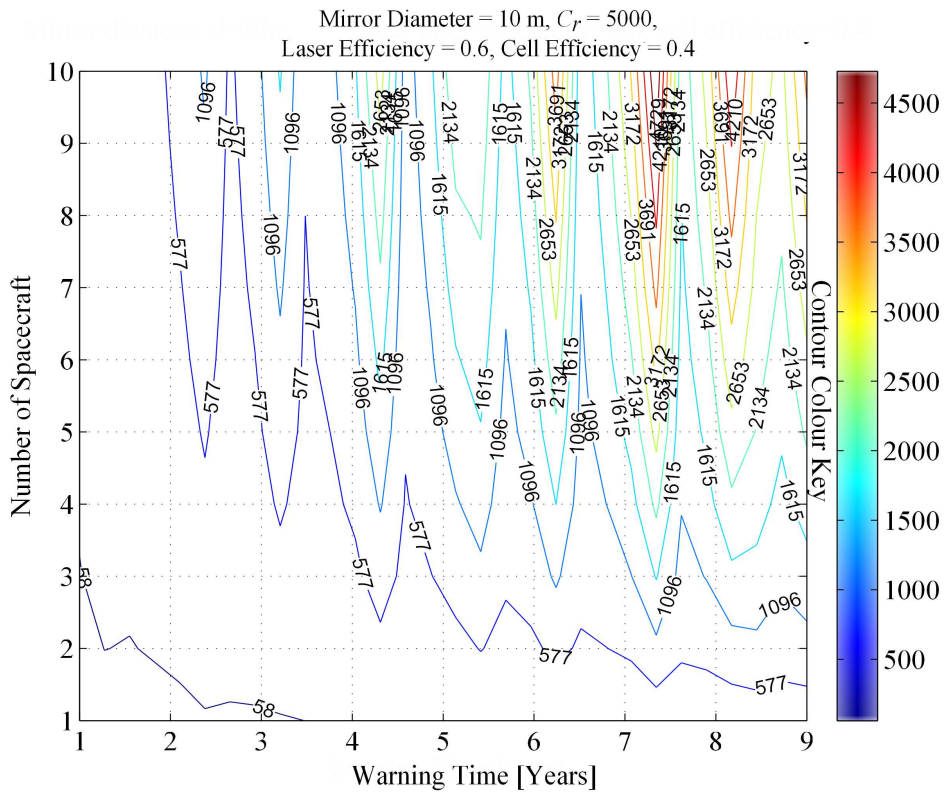


Figure 5.7: Deflection Distance (measured in kilometers) of a 250 m diameter, $2.7 \cdot 10^{10}$ kg (based on Apophis) Asteroid: With Contamination.

5.2.2 Outstanding Issues

Currently compelling, open-ended questions include:

The Physical Evolution of the Ejecta Plume

- Does ablation result in the formation of an exhaust in standard methods of propulsion? Is this limited to the ejection of hot gases, with any solid particles? What is the geometry of the ejecta plume?
- What is the velocity and temperature of the ejecta plume?
- Can the mass flow rate of the ejecta plume be correctly predicted? Is there uniform, hemispheric expansion of the ejecta plume?

The Depositing and Contaminating Effects of the Ejecta Plume

- Is it possible to collect the ablated ejecta? Will all the ablated ejecta immediately re-condense and stick onto an exposed surface? Does it form a permanently attached, thin layer of material? Does its distribution vary with distance and local elevation angle?
- What are the physical (height, mass and density) and chemical properties of the deposited ejecta? How does this vary with the local elevation angle? How does its composition compare to the original, pre-ablated material?
- How does the deposited ejecta affect the behavior (transmittance, absorptivity and collection rate) of the underlying substrate?

The Space-based Mission Considerations

- How does the performance of laser ablation compared to other methods of contactless low thrust deflection? Is there a minimum power requirement? Is it this achievable with the required spot size radius and optical control? What is the achievable momentum coupling? How can this be maximised?
- What is the most significant parameter to define the efficiency of laser ablation? Is it momentum coupling, an efficiency factor or the deflection system mass?
- How much contamination can a given spacecraft tolerate? How does this affect the lifetime of the mission and the achievable deflection distance? It is possible to maximise the survivability of any laser-based ablation system?
- How does the integration of a laser-ablation system affect the design of a spacecraft?

The overall effectiveness of the ablation process is heavily dependent on the distribution and interaction of the ejecta plume. The accumulation of the deposited ejecta is a current show-stopper. It will affect the design, material selection and operational margins - performance, lifetime and tolerance - of any given surface or structure. The potential for contamination is dependent on the generation, transportation and deposition of the ablated ejecta. A better, more detailed understanding of the contamination process is therefore critical. Contamination reduces the achievable surface power density of the

laser beam and the associated thrust imparted onto the asteroid. It will therefore have a major impact on the overall performance, design and success of any asteroid deflection mission.

To address these outstanding questions a series of laser ablation experiments were performed. This aimed to validate the existing modeling technique given by Kahle et al. [2006]; Sanchez et al. [2009]. The initial assumptions could be confirmed, updated or removed. Presented in Chapter 6, the experiments were used to answer the first two sets of questions. This examined the physical formation of the ejecta plume - mass flow rate, temperature, velocity and divergence geometry - and the contamination effects of the deposited ejecta. It also enabled the additional temperature-dependent absorption effects of the ablation process to be considered. This included the interaction of the laser beam with an optically dense ejecta plume, the formation of a self cleaning hole and the incoherent ablation of the target material. A fundamental assumption is that the thermal model is one dimensional and therefore only includes the heat loss through conduction and radiation. There is no absorption of the ablated gas, nor the ejection of solid particles or the formation of plasma. The asteroid is also assumed to have a constant value of emissivity, specific heat capacity and density.

Chapter 7 shows how the results from the experiments were used to re-evaluate the performance of laser ablation in producing a deflection action. Performance was compared to other forms of contactless low thrust deflection that uses electric propulsion. Chapter 8 demonstrates how a moderately sized laser system can be integrated, and affects the design of, a space-based ablation system. Chapter 7 and 8 therefore addresses the aforementioned space-based mission considerations. It has provided a critical insight into the effectiveness of the laser system, the proposed mission configuration, and most importantly, laser ablation as a viable method for the deflection of NEAs. However, it should be noted that time limited the number of experiments that could be performed. It was not possible to test the response of a wide range of asteroid analogue target material. Under vacuum, only an olivine sample was ablated. The model's subsequent development is therefore limited to the ablation of a rocky and dense body. The affect of porosity has not been included. Future work should therefore examine the ablation response of loose rubble piles, porous bodies and more realistic shape models. This is discussed further in Appendix A and B.

5.3 Momentum Coupling and Energy Efficiency

The mathematical model also enables the momentum coupling C_m between the laser beam and the ablated asteroid to be determined [Phipps, 2002; Phipps and Luke, 2007; Phipps, 2010; Sinko and Phipps, 2009]. For a pulsed laser it is defined by the ratio of momentum ($m\Delta v$) produced relative to the absorbed laser pulse energy E . For a continuous wave laser, it is the ratio of force F_{SUB} relative to the absorbed laser power, P_{IN} . It is expressed as either N/W or Ns/J and is defined as [Schall et al., 2007; Phipps et al., 2000; Phipps, 1997]:

$$C_{mP} = \frac{m\Delta v}{E} \quad (5.21)$$

$$C_{mC} = \frac{F_{SUB}}{P_{IN}} \quad (5.22)$$

At a low intensity, or fluence for a pulsed laser, the ablated material is considered to be within the vapour regime. Momentum is created by intense vaporisation of the target material. [Phipps et al., 2004b; Sinko and Phipps, 2009]. At sufficiently high intensities, the laser-to-surface interaction is dominated by the development of a hot, high pressure, optically thick plasma [Bulgakov and Bulgakov, 1999]. Intense absorption of the laser beam results in the formation of a thin, yet dense layer of electrons, ions and neutrons. This forms above the target's surface and is the main contributor to increasing the localised pressure and temperature of the ejecta plume [Moscicki et al., 2012]. The temperature of the plasma often exceeds the surface temperature of the target. It also complicates and attenuates the interaction of the laser beam and the target material.

Absorption is caused by the Inverse Bremsstrahlung effect. Free electrons absorb the additional energy of the laser beam, and at a certain point, completely shields the target from the incoming laser beam [Phipps et al., 2004b; Yabe and Uchida, 2007; Sinko and Phipps, 2009]. Progressively more energy contained within the laser beam is used to heat-up and accelerate the plasma, rather than in the direct ablation of the target material [Bhargava et al., 2004]. It results in the progressive reduction in the momentum coupling, efficiency and the mass flow rate of the ablation event [Phipps and Luke, 2002; Phipps et al., 2006; Bogaerts et al., 2011; Marla et al., 2011; Phipps and Michaelis, 1994; Bergstue and Fork, 2011; Russo et al., 1999]. Eventually no further ablation event will be induced. An example of this is shown in Figure 5.8. This demonstrates the behaviour of a KrF laser coupling to nylon [Phipps et al., 1988]. The black dashed line is the least-square fit to the data points at intensities greater than I_{max} . The green, solid line is the momentum coupling. This illustrates the transition from the vapour to plasma dominated regime. From the line of best fit, the standard deviation from the point is $\pm 8\%$.

The peak value C_{max} denotes the maximum momentum coupling. It occurs just before the onset of plasma, at a threshold value generally greater than 1 GW/cm^2 to 5 GW/cm^2 [Phipps et al., 1988; Phipps, 1993; Krajnovich, 1995]. The exact value is defined by a specific laser intensity and duration. [Campbell et al., 2002]. No definite boundary exists [Phipps and Dreyfus, 1993]. Beyond this point, momentum can only be created by pulsing the laser beam [Marla et al., 2011]. This would enable the outwards expansion of the plasma plume. A force would be exerted and ejecta deposited onto any exposed surface. The fast dissipation of the ejecta plume would enable the re-illumination and ablation of the target. The pulse spacing must therefore be timed so that it enables the full expansion and dissipation of the ablated material. A series of short pulses is often the most effective process [Bergstue and Fork, 2012].

Additionally, Q^* is used to express how much energy E is required to ablate each kilogram of material. It is measured in J/kg and is expressed as [Phipps et al., 2000]:

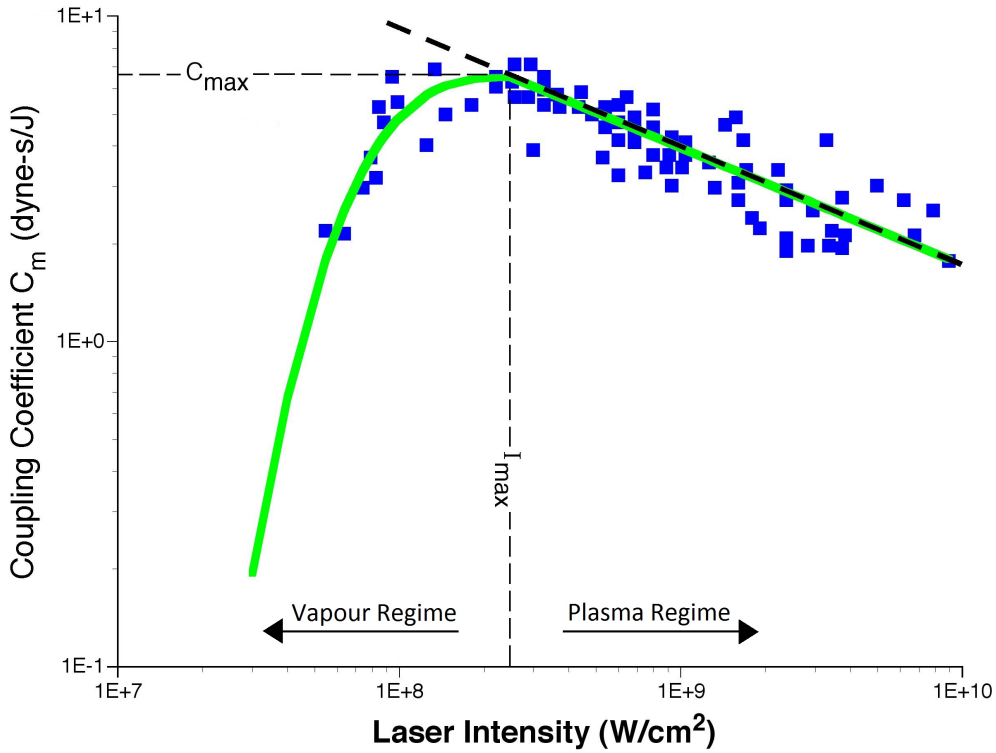


Figure 5.8: Experiment Data of the Mechanical Coupling of a KrF Laser to Nylon ($\lambda_b = 248$ nm, $\tau_b = 22$ ns, $I_{max} = 10^8$ W/cm²). Data gained from Phipps et al. [1988]

$$Q^* = \frac{E}{\Delta m} \quad (5.23)$$

Energy absorption is the product of the absorbed laser power at the spot location multiplied by the ablation time. Δm is the mass of the ablated asteroid in a given time period. From this and the momentum coupling, the efficiency of the ablation process η_{AB} can be determined. This is defined by the efficiency at which the laser energy is converted into ejecta kinetic energy, carried away by the ejecta plume. It is given by [Phipps et al., 2004a, 2000]:

$$\eta_{AB} = \frac{1}{2} C_m^2 Q^* \quad (5.24)$$

It should be noted that the efficiency value is based on the absorbed laser energy and power at the spot location. It does not affect the mass of the laser, which is instead dependent on the momentum coupling. Nor does it include any absorption losses within the ejecta plume. This would limit the impulse generation [Schall et al., 2007].

5.4 Improved Ablation Model

Shown in Chapter 6, the results from a series of laser ablation experiments have enabled the ablation model to be updated. This enabled the existing assumptions to be confirmed, updated or eliminated. For a given input power, a critical discrepancy was in the variation in the predicted and experimentally determined mass flow rate of the ablated

material. This could lead to an overestimation of the imparted thrust provided by the ablation process. Other improvements have also included the energy absorption within the Knudsen layer, the variation of sublimation temperature with local pressure, the temperature dependent thermal conductivity of the target material, and the partial re-condensation of the ablated material.

Based on the experimental analysis, the improved ablation model derives the mass flow rate per unit area of the sublimated material $\dot{\mu}$. This is achieved by the following one-dimensional energy balance at the illuminated spot. It is given by:

$$\dot{\mu} \left[E_v + \frac{1}{2} \bar{v}^2 + C_P (T_{SUB} - T_0) + C_V (T_{SUB} - T_0) \right] = P_I - Q_R - Q_C \quad (5.25)$$

where E_v is the latent heat of complete sublimation, \bar{v} is the velocity of the ejecta plume, C_P is the specific heat capacity of the ejected gas at constant pressure, T_{SUB} is the sublimation temperature, T_0 is the temperature of the material prior to sublimation, C_V is the specific heat capacity of the asteroid at a constant volume, P_I is the absorbed laser beam per unit area, Q_R is the heat loss per unit area through radiation and Q_C is the heat loss per unit area through conduction. C_V is considered to be constant and equal to the maximum heat capacity according to the Debye-Einstein asymptotic heat capacity for solids [Robbie et al., 1982]. C_P is the maximum expected heat capacity value given the range of sublimation temperatures of the target material [Navrotsky, 1995].

The term $C_V (T_{SUB} - T_0)$ accounts for the energy needed to increase a layer of the target material from its initial temperature T_0 to the sublimation temperature T_{SUB} . The term $\frac{1}{2} \bar{v}^2 + C_P (T_{SUB} - T_0)$ accounts for the energy that is absorbed by the vapour in the Knudsen layer from the solid-gas interphase (later in the sublimation it is the liquid-gas interface) and the accelerated gas phase [Knight, 1979]. Under high, steady-state evaporation a thin layer, immediately adjacent to the evaporating surface is formed. This is known as the Knudsen layer and is created by the gaseous collision of near-surface particles during the initial, high pressure expansion of the ejecta plume [Bulgakov and Bulgakov, 1999]. Under equilibrium conditions, the number of molecules evaporated from the liquid phase must be equal to those condensed from the vapour phase. The liquid and vapour temperatures are also assumed to be uniform [Rahimi and Ward, 2005]. The additional heat absorbed in the Knudsen layer is equivalent to increasing the enthalpy of sublimation by approximately $1 - 2 \cdot 10^6$ J/kg [Knight, 1979]. Heating the gaseous ejecta from 3100 K (the expected sublimation temperature) to 4747 K (recorded value from the spectrometer, shown in Figure 6.6) would consume approximately 2 MW/m² of energy. This assumes a specific heat capacity of 1361 J/kgK.

The heat loss, per unit area, through radiation and conduction was retained from the previous model. Both expressions have been defined previously in equation (5.3) and (5.4). In equation (5.4) C_V is used as an improved, and more accurate value for the specific heat capacity (formerly c_A). The model therefore assumes a constant spot temperature with a one dimensional transfer of heat, where the only heat loss are through conduction and radiation. The time derived value in equation (5.4) accounts

for a rotating asteroid. t is the time that the surface of the asteroid is illuminated under the spot light. Equation (5.3) assumes that the asteroid is acting as a black-body and is dissipation energy per unit area and with time. For a non rotating asteroid (as experienced in the laboratory experiments), before the sublimation process starts, equation (5.26) describes the conditions at the spot location.

$$P_I = -k_A \frac{\partial T}{\partial x} + Q_R \quad (5.26)$$

Using the case of a simple, one-dimensional heat conduction then:

$$Q_C = -k_A \frac{\partial T}{\partial x} \quad (5.27)$$

$\frac{\partial T}{\partial x}$ is the temperature gradient through the asteroid, as the conducting medium.

Equation (5.27) is only valid for a steady-state heat flow, where the heat flux does not change with time. The minus sign indicates the direction of the flow is from hot to cold, down the temperature gradient. Equation (5.26) needs to be solved together with the heat diffusion equation:

$$\frac{k_A}{\rho_A C_V} \frac{\partial^2 T}{\partial x^2} = \frac{\partial T}{\partial t} \quad (5.28)$$

with the additional boundary conditions of:

$$T(0, x) = T_o \quad (5.29)$$

$$T(t, L) = T_o \quad (5.30)$$

The heat diffusion equation describes one-dimensional heat conduction, in a planar medium with constant material properties and no heat generation from external sources. $T(0, x)$ is the initial temperature distribution and $T(t, L)$ describes the later conditions. L is the path length through the asteroid. $\frac{k_A}{\rho_A C_V}$ is the thermal diffusivity of the asteroid. It measures the thermal inertia of the asteroid, defining its ability to respond to change in its thermal environment.

When sublimation starts, it is assumed (as given in Chapter 5.2), that the temperature of the spot remains constant. Therefore the heat diffusion equation can be solved with the boundary condition $T(t, 0) = T_{SUB}$ in place of equation (5.26). The initial hypothesis was that T_o is constant throughout the sublimation process and corresponded to the temperature of an infinite heat sink. In this case, T_o was assumed to be the temperature at the asteroid's core. However, in the laboratory experiments, during ablation, the target displayed a substantial increase in temperature. It is therefore expected that the initial model only provided a conservative estimation of the heat dissipation through conduction. The thermal conductivity from the sublimated material to the inner core

has been improved by taking it to be a function of the sublimation temperature. This is gained through the power law relation:

$$k_A = k_{A_0} \left(\frac{298}{T_{SUB}} \right)^{0.5} \quad (5.31)$$

The model only considers heat diffusion from the illuminated spot to the core of the target. An additional sideways component can drain more energy away from the ablation process. This action will be included in a future model. The velocity of the ejecta plume \bar{v} is calculated as the average of the Maxwell's distribution for an ideal gas. This has been previously defined in equation (5.5). It is governed by the molar mass of the gaseous ejecta, Boltzmann's constant and the sublimation temperature. The sublimation temperature can also be related to the local pressure at the ablation spot. It is gained through the Clausius-Clapeyron equation and is given by:

$$\ln \frac{p_s}{p_{ref}} = \frac{E_v}{R} \left(\frac{1}{T_{ref}} - \frac{1}{T_{SUB}} \right) \quad (5.32)$$

where p_s is the pressure corresponding to the temperature T_{SUB} and p_{ref} is the pressure corresponding to the reference temperature T_{ref} [Bulgakov and Bulgakov, 1999; Ketren et al., 2010]. R is the universal gas constant. Equation (5.32) is used to model any phase transitional event - solid to gas, liquid to gas and solid to liquid. The vapour pressure of a substance at any temperature can be calculated from its known enthalpy of sublimation and its vapour pressure at a given temperature. It is determined by assuming that the enthalpy of sublimation is constant over the interested temperature range, the sublimated material acts as an ideal gas, the vapour pressure is not affected by an external pressure and that the change in volume caused by the sublimation process is equal to the volume of the vapour products.

At the illuminated spot, the ablation of the target material will increase the local vapour pressure. This will increase the temperature of the irradiated asteroid and absorption effects of the ejecta plume. Previous research has shown that the sublimation temperature for a range of Mg-Fe and Si-Fe oxides can vary between 3175-3800 K [O'Keefe and Ahrens, 1971; Yoo et al., 2000]. A lower sublimation temperature can also be caused by the transparency of pure minerals [Nagahara et al., 1992]. Therefore, the reference temperature of 3800 K was taken to be at 1 atmosphere. The enthalpy of complete sublimation is considered to be constant in the range of temperatures in which equation (5.25) is valid.

It is also important to link the mass flow rate of the ablated material to the local pressure. This completes the description of the generation of a gaseous ejecta plume. The mass flow rate given in equation (5.25) is measured from the outer edge of the Knudsen layer. It can be related to the local pressure at the interface between the Knudsen layer and the ablated material. This is achieved through the Hertz-Knudsen equation [Knudsen, 1909]. It is derived from the kinetic theory of gas (assuming the conditions of an ideal gas under equilibrium) and microscopic reversibility [Shorov and Rickman, 1995; Xia and Landman, 1994; Knight, 1979; Nagahara et al., 1994].

This is expressed as:

$$\dot{\mu} = (1 - k) p_s \left(\frac{1}{2\pi R_S T_{SUB}} \right)^{\frac{1}{2}} \quad (5.33)$$

where k is the fraction of molecules that re-condense at the interphase. $(1-k)$ is therefore the fraction of vapour molecules that contributes to the pressure of sublimation, but not the sublimated flux. p_s is the vapour pressure and R_S is the specific gas constant. R_S can be expressed as a function of the molecular mass M_a and the universal gas constant, $R = 8.3144 \text{ J/molK}$, where $R_S = \frac{R}{M_a}$. The maximum rate of evaporation not only depends on the supply of heat (and therefore its temperature), but must also be accompanied with an increase in the vapour pressure that is caused by the sublimation action. The fraction of molecules that re-condense is expected to increase with the local pressure. However the change in the thrust due to the re-condensation is limited. Figure 5.9 plots the resulting thrust against a wide range of recondensation fractions. The maximum variation in thrust is only 4 %. This can be considered negligible.

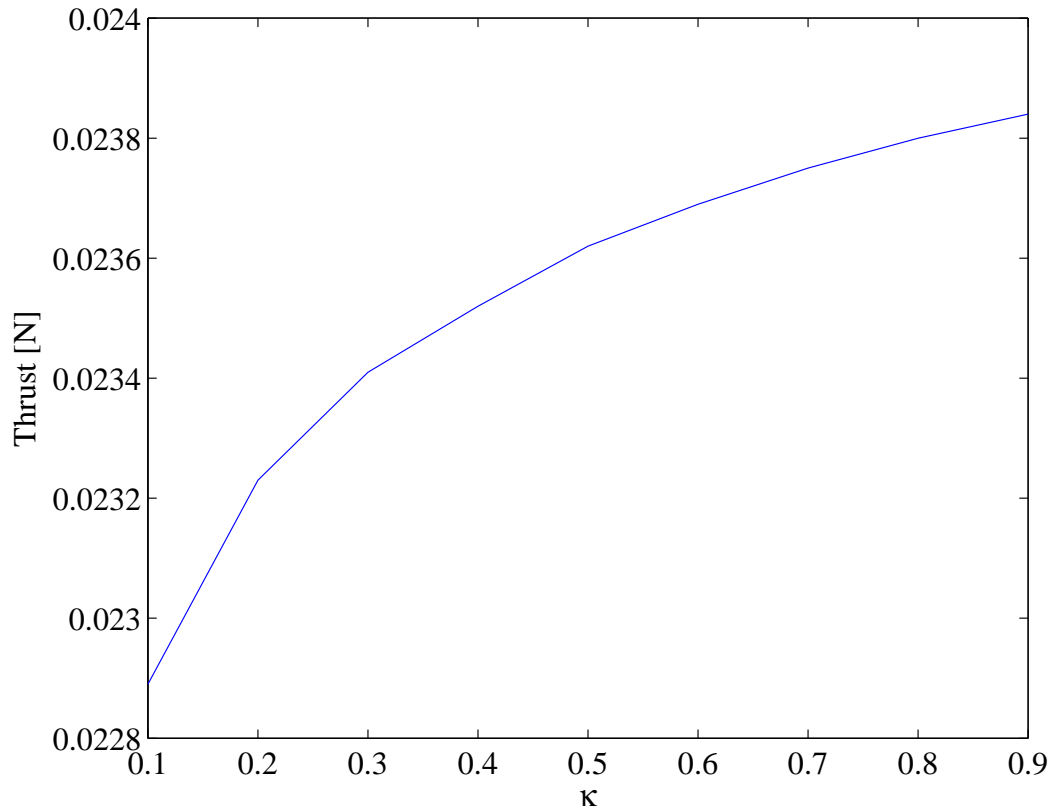


Figure 5.9: Thrust Sensitivity to the Recondensation Ratio

To account for the additional absorption effects of ablation, the absorbed laser power per unit area P_I can be defined as:

$$P_I = \frac{\tau \tau_g \alpha_M \eta_L P_L}{A_{SPOT}} \quad (5.34)$$

where η_L is the efficiency of the laser system and P_L is the input power to the laser. $\alpha_M = (1 - \varepsilon_a \alpha_s)$ is the absorption at the spot. This is dependent on the albedo α_s of the asteroid multiplied by the increment in reflectivity ε_a at the wavelength of the laser beam. Table 2.2 gives the range of albedo for the different classes of asteroids. A standard NEA has an average albedo of 0.154 [Chesley et al., 2002]. The reflectivity of an asteroid is dependent on its mineral composition, chemistry, particle size and temperature. Each reflectance spectrum is characterised with wavelength-dependent absorption features. Figure 5.10 shows the spectral emission of four different asteroids. The spectral response occurs over the visible wavelength from 0.4 to 1.0 μm . Each asteroid has been assigned to a different class of asteroid. This provides an illustrative example, which in practice would vary with time and position. A red spectra refers to an increase reflectance with increasing wavelength. A blue spectra refers to a decreasing reflectance within increasing wavelength.

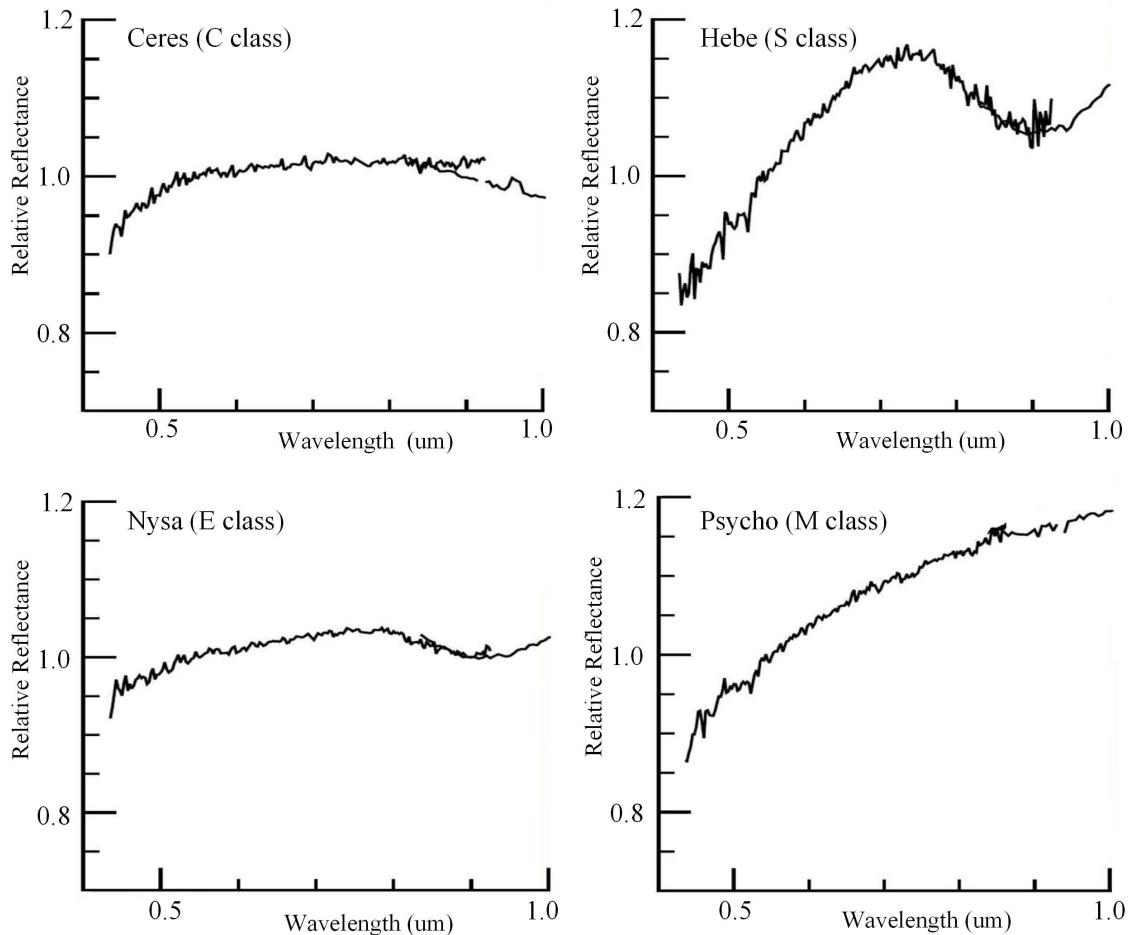


Figure 5.10: Reflective Spectrum of Four Different Classes of Asteroids. All spectral data is available at <http://smass.mit.edu/catalog.php> [Bus and Binzel, 2002]

S class asteroids are described as having a moderate to steep red ($\lambda < 0.75 \mu\text{m}$) and blue ($\lambda > 0.75 \mu\text{m}$) slope [Bus and Binzel, 2002; Bus et al., 2002]. It is associated with a deep 1 μm silicate absorption band [Bus and Binzel, 2002]. They sometimes display shallow absorption features, centered around 0.65-0.7 μm . The spectrum of an average S class asteroid has a peak reflectance of about 1.2 at a wavelength of around 0.73 μm

[Bus and Binzel, 2002]. Its albedo can also vary between 0.1 and 0.3. C class asteroids are more neutral in colour with a featuresless (i.e. linear) to slightly redish ($\lambda > 0.55 \mu\text{m}$) slope. They also tend to have a moderate to deep ultra-violet absorption ($\lambda < 0.55 \mu\text{m}$) [Bus and Binzel, 2002]. The response of M and E class asteroids are similar and are often grouped together. Both can be a flat to a moderately red, featureless spectrum. The only expectation can be an occasional broad convex curvature around 0.5-0.7 μm and a slight ultra-violet absorptive feature ($\lambda < 0.55 \mu\text{m}$) [Bus and Binzel, 2002; Bus et al., 2002].

Equation (5.34) also accounts for the absorption of the laser beam τ_g within the rapidly expanding and absorbing plume of ejecta. From the experimental results, it is expected that the ejecta plume will absorb 10-15 % of the incoming laser beam. This accounts for the fraction of laser light absorbed and scattered by the gaseous ejecta plume. Absorption will increase the temperature of the plume. The input power of the laser beam is also multiplied by a degradation factor τ . This accounts for the degrading effects caused by the re-condensed deposited ejecta material. The re-condensed material does not directly affect the laser beam, but it can reduce the power input generated by the solar array, or any other power source that uses sunlight. The degradation caused by the ablated ejecta is computed using the model developed by Kahle et al. [2006]. This was defined previously in equations (5.8), (5.16) and (5.19).

The mass flow rate of the ablated material can then be computed by integrating $\dot{\mu}$ over the surface area illuminated by the laser beam. This is in accordance to the model initially developed by Sanchez et al. [2009]. For a rotating asteroid this is given by:

$$\dot{m}_{SUB} = 2V_{rot} \int_{y_{min}}^{y_{max}} \int_{t_{in}}^{t_{out}} \frac{1}{E_v^*} (P_I - Q_R - Q_C) dt dy \quad (5.35)$$

where the new term E_v^* is the augmented enthalpy and is equal to:

$$E_v^* = \left[E_v + \frac{1}{2} \bar{v}^2 + C_P (T_{SUB} - T_0) + C_V (T_{SUB} - T_0) \right] \quad (5.36)$$

The force acting on the asteroid F_{SUB} can also be computed using the equation (5.6). The scatter factor λ is the integral of the trigonometric part in equation (5.8).

Experiment Design and Results

6.1 Introduction

To verify the ablation model and to examine the operational constraints of laser ablation, a series of experiments were performed. The experiments examined the formation of the ejecta plume and the ejecta's potential to cause degradation. Assessed factors included the divergence, average mass flow rate and velocity of the ejecta plume, and the absorptivity, height and density of the deposited ejecta. Each experiment was repeated three times and lasted for 10 minutes. Repetition provided viable and calibrated data-points that could be easily repeated. Standard Error of the Mean was used to represent the variability in the originally recorded experimental measurement. Error bar analysis is presented in Appendix I and provided additional confidence in the measuring technique. The error bars are small (and were consistently small throughout the analysis). The experiment duration was long enough to measure the degrading effects of the ablated ejecta. The results gained from the experiments were compared to the expectation of the improved ablation model.

The experiment platform was developed from a series of initial ablation events. These preliminary experiments occurred in a dry, nitrogen purged test chamber, under standard atmospheric conditions [Gibbins et al., 2011b]. The experiment platform was used to develop the proposed methodologies, data collection techniques and expectation of the ablation response. Methodologies that were investigated, but did not yield suitable significant results are reported in Appendix B. Nitrogen was used to create a non-reactive environment that eliminated the occurrence of any atmospheric combustion. Negligible amounts of innate material combustion did still occur. The ablated target material (MgSiO_2 and SiO_2) dislocated into its Mg, Si and O components, which (as shown in Table 6.16) then recombined with its primary and secondary chemical species. It is an intrinsic property of the ablation process and could not be controlled [Hashimoto, 1990].

The ablation experiments were then repeated in a high quality vacuum chamber. Vacuum was needed to enable the free, maximum expansion of the ejecta plume [Dettleff, 1991]. The rate of ablation, as shown in Chapter 5.4, is also pressure dependent. An ambient, background gas would have acted as a moderator. Molecular collisions could slow down the expansion of the ejecta plume. Scattering could change the direction and distribution of the ejecta plume. Laser attenuation would reduce the mass flow rate of the ablated material. Ambient gas reactions would also form unwanted oxides [Dettleff, 1991; Marla et al., 2011; Schall et al., 2007; Bogaerts et al., 2011; Gusarov et al., 2000].

A vacuum chamber was therefore used to provide a more realistic simulation of the laser-to-asteroid, space-based, ablation event. A minimum pump-down base pressure of $2 \cdot 10^{-5}$ mbar was achieved with the combined operations of a mechanical roughing pump (E2MI2) and a diffusion pump (160 Diffstack). Both pumps were supplied by Edwards Vacuum. Appendix K provides a technical description of the pumping system.

6.2 Laser

A 90 W, continuous wave, fibre-coupled semiconductor laser (LIMO 90-F200-DL8080) was used to initiate the ablation process. The laser operated at a wavelength of 808 nm and was below the threshold of plasma formation. The health and safety issues of operating the laser are addressed in Appendix C. The operating procedure is given in Appendix D. The laser was mounted horizontally, on an optical bench, and cooled via a fast flow rate recirculating chiller. The initial output of a 2 m long, 200 μm -core fibre umbilical was collimated with an aspheric lens. This allowed the laser beam to propagate across the optical table to fill ($\sim 75\%$) a 50.8 mm diameter lens. A second lens was used to focus the laser beam onto the surface of the target. Each lens was coated against any anti-reflections that might occur at the wavelength of the laser beam. The propagation of the laser beam into the test chamber is illustrated in Figure 6.1. Photographic images showing this arrangement in the laboratory can be found in Appendix E.

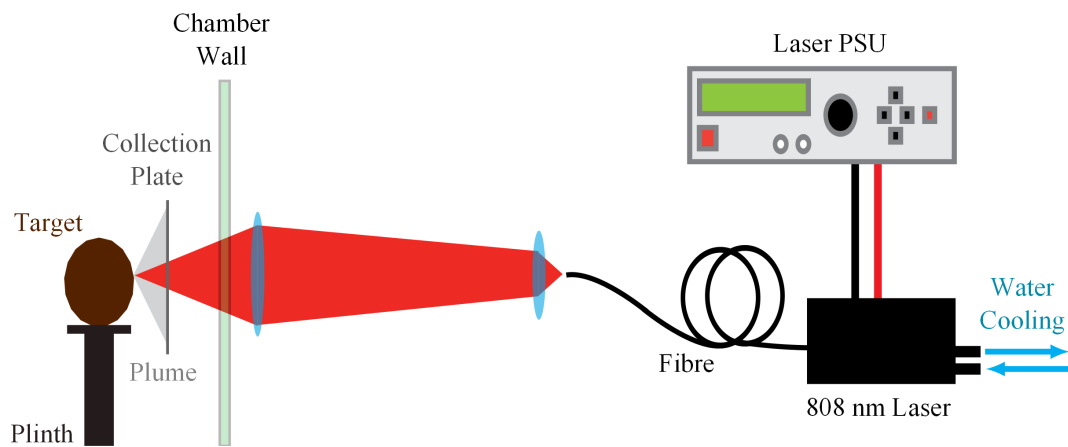


Figure 6.1: Illustration of the Laser Beam and Experiment Set-up

The laser beam was always aligned perpendicular to the surface of the target. For all alignment activities the laser beam was operated at 2 W. This is just above the threshold of the laser and created a red, visible, residual spot. When required, a beam blocker was used to block the incoming laser beam.

The system provided an approximate spot size radius of 0.9 mm and a surface power density of $2.44\text{--}1.69 \text{ kW/cm}^2$ (accounting for losses). The surface power density was calculated from the energy of the laser beam and the surface spot area [Shannon et al., 1995]. The spot size area was calculated using geometric optical principles and compared to burn pattern measurements [Fernandez et al., 1995]. The depth-of-focus was approximately 8.43–9.25 mm. This is the distance over which the focused laser beam has

roughly the same illumination footprint and intensity. Shown in Figure 6.1, energy is lost through the transmittance of the window and the central collection plate. Transmittance losses were confirmed by placing a power meter in the path and at the focus of the laser beam. The windows were also periodically cleaned. This removed any unwanted, deposition of the ablated ejecta that did not collect on the collection plates.

6.3 Target Material

Each tested sample needed to be solid with inherent material strength and be an effective absorber. The latter is relative to the wavelength of the laser beam [Phipps et al., 1988]. Strength is needed as each target material had to be carried about and managed within the laboratory. Quartz sandstone and a highly porous composite mixture represented a dense, solid and highly porous, rubble pile asteroid respectively. Both samples were ablated in the preliminary nitrogen purge experiments. The manufacturing process of the highly porous samples is given in Appendix A. Olivine represented a dense, rocky, S class asteroid. It was used exclusively in the vacuum chamber experiments.

Olivine is a low iron, magnesium silicate with a measured bulk density of 3500 kg/m^3 . The bulk density was measured from the mass and volume of each sample. All other values, as given in Table 6.1, were assumed based on the existing literature. The ambient temperature T_{AMB} coincided with the local temperature (298 K) of the laboratory. For space-based conditions, this was taken to be 4 K, the temperature of background radiation.

Parameter	Value
Bulk Density ρ	3500 kg/m^3
Sublimation Enthalpy E_v [Marinova et al., 2011; Melosh and Nemchinov, 1993; Melosh et al., 1994]	$14.5 \cdot 10^6 \text{ J/kg}$
Black Body Emissivity ε [Vasile and Maddock, 2010]	0.97
Temperature at the Centre of the Asteroid T_o	298 K
Specific Heat Capacity of the Asteroid C_V	1361 J/kgK
Specific Heat Capacity of the Ablated Gas C_P [Knight, 1979]	1350 J/kgK
Thermal Conductivity κ_{A_0} [Lindgrad and Jonansen, 1996]	4.51 W/mK

Table 6.1: Material Characteristics of Olivine

The enthalpy of sublimation combines the enthalpy of vaporisation and the heat fusion. It is the complete enthalpy of vaporisation rather than the incident of vaporisation. E_v therefore defines the energy per kilogram of material needed to remove it from the bulk. The values given in Table 6.1 are critical to the ablation process and are quite controversial. A large amount of uncertainty exists. Little information is known on the physical, compositional and surface properties of asteroids and their appropriate

analogues [Opeil et al., 2010].

Before each experiment, the olivine sample was cut into a cube and inspected with the SEM. Cutting permitted the laser beam to illuminate a flat face, under direct, perpendicular irradiation. It avoided, or severely limited, the ablation process being affected by any surface irregularities. This included surface curvature and roughness. The aim was to provide illumination of a tightly focused laser beam. It was also considered to be a realistic analogue of the space-based event. The size of the laser beam would be small in comparison to the size of the asteroid and its largest geological feature. The model also assumed a two dimensional flat surface spot.

Cutting was achieved with a diamond coated circular saw blade. The cut samples were then cleaned in an ultra sonic bath of ultra-pure deionised water. This removed any contaminated particles that might have adhered to the surface. The samples were then oven-dried overnight at 30 °C and stored in a small polythene bag. It followed the same procedure reported in Lee et al. [2006].

6.4 Cameras and the Spectrometer

Shown in Figure 6.2 the test chamber was surrounded with two high speed, high resolution cameras (CMOS Panasonic HDC-SD60) and a dual channel spectrometer. Viewing access into the vacuum chamber was provided by three, fused quartz, optical windows. Each window had a transmittance of approximately 94 %. Before each ablation experiment the test chamber was covered with a dense, black cotton sheet. This removed any unwanted ambient reflections from the surrounding laboratory environment.

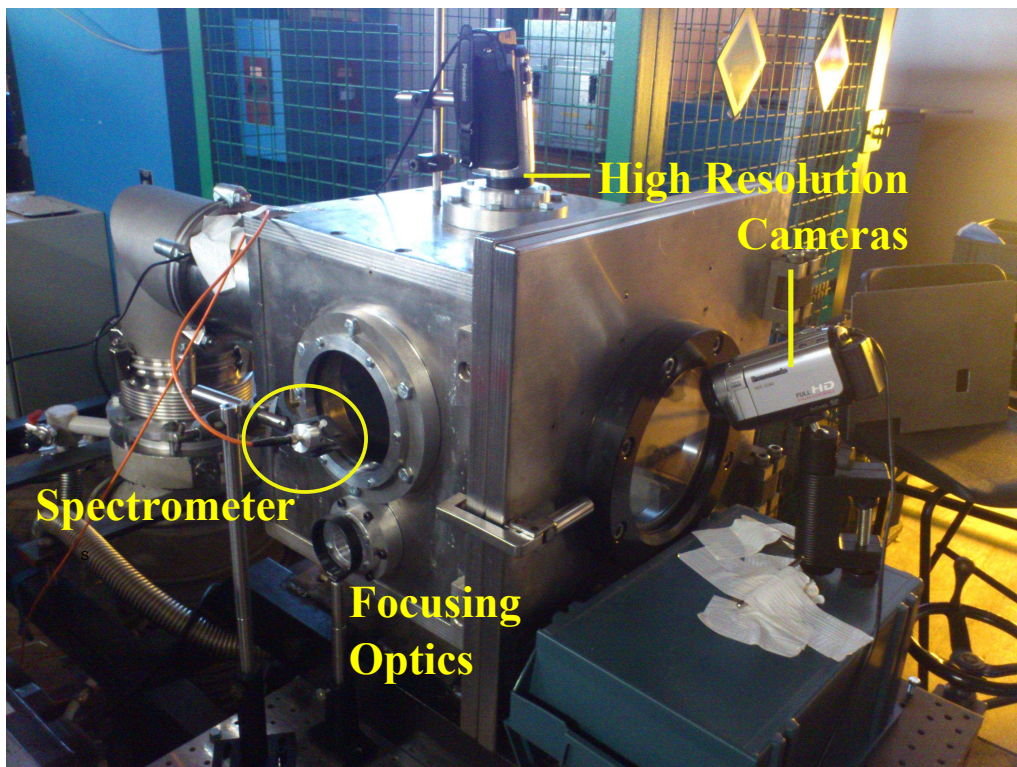


Figure 6.2: External Arrangement of the Test Chamber

Each camera was mounted to be near-orthogonal to each other. The cameras measured the divergence of the ejecta plume. It was used to validate whether or not the expansion of the ejecta plume is similar to the formation of a rocket exhaust. The cameras were able to distinguish between the ejection of hot gas and solid particles. The field-of-view of each camera covered the entire ablation volume. A filter was mounted onto the lens of each camera. This removed the excessive laser light (at the wavelength of the laser beam), limited the occurrence of stray light and prevented the saturation of the camera's CCD. Post-processing of the collected data enabled the maximum cone angle of the ejecta plume to be examined. Together, with the static images, it was possible to assess the shape model of the expanded plume of ejecta. Data was extracted with the open sourced *Kinovea* and *ImageJ* programmes. Each video was segmented into a series of images. Segmentation occurred every 0.04 s.

The cameras recorded the volumetric removal of the target material. This was caused by the evacuation of the initially illuminated surface and subsurface material, where a small and narrow hole extended into the target material. In all experiments a small, yet extended plume of ejecta was created. This occurred perpendicular to the target's surface. Shown in Figure 6.3a, ablation was dominated by the gaseous and hemispheric expansion of the illuminated material. It was similar, although not identical to, the formation of the rocket exhaust in standard methods of rocket propulsion. Ablation also resulted in the initial, additional ejection of small, yet solid particles of ejecta. This is shown in Figure 6.3b with the creation of white streaks.

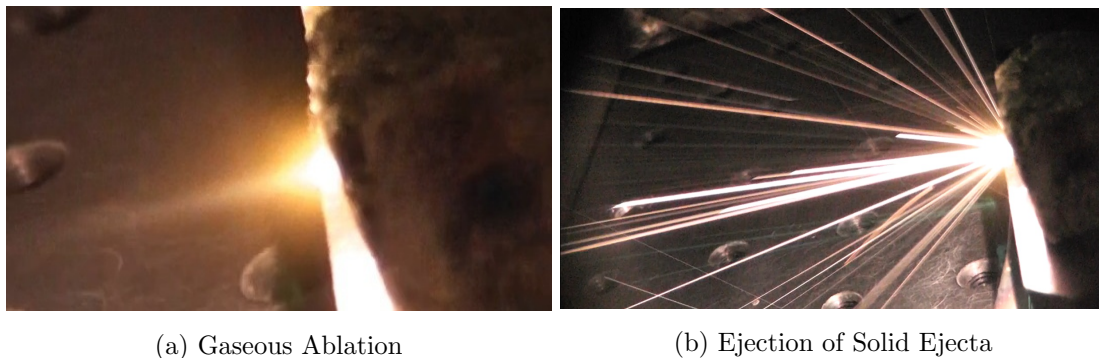


Figure 6.3: Formation of the Ejecta Plume

Figure 6.3b indicated that each particle had a direct, forward velocity that originated from the laser-to-surface interaction point. Ejection is a fast and short-lived process. Shown in Figure 6.4, ejection of solid material was concentrated at the start of the ablation process. The majority of the ejected material was distributed over ± 90 degs and was symmetric from the surface normal. In the later stages of sublimation the material that is ejected come from the inhomogeneous layers of the target material, which may have a lower sublimation temperature.

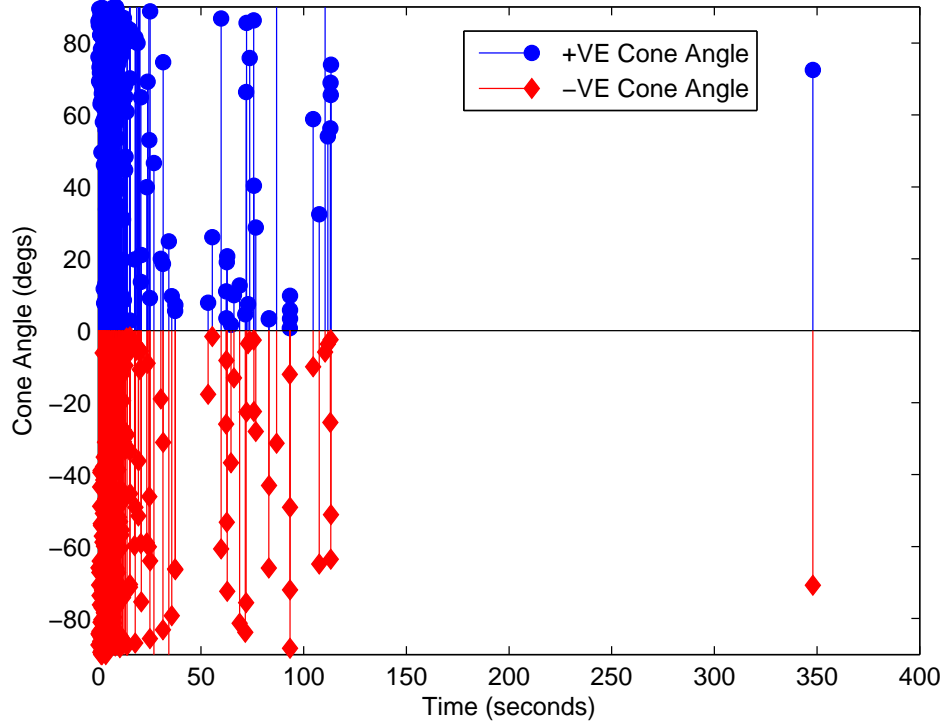


Figure 6.4: Time-averaged Ejection of the Solid Ejecta

The ejection of solid material is representative of an explosive and volumetric removal of mass. It is similar to a surface detonation or explosive event [Domen and Chuang, 1989; Kelly and Miotello, 1996]. Intense heating from the laser beam results in the thermal breakdown and the build-up of pressure beneath the surface of the target material [Domen and Chuang, 1989; Vidal et al., 2001]. Thermal breakdown is therefore dependent on the absorptive, optical, chemical and thermal properties of the target material. The increased pressure, combined with imperfections in the target material, such as voids, cracks, crevices and other surface features, leads to local mechanical fragmentation [Domen and Chuang, 1989; Clauser and Huenges, 1995].

The generation of solid ejecta is not currently accounted for in either ablation models. It is currently an unmodelled, observed parameter. Instead a constant scatter factor is used to account for the uniform dispersion of the gaseous-only ejecta plume. The inclusion of solid particles should therefore be a topic of future work. The additional ablation of solid material would affect the modified linear momentum of the target material. It would result in the temporal variation of the cone angle and affect the resultant thrust vector.

The spectrometer was used to infer the temperature and velocity of the gaseous ejecta plume. It measured the intensity, wavelength and peak wavelength λ_{PEAK} of the emitted spectra. The temperature of the gaseous ejecta T_{gas} could then be calculated from the peak wavelength. This was inferred from the Wien Displacement law. It assumes the characteristics of a black-body radiator and is given by:

$$T_{gas} = \frac{2.898 \cdot 10^{-3}}{\lambda_{PEAK}} \quad (6.1)$$

It is a useful technique for determining the temperature of any object whose temperature is much greater than its surroundings. From the temperature, the velocity of the gaseous ejecta (as given in equation (5.5)) was also calculated. It is based on the temperature of sublimation and assumed Maxwell's distribution of an ideal gas.

The spectrometer was used by first aligning it to the known surface spot location on the target. Here, the laser beam was operated at a minimum current level of 15 amp. This provided a red, visible spot, but there was not enough energy to ablate the illuminated material. There was no noticeable change in the target material's structure or appearance. The position of the spectrometer was adjusted until it became sensitive to the known wavelength of the laser beam. A typical alignment response of the spectrometer is given in Figure 6.5. The spectrometer was aligned in the infrared, but recorded the spectral emission in the visible wavelength band. It ensured no overlap between the incoming laser beam and the inferred temperature recording of the ejecta plume. The results recorded and inferred from the spectrometer are given in Figure 6.6 and Table 6.2. Ablation resulted in a gaseous ejecta velocity of approximately 1.51 km/s.

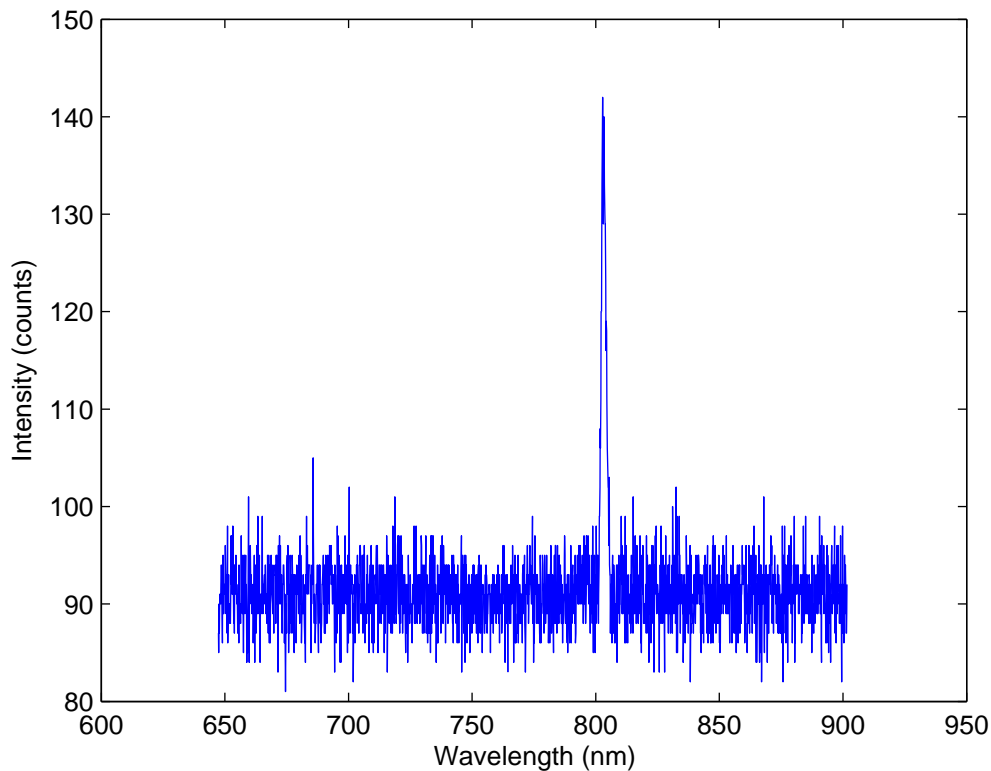


Figure 6.5: Alignment of the Spectrometer - Showing the Operational Wavelength of the Laser Beam

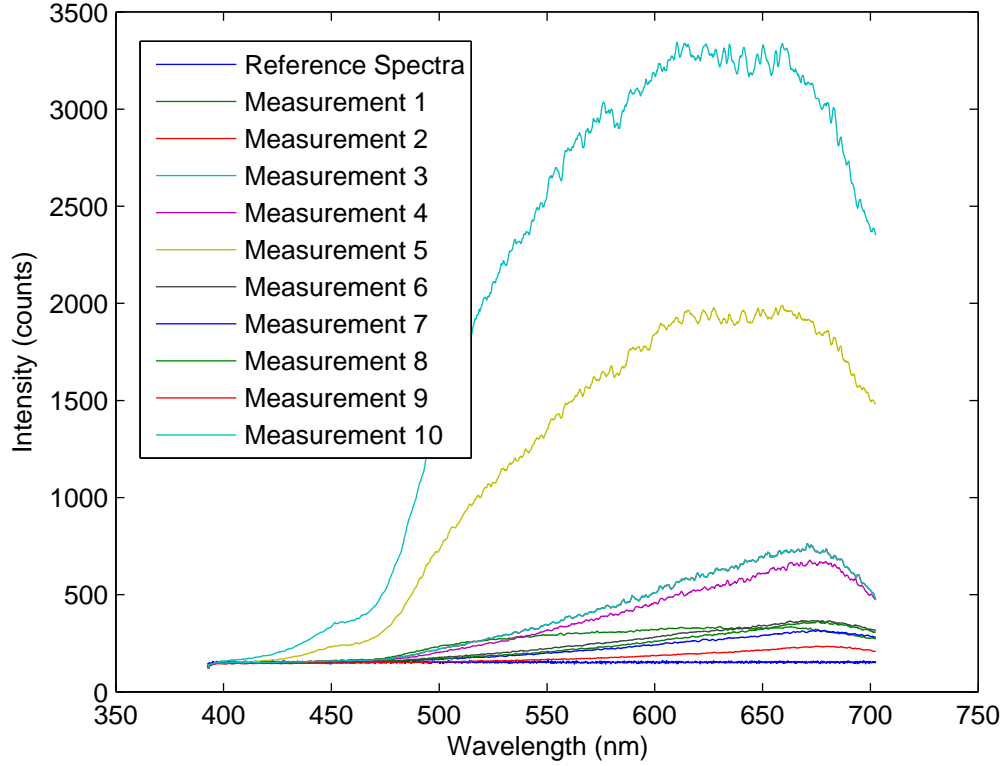


Figure 6.6: Data Recorded by the Spectrometer - Olivine Sample Under Vacuum

	λ_{PEAK} (nm)	T_{gas} (K)	\bar{v} (km/s)
Measurement 1	630	4599	1.56
Measurement 2	671	4320	1.51
Measurement 3	610	4747	1.58
Measurement 4	668	4336	1.51
Measurement 5	672	4312	1.51
Measurement 6	659	4396	1.52
Measurement 7	669	4332	1.51
Measurement 8	676	4285	1.51
Measurement 9	675	4289	1.51
Measurement 10	675	4292	1.51

Table 6.2: Recorded and Inferred Results from the Spectrometer

Shown in Figure 6.2, the spectrometer indicated a spot temperature of 4285-4747 K. If this temperature corresponds to the sublimation temperature, then the heat diffusion equation (5.28), with the boundary conditions of equation (5.26) can be used to plot Figure 6.7a. This displays the temperature of the olivine target material as a function of time and thickness. The figure was generated assuming the material properties in Table 6.1, an effective power of 60 W (part of the laser light is lost through absorption in the window of the vacuum chamber) and a spot size diameter ranging between $1 \cdot 10^{-3}$ and $1.4 \cdot 10^{-3}$ m at the beginning of the ablation process. This resulted in a surface power density of $7.64 \cdot 10^7$ - $3.89 \cdot 10^7$ W/m².

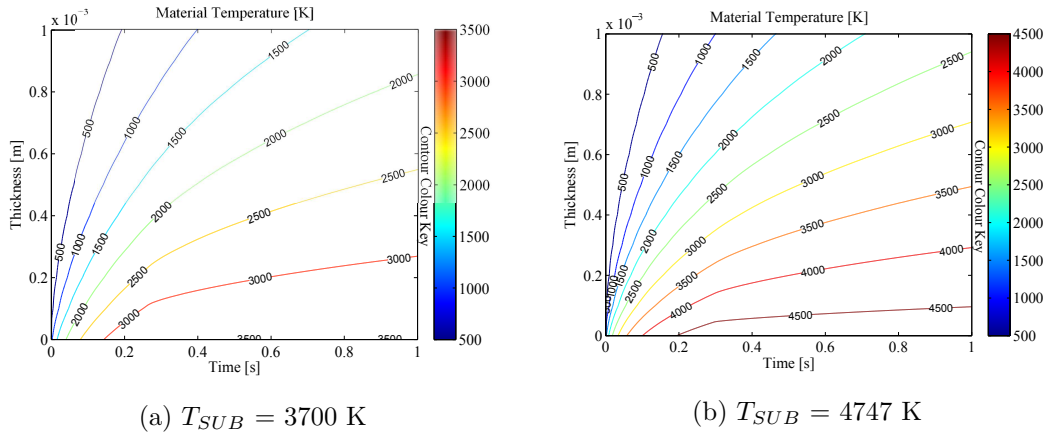


Figure 6.7: Solution of the Heat Diffusion Equation

However, the model's expectation was to predict a sublimation temperature to be about 1000 K lower than the temperature registered with the spectrometer. In this later case, the solution of the heat diffusion equation is shown in Figure 6.7b. For both cases the sublimation point is reached in less than a couple of tens of seconds, as observed in the experiment.

6.5 Collection Plates

Inside the test chamber, each target material was mounted on a raised pedestal. This was at a pre-determined location relative to the known focal point of the laser beam. The target material was also surrounded by a number of collection plates. These were used to collect the deposited ejecta. It enabled the physical and chemical properties of the deposited ejecta to be examined. Assessed parameters included its distribution, chemical composition, absorptivity, height and density. Each collection plate was positioned at a fixed radius, either 3, 7 or 10 cm away from the focus. Shown in Figure 6.8, each collection plate was a highly cleaned microscope slide, manufactured from fused quartz. The microscope slides were sourced from UQG Optics.

A pre-fabricated steel mount was used to hold each collection plate. This, together with the local accessible angles from the surface normal is shown in Appendix F. Each collection plate had a transmittance (at the wavelength of the laser beam) of ~ 98 % and

dimensions of 22·75·1.2 mm. Kapton tape was used as alignment markers. It is a low out-gassing, anti-static and high temperature polyimide film with a silicone adhesive.

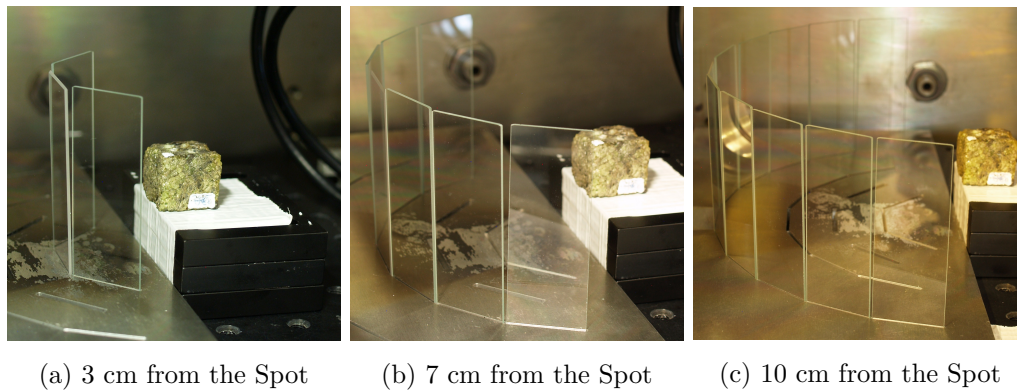


Figure 6.8: Arrangement of the Collection Plates

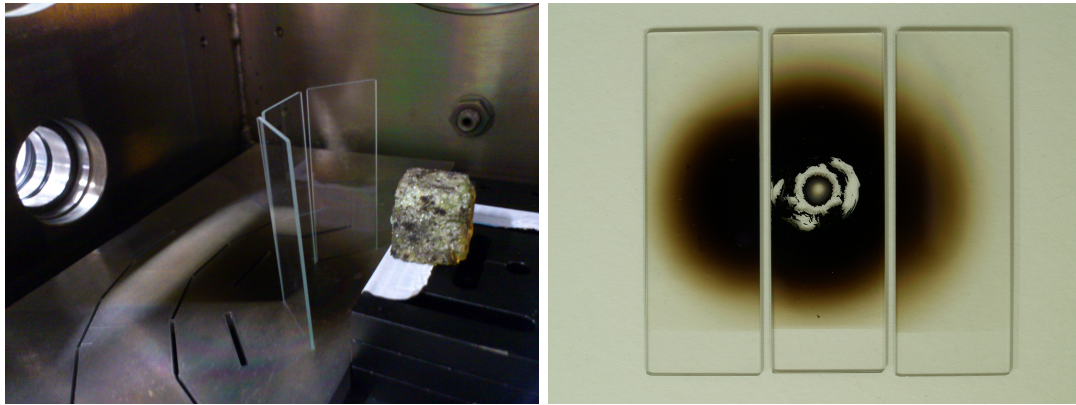
Similar to Cummings and Walsh [1993]; Meier et al. [1995]; Ohkoshi et al. [1994], the collection plates were used to:

1. Examine the Elemental Composition of the Deposited Ejecta

The contaminated collection plates were viewed under an optical microscope (magnification ranging from x5 to x100) and a SEM. Results were also compared with the bulk properties of the original, pre-ablated target material.

All SEM analysis, reported herein, was obtained from the Imaging Spectroscopy and Analysis Centre at the School of Geographical and Earth Science, University of Glasgow. The FEI Quanta 2007 Environment SEM with EDAX microanalysis provided information on the surface morphology, microstructure and elemental composition of each sample. Under vacuum, a focused beam of high-energy electrons was used to interact with the surface atoms in a solid sample. This produced various electron-to-sample interaction signals. Data gained from scattered, secondary and backscattered electrons provided high resolution images of the sample. Images showed the morphology and topography of the sample. The crystalline structure, orientation and composition of the sample were also determined. Elemental mapping showed the textural content and elemental spatial distribution (including zoning) of the sample.

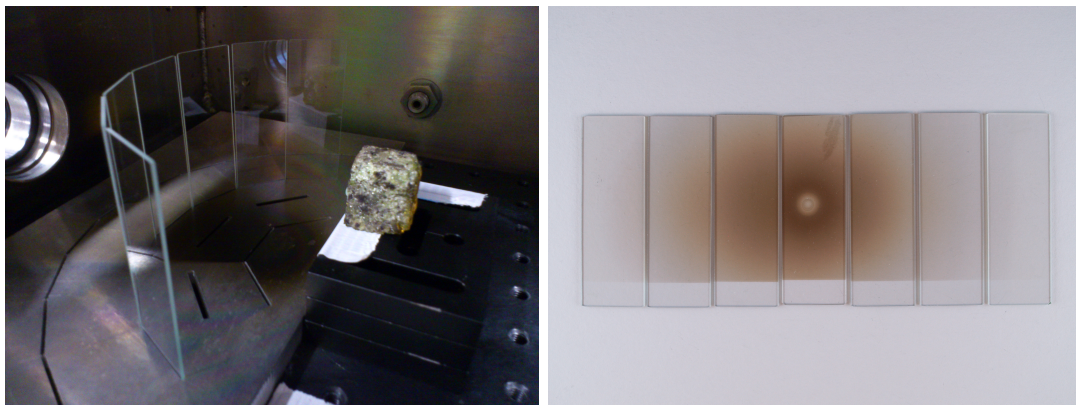
Shown in Figures 6.9-6.11, laser ablation resulted in the accumulation of a dark layer of deposited material. This was formed by the incoherent ablation of the olivine sample. Incoherent ablation occurs when the $\frac{Fe}{Mg}$ ratio of the pre-ablated sample and deposited ejecta is different [Nagahara et al., 1994, 1988, 2009]. Inspected by the SEM, the initial $\frac{Fe}{Mg}$ ratio of the target was 0.218. This reduced to 0.165 for the deposited ejecta. Reduction was caused by the full, partial and failed vaporisation process of the inhomogeneous target material, and can occur over a range of temperature limits [Lindgrad and Jonansen, 1996]. At 3 cm from the spot the deposited ejecta formed a symmetrical, elliptical pattern. The shape of the ejecta plume will control the density distribution, and therefore the spatial formation of the deposited ejecta. At 7 and 10 cm from the spot, the deposited ejecta was more evenly distributed. This was due to the extended expansion and distribution of the ejecta plume.



(a) Collection Plate

(b) Deposited Ejecta

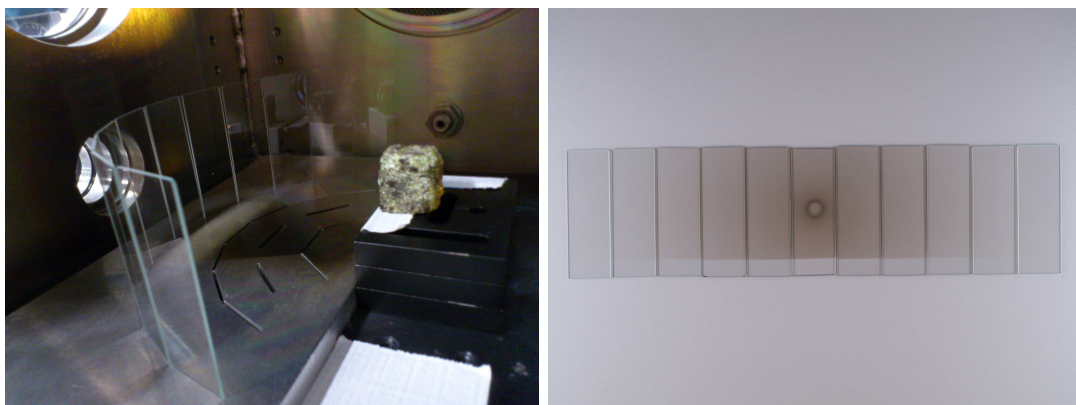
Figure 6.9: Collection of the Deposited Ejecta - 3 cm from the Spot Location



(a) Collection Plate

(b) Deposited Ejecta

Figure 6.10: Collection of the Deposited Ejecta - 7 cm from the Spot Location



(a) Collection Plate

(b) Deposited Ejecta

Figure 6.11: Collection of the Deposited Ejecta - 10 cm from the Spot Location

2. Measure the Height of the Deposited Ejecta

The height of the deposited ejecta h_{EXP} was measured at the centre line of each collection plate, along the x-axis. This is illustrated further in Figure 6.12. It provided data points at all points of interest. These values corresponded to a few, but discrete and representative samples.

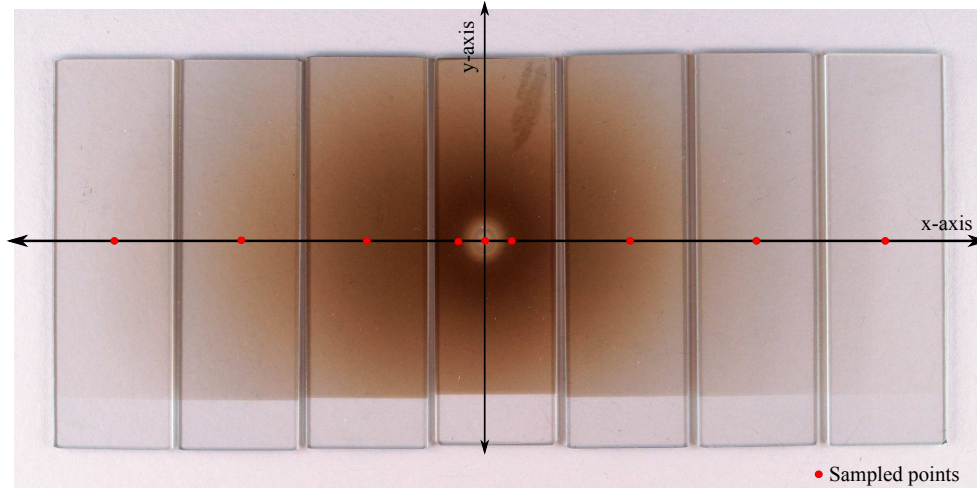


Figure 6.12: Sample Points on the Collection Plate

Measurements were taken with a Nikon Nomarski microscope. At a constant ($\times 20$) magnification the microscope was focused onto a clean, non-contaminated collection plate. The position of the focus was recorded. The microscope was then re-focused onto the top, outermost surface of the deposited ejecta. The difference in focus corresponded to a difference in height. This was measured in micro-meters.

Figures 6.13-6.15 show the accumulated height of ablated material that was deposited on each collection plate. Reported in each figure, each test (i.e. experiment) produced a different measured mass flow rate. The measured mass flow rate was the average value that was reported over an ablation period of 10 minutes. Variation was caused by the inhomogeneous nature of the target material. For comparison, the modelled mass flow rate in each legend was calculated from the improved ablation model given in Chapter 5.4. Inspected in each figure, the improved ablation model provides a much better prediction to the experimentally measured ablated mass flow rate. The same is also reported for the Figures that show the accumulated mass per unit area of the deposited ejecta. There is a direct correlation between the amount of deposited material and the ablated mass flow rate.

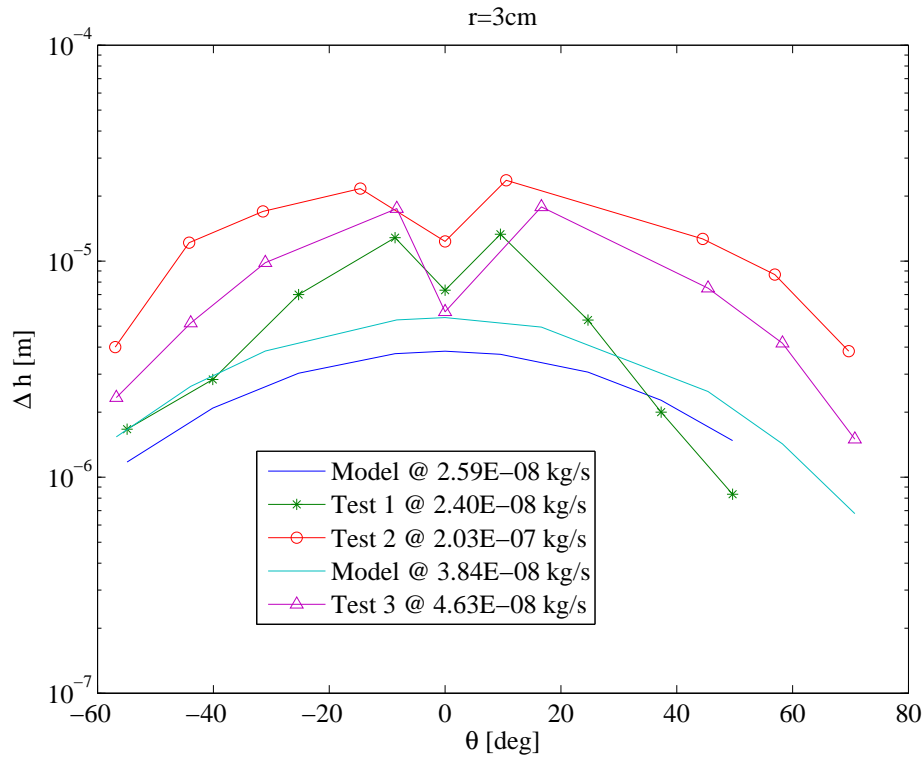


Figure 6.13: Height of the Deposited Ejecta on the Collection Plate - Comparison between the Experimental Measurements and Improved Simulation. Results at 3 cm from the Spot

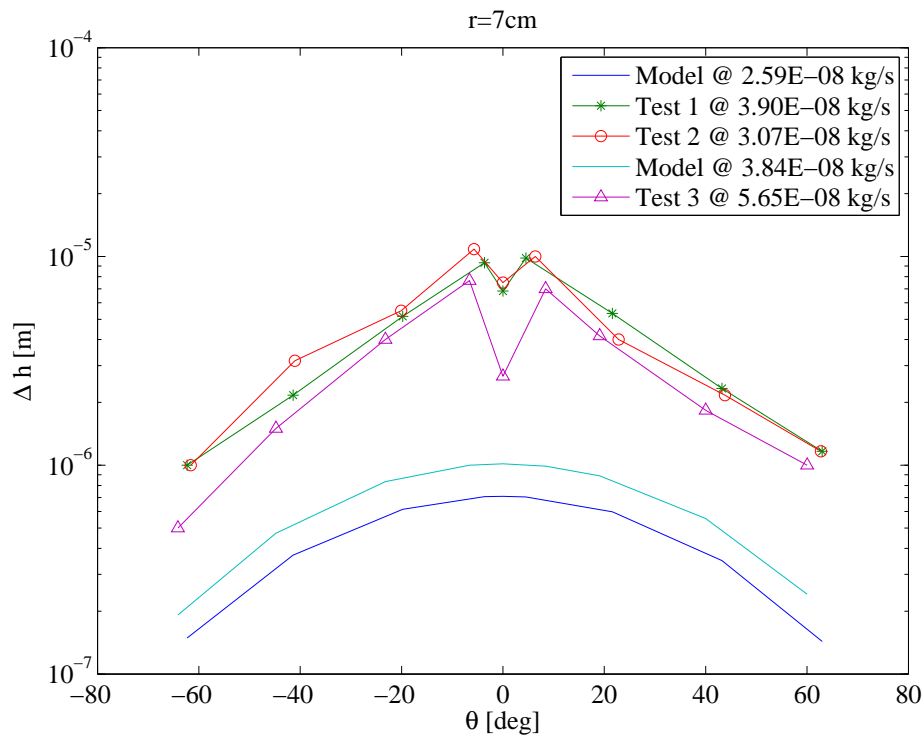


Figure 6.14: Height of the Deposited Ejecta on the Collection Plate - Comparison between the Experimental Measurements and Improved Simulation. Results at 7 cm from the spot

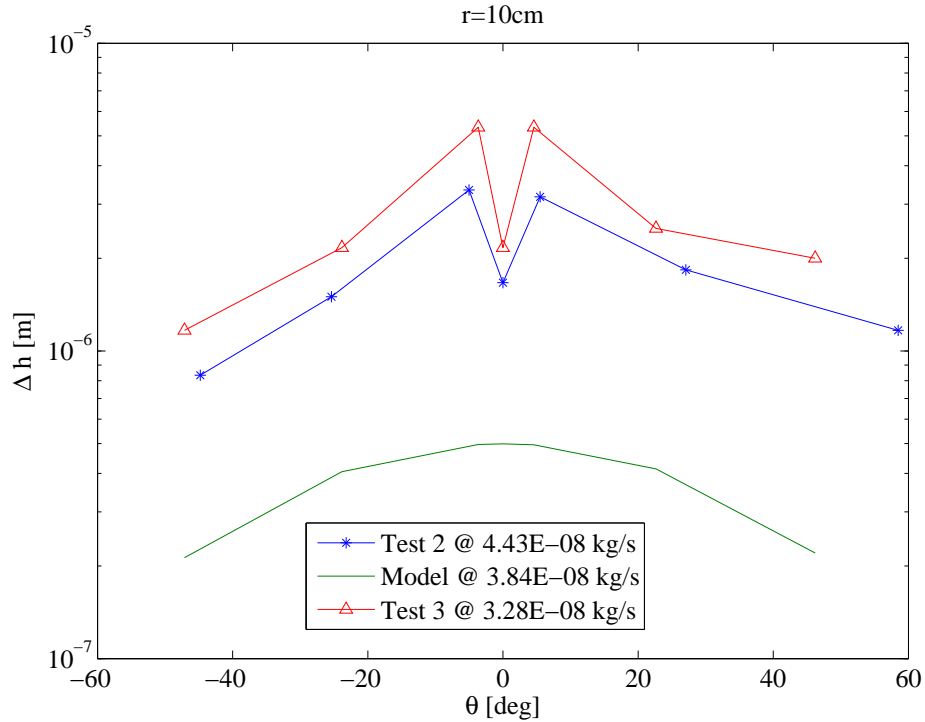


Figure 6.15: Height of the Deposited Ejecta on the Collection Plate - Comparison between the Experimental Measurements and Improved Simulation. Results at 10 cm from the Spot

These three figures show that the experimentally measured height of the deposited ejecta is significantly higher than predicted in the improved model, although it does follow a similar variation with the local elevation angle. The only exception to this occurred at the central point, with a local elevation of zero degrees.

A rapid reduction in height is caused by the self cleaning action of the laser beam, where there is no apparent visual deposition of material. As the laser beam passes through the central collection plate localised heating from the laser beam either: [1] thermally re-ablates the previously deposited ejecta or [2] re-excites and re-directs any ejecta that enters the laser beam. Re-excitation will prevent the ejecta from reaching and depositing onto the central collection plate. No opaque material will be able to re-condense along the path length of the laser beam as it would be constantly excited. This would serve to increase the lifetime of any laser ablation system and the associated optics.

Inspected through optical microscopy and the SEM, remains of carbon, oxygen, magnesium, silicon, chromium, iron and nickel were present within the self-cleaning hole. Shown in Figure 6.16a, these are particles that failed to be re-excited and removed by the passing laser beam. Figure 6.16b also showed the occurrence of micro-cracking. This only occurred at 3 cm from the spot. It was believed to be caused by the ablated ejecta impinging onto the collection plate, or the cooling and cracking of the accumulated ejecta layer. It was not caused by the passing laser beam. Each deposition imparts a small, but accumulative transfer of kinetic energy. This theory was validated by performing a controlled experiment. For the duration of the experiment, the laser beam was passed

through the collection plate, but no target material was ablated. Inspected through optical microscopy, no micro-cracking occurred. Nor did any structural changes occur. Micro-cracking could decrease the performance of the underlying substrate.

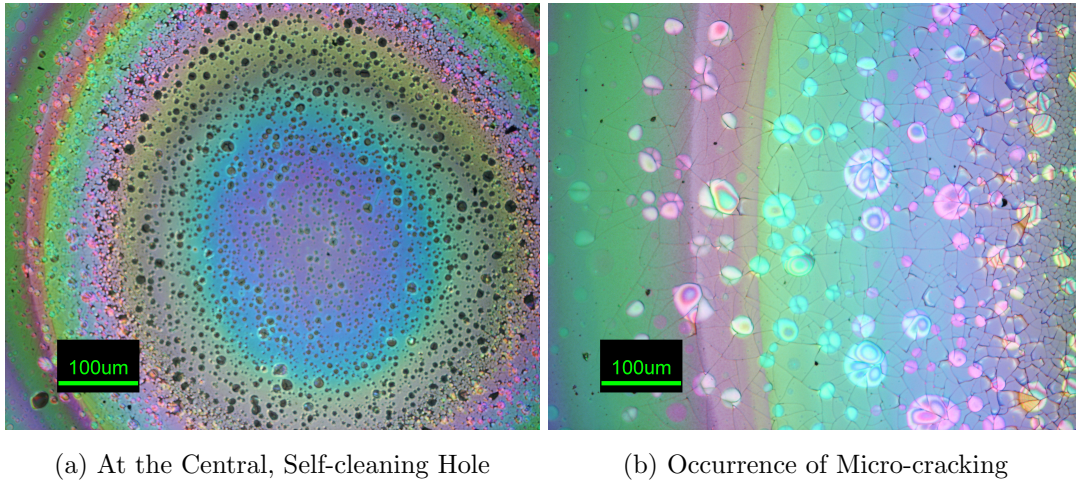


Figure 6.16: Microscopic Imagery of Ejecta Deposited on the Collection Plates

The continual re-evaporation and illumination of the ablated ejected will also increase the absorption of the gaseous ejecta plume. It will contribute to the ongoing heating and formation of an optically dense plume of ejecta. After the initial ablation event, the ablated particles will recombine and separate into much simpler molecules and atoms. More energy will be released into the ejecta plume and assist in increasing its overall temperature [Pabani and Pathak, 2012].

The additional augmented absorption effects can explain the temperature difference between the expected spot temperature (3100-3800 K, based on the improved model given in Chapter 5.4) and the result measured with the spectrometer (4285-4747 K). The inclusion of the Knudsen layer also provides some of the corrective factors [Gibbings et al., 2013].

3. Measure the Absorbance of the Deposited Ejecta

This was achieved by measuring the one-way light transmittance and absorbance effects across each contaminated collection plate. Initially a power meter was used, but this was replaced with photographic analysis. After each experiment, a Canon SLR camera mounted with a macro lens was used to image the contaminated collection plates. Imaging occurred under constant illumination conditions and at a fixed distance. Each image was assessed at a resolution of 640·480 pixels. A light box provided background lighting. This eliminated any shadowing and surface glare.

Photographic, computational analysis was achieved through *CamSam*. The programme was developed internally at the Institute of Photonics, University of Strathclyde. It measured the light intensity across each pixel. The deposited ejecta will decrease the transmittance T_m and increase the absorbance α_b of the collection plates. A transmittance value of one would describe an optically transparent material, whereas a value of zero would indicate a highly absorptive material. The increase in absorbance was calculated from the Beer-Lambert-Bougier law for optical absorbance. For one-way transmittance

this is given by:

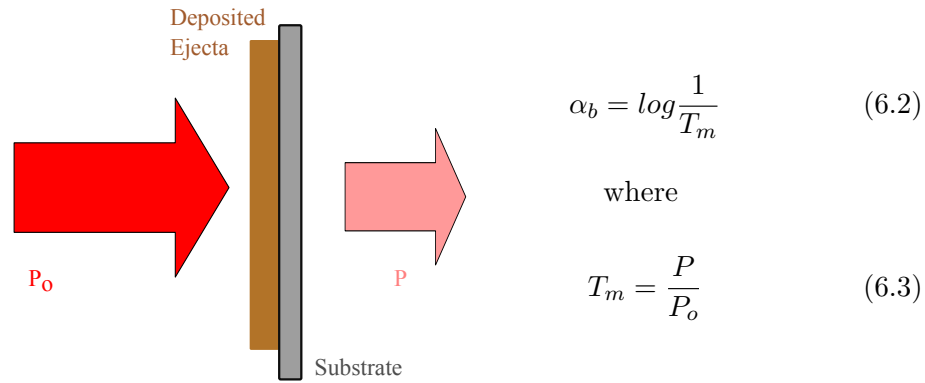


Figure 6.17: Measuring the Transmittance and Absorbance Effects of the Deposited Ejecta

where P_o is the initial power and P is the power transmittance through the collection plate. Data pertaining to α_b and T_m was extracted at the centre line of each collection plate, along the x-axis. The data points coincided with the location of each height measurement. The transmittance of light across each collection plate is shown in Figure 6.18. It was evaluated as a function of elevation angle. The rapid peaks indicate the boundary of each collection plate. Relative to Figures 6.9-6.11, an error is introduced by the use of a flat plate on a curved surface.

Results from each data set is given in Tables 6.3-6.10 and was used in the subsequent analysis. Due to the small step size of the processed data, around each reading of elevation, an average value was used. Averaging smoothed and filtered the raw data so that it could be easily manipulated into a meaningful result. Shown in Figures 6.19-6.21, the degrading effect of the deposited ejecta can be evaluated in more detail by assessing the absorptivity and degradation factor of the affected and exposed surface.

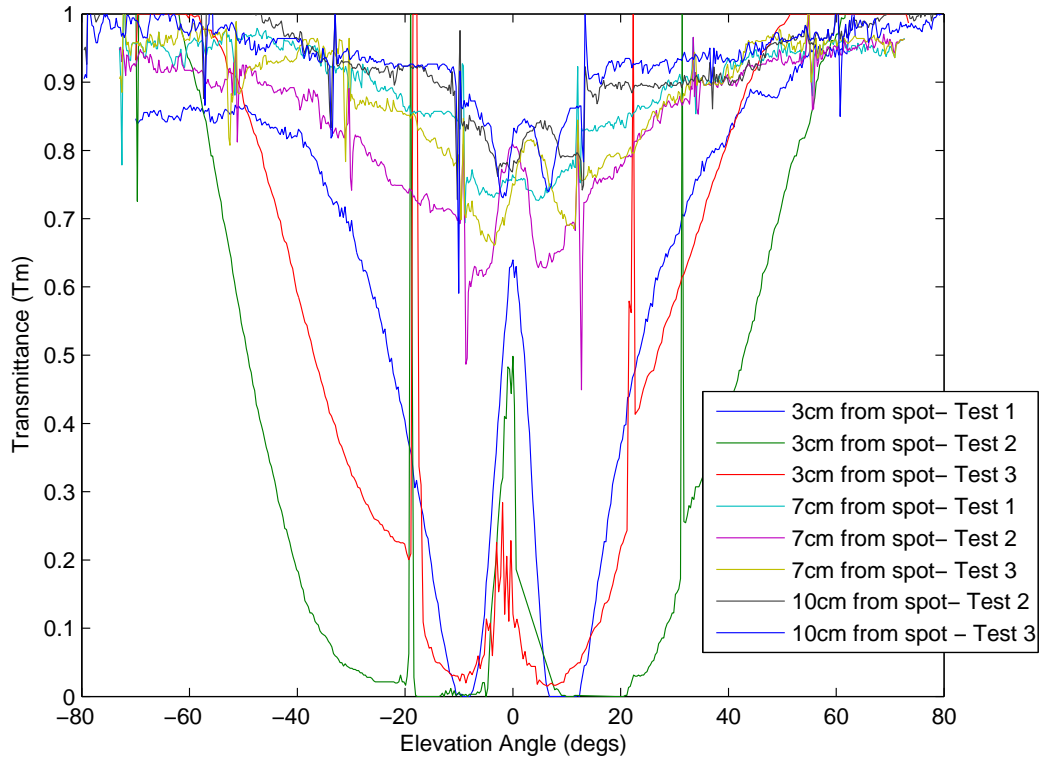


Figure 6.18: Measured Transmittance of the Collection Plates

θ (degs)	T_m	a_b
-55	0.843	0.074
-40	0.820	0.086
-25	0.570	0.244
-9	0.000	1.000
0	0.639	0.000
10	0.000	1.000
25	0.553	0.257
37	0.796	0.099
50	0.891	0.050

Table 6.3: 3 cm from the Spot (Test 1): Measured Transmittance and Absorbance Effects

θ (degs)	T_m	a_b
-57	0.832	0.075
-44	0.315	0.501
-31	0.045	1.351
-15	0.000	1.000
0	0.498	0.303
11	0.000	1.000
44	0.549	0.260
57	0.925	0.034
70	1.000	0.000

Table 6.4: 3 cm from the Spot (Test 2): Measured Transmittance and Absorbance Effects

θ (degs)	T_m	a_b
-57	0.978	0.010
-41	0.716	0.145
-31	0.349	0.457
-8	0.020	1.708
0	0.150	0.853
17	0.133	0.875
45	0.919	0.037
58	1.000	0.000
71	1.000	0.000

Table 6.5: 3 cm from the Spot
(Test 3): Measured Transmittance
and Absorbance Effects

θ (degs)	T_m	a_b
-62	0.941	0.027
-41	0.956	0.019
-20	0.861	0.065
-4	0.734	0.134
0	0.760	0.119
5	0.729	0.137
22	0.853	0.069
43	0.931	0.031
63	0.952	0.021

Table 6.6: 7 cm from the Spot
(Test 1): Measured Transmittance
and Absorbance Effects

θ (degs)	T_m	a_b
-62	0.934	0.030
-41	0.892	0.050
-20	0.742	0.129
-6	0.621	0.207
0	0.806	0.094
6	0.692	0.201
23	0.817	0.088
44	0.924	0.034
63	0.948	0.023

Table 6.7: 7 cm from the Spot
(Test 2): Measured Transmittance
and Absorbance Effects

θ (degs)	T_m	a_b
-64	0.965	0.016
-45	0.930	0.032
-23	0.805	0.094
-7	0.694	0.159
0	0.746	0.127
8	0.734	0.135
19	0.764	0.117
40	0.889	0.051
60	0.989	0.005

Table 6.8: 7 cm from the Spot
(Test 3): Measured Transmittance
and Absorbance Effects

θ (degs)	T_m	a_b
-47	0.949	0.023
-24	0.929	0.032
-4	0.823	0.085
-0	0.818	0.087
5	0.790	0.103
23	0.927	0.033
46	0.948	0.023

Table 6.9: 10 cm from the Spot (Test 2): Measured Transmittance and Absorbance Effects

θ (degs)	T_m	a_b
-45	0.907	0.042
-25	0.989	0.050
-5	0.822	0.084
0	0.80	0.082
6	0.822	0.084
27	0.894	0.049
58	0.968	0.014

Table 6.10: 10 cm from the Spot (Test 3): Measured Transmittance and Absorbance Effects

4. Calculate the Absorptivity of the Deposited Ejecta

The absorptivity η_{EXP} of the deposited ejecta was calculated by dividing the experimentally measured absorbance with the experimentally measured height of the deposited ejecta. Absorptivity is defined as the absorbance per unit length. Therefore:

$$\eta_{EXP} = \frac{a_b}{h_{EXP}} \quad (6.4)$$

Degradation of the collection plates is dependent on the mass, height and absorptivity of the deposited material. These factors depend on the surface growth of the deposited ejecta layer. By measuring h_{EXP} over time, it was possible to derive a correction factor to equation (5.19) and compute a degradation factor that was consistent with the experimental results.

Shown in Figures 6.19-6.21, at specific locations across the collection plates, the experimentally derived degradation factor was determined. The location of each sample point was prearranged (as defined by Figure 6.12) to coincide with the reported height and absorbance value (given by equations (6.4) and (5.19)). In Figures 6.19-6.21 the experimentally derived degradation factor, as given in equation (5.19), is denoted T . It was calculated by combining equation (5.19) with equation (6.4).

Where:

$$\tau = e^{-2\eta h_{layer}} \quad (6.5)$$

Becomes:

$$T = e^{-2\eta_{EXP} h_{EXP}} \quad (6.6)$$

And can be reduced further to:

$$T = e^{-2a_b} \quad (6.7)$$

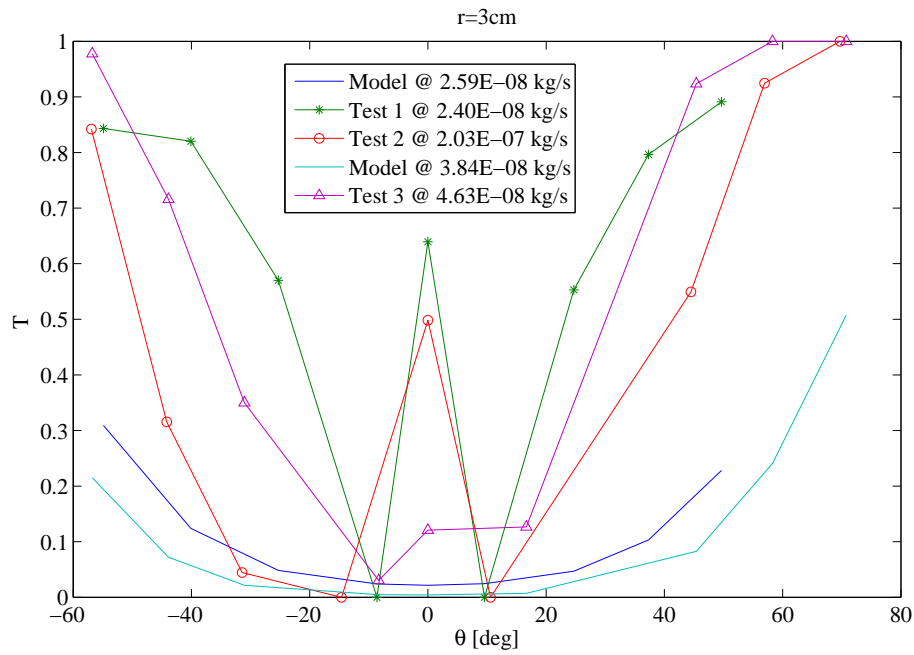


Figure 6.19: Degradation Factor: Comparison between the Experimental Results and Improved Model Prediction at 3 cm from the Spot

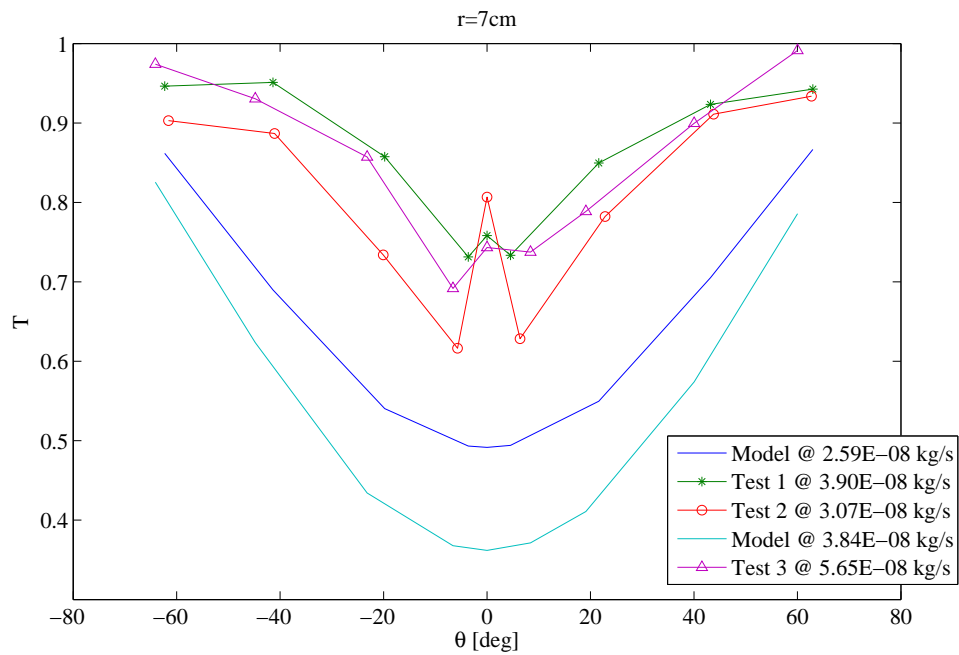


Figure 6.20: Degradation Factor: Comparison between the Experimental Results and Improved Model Prediction at 7 cm from the Spot

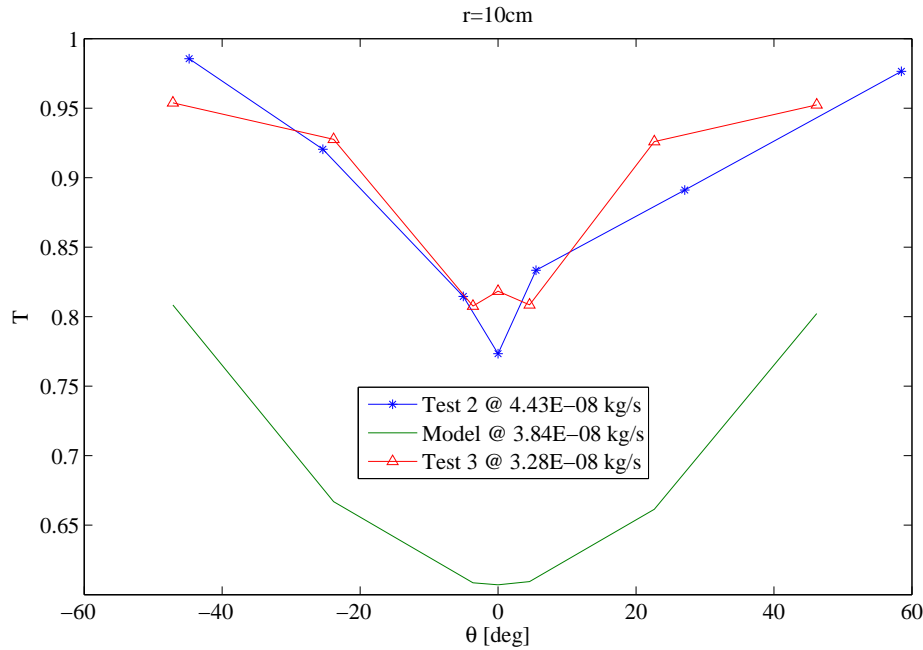


Figure 6.21: Degradation Factor: Comparison between the Experimental Results and Improved Model Prediction at 10 cm from the Spot

The profile of the degradation factor follows closely to the distribution of the deposited ejecta height shown in Figures 6.13-6.15. It is symmetric about the central point and shows the characteristics of a self cleaning hole. These results are, in part, expected as a thinner film will have a higher transmittance (and vice-a-versa). Degradation is expected to be higher at lower elevation angles where the plume density is larger. More ejecta is available to be re-deposited from the ablation volume. However, although the shape model is fairly accurate the amount of degradation produced is significantly different. At all three distances from the spot, the improved model was overly conservative. It predicted a much larger degradation factor than was otherwise observed. This will, critically, affect the lifetime of any ablation event and the achievable rates of deflection.

At 3 cm from the spot, the degradation factor over an elevation angle of ± 20 degs should of caused the complete saturation of the collection plates. Instead the degradation factor is 0.2, and increases with increasing elevation. There is a consistent difference between the experimentally and theoretically predicted result. The same result occurs at 7 and 10 cm from the spot location. Although complete saturation does not occur, the difference between the measured and predicted data sets are consistent. The only expectation in the shape profile occurs at zero degs elevation. A rapid peak in the degradation factor is caused by the effects of the self-cleaning hole. Material previously re-evaporated or re-excited increases the transmittance and decreases the absorbance of the deposited ejecta. Data in Tables 6.11-6.15 show that the average absorptivity at 7 and 10 cm from the spot is around 10^4 m^{-1} . At 3 cm from the spot, on the central slide the average absorptivity increases to about 10^5 m^{-1} . The absorptivity value then dropped off rapidly below 10^4 m^{-1} over the two collection plates positioned at ± 45 degs. Importantly, the experimentally determined absorptivity value is two orders of magnitude lower than previously assumed in the initial model and reported in Kahle et al. [2006].

θ (degs)	η_{EXP} (m^{-1})
-47	$1.97 \cdot 10^4$
-25	$1.48 \cdot 10^4$
-4	$1.59 \cdot 10^4$
0	$4.02 \cdot 10^4$
5	$1.93 \cdot 10^4$
23	$1.32 \cdot 10^4$
46	$1.15 \cdot 10^4$

Table 6.11: 10 cm from the Spot
(Test 2): Absorptivity Results

θ (degs)	η_{EXP} (m^{-1})
-45	$5.04 \cdot 10^4$
-25	$3.33 \cdot 10^4$
-5	$2.52 \cdot 10^4$
0	$4.92 \cdot 10^4$
6	$2.65 \cdot 10^4$
27	$2.67 \cdot 10^4$
58	$1.20 \cdot 10^4$

Table 6.12: 10 cm from the Spot
(Test 3): Absorptivity Results

θ (degs)	η_{EXP} (m^{-1})
-62	$2.70 \cdot 10^4$
-41	$8.77 \cdot 10^3$
-20	$1.26 \cdot 10^4$
4	$1.45 \cdot 10^4$
0	$1.75 \cdot 10^4$
5	$1.39 \cdot 10^4$
22	$1.29 \cdot 10^4$
43	$1.33 \cdot 10^4$
63	$1.80 \cdot 10^4$

Table 6.13: 7 cm from the Spot
(Test 1): Absorptivity Results

θ (degs)	η_{EXP} (m^{-1})
-62	$3 \cdot 10^4$
-41	$1.58 \cdot 10^4$
-20	$2.35 \cdot 10^4$
-6	$1.91 \cdot 10^4$
0	$1.25 \cdot 10^4$
6	$2.01 \cdot 10^4$
23	$2.20 \cdot 10^4$
44	$1.57 \cdot 10^4$
63	$1.97 \cdot 10^4$

Table 6.14: 7 cm from the Spot
(Test 2): Absorptivity Results

θ (degs)	η_{EXP} (m^{-1})
-64	$3.20 \cdot 10^3$
-45	$2.13 \cdot 10^4$
-23	$2.35 \cdot 10^4$
-7	$2.07 \cdot 10^4$
0	$4.76 \cdot 10^4$
8	$1.93 \cdot 10^4$
19	$2.81 \cdot 10^4$
40	$2.78 \cdot 10^4$
60	$5.00 \cdot 10^3$

Table 6.15: 7 cm from the Spot
(Test 3): Absorptivity Results

It is therefore reasonable to assume that at 3 cm from the spot location that the plume is very focused and that the deposited material appears to be the subject of compression. The deposited ejecta is mainly distributed over the central slide. High kinetic energy results in the compaction of the film and will disrupt the development of the material lattice. This will lead to an inferior film quality. Shown in Figure 6.22, spontaneous

peeling of the deposited material occurred.

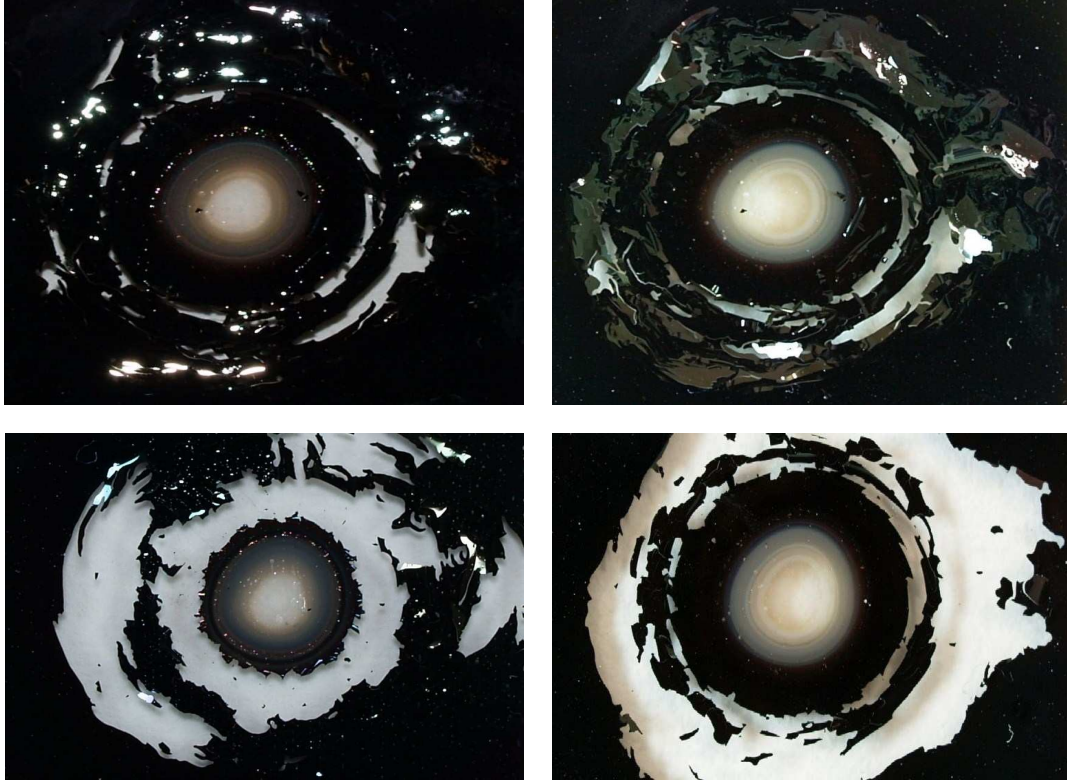


Figure 6.22: Spontaneous Peeling of the Deposited Ejecta on the Central Collection Plate, 3 cm from the Spot

The conditions at 3 cm from the spot are not representative of the space-based ablation environment, which the spacecraft will be exposed to. The collection plate is positioned too close to the ejecta plume. The collection plates positioned at 7 and 10 cm from the spot are far more representative. Here, the plume is more expanded and therefore leads to a more even distributed layer of deposited ejecta. In all cases the deposited ejecta could also be easily removed by applying a small vibration or increase in temperature. The deposited material was not fully bounded to the underlying substrate of the collection plates.

5. Calculate the Density of the Deposited Ejecta

The density of the deposited ejecta $\rho_{layer_{EXP}}$ was calculated by first measuring the deposited mass per unit area of each collection plates $\left[\frac{\Delta m(r,\theta)}{A}\right]_{Plates}$. Before and after each experiment, an electronic mass balance was used to measure the mass of each collection plate. The mass balance had a readability of 0.0001 g and was supplied by Elvet Scientific. From this, the density of the deposited ejecta (the ejecta layer) could be calculated. This is given by:

$$\rho_{layer_{EXP}}(r, \theta) = \frac{\left[\frac{\Delta m(r,\theta)}{A}\right]_{Plates}}{h_{EXP}} \quad (6.8)$$

where A is the known area of each collection plate.

It is also possible to derive the expected collection rate of ejecta on each collection plate. Based on the model, given in equation (5.16), and assuming that all the ablated mass is following perpendicular ($\cos\psi=1$) to the collection plates, then:

$$\rho_{layer} \left[\frac{dh}{dt} \right]_{layer} = 2\bar{v}\rho \quad (6.9)$$

Using dimensional analysis this is equivalent to:

$$\frac{1}{A} \frac{dm}{dt} = 2\bar{v}\rho \quad (6.10)$$

Therefore, during the experiment, at each collection plate:

$$\left[\frac{1}{A} \frac{dm}{dt} \right]_{Plates} = 2\bar{v}_{EXP}\rho_{EXP}(r, \theta) \quad (6.11)$$

where $\left[\frac{1}{A} \frac{dm}{dt} \right]_{Plates}$ is the expected collection rate of the ejecta on each collection plate, \bar{v}_{EXP} is the calculated velocity of the ejecta plume and $\rho_{EXP}(r, \theta)$ is the density of the ejecta plume. Equations (6.10)-(6.11) assumes that the velocity of the gas is $2\bar{v}$. This is used to account for the full expansion of gas into a vacuum. It also assumes that the impinging particles of ejecta will immediately recondense and stick onto the surface of each collection plate. From this, an alternative method of calculating the density of the deposited ejecta can be derived. By substituting equation (6.9) into (6.11) then:

$$\left[\frac{1}{A} \frac{dm}{dt} \right]_{Plates} = \rho_{layer} \left[\frac{dh}{dt} \right]_{layer} \quad (6.12)$$

In the experiment:

$$\left[\frac{1}{A} \frac{dm}{dt} \right]_{Plates} = \rho_{layerEXP} \left[\frac{dh}{dt} \right]_{Plates} \quad (6.13)$$

Therefore,

$$\rho_{layerEXP} \left[\frac{dh}{dt} \right]_{Plates} = 2\bar{v}_{EXP}\rho_{EXP}(r, \theta) \quad (6.14)$$

Accounting for the sticky coefficient of the ejecta, then:

$$\rho_{layerEXP} \left[\frac{dh}{dt} \right]_{Plates} = 2\bar{v}_{EXP}\rho_{EXP}(r, \theta)\gamma \quad (6.15)$$

The density of the deposited ejecta can therefore be derived from the velocity and density of the ejected plume and the height of the deposited ejecta.

Figures 6.23-6.25 show the mass per unit area of deposited material on each collection plate. The distribution of material with the local elevation angle is correctly predicted with the improved model. Both factors are very similar to the experimental results.

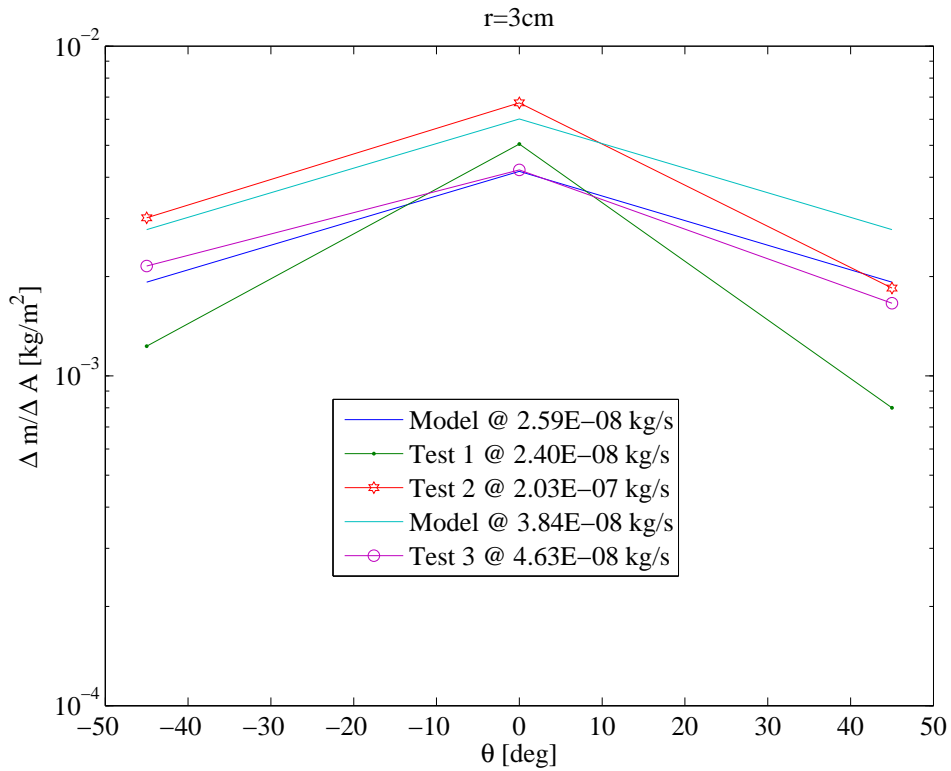


Figure 6.23: Deposited Mass per Unit Area: Experimental Results vs Improved Model Prediction at 3 cm from the Spot

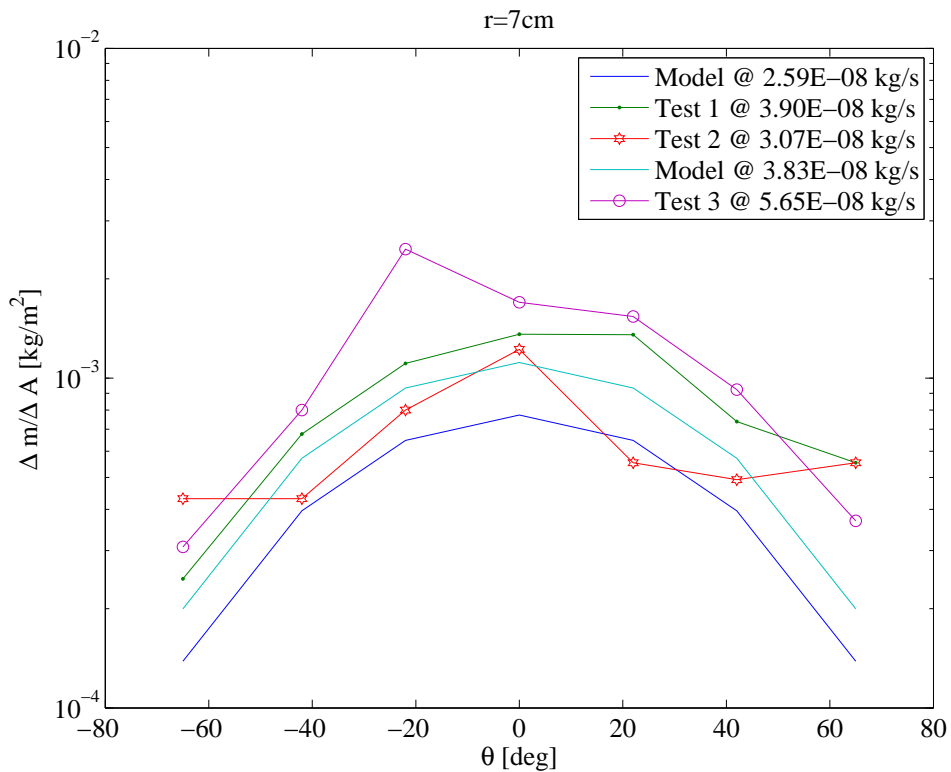


Figure 6.24: Deposited Mass per Unit Area: Experimental Results vs Improved Model Prediction at 7 cm from the Spot

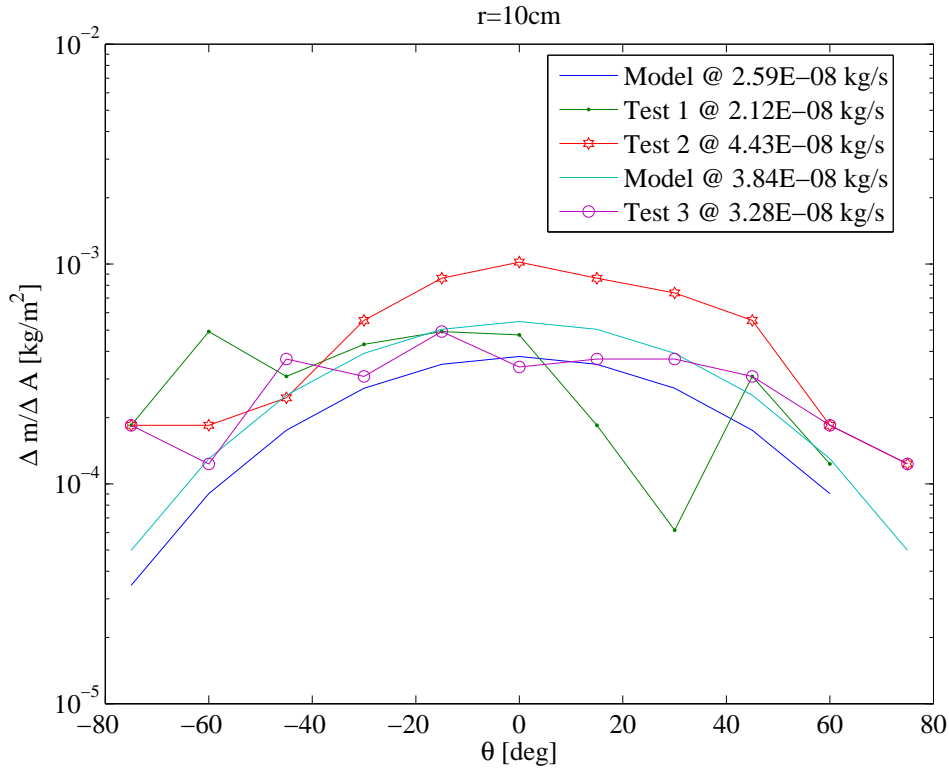


Figure 6.25: Deposited Mass per Unit Area: Experimental Results vs Improved Model Prediction at 10 cm from the Spot

The deposited mass over area is correctly predicted with the improved model. However, there is still a significant variation in the height of the deposited ejecta. When these three figures are evaluated with Figures 6.13-6.15, it can be concluded that the deposited ejecta density is much lower than the 1000 kg/m^3 assumed in the initial model as given by Kahle et al. [2006]. The experiment resulted in a much higher thickness, but with an equal mass per unit area. From inspection, at 7 and 10 cm from the spot the average deposited ejecta is about 250 kg/m^3 . At 3 cm this is much higher with an average over the central slide of about 700 kg/m^3 . Here, the plume is very focused and the majority of the deposited ejecta is distributed over the central collection plate.

6.6 Rock Analysis

High resolution images of the ablation site were also taken. This enabled the diameter of the ablation hole and any areas of recrystallisation or local depositions around the ablation rim to be assessed. Using *ImageJ*, pixel width was converted into length. The depth and internal angle α of the ablation hole was also measured. Illustrated in Figure 6.26 it enabled the shape of the ablation hole to be determined. It was achieved by measuring the vertical length (i.e the depth) L_v and angle length L_a of the ablation hole.

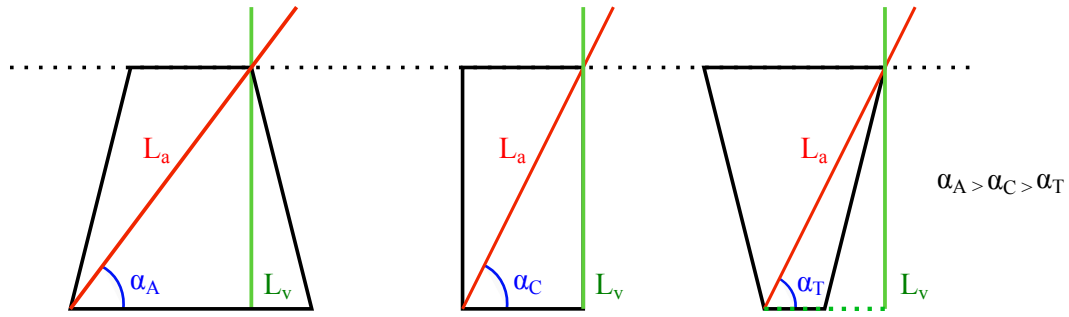


Figure 6.26: Determining the Shape Profile of the Ablation Hole

Where for each condition:

$$\alpha_A = \sin^{-1} \left(\frac{L_v}{L_a} \right) \quad \alpha_C = \sin^{-1} \left(\frac{L_v}{L_a} \right) \quad \alpha_T = \sin^{-1} \left(\frac{L_v}{L_a} \right) \quad (6.16)$$

Rim deposition was not observed in vacuum. It would have represented an inefficiency within the ablation process. It is material that has been ablated by the laser beam, but failed to contribute to the fully formed and developed plume of ejecta. Therefore, surface deposition does not contribute to the measurable ablated mass flow rate or change in the target's linear momentum. Deposition is dependent on the size of the focused laser beam and the pressure, temperature and composition of the ejecta plume.

In the experiment however the rim was partially evaporated. Shown in Figure 6.27, the ablated hole was always larger than the initially illuminated spot size. It implies that the ablation process is not limited to the area immediately under the spot, but also extends around the local area. A relatively large layer of semi-melted, re-formed material was also formed around the ablation rim.



(a) Olivine - Test 2, 7 cm from spot

(b) Olivine - Test 2, 3 cm from spot

Figure 6.27: Ablation Response at the Rim

Inspected further with a macro lens camera (Canon SLR) and the SEM, Figure 6.28 shows recrystallisation of the original source material. Recrystallisation occurred under intense temperatures and pressures. A new micro-structure was created which, as shown in Appendix H, has a prevalence of magnesium, silicon and oxygen. It was caused by the

thermal absorption and propagation of the laser beam inside the target material. The smooth appearance in Figure 6.27 suggests that it is not associated with any explosive melting or phase explosion event. It does however have the potential to extend the ablation area and increase the internal gas pressure.

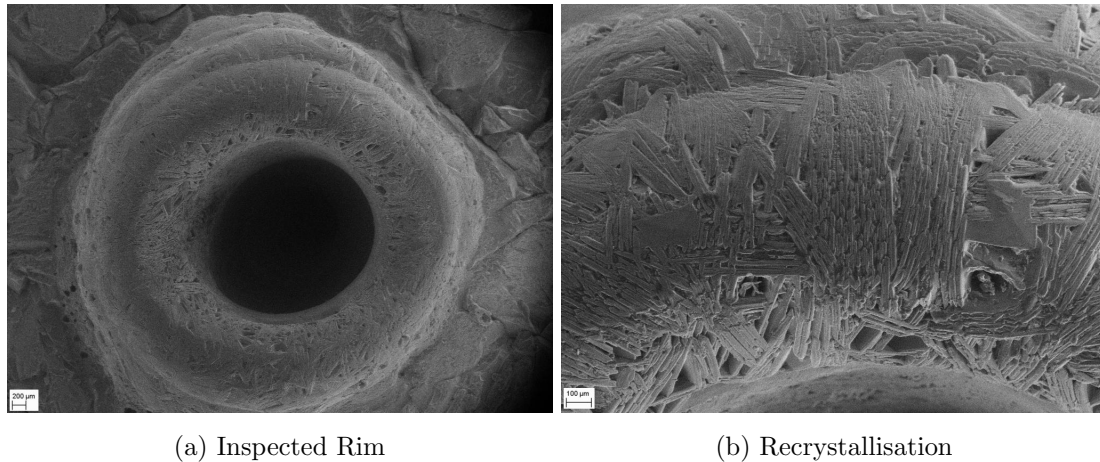


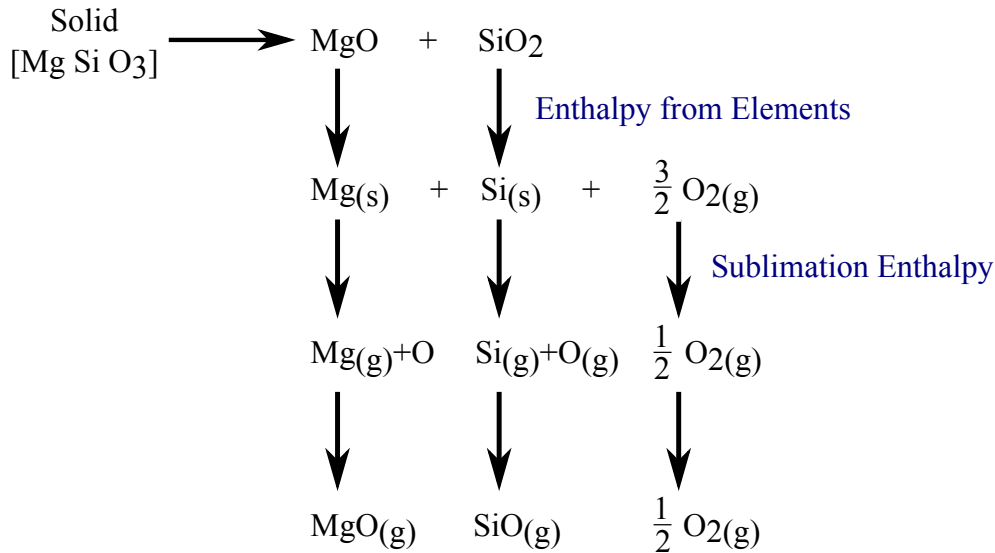
Figure 6.28: SEM Image of Recrystallisation at the Ablation Rim

During ablation, as the illuminated surface material is ablated away, new underlying material is exposed. A mixture of melted, subsurface material is sourced, pushed from the bottom of the ablation hole, and from within the material matrix of the target material. Ablation results in the release of additional secondary and tertiary elements [Moroz et al., 1996]. It is caused by the chemical breakdown, evaporation, condensation, recombination and decomposition of the target material [Hashimoto, 1990]. Dissociation of the silicon and magnesium molecules can also occur. Inspected by the SEM, and shown in Appendix G, the original olivine sample was a magnesium silicate rock (Mg_2SiO_4). It contained secondary elements of oxygen and iron, and smaller amounts of aluminium, calcium, carbon and sodium. The ablated surface also became enriched with chlorine and potassium. The target material is therefore an inhomogeneous mixture of SiO_2 , MgSiO_3 , $\text{CaAl}_2\text{Si}_2\text{O}_8$, $\text{NaAlSi}_3\text{O}_8$, $\text{CaMgSi}_2\text{O}_6$, $\text{CaFeSi}_2\text{O}_6$, $\text{NaAl}(\text{SiO}_3)_2$ and KAlSi_3O_8 [O’Keefe and Ahrens, 1971; Farquhar and Rumble, 1998]. Silica is a mixture of the pure and oxide Si regions. The ablated material dissociates into diatomic oxides, which shown in Table 6.16, has a prevalence of Mg and SiO [Robbie et al., 1982; O’Keefe and Ahrens, 1971; Farquhar and Rumble, 1998; Hashimoto, 1990; Wang et al., 1999; Brown and Prewitt, 1973; Schick, 1960; Brewer, 1953]. This has a molar mass of 0.06 kg/mol. It is governed by the gaseous ablation of MgO, SiO, SiO_2 , O and O_2 [Hashimoto, 1990]. Lighter, more reactive elements, with a low sub-atomic mass are more susceptible to the ablation process. The forward direction of the arrow in Table 6.16 indicates evaporation, where the backwards reaction is condensation [Hashimoto, 1990].

Solid Silicate		Oxide Gas
PRIMARY		
Mg_2SiO_4	\rightleftharpoons	$2\text{MgO} + \text{SiO} + \frac{1}{2}\text{O}_2$
Mg_2SiO_4	\rightleftharpoons	$2\text{MgO} + \text{SiO} + \text{O}$
Mg_2SiO_4	\rightleftharpoons	$2\text{MgO} + 2\text{SiO}_2$
Mg_2SiO_4	\rightleftharpoons	$2\text{Mg} + \text{SiO}_2 + 2\text{O}$
Mg_2SiO_4	\rightleftharpoons	$2\text{Mg} + \text{SiO}_2 + \text{O}_2$
Mg_2SiO_4	\rightleftharpoons	$2\text{Mg} + \text{Si} + 2\text{O}_2$
SECONDARY		
SiO_2	\rightleftharpoons	SiO_2
SiO_2	\rightleftharpoons	$\text{SiO} + \text{O}_2$
SiO_2	\rightleftharpoons	$\text{SiO} + \frac{1}{2}\text{O}_2$
MgSiO_3	\rightleftharpoons	$\text{MgO} + \text{SiO} + \frac{1}{2}\text{O}_2$
$\text{CaAl}_2\text{Si}_2\text{O}_8$	\rightleftharpoons	$\text{CaO} + 2\text{AlO} + 2\text{SiO} + \frac{3}{2}\text{O}_2$
$\text{CaMgSi}_2\text{O}_6$	\rightleftharpoons	$\text{CaO} + \text{MgO} + 2\text{SiO} + \text{O}_2$
$\text{CaFeSi}_2\text{O}_6$	\rightleftharpoons	$\text{CaO} + \text{FeO} + 2\text{SiO} + \text{O}_2$
TERTIARY		
$\text{NaAlSi}_3\text{O}_8$	\rightleftharpoons	$\text{Na} + \text{AlO} + 3\text{SiO} + 2\text{O}_2$
$\text{NaAl}(\text{SiO}_3)_2$	\rightleftharpoons	$\text{Na} + \text{AlO} + 2\text{SiO} + \frac{3}{2}\text{O}_2$
KAlSi_3O_8	\rightleftharpoons	$\text{K} + \text{AlO} + 3\text{SiO} + 2\text{O}_2$

Table 6.16: Vaporisation Products and Reactions

The list in Table 6.16 is not exhaustive, but is representative of a range of possible reaction products [Wang et al., 1999]. Shown in Figure 6.29, the first enthalpy change is the formation of crystals from the oxides. This is followed by the formation of elements in their standard state and the direct sublimation of a solid to a gas. It includes the reactions and dissociations of the gas to form the vapour species [O’Keefe and Ahrens, 1971]. These additional reactions will increase the temperature of the ejecta plume. Energy is released in the gaseous formation of the vapour species.


 Figure 6.29: Enthalpy Change of MgSiO_3 - Adapted from O’Keefe and Ahrens [1971]

Additional compounds represent an impurity within the olivine sample. Each will have a different sublimation temperature, which will affect the mass flow rate of the ejecta plume, the induced vapour pressure and also result in the incoherent ablation of the target material [Wei et al., 1975]. The ablation rate will vary as the composition of the illuminated material changes. The laser beam will have to heat the target material to a higher temperature, while also experiencing the effects of a slightly defocused laser beam (with an increased spot size diameter). The affect will vary on a case-by-case basis and is element and molecule dependent. Eventually the surface power density will fall below the ablation limit. This occurs when the propagation of the laser beam has deviated too far away from the initially illuminated focus point.

For a non-rotating asteroid this affect can be controlled with adaptive optics or with a precisely controlled collimated laser beam. For a rotating body the tunnelling action of the ablation process would create a subsurface groove. The groove assists in collimating the formation of the ejecta plume, making it more directional with a progressively smaller divergence angle. It will also contribute to the volumetric heating of the target material. The control of the focus will therefore have to be considered throughout the mission design of any ablation-based deflection action. This issue is addressed further in Chapter 8.3.1.

6.7 Momentum Coupling and Mass Flow Rate

Limitations in the experimental design prevented the force F_{SUB} of the ablation event to be directly measured. It was instead calculated from the measured, average mass flow rate and calculated velocity of the ablated ejecta. This has been previously defined in equation (5.6). The average mass flow rate was determined by measuring the mass of the target material before and after each experiment, then dividing the difference by the experiment duration. All mass measurements were taken using an electronic mass balance. The mass balance was supplied by Elvet Scientific and had a readability of

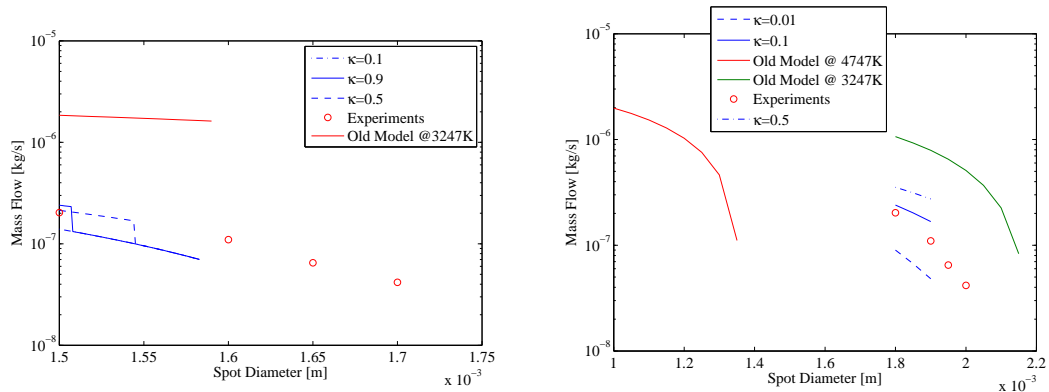
0.0001 g. It also enabled an estimation of the momentum coupling coefficient. Previously defined in equation (5.22), at the spot location, it is the force relative to the incoming absorbed laser power P_{INEXP} .

This is expressed as:

$$C_m = \frac{F_{SUB}}{P_{INEXP}} \quad (6.17)$$

The absorbed power combines the known power illumination at the spot and the assumed absorption of both the target material and the laser beam within the ejecta plume. The experiment recorded an initial mass flow rate of the ablated ejecta of $2 \cdot 10^{-7}$ kg/s. At the end of the ablation period (10 minutes) the experimental mass flow rate of the ejecta plume had reduced to $2.5 \cdot 10^{-8}$ kg/s. The rapid reduction in the mass flow rate is expected, in part, due to the defocusing of the laser beam at the ever increasing depth of ablation, and the additional thermal effects that are not currently accounted for in the numerical model. Presented in Chapter 5.2, the model does not account for the three dimensional thermal diffusivity. It is limited to a one-dimensional transfer of heat. It also assumes a constant value of emissivity, heat capacity, density and thermal conductivity. These parameters have a temperature dependent effect on the optical and thermal properties of the target material [Anisimov and Luk'yanchuk, 2002]. Each factor will contribute to increasing the localised temperature of the target material and the temperature, velocities, species and pressure of the ejecta plume [Brewer, 1953].

Figure 6.30 shows two possible scenarios for predicting the mass flow rate of the ablated ejecta. The red line is the prediction based on the old ablation model given in Chapter 5.2. The red circles are the experimental results. The blue is the improved ablation model given in Chapter 5.4, but with different recondensation fractions.



(a) Conduction Loss is Twice the Value in the Dimensional Heat Diffusion Model (b) Conduction Loss is Estimated by the Dimensional Diffusion Model

Figure 6.30: Predicted Mass Flow Rate vs the Measured Mass Flow Rate for Two Different Estimated Spot Diameters and Different Recondensation Factors

From the experiments, it can be observed that there can be different possible diameters for the ablated spot. These two figures represent the two extreme cases, where the registered mass flow rate was loosely related to the mean diameter of the spot that was

measured after the ablation event. In Figure 6.30a the measured diameter of the spot is between $1.5 \cdot 10^{-3}$ and $1.75 \cdot 10^{-3}$ m. In Figure 6.30b the measured diameter is between $1.8 \cdot 10^{-3}$ and $2.1 \cdot 10^{-3}$ m.

According to both models, at this power level, the minor variation in the surface spot diameter has a substantial consequence. In order to fit the experimental data with the new model, as shown in Figure 6.30a, the heat dissipation through conduction had to be assumed to be twice the value predicted by the one dimensional heat diffusion model. In this case, the variation in the mass flow rate due to a variation in the recondensation fraction is very small, and a 50 % recondensation fraction correlates well to the experiment. Figure 6.30b suggests a different scenario. If the heat conduction loss is exactly predicted by the one dimensional model, then the recondensation is around 90 %. In both cases the old model predicts a mass flow rate that is one order of magnitude higher than the new model. Note that the curve associated to the new model stops before reaching a maximum registered spot size. This occurs as the mass flow rate predicted by the model drops to zero. The measured mass flow rate, on the other hand, is an average value over the sublimation period. The observed ablation event did cease due to the defocusing of the laser beam.

In addition, the outcome of the old model in Figure 6.30b suggests that if the sublimation temperature of the spot corresponds to the spectrometer, then the mass flow rate should be substantially higher and the spot size smaller. Although the new model never converges to a temperature that high for the target material. A possible explanation for the higher temperature registered by the spectrometer is the interaction between the gas and ejecta, and the laser beam during the expansion of the ejecta plume. Interaction can have two effects: one is heating up the gas and the other is to induce the gas to emit at a higher frequency than the simple temperature (via the spectrometer) would suggest. The latter may include plasma. These two points remain open and more experiments are required to fully complete the model. It is a discrepancy that is not yet fully understood.

If it is assumed that the laser beam increases the temperature of the gas by 1000 K, an additional 1.35 MW/m^2 needs to be included in the amount of dissipated energy. It is also interesting to note that the new model shown in Figure 6.30a predicts a transition in the mass flow rate. This occurs when the power density diminishes and the heat transfer is twice the one in the one-dimensional model. The transition corresponds to a sudden drop in performance and a change in the equilibrium sublimation temperature. This was not measured experimentally, and therefore needs more thorough experimental analysis.

In the experiment, the efficiency of the ablation process varied between 0.022 % and 0.148 %. This corresponded with an inferred momentum coupling coefficient between $6.15 \cdot 10^{-7} \text{ N/W}$ and $4.10 \cdot 10^{-6} \text{ N/W}$ and an energy usage of between $1.78 \cdot 10^8 \text{ J/kg}$ and $1.17 \cdot 10^9 \text{ J/kg}$. The range of data was caused by the inhomogeneous nature of the target material. It resulted in a variation of the ablated material's mass flow rate. All values given are, in part, calculated from the average ablated mass flow rate (over the ablation period) gained from the experiment.

The momentum coupling coefficient was considered to be a more important parameter

than the energy usage and efficiency of the ablation process. An increase in the momentum coupling coefficient implies an increase in the ablated mass flow rate. Also unlike conventional propulsion-based ablation, the deflection of asteroids through laser ablation is not fuel (i.e. mass) limited. If required the entire asteroid could be ablated. This could provide a potentially endless supply of propellant for the ablation process. However the current show-stopper is in the degrading and contamination effects of the ablated ejecta. Factors include the height, density, absorptivity and growth rate of the deposited material.

Performance Analysis

7.1 Introduction

The improved ablation model, together with the experimentally determined values of absorptivity and density of the deposited ejecta, can be used to re-evaluate the performance of laser ablation in providing a deflection action. Its effectiveness can also be compared to other forms of low thrust contactless deflection. This includes ion engines - RIT10 and RIT22 - and a Hall Effect thruster (PPS1350G). These three generic low-thrust electric propulsion (EP) systems could be used for ion beaming and on the gravity tractor. Critical parameters include the absorptivity of the deposited ejecta, momentum coupling, Δv , deflection system mass, input power of the laser, spot size radius and the distance between the spot and the laser. The first three parameters define the mission performance of the ablation process, and the last three define the operational conditions of the laser system.

7.2 Revised Absorptivity as a Contamination Factor

Using the improved model and the new, experimentally determined value of absorptivity (10^4 m^{-1}) the performance of laser ablation in providing an achievable deflection distance was re-examined. Identical to the mission simulations used in Chapter 5.2.1, the same mission design and overall system level efficiencies were used throughout. This permitted a direct comparison with the initial simulations presented in Figure 5.7. The deflection distance of a small, 250 m diameter asteroid is given as a function of warning time and the number of spacecraft that fly in formation with the asteroid.

Shown in Figure 7.1, a revised deflection distances between 85 and 10,000 km can be achieved. This occurs over a one to nine year operational period, with an increasing number of spacecraft. Figure 7.1 therefore demonstrates a substantial increase in performance. The achievable miss distance doubles in magnitude, which results in an increase in performance of 122 %. The increase in performance is caused by the reduction in the deposition and contamination effects of the ejecta plume. Degradation is still present, but it is reduced with respect to the expectation given in the previous model.

It should also be noted that this new simulation does not take into account the higher sublimation temperatures that were registered during the experiments, nor the additional

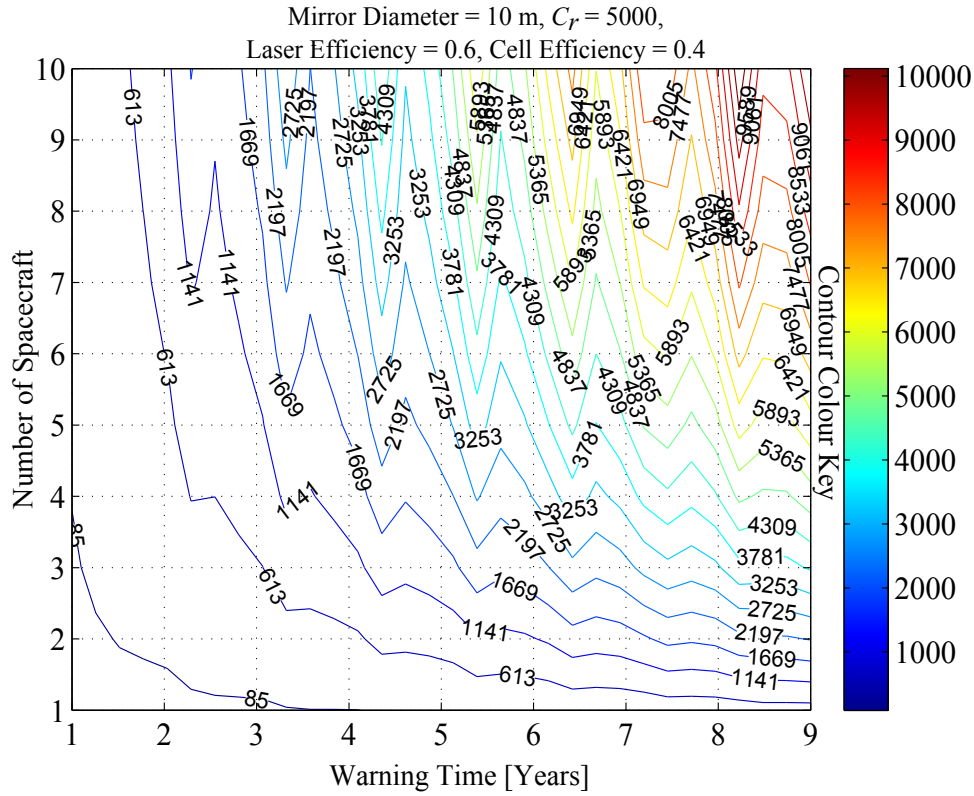


Figure 7.1: Revised Deflection Distance of a 250 m Diameter, $2.7 \cdot 10^{10}$ kg (based on Apophis) Asteroid: With the Experimentally Measured Degradation Factor

energy drains. From preliminary calculations, if the additional energy drains and a higher sublimation temperature (in the 3100-3800 K range) are considered then, to achieve an equivalent performance the concentration ratio would need to be increased to 60000. During the experiment, each collection plate was at room temperature (25 °C). It is therefore reasonable to expect that a higher collection plate temperature would decrease the condensation and deposition of the ejected material. Contamination could be reduced by maintaining the collectors at a moderately high temperature, over 100 °C.

7.3 Momentum Coupling Analysis

The momentum coupling was first evaluated over a range of laser input power, surface spot size radius, and then compared against the three EP methods. For the laser, the momentum coupling used herein relates the achievable thrust delivered by the ablation process to the input power installed onto the spacecraft for the laser system, P_L . This definition is slightly different than previously defined in Chapter 5.3 and found in Phipps et al. [2000]; Phipps [1997, 2011a]. The modification was essential to be able to compare the performance of the laser to the EP systems. The interest was to size the power system onboard the spacecraft. The revised expression for momentum coupling therefore becomes:

$$C_m = \frac{F_{SUB}}{P_L} \tag{7.1}$$

Equation (7.5) defines the input power to the laser. Discussed in Chapter 3.3, two engines are needed for ion beaming and on the gravity tractor. RIT22 has an I_{SP} of 4500 s. This occurs at a thrust of 150 mN and an input power of 5000 W. With two engines a momentum coupling of $1.5 \cdot 10^{-5}$ N/W is achieved. RIT10 has an I_{SP} of 3325 s, at a nominal thrust of 15 mN and an input power of 460 W. Its momentum coupling would therefore be $1.63 \cdot 10^{-5}$ N/W. PPS13505 has a higher momentum coupling. Systems with an average thrust of 67 mN at 1190 W and a I_{SP} of 1540 s have been demonstrated. The expected momentum coupling would be $2.81 \cdot 10^{-5}$ N/W.

The laser was assumed to operate with a plug-in efficiency of 55 %. This is based on the performance of electrically pumped, high power (~ 1.5 kW) fiber laser systems. Here, high power semiconductor lasers are coupled with a length of doped fibre that is placed in a laser resonator. The efficiency of the diodes (~ 75 % state-of-the-art) and fibre laser (>70 %), at an output wavelength of 1070 nm (based on existing industrial kilo-watt class lasers), results in a laser with an electrical-to-optical efficiency of 55 %. These values are based on the current and perceived near-future advancement in fibre technology and system efficiencies. For example, recent advancement by nLIGHT Photonics demonstrated, through the DARPA Super Efficiency Diode Sources and Architecture for Diode High Energy Laser Systems programmes, a diode laser pumped efficiency greater than 75 %. These pumped lasers represent the most compact, efficient and highest power currently available for a continuous wave light source.

Figure 7.2 shows the momentum coupling as a function of the power input to the different deflection systems. It was assumed that the efficiency of the ion engines does not change with the power level. This assumption is valid for high power systems, but is not generally true for very low propulsion levels, where the efficiency can drop below 40 % or less. The momentum coupling is therefore expected to be lower for much smaller thrust levels. The asteroid was assumed to be a small, 4 m diameter silica-based body. It was characterised with an assumed mass and rotational period of $1.3 \cdot 10^5$ kg and 500 rotations per day respectively [Vasile et al., 2013b].

To exceed the performance of the three EP systems (RIT22, RIT10 and PPS13505), Figure 7.2 shows that the laser unit would have to have an input power laser of at least 480 W. This corresponds with a minimum spot size radius of 0.5 mm. The small size of the spot would therefore limit the in-orbit flexibility of the laser system and require rigid control of the optics. To relax this requirement, but still exceed the performance of the EP system, then the spot size radius can be increased to 0.8-1 mm. This would provide a momentum coupling coefficient of $1.5 \cdot 10^{-5}$ N/W and a peak thrust of 10 mN. It would allow for a much larger, uncontrolled excursion of the spot radius.

There is a strong dependency between the input power of the laser, the spot size radius, the desired momentum coupling, and the thrust level. Figure 7.3a and Figure 7.3b show this dependency as a function of the input power and spot radius respectively.

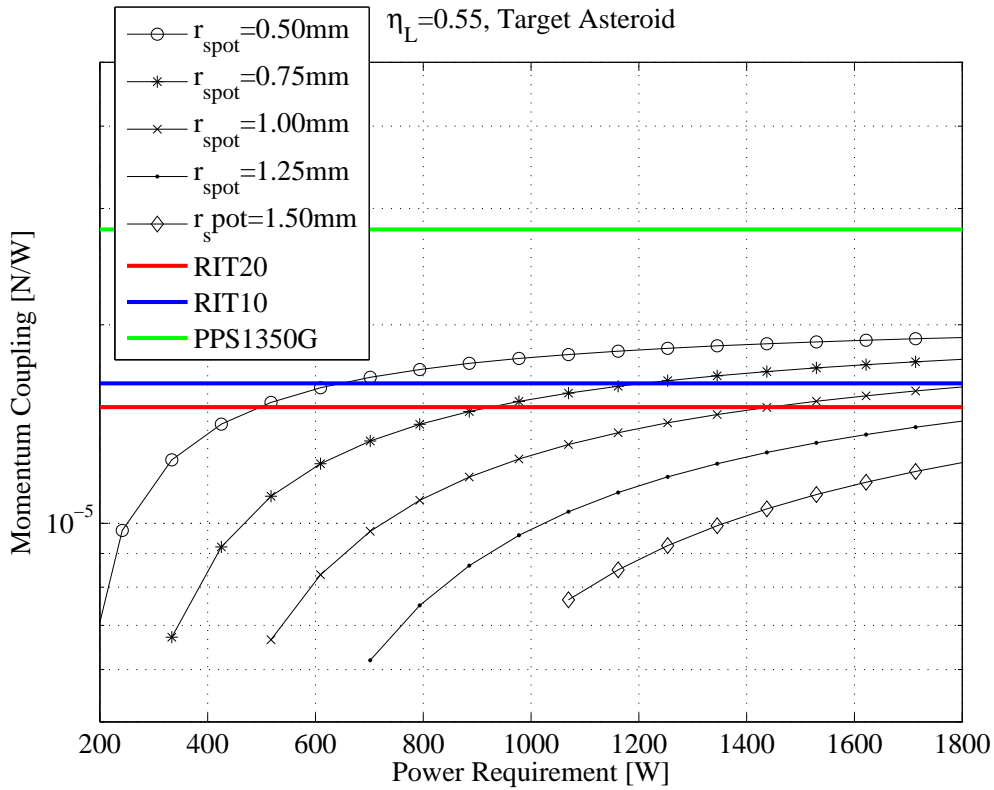


Figure 7.2: Momentum Coupling for Different Spot Sizes (Laser Efficiency 55 %)

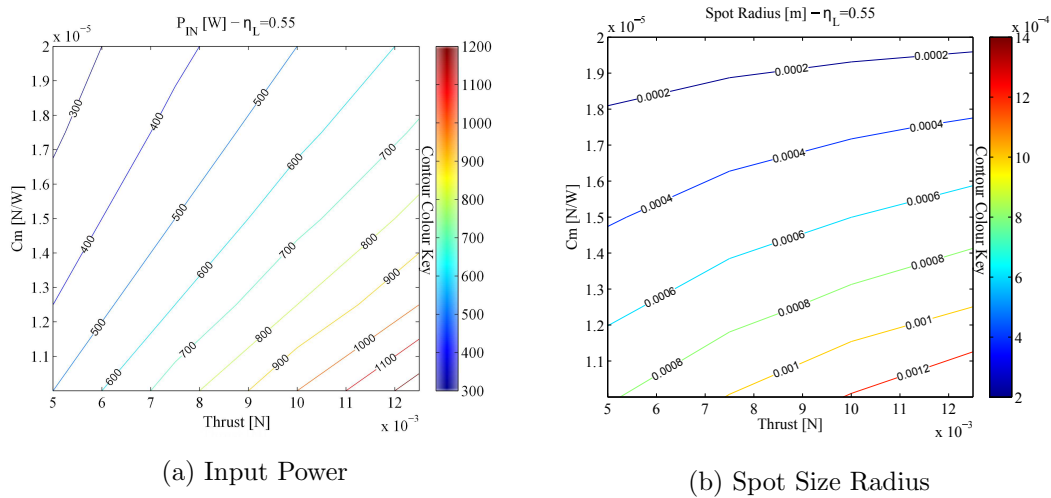


Figure 7.3: Input Power and Spot Size Radius as a function of Momentum Coupling and Thrust Level

If the spot size can be controlled down to a fraction of a millimeter, then the momentum coupling can be extremely large. This translates directly into requiring a smaller sized laser system with a much lower input power. For example, a 300 W laser can deliver almost $2 \cdot 10^{-5}$ N/W at a thrust level of 5 mN, if the spot size can be reduced to 0.2 mm. A 0.2 mm spot size is a very demanding requirement on the optical system. Illustrated in Figure 8.4, controlling the beam radius to 0.2 mm (or smaller) is possible, but would require precise control as the $2Z_R$ value drops rapidly below 1 m. A spot size between 0.6-1 mm is far more reasonable and enables the requirements on the focusing distance to

be relaxed. Although the laser to spot distance, known herein as the shooting distance, will impact on the sublimation time. Contamination caused by the ablated ejecta will reduce the surface power density. This could fall below the sublimation limit. The size and mass of the laser system (including its optical control) must also be considered.

7.4 Δv for Different Operational Conditions

Results shown in Figure 7.4 assessed the achievable Δv at different laser input powers, spot size radius and shooting distances. The Δv was computed by integrating the resulting thrust action on the asteroid over the ablation time. This is therefore defined as:

$$\Delta v = \int_{t_i}^{t_f} \frac{F_{SUB}(t)}{m_A(t)} dt \quad (7.2)$$

where the total sublimation time can be expressed as $\Delta t = t_f - t_i$. The sublimation process will decrease the mass m_A of the asteroid. The asteroid was assumed to complete one rotation a day and have an initial mass, diameter and average density of $1.1 \cdot 10^9$ kg, 84 m and 3500 kg/m^3 respectively. All other material properties were based on the assumed values given previously in Table 6.1. The sublimation time was also assumed to be 10 years. This is therefore representative of a low thrust, long-duration deflection technique.

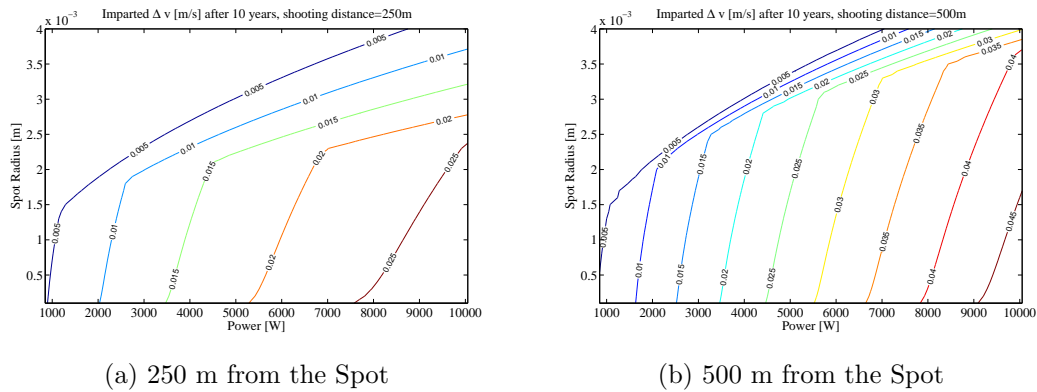


Figure 7.4: Imparted Δv as a Function of Spot Size and Input Power to the Laser

A longer shooting distance is always preferable. Contamination caused by the ejecta plume is lower. It will however impact on the size of the optics that are required to focus the laser beam. For example, a 1.5 mm spot at 500 m would theoretically require a focusing mirror with a diameter of 430 mm. The same spot size at 250 m would require a focusing mirror with a diameter of 210 mm. This reduction is advantageous in reducing the mass of the optical system. A 100 mm diameter mirror would require 10 kg of optics. This is based on system level design considerations reported in Vasile et al. [2013b]. Assuming that the mass of the optics can be scaled to the area of the mirror, then a 210 mm in diameter mirror would have an optical mass of 44 kg. A 430 mm diameter mirror would have an optical mass of 185 kg. Reported in Vasile et al.

[2013a,b], the analysis assumed a fiber laser with a standard beam quality ≤ 1.1 . The actual scalability of the optical system and the beam quality remains an open issue.

7.5 Deflection System Mass

Performance can also be evaluated by the deflection system mass. This defines the mass of the deflection system that is required to obtain a given Δv [Vasile et al., 2013b,a, 2014]. For laser ablation, the deflection system mass includes the mass of the laser, the laser-pumping power system, any optical elements, and the radiators that are dedicated to only rejecting the heat of the laser. Given this, the mass of the laser system m_{LS} can be estimated as:

$$m_{LS} = \alpha_P P_L + \rho_R (1 - \eta_L) \frac{P_L}{\sigma_{SB} \epsilon_R T_R^4} + m_L \quad (7.3)$$

where m_L is the mass of the laser (including optics). It was derived from system design considerations reported in Vasile et al. [2013b] and was assumed to be 10 kg/kW. The first and second expression in equation (7.3) describes the power and thermal subsystem mass of the laser system respectively. σ_{SB} is the Stefan-Boltzmann constant. ρ_R , A_R , ϵ_R and T_R are the specific mass, area, emissivity and operating temperature of the radiators respectively. ρ_R was calculated, assuming 0.5 kg/m². The area of the radiators were derived from a simple, steady state thermal equation. This is given by:

$$Q_{laser} = \sigma_{SB} \epsilon_R A_R T_R^4 \quad (7.4)$$

The emissivity and temperature (based on the operating temperature of the diodes of the laser) of the radiators were assumed to be 0.8 and 283 K respectively. It was also assumed that the radiators provide a heat sink in the thermal control subsystem. Q_{laser} is the radiating power of the laser. α_P is the mass per unit power of the power system. It was derived from system design considerations reported in Vasile et al. [2013b] and was assumed to be 40 kg/kW. P_L is the input power to the laser. η_L is the efficiency of the laser. This was assumed to be 55 %. The input power to the laser is assumed to be generated by a set of solar arrays. This is given by:

$$P_L = \eta_P \eta_S \frac{P_{1AU} A_{SA}}{R_{AU}^2} \quad (7.5)$$

where A_{SA} is the area of the solar arrays, R_{AU} is the distance from the Sun in AU. P_{1AU} is the power per square meter at 1 AU, η_P is the efficiency of the power system and η_S is the efficiency of the solar arrays.

The mass of the EP system should include the mass of two engines (whether it is ion beaming or a gravity tractor), the related power system, the radiators, propellant and the mass of the tanks. It is assumed that each EP system employs two identical engines, which are operating at the same time. The mass of the radiators and the power system

was computed using the same figures and assumptions used in the laser system, except for the efficiency of the engines. The efficiency of the engines was assumed to always equal 60 %. It does not change if the engine is scaled down and the power level changed. This is a rather optimistic assumption as the efficiency does not always scale with the thrust level. For example, current nano-ion engines can achieve an optimistic efficiency of 40-50 %. Larger engines, delivering 100 mN can achieve an efficiency of 60 %. The momentum coupling is therefore expected to be lower for low thrust levels.

The mass of the propellant m_p is simply:

$$m_p = \frac{2F_{EP}\Delta t_{thrust}}{I_{SP}g_0} \quad (7.6)$$

where I_{SP} , F_{EP} and Δt_{thrust} are the specific impulse, force and thrust time of a single engine respectively. The specific impulse was assumed to be 3500 s. g_0 is the standard acceleration due to free fall.

The mass of the EP system is therefore:

$$m_{EP} = 2.2 \frac{F_{EP}}{g_0 I_{SP}} \Delta t_{thrust} + \alpha_P P_{EP} + \rho_R (1 - \eta_{EP}) \frac{P_{EP}}{\sigma_{SB} \epsilon_R T_R^4} + 2m_e \quad (7.7)$$

where m_e is the mass of a single engine. P_{EP} and η_{EP} is the input power and efficiency for the EP system respectively. The efficiency and I_{SP} values used were the values quoted by each supplier of the engines. The thrust and mass were scaled down linearly. Both engines are also assumed to be operational at the same time. The mass of the propellant tanks was assumed to be only 10 % the mass of the propellant. This is accounted for in the first expression of equation (7.7). It therefore assumes that the mass of the propellant has no impact on the structural mass of the spacecraft. The transfer of momentum was also equal to one. This only occurs under ideal conditions, providing the best possible momentum transfer. The asteroid is subject to the full thrust delivered by one of the engines. The mass per unit power of the engine was 5 kg/kW. This excludes any electronics and the power, control and distribution unit (PDCU). These additional units are assumed to be included in the power system. The temperature of the radiators for the laser system is lower than the EP system. It is assumed that the laser needs to operate at 283 K while the EP system can operate at 374 K.

Figures 7.5-7.6 show the mass of the LP and EP deflection system against a wide range of achievable Δv . Each system has a different momentum coupling, specific pulse and thrust level. Figure 7.5a and Figure 7.5b show the comparison of the laser system against RIT10. This assumed a momentum coupling of the laser of $1.4 \cdot 10^{-5}$ N/W and $1.16 \cdot 10^{-5}$ N/W respectively. For the same momentum coupling, Figure 7.6a and Figure 7.6b compared the laser system against PPS1350G. The laser system was also evaluated at a different spot size radius. The analysis assumed that the mass of the power and thermal subsystem remained constant, and that a constant thrusting action is always applied to the asteroid. No gravity losses were included in the analysis, nor was the effect of contamination (this is reported further in Chapter 8.2). The asteroid was assumed to be a small, 4 m diameter silica-based body. It was characterised with an assumed mass

and rotational period of $1.3 \cdot 10^5$ kg and 500 rotations per day respectively [Vasile et al., 2013b].

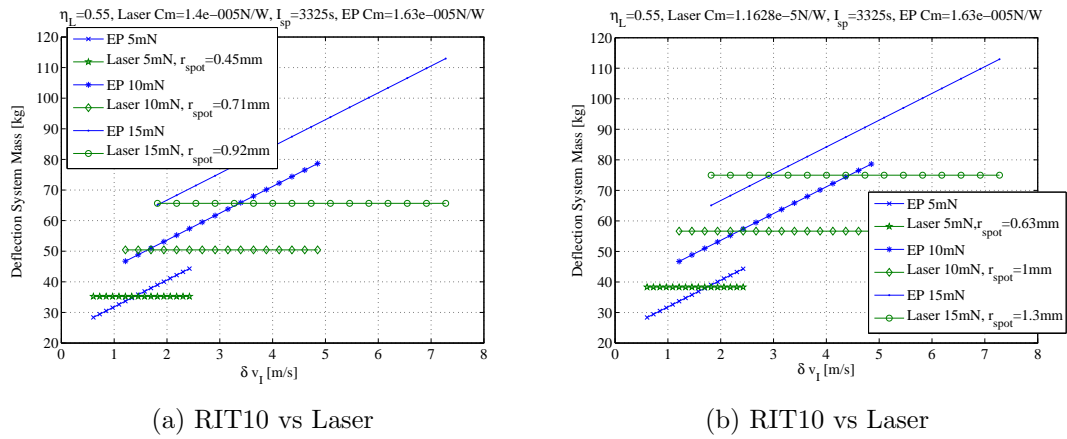


Figure 7.5: RIT System - Total Deflection System Mass as a Function of Δv

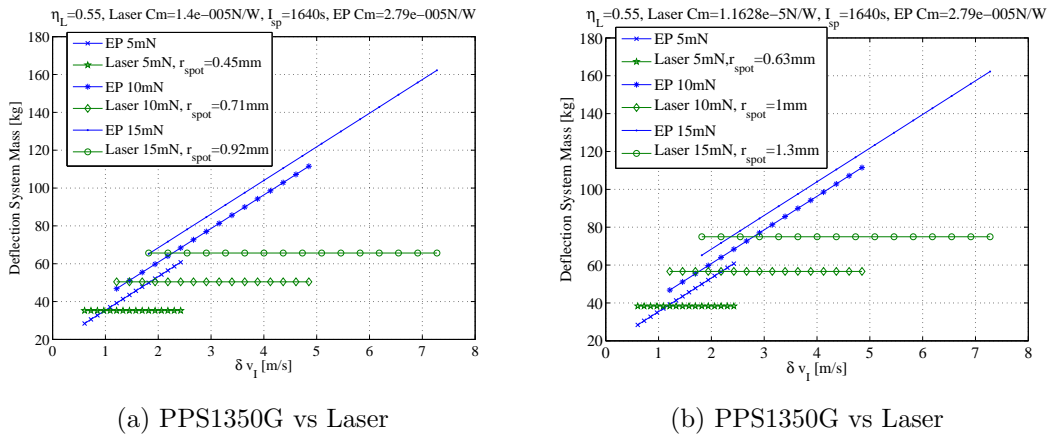


Figure 7.6: PPS1350G - Total Deflection System Mass as a Function of Δv

For the EP systems the imparted Δv increases linearly with the deflection system mass. More mass is required from the propulsion - tanks, propellant, more pipe work, larger hardness and structure mass - subsystem to provide the required deflection action. The radiator mass has a small impact on the deflection system mass and the mass of the power system would be the same. This is not an issue for laser ablation. The propellant to sustain the deflection action is provided for free. Mission mass and system complexity is therefore saved by the direct ablation of the asteroid's surface and subsurface material. As the Δv increases, the performance of the laser system always becomes more advantageous. The laser system requires significantly less deflection system mass than the other three forms of EP. For a given deflection system mass, the laser ablation process becomes effective over an ever increasing range of Δv . This increases the operational flexibility of the system as the deflection process can be used over a wider range of energy levels. Analysis clearly demonstrates that if the laser system had the same momentum coupling as the EP system, then for a given Δv , the deflection system mass would always favour the laser system. It could be used for the deflection of small to medium size asteroids.

To make the dependency on the Δv more explicit, equations (7.3) and (7.7) were recasted. Figure 7.7 shows the mass of the laser and EP system against the mass of the asteroid and imparted Δv . The EP system was assumed to have the same input power as the laser and delivered the same Δv . Both systems also operated with a shooting distance of 250 m. For a correct and fair comparison between the two concepts, it was assumed that the thrust of the EP system (as shown in Figure 7.7b) follows the same thrust profile as the laser system. It is also operational for the same amount of time (10 years). In Figure 7.7a the laser system was assumed to deliver a spot size of 1 mm. The mass of the optics does not change with power as the shooting distance and the spot size are constant. To account for this, a fixed mass of 10 kg was added to the mass of the deflection system. This corresponded to a 100 mm diameter optic [Vasile et al., 2013b]. These simulations were for a much larger, 84 m diameter asteroid (as used in Chapter 7.4). For the same installed power, resulting in the same Δv , the laser system is always more advantageous. The main difference in mass is due to the propellant consumption and associated tanks.

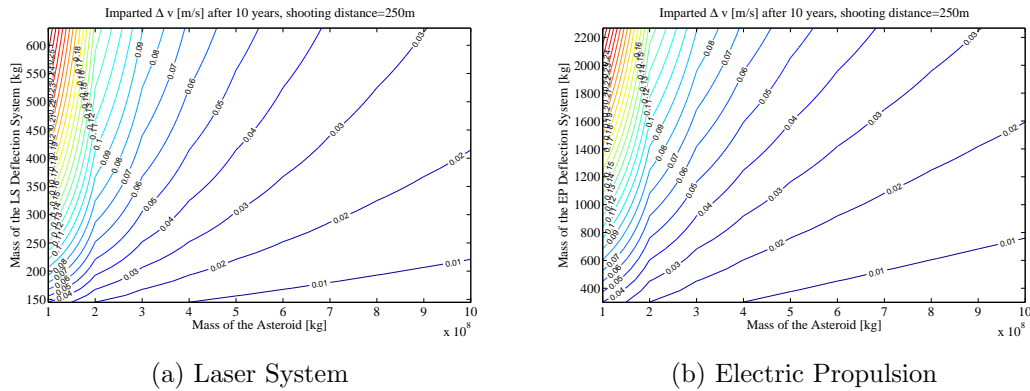


Figure 7.7: Imparted Δv - Function of the Asteroid Mass and Deflection System Mass

However it should be noted that this analysis is sensitive to the expected level of contamination caused by the ablated ejecta plume and the efficiency of the EP system. With the same overall system mass, an EP system with highly efficient engines could potentially induce a faster deflection action. The laser system may need to cope with an actual contamination rate that is higher than predicted by the model and current experimental investigations. If a three dimensional heat diffusion model is considered, the energy efficiency of the ablation process may also be lower than expected. The latter should therefore be the subject of future investigations

Technology Demonstration Mission

8.1 Introduction

Following the development of the improved ablation model, it was possible to assess the preliminary mission feasibility and spacecraft design of a small, laser ablation deflection system. It aimed to demonstrate the technological capabilities of laser ablation in providing a sufficiently high and measurable deflection action. The mission objective, to which the performance of the deflection action was compared, was to deflect a small and irregular 4 m diameter asteroid by at least 1 m/s. Deflection had to be completed with a total mission lifetime of less than three years, and be developed from highly innovative, yet achievable technologies within the 2025+ timeframe.

Following launch and rendezvous, a moderately size spacecraft would be used to successfully ablate the asteroid's surface. Deflection is assessed by either measuring the integral of acceleration imparted onto the asteroid or through the variation in the asteroid's orbital position and velocity [Vasile et al., 2013a]. Variation is with respect to the nominal, pre-ablated orbit. Each method gives a measure of the imparted Δv . The design of the spacecraft was developed by first considering the performance and specifications of the laser. Critical parameters included the minimal input power, spot size radius, expected level of contamination and shooting distance. These factors will affect the overall thrust time of the mission and the required optical alignment, stability and control of the laser system. The laser system was developed using simple optical control. The laser was then integrated into the subsystem analysis of the spacecraft. The specifications of the laser will govern the size and mass of the solar arrays and radiators, the physical configuration and accommodation of all payload, hardware and supporting units, and the close proximity operations between the spacecraft and the asteroid. The design approach maximised the use of near-term technologies and embraced a robust design philosophy of simplicity, reliability and mission heritage. The mission concept was called LightTouch² and the spacecraft was called AdAM (Asteroid Ablation Mission).

The study demonstrated how a relatively simple, laser ablation system could be integrated into a moderately sized spacecraft design. The laser system is powered by conventional solar arrays. It therefore verified the laser's proof-of-concept, performance and feasibility of its space-based application [Vasile et al., 2013a]. This also supports the general diversity and durability of using space-based lasers and the applicability of

the model's experimental verification. Work was supported by the 2012/13 SYSNova Challenge Opportunity (ESA, General Studies Programme).

8.2 Mission Architecture

Launched in 2027, AdAM will be injected into a geosynchronous transfer orbit (200·36000 km, 16 degs inclination) via a PSLV launch vehicle. An onboard bipropellant chemical propulsion system would be used to escape, transfer and rendezvous with the target asteroid (2006 RH120). This is achieved by two initial Earth apogee raising manoeuvres and an interplanetary transfer. The interplanetary transfer includes one deep space manoeuvre. The nominal time-of-flight to the asteroid is 306.5 days.

2006 RH120 is a small, monolithic, rocky, S class asteroid that completes approximately 500 rotations per day [Granvik et al., 2011; Kwiatkowski et al., 2009]. Due to its small size, 2006 RH120 is not a PHA. Laser-induced deflection poses no risk to the Earth. Target selection was based on the asteroid's observability, knowledge of its orbital ephemeris and the ability to provide a reliable rendezvous. If the asteroid is visible from Earth before the spacecraft rendezvous occurs, then the ephemeris of the asteroid can be updated. Radar observations can significantly reduce the uncertainty in its size, mass and orbital elements. It is also important to track the transfer trajectory of the spacecraft from Earth during its approach and rendezvous.

The design of the AdAM spacecraft was driven by its primary payload; a laser system and an impact sensor. A diode pumped fibre laser was selected to initiate the ablation process. An impact sensor would be used to measure the momentum created by the ablated ejecta. It would also monitor the deposition and degrading effects caused by the ejecta plume. Results gained from the impact sensor can improve the current contamination model for spacecraft design. To first design the system, the required accumulative thrust time needed to achieve a deflection of 1 m/s was assessed. Shown in Figures 8.1a-8.2b, the thrust time was evaluated at different input powers (850-1000 W), spot size radius (0.8-1 mm) and shooting distances (20-50 m). The contours in each plot show the thrusting time. Analysis included the degrading effects of the ablated ejecta.

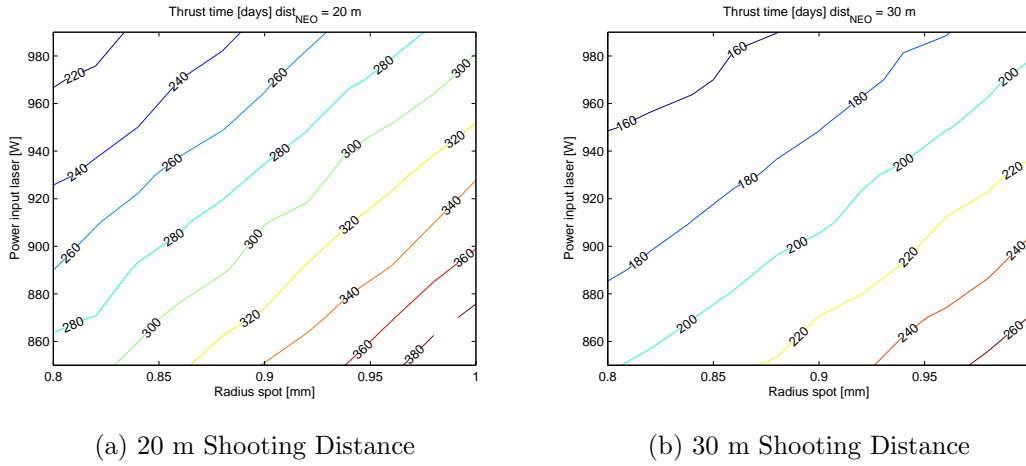


Figure 8.1: Thrusting Time to Achieve a Δv of 1 m/s - 20 and 30 m Shooting Distance. Reproduced from Vasile et al. [2013a]

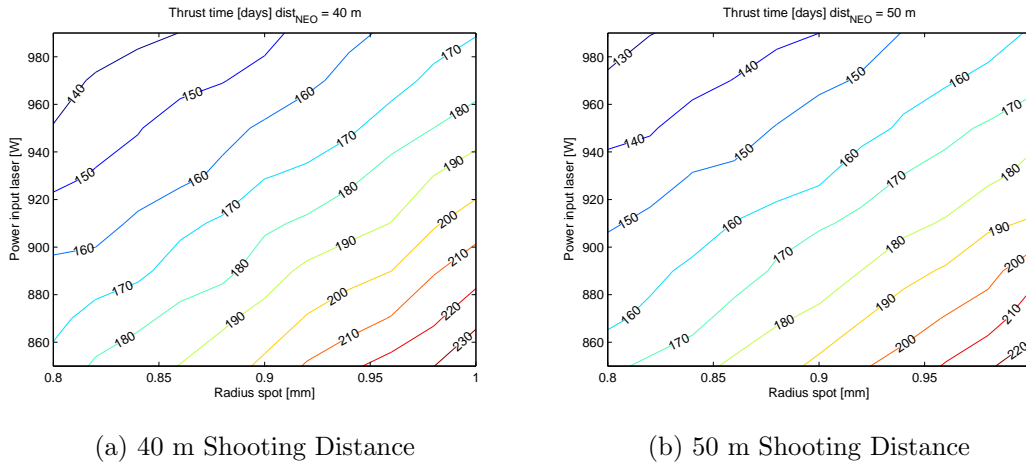


Figure 8.2: Thrusting Time to Achieve a Δv of 1 m/s - 40 and 50 m Shooting Distance. Reproduced from Vasile et al. [2013a]

Ablation becomes more effective when the spacecraft is 50 m from the asteroid. Here, the contamination caused by the ejecta plume is considerably lower. The spacecraft is trailing the asteroid and the solar arrays have a maximum aspect angle of 15 degs with respect to the impinging ejecta plume. Contamination of the solar arrays only results in a 5 % reduction of power. The laser beam will also have a self-cleaning effect on the impinging ejecta plume. A small spot can lower the laser input power. Shown in Figure 8.2b, a laser system with an input power of 860 W and a spot size radius of 0.8-1 mm, operating 50 m from the asteroid, would require an accumulative thrust time of 165-200 days. It would result in a surface power density between 428-274 MW/m².

Combined with the fast transfer, the mission objective of deflecting the asteroid by 1 m/s can therefore be achieved in just over two years. The total thrust time will be divided into several ablation phases, each lasting 30 days. Each ablation phase is followed by a dedicated orbit determination campaign. The sequential ablation of the asteroid's surface is used to improve the robustness and reliability of the deflection action. New procedures can be tested and verified. The ablation response can also

be monitored throughout. The remaining mission year of operations can be used to increase the robustness (by providing a larger contingency margin) of the mission and to perform additional opportunistic science objectives. Opportunistic science objectives can be achieved with the inclusion of a combined Raman/Laser Induced Breakdown Spectrometer (LIBS). Selected to best complement the ablation process, the LIBS can examine the chemical, mineralogical and isotopic composition of the ejecta plume. It includes both volatile and refractory elements.

The scientific return of the mission is also supported with the operations of the narrow angle camera (NAC) and the wide angle camera (WAC). Both cameras are used primarily for GNC purposes, but will be operational before, during and after the ablation event. Each camera will therefore provide high resolution, scientific images. Local and global images of the ejecta plume and the target asteroid can be obtained. This enables the definition of the asteroid's shape, size model and rotational state (for example, period and axial orientation) [Vetrisano et al., 2013]. The formation, bulk density and mass of the ablated ejecta plume can also be derived. These additional science objectives were derived from the flight heritage gained from the previous Rosetta, Stardust, Deep Space 1, Venus Express and Hayabusa missions. Technological advances were also taken from the planned Marco Polo-R mission.

8.3 Spacecraft Design

8.3.1 Laser

Selection of the laser was based on the power, beam quality and focusing requirement needed for the ablation process. Based on current technological development (presented in Chapter 7) a fibre coupled diode laser was selected. It covers a range of wavelengths and is used widely in laser-based manufacturing. The laser system was therefore assumed to operate with a laser input power and overall efficiency of 860 W (increasing to 1032 W with a 20 % design margin) and 55 % respectively (as previously discussed and justified in Chapter 7), a temperature of 10 °C (based on the diodes), a wavelength of 1070 nm (previously justified in Chapter 7) and have a system mass of 24 kg. The system mass was based on the performance of existing kilo-watt class industrial lasers, the heritage of previously flown and therefore space qualified reflective telescopes (for example, the HiRISE instrument on the Mars Reconnaissance Orbiter) and the achievable technological developments within the 2025+ timeframe.

The laser system has been designed using a simple, combined beam expansion and focusing telescope. Here, with a nominal focus length of 50 m, a collimated beam (that appears as a point source) will be expanded and refocused onto the desired point on the surface of the asteroid. Shown in Figure 8.3, the telescope will expand the collimated output of the high-power fibre laser to about 75 mm in diameter. The laser beam will then be focused by a highly reflective and metallic off-axis parabolic or aspheric mirror, with an approximate diameter of 100 mm. The focusing laser beam will then be reflected from a right-angle, half-cube reflector. This will allow for the final position and

orientation of the output laser beam. For repositioning of the exit laser beam, the end optic could be placed in a domed window. Beam steering will be provided by motorised actuators on the focusing optics. Movement of the focus will also be provided by an actuator mounted on the expansion telescope mirror. This can improve the pointing and stability of the laser beam, and so minimises any focusing errors. The motion of the laser beam can also be tracked. Tracking could be achieved with an onboard laser range finder, or similar instrument.

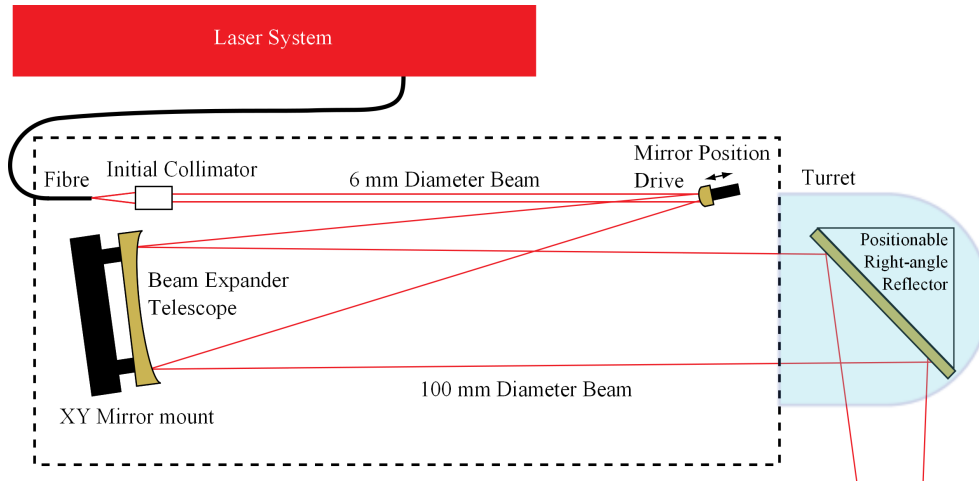


Figure 8.3: Schematic of the Laser System and Telescope Beam Expander. Image reproduced from Vasile et al. [2013a]

The laser output is fed from the fibre enclosure via a fibre umbilical to a collimation unit. This couples the output to free-space. The use of off-axis reflective optics will provide the maximum transmission of the optical system, with minimal component heating and loss. This system provides a m-squared factor of 1.1. The m-squared value defines how much the laser beam departs from an ideal Gaussian beam. The smaller the value the better the quality - focusing and depth-of-field - of the laser beam. This translates directly into the ability of the laser beam to achieve a small focused spot with nearly all the laser power tightly focused.

Figure 8.4 shows the relationship between the beam diameter at the exit of the focusing mirror and the focused spot radius at 50 m from the surface. This is for a laser wavelength of 1070 nm. The distance from the focus, over which the laser beam will double its area is known as the Rayleigh Range, Z_R [Siegman, 1990]. It is a measure of the focusing power of the laser beam. For a Gaussian beam, propagating in free space, the Rayleigh Range is defined in Figure 8.5. λ_b is the wavelength of the laser and ω_o is the beam waist. The beam waist is the narrowest radius of the spot under nominal conditions.

In Figure 8.4, the distance between the corresponding points on either side of the focus is $2Z_R$. $2Z_R$ is therefore given as a function of the beam diameter and beam radius. For a 100 mm beam diameter the $2Z_R$ value is 2 m. Therefore, either side of the focus, the beam intensity will not change appreciably over 1 m. Ablation can still occur with a de-focused laser beam. For a 70 mm beam diameter and a 0.8 m spot radius, the $2Z_R$ value is over 3 m.

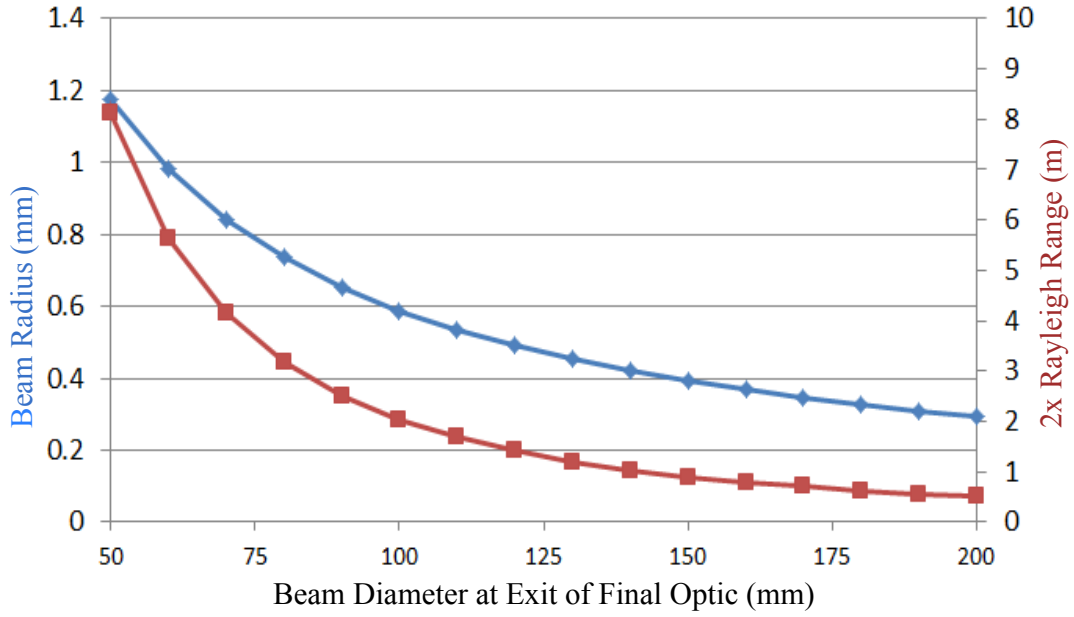


Figure 8.4: Beam Behaviour of a 1070 nm Fibre and a $f = 50$ m Optic. Data reproduced from Vasile et al. [2013a]

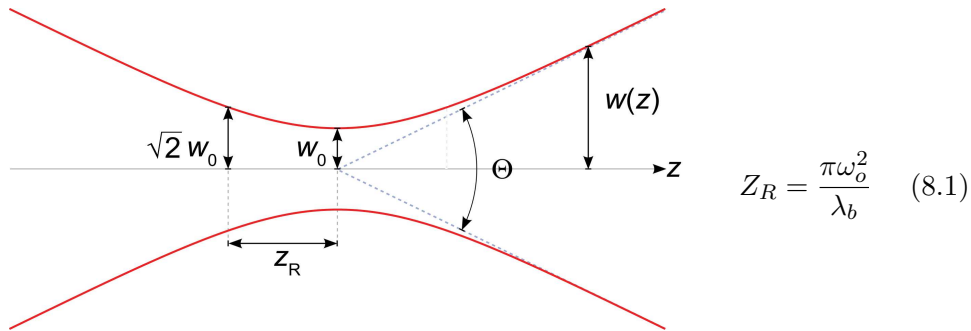


Figure 8.5: Parameters of the Laser beam

The $2Z_R$ value provides a degree of operational flexibility and control in the focusing of the laser beam. It can account for any irregularities in the asteroid’s shape, rotational velocity and surface features. A precise, distance measurement, between the spacecraft and the spinning asteroid may be difficult to achieve. It also reduces the control and size requirements of the optics. With the active alignment of the telescope’s optical separation, the focus point of the system can be easily manipulated. This can occur over many meters, where the focus point of the laser beam on the surface of the asteroid can be tracked with an onboard laser range finder, or similar instrument.

8.3.2 Impact Sensor

The impact sensor consists of five piezoelectric transducers (PZT). PZT have been used as impact sensors for many years and have therefore demonstrated a high level of reliability [Bussoletti et al., 1999]. It is a fundamental impact detection technique [Leese et al., 1999]. Five PZTs are mounted underneath a 0.5 mm thick, squared aluminium

diagraphm plate; one in each corner and one in the centre [Esposito et al., 2002]. This provides an exposed detecting area of 100·100 mm.

Each impact event, caused by the ablated ejecta, will generate an acoustic wave. The wave carries the impulse momentum, which is propagated along the aluminium plate. The PZT then converts this wave into an electrical signal, where the output voltage is proportional to the momentum of the impinging particle. The proportionality factor is $(1+e_I)$, where e_I is the coefficient of restitution of the particle [Esposito et al., 2002].

A similar, yet more multi-purpose instrument is currently flying on the Rosetta mission. The impact sensor is a subsystem of a much larger Grain Impact Analyser and Dust Accumulator (GIADA) instrument. GIADA aims to analyse the physical, chemical and dynamic evolution of the individual particles ejected by the comet's nucleus and to examine the spatial and temporal distribution of the dust population [Bussoletti et al., 1999; Colangeli et al., 2007]. It is achieved by three different remote sensing methods, including, the Grain Detection System (GDS), an impact sensor and a network of five micro-balance sensors. The GDS is used to detect the optical transit and cross-section of each particle entering the instrument. It is placed in cascade with an impact sensor which can determine the velocity and mass of each particle with a diameter ranging between 60 and 500 microns [Epifani et al., 2002; Della-Corte et al., 2012]. Momentum measurement ranges from $3\cdot 10^{-11}$ to $3\cdot 10^{-5}$ Ns [Esposito et al., 2002]. Detection is limited by the electrical and mechanical noise of the system, and the efficiency of the sensing plate and PZT elements. The micro-balance sensors are used to monitor the cumulative incoming dust deposition rate from the different space directions [Esposito et al., 2002; Colangeli et al., 2007; Palomba et al., 2002].

Heritage can also be taken from the In-Orbit Evaluator instrument. This flew on the 2001 PROBA-1 mission as a low cost, low resource, rapid response dust environment monitor. The instrument consists of piezo-electronic microphones with impact-sensing and foil penetration capabilities [Leese et al., 1999; Schwanethal et al., 2002, 2005]. It is presented as a universal instrument for in-situ dust and debris flux measurement that is applicable for Earth orbit and interplanetary space missions.

8.3.3 Raman/Laser Induced Breakdown Spectrometer

The LIBS instrument has been internationally recognised as a powerful, next generation, remote sensing in-situ instrument for asteroid and planetary analysis. It can assess the spectral dispersion and response of the excited species - atoms, molecules and molecular fragments - contained within the ejecta plume [Rohner et al., 2003; Brinckerhoff et al., 2000]. It is based on the vibration frequencies, relative intensities and the number of bands emitted within the spectrum of the plume. The spectral emission lines identify the elemental composition, while the intensity of the emission lines indicate the quantity and concentration of mass contained within the ejecta plume [Russo et al., 2002]. Fast, direct, quantitative analysis enables the simultaneous identification of all major, minor and trace elements [Rohner et al., 2003; Russo et al., 2002]. The LIBS can therefore address multiple science themes [Rohner et al., 2003; Brinckerhoff et al., 2000; Wuest

et al., 2007; Tarcea et al., 2007]. It includes:

- The chemical analysis and structural classification of mineralogical and geochemical material. It includes the identification of any structural changes within the laser irradiated areas and the geological, mineralogical and petrology characteristics of the asteroid.
- The analysis of volatiles, gaseous elements and inclusions within the ejecta plume. It enables scientists to further characterise the chemical processes that has shaped the compositional evolution of the asteroid.
- The determination of the reaction kinetics, molecular fractionation and ablated products within the ejecta plume.

Additional scientific measurements also include the geometry, spatial distribution (at high resolution) and dimensions of the ejecta plume [Courreges-Lacoste et al., 2006]. LIBS analysis can be performed on any sample, regardless of size, and without the need of sample preparation. Samples include all solid, liquid and gaseous states. It is also inclusive of both transparent and opaque samples that have a range of surface textures [Rohner et al., 2003; Russo et al., 2002; Tarcea et al., 2007].

The LIBS can either be mounted onto a planetary rover or orbiting spacecraft. For example, a combined LIBS instrument has been selected as a science payload of the 2018 European ExoMars Rover [Courreges-Lacoste et al., 2006]. Detailed chemical, mineralogical and structural analysis of the Martian landscape will be achieved by ablating small portions of the exposed surface. This includes rocks and boulders and is accomplished through the remote operations of a continuous wave laser (wavelength of 532 nm). Surface illumination of a 50 μm spot size diameter provides an irradiance level of approximately 1.2 kW/cm² [Rull et al., 2011]. It is operational from a stand-off distance from 10-100 m. The LIBS instrument for ExoMars is currently undergoing detailed breadboard modelling. This includes environmental and operational testing - thermal, vibration and radiation - within a simulated Martian environment. The instrument has a mass of 2 kg (including electrical hardness) and a power of 30 W. It also contains three main units. This includes the optical head, the spectrometer and the backend electronics. All units are interconnected via optical and an electrical harness.

The development of the LIBS is also supported by the pioneering technological advancement in laser sources, optical elements, spectrometers and detectors. It has led to the development of robust, compact and miniaturised spectrometers. These spectrometers have the onboard spectral capability (for example, high spatial resolution over an extended wavelength range from UV to near infrared) of any advanced ground-based laboratory system [Rohner et al., 2003; Perez and Martinez-Frias, 2006; Courreges-Lacoste et al., 2006]. The LIBS instrument for the LightTouch² mission opportunity will have to be space qualified, but it does not drive the system performance of the AdAM spacecraft.

8.3.4 Spacecraft Configuration

Following rendezvous, AdAM can operate in two orbital configurations; either trailing the asteroid or in a radial direction. The different orbital configurations correspond to the two operational strategies for ablation. It is important to understand how the close proximity operations of the spacecraft would affect the design of the GNC subsystem and the overall performance of the deflection action.

Shown in Figure 8.6, in the trailing configuration the spacecraft is flying in formation with the asteroid's along track, trailing or leading by 50 m. This limits the contamination effects of the ejecta plume on the performance of the optics, radiators, MLI and solar arrays. In the radial configuration, as shown in Figure 8.7, the spacecraft is located between the asteroid and the Sun. This reduces the number of actuators by balancing the forces acting on the spacecraft, while still providing a measurable deflection action [Vetrisano et al., 2013; Vasile et al., 2013b]. Here, the laser beam operates perpendicular to the spacecraft's solar arrays, from the umbra side. The laser, impact sensor, LIBS and laser rangefinder are located on the top face of the spacecraft. It ensures that all instruments are exposed to the full formation of the ejecta plume. Any ejecta that does deposit, will do so on the rear of the solar arrays. This poses a negligible risk to the power generating ability of the solar arrays. The WAC and the NAC point towards the asteroid.

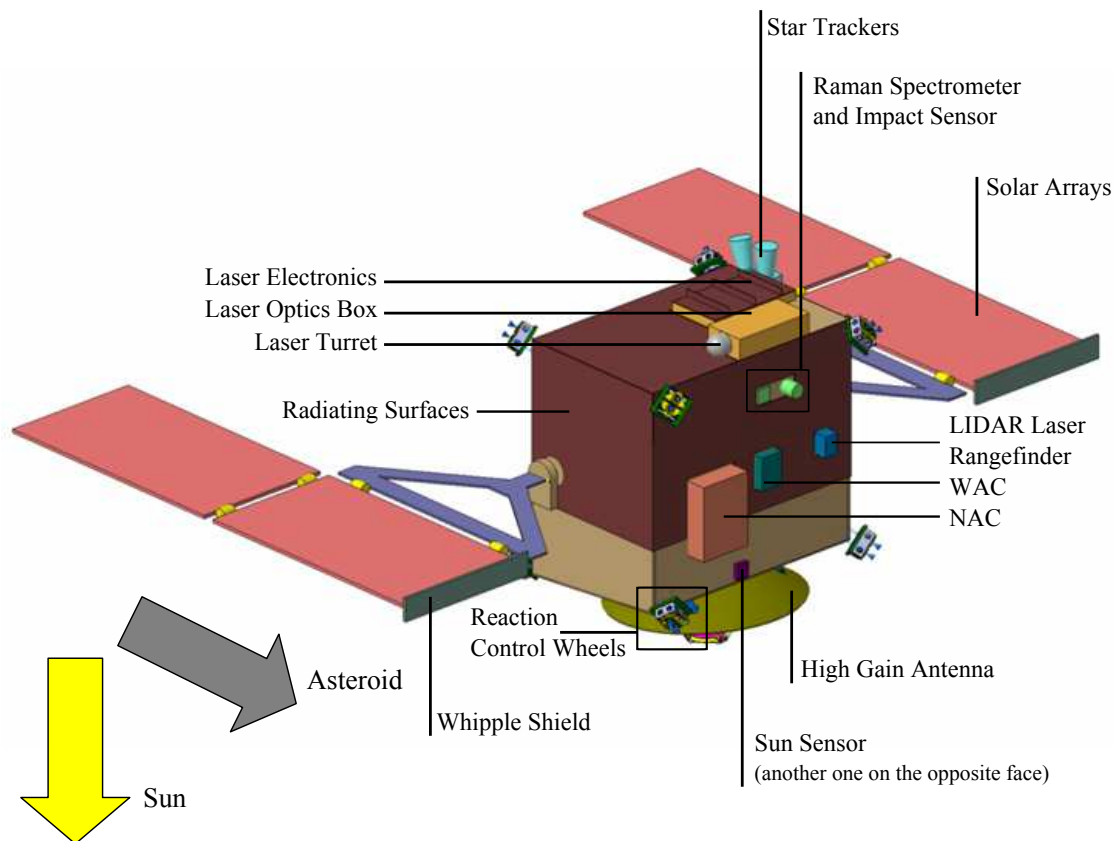


Figure 8.6: Deployed Configuration of AdAM in the Trailing Configuration - All Externally Mounted Instruments and Units

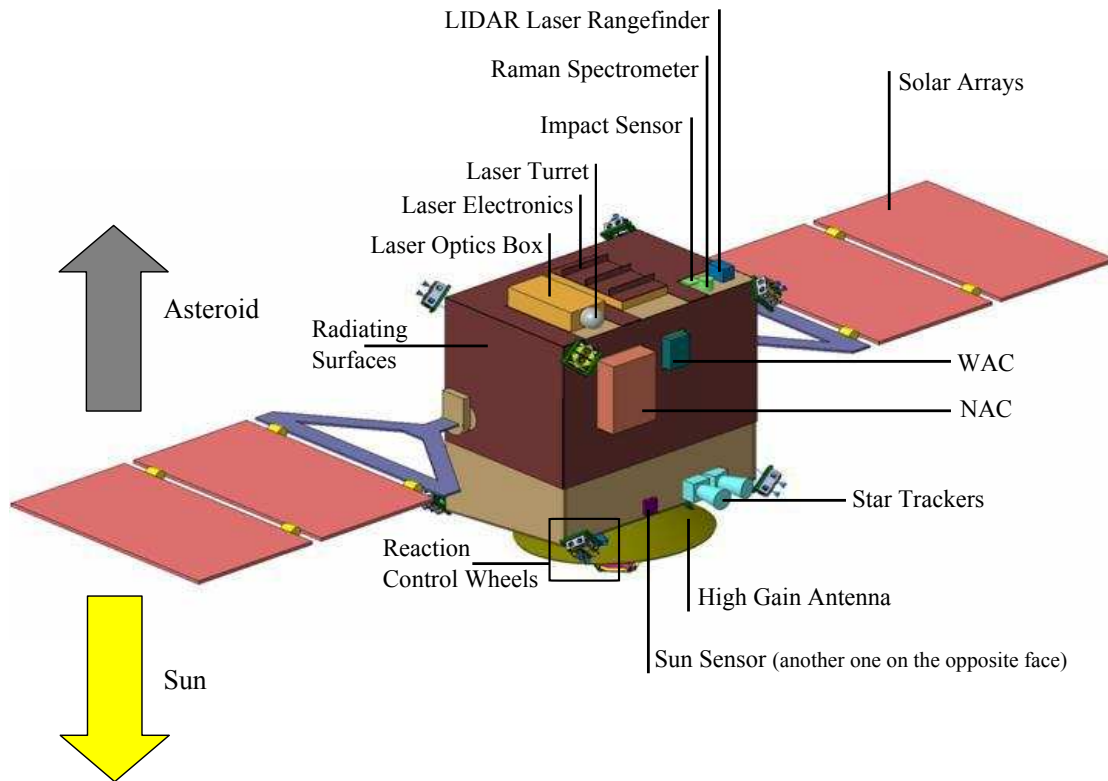


Figure 8.7: Deployed Configuration of AdAM in the Radial Configuration - All Externally Mounted Instruments and Units

In the trailing configuration the laser is again located on the top face of the spacecraft. However the laser beam is directed across, towards the asteroid. The LIBS, impact sensor and laser rangefinder are located on the same face as the NAC and WAC. Each instrument points towards the asteroid. To reduce the deposition effects of the ejecta on the solar arrays, the solar arrays have been rotated. This provides a smaller frontal area to the incoming ejecta plume. Two Whipple Shields have also been included. Each shield is mounted on the front edge of the solar array and can protect the spacecraft (and its system performance) from the abrasive effects of the ablated ejecta. A similar solution was implemented on the NASA Stardust mission to comet Wild2 and is currently flying on both the ISS and the Automated Transfer Vehicle (ATV). Whipple Shields provide an innovative, relatively low mass shielding solution. It consists of a thin, multi-layer structure of mylar and kapton that acts as a sacrificial bumper shield.

In both configurations the laser and radiators are always in the shadow cone of the spacecraft. This allows maximum heat dissipation. All external instruments are body mounted. The high gain antenna points towards the Earth and the solar arrays are oriented towards the Sun. Radiators face into deep-space. The spacecraft is 3-axis stabilised with four reaction wheels and sixteen reaction control thrusters. These units are used to maintain the orientation of the spacecraft. The thrusters are mounted in eight double-nozzled units located on the corner of the spacecraft bus. Each thruster is oriented to avoid direct impingement onto the solar arrays. Acquisition and navigation to the asteroid is provided by two star trackers, sun sensors, an inertia measurement unit (IMU), a laser range finder and two optical cameras. The WAC and NAC will be used

for navigating the far and close approach respectively, and the laser range finder will be used for close proximity operations. The GNC system has been designed to account for the forces of the laser recoil, the gravity of the asteroid, the gravity gradient of the Sun, solar radiation pressure, plume impingement and the induced deflection action. These factors will be used to estimate the spacecraft's trajectory and the asteroid's response to the ablation process [Vetrisano et al., 2013]. It includes changes to the asteroid's rotational state and local acceleration. Solar radiation pressure, plume impingement and the laser recoil can create additional torque. This occurs when the spacecraft's centre of pressure does not coincide with the centre of mass. Plume impingement depends on the cross sectional area of the exposed surface. Passive collision avoidance is also included. If sudden failure occurs, the motion of the spacecraft is driven by the solar radiation pressure and the asteroid's gravitational field. Solar radiation pressure may push the spacecraft along the Sun-spacecraft direction [Vasile et al., 2013b].

Power is supplied by two deployable and steerable solar arrays, with a total array area of 7.4 m^2 . The solar arrays are separated into four panels; two on each opposite sides of the spacecraft. With a specific mass of 2.5 kg/m^2 , this provided a total array mass of 22.2 kg (including a 20 % margin). A solar array drive mechanism will ensure the spacecraft's Sun-pointing direction. The solar arrays will be stored at launch, secured by a hold-down and release mechanism. Power is stored in the onboard batteries. Thermal control is provided passively by large radiators (4.23 m^2), heat pipes, MLI (9.85 m^2) and heaters. Heat pipes will be used to transfer the rejected heat from the laser to the radiators. The size of the radiators were determined by solving a simple, steady state thermal equation given previously in equation (7.4). The emissivity and maximum allowable temperature were 0.8 and 293 K respectively. With an assumed specific mass of 0.3 kg/m^2 , the radiator mass is 1.27 kg . The size of the propellant tanks, the wet mass of the spacecraft, the launch loads and the physical accommodation of all equipment and instruments drive the structural design of the spacecraft. Heritage was also taken from the Venus and Mars Express missions. The external size of the spacecraft bus is $1.3 \cdot 1.7 \cdot 1.6 \text{ m}$ (h-w-d). A liquid apogee engine is located within the launch adapter. Communication is provided by a 1.3 m high gain antenna and a 12 m X-band telecommunication link (planned upgrade from S-band) with the ESA ground station site at Harwell, England. This will provide low-cost telemetry, tracking and command. The ground station at Malindi, Kenya, Africa was selected as the low-cost secondary back-up option. This will be used when the downlink with Harwell is not possible (two months before and after arrival).

Table 8.1 summarised the mass budget for the AdAM spacecraft. This is for a nominal laser input power of 860 W . From the momentum coupling and deflection system mass analysis in Chapter 7, the laser ablation system is equivalent to a small scale EP system that has the same installed power. With responsibly sized optics and realistic optical control, this provides a short deflection time.

The design of the spacecraft was based on a conservative and robust design approach. It therefore included a 5 % mass margin for existing off-the-shelf components, a 10 % margin when small modifications are required and a larger 20 % margin for new design units. A 20 % margin was also added onto the nominal dry mass. This is in accordance

with ESA standards. Shown in Table 8.1, the largest proportion of the spacecraft's mass is the structure, followed by the power and GNC subsystems. Each subsystem also included a conservative 20 % mass margin.

AdAM Mass Budget	Current Mass (kg)	Maturity Margin (%)	Maximum Mass (kg)
Payload	24.4	19.2	29.1
Data Handling Subsystem	17.1	10.9	18.9
Power Subsystem	66.5	16.3	77.3
Communication Subsystem	37.7	8.8	41
GNC & AOCS Subsystem	31.5	9.5	34.4
Thermal Subsystem	12.9	20	15.5
Propulsion Subsystem	59.9	12.3	67.3
Harness	28.2	20	33.9
Structure and Mechanisms	100	20	120
SPACECRAFT DRY MASS			437.4
Subsystem Mass Margin		20	87.5
SPACECRAFT DRY MASS WITH MARGIN			524.9
Propellant			442.2
SPACECRAFT WET MASS			967.1
Launch Vehicle Capability			1074
Launch Vehicle Margin			10.69
MASS MARGIN %			10

Table 8.1: Mass Budget for the 860 W Laser - PSLV XL GTO

A second iteration was also performed. Shown in Table 8.2, this investigated whether a reduction in the laser input power to 480 W would be possible. Analysis presented in Chapter 7 and Figure 7.2, showed this to be the minimum possible input power of the laser. To remain a competitive deflection technique, laser ablation must always provide a higher momentum coupling value than other forms of EP systems. It corresponded with a 0.65 mm spot size radius, a peak thrust of 5.5 mN and a momentum coupling value of $1.15 \cdot 10^{-5}$ N/W. The LIDAR range finder was also replaced with a low-mass and low-power range finder. Shown in Figure 8.4 and discussed in Chapter 8.3.1, the Rayleigh range can be increased to 3 m. This can be used to further reduce the navigation requirement. The spacecraft's mass was also optimised. This included improvements in

the propellant mass, and the thermal, structural and power subsystem mass. It will have a cascade effect on the rest of the spacecraft design. The same margin philosophy was used throughout.

AdAM Mass Budget	Current Mass (kg)	Maturity Margin (%)	Maximum Mass (kg)
Payload	20	19	23.8
Data Handling Subsystem	17.1	10.9	18.9
Power Subsystem	46	14.6	52.8
Communication Subsystem	37.7	8.8	41
GNC & AOCS Subsystem	44.5	12.6	50
Thermal Subsystem	12.4	20	14.8
Propulsion Subsystem	59.9	12.3	67.3
Harness	25.3	20	30.9
Structure and Mechanisms	83	20	99.6
SPACECRAFT DRY MASS			399.2
Subsystem Mass Margin		20	79.8
SPACECRAFT DRY MASS WITH MARGIN			479
Propellant			351.9
SPACECRAFT WET MASS			831
Launch Vehicle Capability			1074
Launch Vehicle Margin			243
MASS MARGIN %			22.6

Table 8.2: Mass Budget for the Revised 480 W Laser - PSLV XL GTO

Reducing the laser input power decreased the size (and therefore the mass) of the solar arrays, radiators, PCDU and the laser itself. A solar array area reduced to 4.25 m². The mass of the laser could also be reduced to 5.6 kg. In the previous analysis, over 50 % of the laser mass was a thermal heat sink. This had already been included in the mass of the spacecraft’s thermal subsystem. The mass of the optics remained the same.

The reduction in the input power was only possible because of the fast transfer time of the baseline trajectory and an reassessment of the accumulative push time. Figure 8.8 shows the thrust history and the imparted Δv of the reduced power solution. The thick red line represents the accumulative push time needed to reach a deflection of 1 m/s. In practice this would be divided into a series of ablation periods, followed by an orbit

determination campaign. The push time plotted on the x-axis is measured as a fraction of the orbital period of the asteroid.

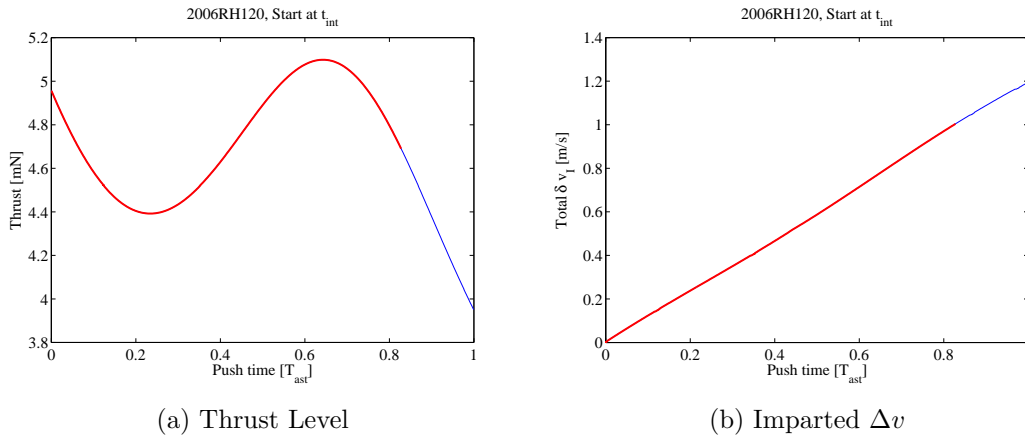


Figure 8.8: Thrust Level and Δv for a Reduced 480 W Laser Input

If the peak thrust is reduced to 5.5 mN and the input power to the laser is 480 W, the push time increases to 83 % of the orbital period of the asteroid [Vasile et al., 2013a,b]. The accumulative thrust time almost doubles to 302-403 accumulative days. Despite this increase, the time to achieve the 1 m/s deflection action is still achievable within the mission duration of three years.

It should also be noted that the substantial reduction in the laser’s input power does not significantly affect the mass of the spacecraft. Only 136 kg is saved. This relates to a reduction of about 0.12 kg/W of laser power. The dry mass is dominated by the structural mass. Here, for reliability reasons a 20 % mass margin was applied. A 20 % margin was also added to existing flight proven components and industry standard hardware. It included the solar array mechanism, impact sensor and thermal components. A more relaxed 10 % mass margin would lower the spacecraft’s total wet mass to 779 kg and the dry mass to 445 kg. The result is comparable with the NEAR Shoemaker mission.

8.4 Opportunistic Potential

The study also demonstrated the additional scientific, exploration and exploitation potential of laser ablation. Shown in Chapter 6, laser ablation results in the subsurface tunnelling and volumetric removal of deeply situated and previously inaccessible material. This is due to the formation of a subsurface groove and the ejection of highly volatile material within the ejecta plume. Confirmed by the SEM, the ablated material is elementally identical to the original source material. However the absorptive properties - deposited ejecta height, density and absorptivity - are considerably different. Deposition results in a fine, powder-like material that can be easily removed.

The exposure, interaction and possible collection of this newly ablated material can maximise the scientific capability of any contactless deflection-based mission. It can

also be used to enhance any remote sensing, in-situ or sample return mission. Deep, subsurface material extraction is not currently possible through conventional exploration techniques. Nor is it being considered in any future asteroid missions (i.e. Marco Polo-R). Sample depth (for an asteroid mission), using current state-of-the-art drilling techniques is limited to a few centimetres below the surface [Mueller et al., 2011]. Laser ablation could therefore be used to advance the scientific return of any planetary, exploration or deflection-based mission. This includes detailed elemental, structural, mineralogical and isotopic analysis.

Mounted onboard a rendezvousing spacecraft, the spectra response of the ablation event could be examined through optical cameras, a laser range finder or a suite of visual-infrared and mid-infrared spectrometers [Koschny et al., 2009]. Data from optical cameras and a laser range finder can determine the shape model, albedo and surface roughness of the asteroid. Spectrometers can perform spectral-thermal analysis and secondary global mineralogical and compositional analysis. A spacecraft passing through the plume can also be used to collect the ablated ejecta. Material could then be examined in-situ or as part of a sample return mission. The composition and velocity of the ablated material could be assessed by an interstellar dust analyser, microwave spectroscopy or ion mass spectroscopy. An externally mounted sticky-pad mechanism (or similar) could also be used to retrieve the ablated ejecta [Lee et al., 2006]. This currently provides a passive collection method for loose surface regolith, but could be developed to collect the ablated ejecta [Lees et al., 2006]. The spacecraft would use the sticky-pad to skim the exposed, ablated surface. Similarly the Stardust mission successfully collected and returned cometary and interstellar material to Earth. Material was captured in aerogel and secured within a sample return capsule.

Laser ablation could also be extended to include the commercial extraction and exploration of resources. The ablation process could be used to mine the extra-terrestrial subsurface material. Any prospecting resource mission would depend on the accessibility of the asteroid, its telescopic spectral analysis, the feasibility of the resource extraction technique and the concentration of material being sought [Elvis, 2013]. Analysis performed by Sanchez and McInnes [2011a, 2012] demonstrated that a substantially large amount of resources (in the order of 10^{14} kg) can be accessed at a relatively low energy level. Using current technologies, neighbouring asteroids ranging from 2-30 m in diameter can be returned for scientific, exploration and resource utilisation purposes [Garcia-Yarnoz et al., 2013]. This can occur across a wide spectrum of energy levels. Some are, in fact, more accessible than the Moon. For example, with only 100 m/s of Δv , approximately $8.5 \cdot 10^9$ kg of asteroid material could be exploited [Sanchez and McInnes, 2013; Yarnoz and Sanchez, 2013]. This is significantly lower than any lunar exploration activity, which (due to the presence of a gravity well) is limited to a minimum threshold of 2.37 km/s [Sanchez et al., 2012; Binzel et al., 2004b].

It is estimated that a C class asteroid contains 60 % of extractable, useful material. This includes a rich mixture of volatile substances (for example, carbon dioxide, nitrogen, ammonia, water, carbon and sulphur), complex organic molecules, dry rocks and metals (for example, iron, nickel, cobalt, platinum group metals, magnesium and titanium)

[Lewis, 1996, 1994; Brophy and Friedman, 2012a; O’Leary, 1977]. Other exotic material, with new and unknown properties, might also form in space [Bindi et al., 2012; Ma et al., 2012]. Platinum group metals are siderophiles as they dissolve readily in molten iron. This makes them rare, and therefore expensive, as they are mostly trapped in the Earth’s core [Kargel, 1994]. The iron content in M class asteroids can be as high as 88 % [O’Leary et al., 1979]. They are also believed to be rich in platinum group metals [Kargel, 1994]. The iron content for a S class asteroid is reduced to 22 %. It is dominated with silicon dioxide (38 % by mass), a magnesium-oxide (24 % by mass) and iron-oxide (10 % by mass) [O’Leary et al., 1979]. Extracted material could provide radiation shielding against galactic cosmic rays, distilled for fuel extraction, provide thermal control, space structures, manufacturing and continued life support [Hills, 1992; Mazanek et al., 2013; Phipps, 2002; Gibbings et al., 2012]. Material could either be processed at the in-situ locations, or returned to Earth. Laser ablation could slice the asteroid into multiple, smaller and more manageable segments. Engineering and scientific precursor missions could also be used to test new surface science and extraction techniques. The captured asteroid could act as a platform for testing and developing future deep-space operational experience. This would enable manned and robotic missions to extend their reach across the solar system. Asteroids could act as staging posts and life support units for future space exploration activities. It could also kick-start an entirely new in-situ resource utilisation industry [Brophy and Friedman, 2012b].

To translate these theoretically perceived benefits into a viable space-based application, certain technologies and system design approaches would need to be developed. Shown in Table 8.3, the most critical component in the design of the AdAM spacecraft (or any other ablation based activity) is the laser system, its associated optics and the cascade effect it has on the design of the power, thermal, GNC and structural subsystems. All other subsystems have a relatively high level of technology readiness. Each TRL level is ranked on a scale of 1 to 9. Levels 1 (basic principle observed) to 4 (component or breadboard validation in a laboratory environment) relate to the use of innovative technologies before or during the mission assessment phase. Analytical or experimental demonstration of emerging hardware or software can provide an initial proof of concept. A breadboard model is a low fidelity system that displays the function of the unit. Modelling occurs without any integration of case hardware or a software platform. Levels 5 (component or breadboard validation in a relevant environment) to 9 (flight proven technology, gained through a successful mission operation) relate to existing technology.

For the AdAM mission concept, the data handling subsystem and the onboard computer can be adapted from the planned Lisa Pathfinder mission (TRL 7 - system prototype demonstrated in a space environment) and the flash mass memory (TRL 5) can be developed from the ESA Cross-scale study. The high gain antenna (TRL 9) was taken from the Venus Express mission. All other components in the communication subsystem were reused from the Marco Polo-R mission (TRL 7). This includes the low gain antenna, transponder, electronics power conditioner and cables. The RF distribution and waveguide (TRL 7) are modified from BepiColombo. The spacecraft bus was modified from Venus Express (TRL 7). The propulsion system was developed from standard flight hardware. Components include a 35 litre helium tank, a 267 litre propellant tank,

pressure regulators and transducers, valves, filters, reaction control thrusters and a liquid apogee engine. The only modification would be in the re-design of the pipework and a height reduction of the propellant tanks.

Platform	TRL	Heritage	Expected Modification
PAYLOAD			
Laser	3/4	Ground-based	Design and Space Qualification
Laser Optics	3/4	Ground-based	Design and Space Qualification
Impact Sensor	5	GIADA Rosetta	Modification and Space Qualification
LIBS	5	ExoMars	Modification and Space Qualification
POWER			
Solar Arrays	5	IMM Cells	Cell Development and Qualification
Whipple Shields	5	ISS and ATV	Significant Modification
Battery	7	Lisa Pathfinder	None - Off the Shelf (still to be flown)
PCDU	6	TerraSAR-X2	Cell Development and Qualification
Solar Array Drive	9	Sentinel 1	None - Off the Shelf
Deployment	5	Marco Polo	Scaled down from Marco Polo-R
GNC			
Star Tracker	9	Haydra - Spot 6	None - Off the Shelf
Sun Sensor	9	Marco Polo	None - Off the Shelf
Reaction Wheels	7	AstroFein	None - Off the Shelf (still to be flown)
IMU	9	Astrix 120HR	None - Off the Shelf
NAC	4	Marco Polo-R	Continued Development
WAC	5	NPAL	Breadboard - Continued Development
Laser Rangefinder	9	ATV, HTV	Testing for a Non-collaborative Target
THERMAL			
Heaters	7	Standard Unit	System-level Design and Qualification
MLI	7	Standard Unit	System-level Design and Qualification
Radiators	7	Standard Unit	System-level Design and Qualification
Heat Pipes	7	Standard Unit	System-level Design and Qualification

Table 8.3: Critical TRL Components of the AdAM Spacecraft

Critical components include the laser (and associated optics), impact sensor, LIBS, solar arrays, Whipple Shields and the NAC. The impact sensor and LIBS are both based on European technology. The impact sensor is currently flying on the ESA Rosetta mission and the LIBS have already undergone extensive breadboard and environmental testing. Both instruments will however need to be adapted to ensure compliance with the system

configuration and mission requirements of AdAM. Other system level considerations include a compact, high power, but low mass PCPU and a high solar-to-electric power conversion system. The development of the solar arrays and NAC are already included in ESA's technology roadmap for general space missions. These systems will therefore be developed and qualified independently of AdAM and the LightTouch² mission opportunity. The development of a highly reliable and efficient ($> 80\%$), high power laser will also have a significant impact on a range of terrestrial applications. This includes, but is not limited to: cleaning, mining, cutting, surgery and wireless power transmission. It is therefore likely that the evolution of lasers will follow a parallel path. The ablation system (including the laser and the optics) must be capable of focusing and steering the beam onto the surface of the asteroid. It must therefore include control algorithms with in-situ dialogistic integration for adaptive control, and an advanced thermal management system for cooling the laser. The system will also have to be space qualified against the effects of radiation, launch loads, thermal cycling, vacuum and electromagnetic compatibility.

The space-based detection, tracking and ablation of small asteroids could be demonstrated through simple precursor missions. This would support the development of a fully developed deflection mission. It could be achieved in LEO with a dummy asteroid, a piece of space debris or combining it into a rendezvous mission with multiple themes. The mission opportunity could test the integration of the attitude motion's reconstruction strategy and the in-situ measurement of the asteroid's rotational state. Alternatively a science dominated precursor mission could test the ability of the laser system to analyse the material properties of an illuminated sample. The opportunistic potential of the laser payload would serve as a technology demonstration of an ablation deflection system. Either option would improve the TRL of the laser, optics and ablation process.

NASA, and a range of private space-based companies, are also investing into asteroid exploration and exploitation missions, and their necessary technological developments. In 2012, Planetary Resources Ltd, Deep Space Industry and Scott Space Industries announced their intention to develop a set of deep-space prosecuting spacecraft. Based on affordable and realistic technologies, they plan to use spacecraft to harvest the precious minerals and materials found on asteroids. Planetary Resources Ltd also intend to develop a network of deep-space propellant deposits. NASA is also investigating highly innovative system concepts for a proposed asteroid re-direct mission. This aims to capture and re-direct a small size asteroid into trans-lunar space. Here, astronauts would be used to explore the asteroid's surface, composition and mechanical properties, and evaluate its resource potential. To further refine the mission concept, NASA is currently evaluating information on advancing asteroid observations, asteroid redirection systems, asteroid deflection demonstrations, asteroid capture systems, crew systems for asteroid exploration and partnership & participatory engagement.

The mission concept was developed from an earlier study performed in 2013 by the Keck Institute for Space Studies. This investigated the feasibility of identifying, capturing and returning a small 7 m diameter asteroid to near-Earth space. Powered by a 50 kW solar

electric propulsion, a single robotic spacecraft could return 1000 metric tonnes of material [Brophy and Friedman, 2012b]. A similar system could also be used to capture a 2 m diameter asteroid to the ISS [Brophy et al., 2011]. These mission concepts were developed to combine NASA's activities in human exploration, space technology and science. It could be used as a stepping stone between LEO operations and a fully developed, long duration, deep-space NEA exploration mission. Laser ablation, as a low thrust orbit modification system, could gravitationally capture an asteroid within an Earth or cis-lunar orbit, or around the liberation points of L_1 and L_2 [Garcia-Yarnoz et al., 2013; Sanchez et al., 2012, 2013; Sanchez and McInnes, 2011b; Hills, 1992]. The same approach could also be used for geo-engineering related purposes. Material extracted from a much larger (> 500 m diameter) captured asteroid could create a solar insulating dust ring around the Earth [Bewick et al., 2013, 2012b; Pearson et al., 2006; Stuck, 2007]. A cloud of ejected and unprocessed material would become gravitationally anchored at, or around, the L_1 point [Bewick et al., 2012a,b, 2010]. By preventing, and controlling how much sunlight is absorbed into the Earth's atmosphere, the effects of global warming could be reduced.

Conclusions and Future Work

This thesis, through a series of laser ablation experiments, has examined the potential effectiveness of laser ablation for the deflection of NEAs. It has studied the development of the ejecta plume and the potential for the deposited ejecta to contaminate any exposed surface. The results from the experiments were used to update the ablation model and to reassess the performance of laser ablation in providing a deflection action.

Laser ablation is dominated with the volumetric removal of gaseous material. Excluding the initial and rapid ejection of solid particles, the plume shape and geometry followed the prediction given in Kahle et al. [2006]. This is applicable for the ablation of a dense and rocky body. It is similar to the formation of an exhaust in standard methods of rocket propulsion. Despite these similarities, the absorptive properties of the deposited ejecta were found to be significantly different. For a given mass flow, the deposited material was much thicker than expected, but had an equal mass per unit area. The density of the deposited material was therefore much lower than the 1000 kg/m^3 originally assumed for forsterite (olivine-like) in the initial ablation model. The initial model also assumed an incorrect surface layer growth and significantly overestimated (by two orders of magnitude) the absorptivity of the deposited ejecta. From the experiment, for the ablation of the olivine sample, the absorptivity of the deposited ejecta was 10^4 m^{-1} and had a deposited density of 250 kg/m^3 . There was no immediate saturation of the exposed surface, nor the formation of a permanently attached opaque surface. Instead the deposited ejecta was loosely bound to the underlying substrate. The laser beam also provided a self-cleaning action. There was no apparent deposition along the path length of the laser beam. The initial ablation model was overly conservative in an unexpectedly benign environment. The original model also excluded the additional optical-thermal effects between the laser beam and the ejecta plume, the occurrence of incoherent ablation from the target's surface and incorrectly predicted the measured mass flow rate of the ablated sample.

Experimental analysis was used to verify the improved ablation model. This enhanced the current understanding and modeling of the ablation and contamination process for a dense and rocky body. The improved model combined the energy balance of sublimation with the absorption within the Knudsen layer, the variation of sublimation temperature with local pressure, the temperature dependent thermal conductivity of the target material and the partial re-condensation of the ablated material. The improved model provided a better prediction of the mass flow rate of the ejecta plume and the thrust induced by the ablation process.

Based on these improvements, the performance of laser ablation was reassessed. For a given Δv , and compared to other methods of contactless low thrust deflection, the deflection system mass of the laser ablation system is always more advantageous. Comparatively large and achievable levels of deflection can be accomplished. The momentum coupling was found to be comparable and, critically, is a key parameter to assessing performance. The size of the laser system is based on a minimum power requirement, the required momentum coupling and the expected level of contamination. The latter will drive the system comparison between laser ablation and electric propulsion deflection techniques. The efficiency of the ablation process does not affect the mass of the laser. It is instead dependent on the momentum coupling. The mass of the EP system, by comparison, is defined by the efficiency and mass per unit power of the low thrust engines. This offers laser ablation a distinct, and advantageous feature. The required mass for the deflection action is provided for free. This is achieved by the ablation of the asteroid's surface. The size of the laser system will drive the surface spot size radius, the onboard optical control and the shooting distance of the laser. The specifications of the laser will then govern the size and mass of the solar array and radiators, and the physical configuration and accommodation of all other units. It was shown that an ablation system can be easily integrated into a conventional solar-powered spacecraft. This can be achieved with current technologies, and following a robust design philosophy of simplicity and reliability.

The results also demonstrated the opportunistic potential of the ablation process. Laser ablation resulted in the subsurface drilling and volumetric removal of deeply situated and previously inaccessible material. The capture of this ejected material could maximise the scientific capability of any remote sensing, in-situ or sample return mission. This would enable scientists to further characterise the composition, formation and evolution of asteroids, develop the commercial exploitation of their natural resources and act as a staging post for the future robotic and scientific exploration of the solar system. These themes could be addressed with the development of a moderately sized space-based laser system.

Future work is still required to fully develop the ablation model. This includes more detailed, inclusive experiments and theoretical modelling. Additional experimental procedures were developed, however time limited their implementation into the test campaign. These are given in more detail in Appendix B6. They include:

- Measuring the online mass flow rate of the ejecta plume
- Measuring the temperature profile of the ejecta plume and the target material
- Measuring the initial expansion, distribution and velocity of the ejecta plume
- Measuring the temperature dependent effects of the ejecta deposition.
- Measuring the ablation response of more realistic and representative shape models

A pulsed or off-axis laser beam could also be used to examine the response of higher energy ablation without the additional absorption effects of the laser beam. Other areas of diagnostic measurement include a mass spectrometer or residual gas analyser

to identify the gaseous composition of the ejecta plume, a shadowgraph to assess the initial expansion of the ejecta plume, and a quartz-crystal micro-balance (QCM) or PZT impact detectors. Highlighted in Chapter 8.3.2, these two instruments can measure the in-situ deposition effects of the ejecta plume and the force imparted onto the target material [Kuper et al., 1992; Pakhomov et al., 2002; Tribble, 1961].

The QCM operates by comparing the resonant frequencies of two quartz crystals. This can occur at a range of temperatures [Kurosaw et al., 2002; Fabreguette et al., 2005; Tribble, 1961]. One crystal is exposed to the ablation event and the other is shielded. The deposition of mass will affect the crystal's resonant frequency, and from this the mass deposition can be inferred. At 25 °C, sensitivities as small as $4.32 \cdot 10^{-9}$ g/cm² at 10 MHz have been recorded [Wallace and Wallace, 1988] - although no information on the absorptive nature of the deposited material can be collected [Tribble, 1961]. Particle Image Velocimetry can reconstruct the three dimensional velocity, wavefront location and particle distribution of the plume [Elsinga et al., 2006; Ganapathisubramani et al., 2007; Boxx et al., 2009]. It is achieved by introducing, then illuminating tracer particles into the ejecta plume. The scattered light is then recorded simultaneously from several different directions. Three dimensional data can be extracted from two dimensional optical tomography [Elsinga et al., 2006]. The deposition effects of the ejecta plume could also be examined on a greater range of more realistic space-based materials. Examples include MLI, solar cells and radiating surfaces.

An improved space-based environment could also be achieved by decreasing the temperature of the vacuum chamber and thermally cycling a rotating sample on a small motorised stage. Experiments could also be performed in microgravity. Microgravity would provide validation of the ablation model in a relevant space environment. It is advantageous as it: [1] provides a free-falling initial state of the target material, [2] enables the ablation events to occur under all the translational and rotational degrees of freedom without any restraining forces, and [3] eliminates the confounding influence of gravity on the long-term motion of the sample. It also includes the motion of an unconstrained three dimensional tumbling body.

Initially proposed by Gibbings et al. [2011c,d], a series of self contained (vacuum chamber) ablation experiments would examine the kinetic response of laser ablation. Microgravity could be accessed through a series of parabolic flights on the Airbus A300 Zero-G aircraft, the Zarm Drop Tower, a sounding rocket launch or as a scientific payload on a privately owned commercial space vehicle. Access to commercial spaceflight could be achieved through the NASA Flight Opportunities Programme. Table 9.1 shows how each method varies in duration and quality [Fitton and Seibert, 2001; Rath, 1995].

Method	Maximum Duration	Gravity (g_0)	Mass (kg)
Zarm Drop Tower	2-10 seconds	10^{-5} - 10^{-6}	300
Sounding Rocket	14 minutes	10^{-4} - 10^{-5}	300-800
Parabolic Flights	20-25 seconds per parabola with ~ 40 parabolic trajectories per flight	10^{-2} - 10^{-4}	500
SpaceShipTwo (Virgin Galactic)	3-5 minutes	10^{-3} - 10^{-6}	600
Lynx (XCOR Aerospace)	3-5 minutes	$< 10^{-1}$	120-650

Table 9.1: Comparison of Different Methods for Accessing Microgravity. The mass is defined as the experiment mass per payload, with possibly multiple payloads per flight opportunity.

Results from these additional experiments can improve the ablation model. It will enable a direct measurement of the initial expansion and development of gas and ejecta, and further improve the model to predict the thrust magnitude of the laser-induced action. It is also important to understand the three dimensional energy balance of sublimation (rather than a mono-dimensional heat diffusion model), the inclusion of solid particles within the ejecta plume, the effects of a de-focused laser beam and the reduction of laser energy during the lifetime of the ablation mission. These factors may lower the energy efficiency of the ablation process. The scalability of the optics and the beam quality required to achieve the necessary spot size is an open issue. This requires further investigation. The model's applicability to a greater range of asteroid analogue target material (including an inhomogeneous structure) should also be improved.

Bibliography

- V.P. Ageev, A.I Barchukov, F.V Bunkin, VI Konov, V.P Korobeinikov, B.V Putjatin, and V.M Hudjakov. Experimental and theoretical modeling of laser propulsion. *Acta Astronautica*, 7:79–90, 1980.
- T.J Ahrens and A.W Harris. Deflection and fragmentation of near-earth asteroids. *Nature*, 360:429–433, 1992.
- T.J Ahrens and A.W Harris. Deflection and fragmentation of near-earth objects. In T Gehrels, editor, *Hazards due to Comets and Asteroids*. University of Arizona Press, 1994.
- L.W Alvarez, W. Alvarez, F Asaro, and H Michel. Extra-terrestrial causes for the cretaceous-tertiary extinction. *Science*, 208:1095–1108, 1980.
- S.I Anisimov and B.S Luk'yanchuk. Selected problems of laser ablation theory. *Physics B*, 43(3):293–324, 2002.
- J.A Atchison and M.A Peck. A passive, sun pointing, millimeter-scale solar sail. *Acta Astronautica*, 67:108–121, 2010.
- B.W Barbee, W.T Fowler, G.W Davis, and D.E Gaylor. Optimal deflection of hazardous near-earth objects by stand-off nuclear detonation and neo mitigation mission design. NASA NEO Workshop, 2006.
- M.A Barucci, A.F Cheng, P. Michel, L.A.M. Benner, R.P. Binzel, P.A. Bland, H. Bohnhardt, J.R Brucato, A.C Bagatin, P. Cerroni, E Dotto, A Fitzsimmons, I.A Franchi, S.F Green, L.-M Lara, J Licandro, B Marty, K Muinonen, A Nathues, J Oberst, A.S Rivkin, F Robert, R Saladino, J.M Trigo-Rodriguez, S. Ulamec, and M. Zolensky. Marcopolo-r near earth asteroid sample return mission. *Experimental Astronomy*, 33:645–683, 2012.
- M.A Barucci, P Michel, H Bohnhardt and J.R Brucaro, E Dotto, P Ehrenfreund, I.A Franchi, S.F Green, L.M Lara, B Marty, D Koschny, D Agnolon, R Chalex, P Martin, and J Romstedt. Marcopolo-r: ESA sample return mission to 2008 EV5 (a potentially

- hazardous asteroid). In *IAA Planetary Defense Conference Proceedings*, volume 1, pages 1–8. International Academy of Astronautics, 2013.
- J Beckers. Adaptive optics for astronomy - principles, performance and applications. *Annual Review of Astronomy & Astrophysics*, 31:13–62, 1993.
- I Bekey. Project orion: Orbital debris removal using ground-based sensors and lasers. In *Proceedings of Second European Conference on Space Debris*, pages 699–701. ESA ESOC ESA-SP 393, 1997.
- M.J Belton, T.H Morgan, N Samarasinha, and D.K Yeomans. *Mitigation of Hazardous Comets and Asteroids*. Cambridge University Press, England UK, 2004.
- G Bergstue and R.L Fork. Beamed energy for ablative propulsion in near earth space. In *62nd International Astronautical Congress*, pages 1–9. International Astronautics Federation, 2011.
- G Bergstue and R.L Fork. Advancing the beamed energy ablation driven propulsion engine concept. In *63rd International Astronautical Congress*, pages 1–9. International Astronautics Federation, 2012.
- R Bewick, J.P Sanchez, and C.R McInnes. An l1 positioned dust cloud as an effective method of space-based geoengineering. In *61st International Astronautical Congress*, volume 1, pages 1–16. International Astronautics Federation, 2010.
- R Bewick, J.P Sanchez, and C.R McInnes. Gravitationally bound geoengineering dust shade at the inner lagrange point. *Advanced in Space Research*, 50(10):1405–1410, 2012a.
- R Bewick, J.P Sanchez, and C.R McInnes. The feasibility of using an l1 positioned dust cloud as a method of space-based geoengineering. *Advanced in Space Research*, 49(7): 1212–1228, 2012b.
- R Bewick, J.P Sanchez, and C.R McInnes. Usage of asteroid resources for space-based geoengineering. In V Badescu, editor, *Asteroids: Prospective Energy and Material Resources*, pages 581–603. Springer Berlin Heidelberg, 2013.
- P Bhargava, M Kumar, H Kumar, P Pandit, R Pandey, and A.K Nath. Impulse coupling in laser-driven targets. *Pramana - Journal of Physics*, 62(4):923–932, 2004.
- L Bindi, J.M Eiler, Y Gunn, L.S Hollister, P.J Steinhardt, and N Yao. Evidence for the extraterrestrial origin of a natural quasicrystal. In *Conference Proceedings of the National Academy of Sciences*, volume 109, pages 1396–1401. National Academy of Sciences, 2012.
- R.P Binzel, D.F Lupishko, M.D Martino, R.J Whiteley, and G.J Hahn. The physical properties of near-earth objects. In W.F Bottke, A Cellino, P Paolicchi, and R. P Binzel, editors, *Asteroids III*, pages 255–271. University of Arizona Press, 2004a.
- R.P Binzel, E Perozzi, A Rivkin, A Rossi, A Arris, S Bus, G Valsecchi, and S Slivan. Dynamical and compositional assessment of near-earth object mission targets. *Meteoritics and Planetary Science*, 39:351–366, 2004b.

- A Bogaerts, M Aghaei, D Autrigue, H Lindner, Z Chen, and W Wendelen. Computer simulations of laser ablation, plume expansion and plasma formation. *Advanced Material Research*, 277:1–10, 2011.
- W.L Bohn. Laser lightcraft performance. Proceedings of SPIE 3885 - High Power Ablation II, 2000.
- C Bombardelli and J Pelaez. Ion beam shepherd for contactless space debris removal. *Journal of Guidance, Control and Dynamics*, 34(3):916–920, 2011a.
- C Bombardelli and J Pelaez. Ion beam shepherd for asteroid deflection. *Journal of Guidance, Control and Dynamics*, 34(4):1270–1272, 2011b.
- C Bombardelli, H Urrutxua, M Merino, E Ahedo, J Pelaez, and J Olympio. Dynamics of ion-beam-propelled space debris. In *Conference Proceedings 22nd International Symposium on Space Flight Dynamics Sao Jose dos Campos Brazil*, 2011a.
- C Bombardelli, H Urrutxua, J Peleaz, M Merino, E Ahedo, and L Summerer. Space debris removal with an ion beam shepherd satellite dynamics and control. In *Conference Proceedings of the International Astronautical Congress*, 2011b.
- C Bonanno. An analytical approximation for the moid and its consequences. *Astronomy & Astrophysics*, 360:411–416, 2000.
- P Bousequet, F Flory, and F Roche. Scattering from multilayer thin films theory and experiment. *Optical Society of America*, 71:1115–1123, 1981.
- E Bowell, C.R Chapman, J.C Gradie, D Morrison, and B Zellner. Taxonomy of asteroids. *Icarus*, 35:313–335, 1987.
- I Boxx, C Heeger, R Gordon, B Bohm, M Aigner, A Dreizler, and W Meier. Simultaneous three-component PIVOH-PLIF measurements of a turbulent lifted, C₃h₈-Argon jet diffusion flame at 1.5 kHz repetition rate. *Combustion Institute*, 32:905–912, 2009.
- L Brewer. Thermodynamic properties of the oxides and their vaporization processes. *Chemical Reviews*, 52(1):1–75, 1953.
- W.B Brinckerhoff, G.G Managadze, R.W McEntire, A.F Cheng, and W.J Green. Laser time-of-flight mass spectrometer for space. *Review of Scientific Instruments*, 71(2): 536–545, 2000.
- D.T Britt, D.J Tholen, and J.F Bell. Comparison of asteroids and meteorite spectra: Classification by principal component analysis. *Icarus*, 99:153–166, 1992.
- D.T Britt, K Housen, and G. Consolmagno. Asteroid density, porosity and structure. In W.F Bottke, A Cellino, P Paolicchi, and R. P Binzel, editors, *Asteroids III*, pages 485–500. University of Arizona Press, 2004.
- J.R Brophy and L Friedman. Returning an entire near-earth asteroid in support of human exploration beyond low-earth orbit. In *Global Space Exploration Conference*, pages 1–20. AIAA, 2012a.
- J.R Brophy and L Friedman. Spacecraft conceptual design for returning entire near-earth

- asteroids. In *AIAA/ASME.SAW/ASEE Joint Propulsion Conference and Exhibit*, pages 1–16. AIAA, 2012b.
- J.R Brophy, R Gershman, D Landau, D Yeomans, J Polk, C Porter, W Williams, C Allen, and E Asphaug. Asteroid return mission feasibility. In *AIAA/ASME.SAW/ASEE Joint Propulsion Conference and Exhibit*, pages 1–20. AIAA/ASME/SAE/ASEE, 2011.
- G Brown and C.T Prewitt. High-temperature crystal chemistry of hortonolite. *American Mineralogist*, 58:577–587, 1973.
- I Brown, J.E Lane, and R.C Youngquist. A lunar-based spacecraft propulsion concept - the ion beam sail. *Acta Astronautica*, 60:834–845, 2007.
- J.C Brown, H.E Potts, L.J Porter, and G. Le-Chat. Mass loss, destruction and detection of sun-grazing and impacting cometary nuclei. *Astronomy & Astrophysics*, 535(71): 1–12, 2011.
- A.P Bruckner. The ram accelerator: Overview and state of the art. In K Takayama and A Sasoh, editors, *Ram Accelerators*, pages 3–23. Springer-Verlag, 1998.
- R Brunetto, F Romano, A Blanco, S Fonti, M Martino, V Orofino, and C Verrienti. Space weathering of silicates simulated by nanosecond pulse UV excimer laser. *Icarus*, 180(1):546–554, 2006.
- A.V Bulgakov and N.M Bulgakov. Thermal model of pulsed laser ablation under the conditions of formation and heating of a radiation-absorbing plasma. *Quantum Electronics*, 29(5):433–437, 1999.
- T.H Burbine, T.J McCoy, A Meibom, B Gladman, and K Keil. Meteoritic parent bodies: Their under and identification. In W.F Bottke, A Cellino, P Paolicchi, and R. P Binzel, editors, *Asteroids III*, pages 653–667. University of Arizona Press, 2004.
- S.J Bus and R.P Binzel. Phase ii of the small main-belt asteroid spectroscopic survey: A feature-based taxonomy. *Icarus*, 158:146–177, 2002.
- S.J Bus, F Vilas, and M.A Barucci. Visible-wavelength spectroscopy of asteroids. *Asteroids III*, 1:169–182, 2002.
- E Bussoletti, L Colangeli, J.J Lopez-Moreno, E Epifani, and V Mennella. The giada experiment for the rosetta mission to comet 46p/wirtanen: Design and performance. *Advances in Space Research*, 24(9):1139–1148, 1999.
- J Campbell, C Phipps, L Smalley, J Reilly, and D Boccio. The impact imperative - laser ablation for deflecting asteroids, meteoroids and comets from impacting the earth. In *First International Symposium on Beamed Energy Propulsion*, pages 1–25. Huntsville Alabama, 2002.
- J.W Campbell. Project orion: Orbital debris removal using ground-based sensors and lasers. NASATM 108522, 1996.
- J.W Campbell. Using lasers in space - laser orbital debris removal and asteroid deflection. Occasional Paper No 20, Centre for Strategy and Technology, Air War College, 2000.

- G.H. Canavan. Laser deflection of space objects - an overview. In *International Conference on Lasers and Applications*, pages 1–11. Portland, USA, 1996.
- A. Carusi, G.B. Valsecchi, G. D’Abramo, and A. Boattini. Deflecting neos in route of collision with the earth. *Icarus*, 159:417–422, 2002.
- C.R. Chapman. S-type asteroids, ordinary chondrites, and space weather: The evidence from galileo’s flybys of gaspra and ida. *Meteoritics & Planetary Science*, 31:669–725, 1996.
- N.H. Chen. Simplified solution for ablation in a finite slab. *AIAA*, 3(6):1148–1149, 1965.
- P.T. Chen, N.D. Abe, C.R. Mullen, and C.C. Gilbert. Contamination sensitivity and control of optical sensors. *SPIE Optical System Contamination Effects Measurement Control*, 777:97–126, 1987.
- P.T. Chen, R.J. Hedgeland, and S.R. Thomson. Surface accommodation of molecular contaminants. *SPIE - Optical System Contamination: Effects, Measurement, Control II*, 1329:327–336, 1990.
- A.F. Cheng. Collisional evolution of the asteroid belt. *Icarus*, 169:357–372, 2004.
- S. Chesley. Potential impact detection for near-earth asteroids: The case of 99942 apophis (2004 mn4). In S. Ferraz-Mello and D. Lazzaro, editors, *Asteroids, Comets and Meteors*, pages 215–218. Cambridge University Press, 2006.
- S.R. Chesley and T.B. Spahr. Earth impactors: orbital characteristics and warning times. In M.J. Belton, T.H. Morgan, N. Samarasinha, and D.K. Yeomans, editors, *Mitigation of Hazardous Comets and Asteroids*, pages 22–37. Cambridge University Press, 2004.
- S.R. Chesley, P.W. Chodas, A. Milani, G. Valsecchi, and D. Yeomans. Quantifying the risk posed by potential earth impacts. *Icarus*, 159:423–432, 2002.
- S.R. Chesley, J.O. Elliot, P.A. Abell, E. Asphaug, S. Bhaskaran, T. Lam, and D.S. Lauretta. The ISIS mission concept: An impactor for surface and interior science. In *IAA Planetary Defense Conference*, volume 1, pages 1–7. International Academy of Astronautics, 2013.
- B.E. Clark, B. Hapke, C. Pieters, and D. Britt. Asteroid space weathering and regolith evolution. In W.F. Bottke, A. Cellino, P. Paolicchi, and R. P. Binzel, editors, *Asteroids III*, pages 585–599. University of Arizona Press, 2004.
- C. Clauser and E. Huenges. Thermal conductivity of rocks and minerals. In T.J. Ahrens, editor, *Rock Physics and Phase Relations: A Handbook of Physical Constants*, pages 105–126. American Geophysical Union, 1995.
- L. Colangeli, J.J. Lopez-Moreno, P. Palumbo, J. Rodriguez, E. Bussoletti, V. Della-Corte, F. Esposito, M. Herranz, J.M. Jeronimo, A. Lopez-Jimenez, M. Epofani, R. Morales, E. Palomba, and A. Rotundi. Giada: The grain impact analyser and dust accumulator for the rosetta space mission. *Advances in Space Research*, 39:446–450, 2007.
- C. Colombo and C. McInnes. Orbital dynamics of smart dust devices with solar radiation pressure and drag. *Journal of Guidance, Control and Dynamics*, 6:1613–1631, 2011.

- C Colombo, M Vasile, and G Radice. Semi-analytical solution for the optimal low-thrust deflection of near-earth objects. *Journal of Guidance, Control and Dynamics*, 32(3): 796–809, 2009.
- B.A Conway. Near-optimal deflection of earth-approaching asteroids. *Guidance, Control and Dynamics*, 24(5):1035–1037, 2001.
- G.B Courreges-Lacoste, B Ahlers, E Bosloper, F Rull-Perez, and S Maurice. Combined raman spectrometer/laser-induced breakdown spectrometer design concept. In *6th International Conference on Space Optics*, pages 1–6. ESTEC, 2006.
- J.F Crifo. A general physicochemical model of the inner coma of active comets. i implications of spatially distributed gas and dust production. *Astrophysical Journal*, 445:470–488, 1995.
- J.P Cummings and J.T Walsh. Tissue tearing caused by pulsed laser-induced ablation pressure. *Applied Optics*, 32:494–503, 1993.
- V.A David, B Gardner, I Katz, and D Brinza. Predictions of NSTAR charge exchange ions and contamination backflow. In *Conference Proceedings of International Electric Propulsion Conference*, 1997.
- M Delbo, A Cellino, and E Tedesco. Albedo and size determination of potentially hazardous asteroids: (99942) apophis. *Icarus*, 188:266–269, 2007.
- V Della-Corte, M Accolla, M Ferrari, S Ivanovski, F Lucarelli, E Epifani, F.J.M Rietmeijer, R Sordini, and A Rotundi. GIADA (grain impact analyser and dust accumulator) prepares for the comet 67p/churyumov-gerasimenko encounter. *European Planetary Science Congress*, 12:1–2, 2012.
- K Demyk, E Dartois, H Wesemeyer, A.P Jones, and L D’Hendecourt. Structure and chemical composition of the silicate dust around OH/ICH stars. *Astronomy and Astrophysics*, 364:170–178, 2000.
- G Dettleff. Plume flow and plume impingement in space technology. *Aerospace Science*, 28:1–71, 1991.
- F Dimroth, W Guter, J Schane, E Welser, M Steiner, E Oliva, A Wekkeli, G Siefer, SP Philipps, and AW Bett. Metamorphic gainp/gainas/ge triple-junction solar cells with greater than 41 & efficiency. In *34th IEEE Photovoltaic Specialists Conference*, pages 1933–1937. IEEE, 2009.
- T Vladimirova D.J Barnhart and M Sweeting. Very-small-satellite design for distributed space mission. *Journal of Spacecraft and Rockets*, 44:1294–1306, 2007.
- K Domen and T.J Chuang. Laser induced photodissociation and desorption. ii. ch₂i₂ adsorbed on ag. *Journal of Chemistry Physics*, 90:3332–3338, 1989.
- H Dursch, G Bohnhoff-Hlavacek, D Blue, and P Hansen. Analysis of systems hardware flown on ldef: New findings and comparison to other retrieved spacecraft hardware. *Spacecraft Design, Testing and Performance*, 1995.

- R.K Dwivedi and R.K Thareja. Optical emission diagnostics of c60-containing laser-ablated plumes for carbon film deposition. *Physical Review B*, 51(11):7160–7167, 1995.
- J.T Early, C Bibeau, and C Phipps. Space debris de-orbiting by vaporization impulse using short pulse laser. In *Proceeding of SPIE 5448*, pages 441–449, 2004.
- G.E Elsinga, F Scarano, B Wieneke, and B.W Van-Oudheusden. Tomographic particle imaging velocimetry. *Experimental Fluids*, 41:933–947, 2006.
- M Elvis. Prospecting asteroid resources. In V Badescu, editor, *Asteroids: Prospective Energy and Material Resources*, pages 81–130. Springer Berlin Heidelberg, 2013.
- E.M Epifani, E Bussolletti, L Colangeli, P Palumbo, A Rotundi, S Vergara, J.M Perrin, J.J.L Moreno, and I Olivares. The grain detection system for the giada instrument design and expected performance. *Advances in Space Research*, 29(8):1165–1169, 2002.
- S.J Espinasse, J Klinger, and B Schmitt. Modelling of the thermal behavior and the chemical differentiation of cometary nuclei. *Icarus*, 92:35–365, 1991.
- F Esposito, L Colangeli, D Corte, and P Palumbo. Physical aspects of an impact sensor for the detection of cometary dust momentum onboard the rosetta space mission. *Advances in Space Research*, 29(8):1159–1163, 2002.
- F.H Fabreguette, Z.A. Sechrist, J.W Elam, and S.M. George. Quartz crystal microbalance study of tungsten atomic layer deposition using wf6 and si2h6. *Icarus*, 488(1):103–110, 2005.
- J Farquhar and D Rumble. Comparison of oxygen isotope data obtained by laser fluorination of olivine with krf excimer laser and co2 laser. *Geochimica et Cosmochimica Acta*, 62(18):3141–3149, 1998.
- A Fernandez, X.L Mao, W.T Chan, A Shannon, and E.R Russo. Correction of spectral emission intensity in the inductively coupled plasma and laser-induced plasma during laser ablation of solid samples. *Analytical Chemistry*, 67:2444–2450, 1995.
- B Fitton and G Seibert. A world without gravity. *ESA Publication*, 1:1–50, 2001.
- R Fork. Preventing asteroid earth impacts with laser technology: Progress and prospects. *IEEE*, 85:847–848, 2007.
- A Fujiwara, J Kawaguchi, D Yeomans, M Abe, T Mukai, T Okada, J Saito, H Yano, M Yoshikawa, D Scheeres, O Barnouin-Iha, A Cheng, H Demura, R Gaskell, N Hirata, H Ikeda, T Kominato, H Miyamoto, and A Nakamura. The rubble-pile asteroid itokawa as observed by hayabusa. *Science*, 312:1330–1334, 2006.
- M.J Gaffey, E.A Cloutis, M.S Kelly, and K.L Reed. Mineralogy of asteroids. In W.F Bottke, A Cellino, P Paolicchi, and R. P Binzel, editors, *Asteroids III*, pages 183–204. University of Arizona Press, 2004.
- B Ganapathisubramani, K Lakshminarasimhan, and N.T Clemens. Determination of complete velocity gradient tensor by using cinematographic stereoscopic PIV in a turbulent jet. *Experimental Fluids*, 42:923–939, 2007.

- D Garcia-Yarnoz, J.P Sanchez, and C.R McInnes. Easily retrievable objects among the NEO population. *Celestial Mechanics and Dynamical Astronomy*, 116:367–388, 2013.
- J Gattacceca, P Rochette, and M Bourot-Denise. Magnetic properities of a freshly fallen LL ordinary chondrite: The Bensour meteorite. *Physics of the Earth and Planetary Interiors*, 140:343–358, 2003.
- A Ghost and HY McSween. Temperature dependence of specific heat capacity and its effects on asteroid thermal models. *Meteoritics and Planetary Science*, 34:121–127, 1999.
- A Gibbings and M Vasile. Impact cratering experiments into highly porous bodies. In *IAA Planetary Defense Conference Proceedings*, pages 1–8. International Academy of Astronautics, 2011.
- A Gibbings and M Vasile. Smart swarm to deflect killer asteroids. *New Scientist*, 2863:14, 2012a.
- A Gibbings and M Vasile. A smart cloud approach to asteroid deflection. In *Conference Proceedings 62nd International Astronautical Congress*, volume 1, pages 1–14. International Astronautics Federation, 2012b.
- A Gibbings, E Komninou, and M Vasile. Large scale impact cratering onto highly porous asteroidal bodies. Final Experiment Report (Team No 1294), ESA Education Office Spin Your Thesis Campaign, 2010.
- A Gibbings, E Komninou, and M Vasile. Investigation and modelling of large scale cratering events - lessons learnt from experimental analysis. In *62nd International Astronautical Congress*, pages 1–7. International Astronautics Federation, 2011a.
- A Gibbings, M Vasile, J-M Hopkins, and D Burns. On testing laser ablation processes for asteroid deflection. In *IAA Planetary Defense Conference Proceedings*, volume 1, pages 1–8. International Academy of Astronautics, 2011b.
- A Gibbings, M Vasile, F Zuiani, and E Komninou. Experiment safety data package - experimental investigation of laser momentum coupling and ejecta plume formation. Fly Your Thesis 2011 Engineering Proposal, 2011c.
- A Gibbings, M Vasile, F Zuiani, and E Komninou. Asteroid ablation - experimental investigation of laser momentum coupling and ejecta plume formation. Fly Your Thesis 2011 Scientific Proposal, 2011d.
- A Gibbings, M Vasile, J-M Hopkins, D Burns, and I Watson. Potential of laser-induced ablation for future space applications. *Space Policy*, 283(3):149–153, 2012.
- A Gibbings, M Vasile, I Watson, J-M Hopkins, and D Burns. Experimental analysis of laser ablated plumes for asteroid deflection and exploitation. *Acta Astronautica*, 90(1):85–97, 2013.
- M Granvik, J Vaubaillon, and R Jedicke. The population of natural earth satellites. *Icarus*, 218:262–277, 2011.

- R.A Grieve and E.M Shoemaker. The records of past impacts on earth. In T Gehrels, editor, *Hazardous due to comets and asteroids*, pages 417–462. University of Arizona Press, 1994.
- C Gritzner and R Kahle. Mitigation technologies and their requirements. In M.J Belton, T.H Morgan, N Samarasinha, and D.K Yeomans, editors, *Mitigation of Hazardous Comets and Asteroids*, pages 167–200. Cambridge University Press, 2004.
- C.H Gritzner, R Kahle, and S Fasoulas. Solar concentrators for neo deflection. In *Proceedings of Asteroids, Comets and Meteors*, pages 67–70. Asteroids, Comets and Meteors Conference, 2002.
- G.F Gronchi and A Milani. Proper elements for earth crossing asteroids. *Icarus*, 152: 58–69, 2001.
- E Grun, H Kochan, K Roessler, and D Stoeffler. Simulation of cometary nuclei. In *International Symposium on the Diversity and Similarity of Comets Conference Proceedings*, volume 1, pages 501–508. European Space Agency, 1987.
- E Grun, H Kochman, and K.J Seidensticker. Laboratory simulations, a tool for comet research. *Geophysics Letters*, 18:245–248, 1991.
- E Grun, J Gebhard, A Bar-Nun, J Benkhoff, H Duren, G Eich, R Hische, W.F Huebner, H.U Keller, G Klees, H Kochan, G Kolzer, H Kroker, E Kuhrt, P Lammerzahl, E Lorenz, W.J Markiewicz, D Mohlmann, A Oehler, J Scholz, K.J Seidensticker, K Roessler, G Schwehm, G Steiner, K Thiel, and H Thomas. Development of dust mantle on the surface of an isolated ice-dust mixture: results from the KOSI-1 experiment. *Geophysical Research*, 98(E8):15091–15104, 1993.
- J Grun and B.H Ripin. Ballistic pendula for measuring the momentum of a laser-produced plasma. *Review of Science Instruments*, 53(12):1878–1881, 1982.
- A.V Gusarov, A.G Gnedovets, and I Smurov. Gas dynamics of laser ablation: Influence of ambient atmosphere. *Journal of Applied Physics*, 88(7):4352–4364, 2000.
- C.D Hall and I.M Ross. Dynamics and control problems in the deflection of near-earth objects. In *AAS/AIAA Astrodynamics Specialist Conference*, 1997.
- D.F Hall, T.B Stewart, and R.R Hayes. Photo-enhanced spacecraft contamination deposition. AIAA Paper 85-0953 20th Thermo physics Conference, 1985.
- O Hamberg and F.D Tomlinson. Sensitivity of thermal surface solar absorptance of particulate contamination. AIAA Paper 71-473 6th Thermo physics Conference, 1971.
- P Hammerling and J.L Remo. Neo interaction with nuclear radiation. *Acta Astronautica*, 36(6):337–356, 1995.
- A Harris. A global approach to near-earth object impact threat mitigation conference. In *Planetary Deference Conference*,, page 1. AIAA, 2011.
- A.W Harris. The rotation rates of very small asteroids: Evidence for rubble pile structure. *Lunar and Planetary Science*, 27:493–494, 1996.

- A.W Harris. Scientific requirements for understanding the near-earth asteroid population. In M.J Belton, T.H Morgan, N Samarasinha, and D.K Yeomans, editors, *Mitigation of Hazardous Comets and Asteroids*, pages 141–152. Cambridge University Press, 2004.
- A.W Harris and P Pravec. Rotational properties of asteroids, comets and TNOs. In *Asteroids, Comets, Meteors - IAU Symposium No 229*, pages 439–447. International Astronomical Union, 2006.
- A.W Harris, E. G Fahnestock, and P Pravec. On the shapes and spins of rubble piles asteroids. *Solar System Bodies: From Optics to Geology*, 2008.
- A.W Harris, M.A Barucci, J.L Canocand A Fitzsimmons, M Fulchignoni, S.F Green, D Hestroffer, V Lappas, W Lork, P Micheli, D Morrison, D Payson, and F Schafer. The european union funded neoshield project: A global approach to near-earth object impact threat mitigation. *Acta Astronautica*, 90(21):80–84, 2013.
- A Hashimoto. Evaporation metamorphism in the early solar nebula - evaporation experiments on the melt feo-mgo-sio2-cao-al203 and chemical fractiontions of primitive materials. *Geochemical Journal*, 17:111–145, 1982.
- A Hashimoto. Evaporation kinetics of forsterite and implications for the early solar nebula. *Nature*, 347:53–55, 1990.
- Z He, J Wu, and D Zhang. Trajectory optimisation of ground based laser launch for two launch schemes. In *62nd International Astronautical Congress*, pages 1–7. International Astronautics Federation, 2011.
- A Hertzberg, A.P Bruckner, and D.W Bogdaboff. Ram accelerator a chemical method for accelerating projectiles to ultra high velocities. *AIAA*, 26:195–203, 1988.
- J.G Hills. Capturing asteroids in bound orbits around the earth: Massive early return on an asteroid terminal deflection system. In *Near Earth Object Interception Workshop*, pages 928–934. Workshop Proceedings, 1992.
- K.A Holsapple. About deflecting asteroids and comets. In M.J Belton, T.H Morgan, N Samarasinha, and D.K Yeomans, editors, *Hazards due to Comets and Asteroids*, pages 113–140. Cambridge University Press, 2004.
- K.A Holsapple. Spin limits of solar system bodies: From the small fast rotators to 2003 el61. *Icarus*, 187:500–509, 2007.
- H Horisawal, S Hagiwara, and I Funaki. Micro-multi-plasmajet array thrust. In *46th Joint Propulsion Conference and Exhibit*, 2010.
- K Housen and K Holspple. Momentum transfer via direct impact: Experimental measurements. In *IAA Planetary Defense Conference Proceedings*, volume 1, pages 1–7. International Academy of Astronautics, 2013.
- K.R Housen. Collisional fragmentation of rotating bodies. Lunar and Planetary Science XXXV Extended Abstract, 2004.

- K.R Housen. Material characterisation - highly porous bodies. Personal Communication, 2010.
- K.R Housen and K.A Holsapple. Compaction as the origin of the unusual craters on the asteroid mathilde. *Nature*, 402:155–157, 1999.
- K.R Housen and K.A Holsapple. Impact cratering on porous asteroids. *Icarus*, 163: 102–119, 2003.
- W.F Huebner and J.M Greenberb. Needs for determining material strengths and bulk properties of neos. *Planetary and Space Science*, 48:797–799, 2000.
- W.F Huebner and J.M Greenberg. Methods of determining strength and bulk properties of neos. *Advanced Space Research*, 28:1129–1137, 2001.
- V.V Ivashkin. Possibilities of using laser action in a celestial body approaching the earth. *Physics*, 49:476–479, 2004.
- D Izzo, C Negueruela, F Ongaro, and R Walker. Strategies for near earth object impact hazard mitigation. Advanced Concepts Team, European Space Agency, 2005.
- D Izzo, A Bourdoux, R Walker, and F Ongaro. Optimal trajectories for the impulsive deflection of near earth objects. *Acta Astronautica*, 59:294–300, 2006.
- N.A Johnson. Evolution of the artificial earth satellite environment. In J.P Loftus, editor, *Orbital Debris from Upper Stage Break-up*, page 15. Progress in Astronautics and Aeronautics 121, 1989.
- R Johnson and D Holbrow. Space settlements, a design study. NASA Report SP-413, 1977.
- H.S Judeikis, G.S Arnold, R.C Young-Owl, and D.F Hall. Design of a laboratory study of contaminant film darkening in space. Aerospace Report No. TR-94(4935)-3, 1993.
- R Kahle, E Kuhrt, G Hahn, and J Knollenberg. Physical Limits of Solar collectors in deflecting earth-threatening asteroids. *Aerospace Science and Technology*, 10:256–263, 2006.
- A Kantrowitz. A propulsion to orbit by ground based lasers. *Astronautics and Aeronautics*, 10(5):74–76, 1972.
- J.S Kargel. Matalliferous asteroids as potential sources of precious metals. *Geophysical Research*, 99(10):21129–21141, 1994.
- J Kawaguch, K Uesugi, and A Fujiwara. The muses-c mission for the sample and return - its technology development status and readiness. *Acta Astronautica*, 52:2–6, 2003.
- H.U Keller. Comets - dirty snowballs or ice dirtballs? In *International Workshop on Physics and Mechanics of Cometary Materials Proceedings*, volume 1, pages 39–45. European Space Agency SP-302, 1989.
- R Kelly and A Miotello. Comments on explosive mechanisms of laser sputtering. *Applied Surface Science*, 96:205–215, 1996.

- D.J Kessler. Current orbital debris environment. In J.P Loftus, editor, *Orbital Debris for Upper-Stage Break-up*, pages 3–15. Progress in Astronautics and Aeronautics, 1989.
- D.J Kessler and B.G Cour-Palais. Collision frequency of artificial satellites: The creation of a debris belt. *Geophysical Research*, 83(6):2637–2646, 1978.
- W Ketren, P Vallikul, A Garo, and G Grehan. Numerical simulations on effects of laser fluence on temporal and time integrated lii-process of soot particles. *Sustainable Energy and Environment*, 1:173–179, 2010.
- H Kimura, I Mann, and E.K Jessberger. Dust grains in the comae and tails of sungrazing comets: Modeling of their mineralogical and morphological properties. *Icarus*, 159: 529–541, 2002.
- S Kitamura. Large space debris reorbiter using ion beam irradiation. In *Conference Proceedings of the International Astronautical Congress*, 2010.
- C.J Knight. Theoretical modeling of rapid surface vaporisation with back pressure. *AIAA*, 15(5):519–523, 1979.
- M Knudsen. Die molekularstrmung der gase durch ffnungen und die effusion. *Annalen der Physik*, 28:999–1016, 1909.
- J Koenig and C Chyba. Impact deflection of potentially hazardous asteroids using current launch vehicles. *Science and Global Security*, 15:57–83, 2007.
- N.I Komle. Jet and shell structure in the cometary coma: modelling and observations. In J.W Mason, editor, *Comet Halley: Investigations, Results, Interpretations*, pages 232–243. Chichester Ellis Horwood, 1990.
- N.I Komle, G Dettleff, and C Dankert. Thermal behaviour of pure and dusty ices on comets and icy satellites. *Astronomy & Astrophysics*, 227:246–254, 1990a.
- N.I Komle, Steiner G, Dankert C, Dettleff G, H Hellmann, H Kochan, M Baguhl, H Kohl, G Kolzer, and K Thiel. Ice sublimation below artificial crusts: results from comet simulation experiments. *Planet Space Science*, 39(3):515–524, 1990b.
- D.G Korycansky and E Asphaug. Low-speed impacts between rubble pile modelled as collections of polyhedra. *Icarus*, 181:605–617, 2006.
- D Koschny, A Barucci, M Yoshikawa, H Bhnhardt, J Brucato, M Coradini, E Dotta, I Franhi, S Green, J-L Josset, J Kawaguchi, P Michel, K Muinonen, J Oberst, H Yano, R Binzel, D Agnolon, and J Romstedt. Marco polo - a mission to return a sample from a near earth object - science requirements and operational scenarios. In *27th International Symposium on Space Technology and Science*, volume 1, pages 1–7. Japan Society for Aeronautical and Space Sciences, 2009.
- K.J Kossacki, N.I Komle, J Leliwa-Kopystynski, and G Karg. Laboratory investigation of the evolution of cometary analogs: Results and interpretation. *Icarus*, 128:127–144, 1997.
- D.J Krajnovich. Laser sputtering of highly oriented pyrolytic graphite at 248 nm. *Chemical Physics*, 726:541–546, 1995.

- E Kuhrt, U Keller, and E Lorenz. Interpretation of surface temperatures and activity of KOSI samples. *Planetary Space Science*, 43(3/4):333–340, 1995.
- S Kuper, J Brannon, and K Brannon. Threshold behavior in polyimide photoablation: Single-shot rate measurements and surface-temperature modeling. *Applied Physics A*, 56:43–50, 1992.
- S Kurosaw, H Aizaw, J Miyake, M Yoshimoto, J Hilborn, and Z.A Taliba. Detection of deposition rate of plasma-polymerized silicon-containing films by quartz crystal microbalance. *Thin Solid Films*, 407(1):1–6, 2002.
- T Kwiatkowski, A Kryszczyńska, M Polinska, D.A.H Buckley, D O’Donoghue, P.A Charles, L Crause, S Crawford, Y Hashimoto, A Kniazev, N Loaring, E.R Colmenero, R Sefako, M Still, and P Vaisanen. Photometry of 2006 rh120: An asteroid temporary captured into a geocentric orbit. *Astronomy and Astrophysics*, 495:967–974, 2009.
- G.A Landis. Prospects for solar pumping semiconductor lasers. *Laser Power Beaming SPIE*, 2121:58–65, 1994.
- M Lando, J Kagan, B Linkekin, and V Dobrusin. A solar pumped nd:yag laser in the high collection efficiency regime. *Optics Communications*, 222:371–381, 2003.
- R.J Lawrence. Enhanced momentum transfer for hypervelocity impacts. *International Journal of Impact Engineering*, 10:337–349, 1990.
- M.R Lee, C.L Smith, S.H Gordon, and M.E Hodson. Laboratory simulation of terrestrial meteorite weathering using the Bencourt (ll6) ordinary chondrite. *Meteoritics & Planetary Science*, 41:1–16, 2006.
- W.J Lees, N Chabot, D Persons, and T Hartka. Small body sampling techniques being developed at Johns Hopkins University Applied Physics Laboratory. In *57th International Astronautical Congress*, volume 1, pages 1–12. International Astronautics Federation, 2006.
- M.R Leese, J.A.M McDonnell, M.J Burchell, S.F Green, H.S Jolly, P.R Ratcliff, and H.A Shaw. Debie - a low resource dust environment monitor. In *Symposium on Space Station Utilisation*, volume 1, pages 417–420. ESA, 1999.
- H Legge and R.D Boettcher. Modelling control thruster plume flow and impingement. In *13th International Symposium on Rarefield Gas Dynamics*, 1982.
- A Lenk and T Witke. In situ investigation of laser ablation. *Analytical Chemistry*, 353:333–336, 1995.
- A Lenk, B Schultrich, and T Witke. Diagnostics of laser ablation and laser induced plasmas. *Applied surface science*, 106:473–477, 1996.
- A Lenk, B Schultrich, T Witke, and H.J Weib. Energy and particle fluxes in PLD processes. *Applied Surface Science*, 109(110):419–423, 1997.
- J Leonard. Project echo - results. *Astronautics*, 1961.
- H.G Lewis, A Saunders, G Swinerd, and R.J Newland. Effects of thermosphere

- contraction on remediation of the near-earth space debris environment. *Journal of Geophysical Research*, 116:1–10, 2011.
- J.S Lewis. Platinum apples of the asteroids. *Nature*, 372:499–500, 1994.
- J.S Lewis. *Mining the Sky: Untold Riches from the Asteroids, Comets and Planets*. Helix Books, New York, USA, 1996.
- J Lin and A.V Pakhomov. Angular distribution of plasma edge velocity and integrated intensity: updated on specific impulse for ablative laser propulsion. In *Third International Symposium on Beamed Energy Propulsion*, pages 414–422. Beamed Energy Propulsion, 2005.
- J Lindgrad and K Jonansen. Production and testing of concrete with high specific heat. Proceedings of the International RILEM Conference, 1996.
- J.C Liou. A parametric study on using active debris removal for leo environment remediation. In *61st International Astronautical Congress*, pages 1–11. International Astronautics Federation, 2010.
- J.C Liou. An active debris removal parameteric study for leo environment remediation. *Advances in Space Research*, 47(11):1865–1876, 2011.
- J.C Liou and N.A Johnson. Instability of the present leo satellite populations. *Advanced Space Research*, 41:1046–1053, 2008.
- J.C Liou and N.A Johnson. Sensitivity study of the effectiveness of active debris removal in leo. *Acta Astronautica*, 64:236–243, 2009.
- D.H Lowndes. Growth and doping of compound semiconductor film by pulsed laser ablation. In J.C Miller and R.F Haglund, editors, *Laser Ablation and Desorption Experimental Methods in the Physical Sciences*, volume 30, pages 475–571. Academic Press, New York, 1998.
- E Lu and S Love. Gravitational tractor for towing asteroids. *Nature*, 438:177–178, 2005.
- D.A Lunan. Need we protect earth from space objects and if so, how? *Space Policy*, 8: 90–91, 1992a.
- D.A Lunan. Nasa considers asteroid threat space policy. *Space Policy*, 8:336, 1992b.
- C Ma, O Tschauner, J.R Beckett, G.R Rossman, and W Liu. Panguite (ti₄+, sc, al, mg, zr, ca) 1.8o₃, a new ultra-refractory titania mineral from the allende meteorite: Synchrotron micro-diffusion and ebsd. *American Mineralogist*, 97(1):12191225, 2012.
- C Maddock, J.P. Sanchez-Cuartielles, M Vasile, and G Radice. Comparison of single and multi-spacecraft configurations for nea deflection by solar sublimation. In *New Trends in Astrodynamics and Applications III*, pages 303–316. American Institute of Physics, 2007.
- C.M Maddock, M Vasile, and C McInnes. Design of a multi-spacecraft swarm for the deflection of apophis by solar sublimation. In *Planetary Deference Conference*, pages 1–5. AIAA, 2009.

- M.M. Marinova, O. Aharonson, and E. Asphaug. Geophysical consequences of planetary-scale impacts into a mars-like planet. *Icarus*, 211:519–523, 2011.
- D. Marla, U.V. Bhandarkar, and S.S. Joshi. Critical assessment of the issues in the modelling of ablation and plasma expansion processes in the pulse laser deposition of metals. *Applied Physics*, 109:1–16, 2011.
- J. Mason, J. Stupl, W. Marshall, and C. Levit. Orbital debris-debris collision avoidance. *Advanced in Space Research*, 48(10):1643–1655, 2011.
- S. Matteson. Particulate contamination in atomic and molecular-beam deposition system. *Vacuum Science and Technology A - Vacuum, Surfaces and Films*, 6(4):2504–2507, 1988.
- L.S. Mayboudi. Heat transfer modelling and thermal imaging experiments in laser transmission welding of thermoplastics. Phd thesis, Queens University, Kingston, Canada, 2008.
- D. Mazanek. Comet/asteroid protection system: Concept study executive summary. In D. Mazanek, C.M. Roithmayr, J. Antol, S-Y. Park, R.H. Koons, J.C. Bremer, D.G. Murphy, J.A. Hoffman, R.R. Kumar, H. Seywald, L. Kay-Bunnell, M.R. Werner, M.A. Hausman, and J.L. Stokum, editors, *Comet/Asteroid Protection System: Preliminary Space-based System Concept and Study Results*, pages 1–11. NASA/TM-2005-213758, 2005.
- D. Mazanek, C. Roithmayr, J. Antol, L. Kay-Bunnell, M. Werner, S. Park, and R. Kumar. Comet/Asteroid Protection System: A space-based system concept for revolutionizing earth protection and utilization of near-earth objects. In *53rd International Astronautics Congress*, pages 1–18. International Astronautics Federation, 2002.
- D. Mazanek, C.M. Roithmayr, J. Antol, L. Kay-Bunneh, M.R. Werner, S-Y. Park, and R.R. Kumar. Comet/asteroid protection system (CAPS: A space-based system concept for revolutionizing earth protection and utilization of near-earth objects. *Acta Astronautica*, 53:405–422, 2003.
- D.D. Mazanek, J.R. Brophy, and R.G. Merrill. Asteroid retrieval mission concept - trailblazing our future in space and helping to protect us from earth impactors. In *IAA Planetary Defense Conference Proceedings*, volume 1, pages 1–16. International Academy of Astronautics, 2013.
- C.R. McInnes. Deflection of near-earth asteroids by kinetic energy impacts from retrograde orbits. *Planetary and Space Science*, 52:587–590, 2004.
- T. Meier, B. Treffler, and L. Weber. Spatial distribution of plume and particulate debris during laser tissue ablation. In *Proceeding of SPIE 2323 380*, pages 441–449, 1995.
- H.J. Melosh. Asteroid deflection: The mirror ablation approach. In *Proceedings of Planetary Defence Conference*, pages 407–411. AIAA, 2004.
- H.J. Melosh and I.V. Nemchinov. Solar asteroid diversion. *Nature*, 336:21–22, 1993.
- H.J. Melosh, I.V. Nemchinov, and Y.I. Zetzer. Non-nuclear strategies for deflecting comets

- and asteroids. In T Gehrels, editor, *Hazards due to Comets and Asteroids*, pages 1111–1132. University of Arizona Press, 1994.
- M. Merino, E Ahedo, C Bombardelli, H Urrutxua, J Pelaez, and L Summerer. Space debris removal with an ion beam shepherd satellite: Target-plasma interaction. In *47th Joint Propulsion Conference and Exhibit San*, pages 1–13. AIAA/ASME/SAE/ASEE, 2011.
- P Michel and M Jutzi. Final report - determination of asteroid fragmentation energy from an impactor and post-fragmentation dynamics. ESA Call for Ideas: NEO Encounter 2029, 2009.
- T Michukami, K Moriguchi, S Hasegawa, and A Fujiwara. Ejecta velocity distribution for impact cratering experiments on porous and low strength targets. *Planetary and Space Science*, 55:70–88, 2007.
- A Milani, G Valsecchi, P Paolicchi, P Lognonne, W Benz, R Foerstner, M Bello, J Gonzalez, and A Galvez. Near earth objects space mission preparation: Don quijote mission executive summary. ESA Study Contract NEO-DMS-EXS, 2003.
- A Milani, S.T Chesley, P Chodas, and G.B Valsecchi. Asteroid close approaches: Analysis and potential impact detection. In W Bottke, A Cellino, P Paolocchi, and R.P Binzel, editors, *Asteroids III*, pages 55–69. University of Arizona Press, 2004.
- R Mink, B Boynton, D Lauretta, B Sutter, B Bierhaus, and J Russell. OSIRIS-REx mission design to return a sample from asteroid 1999 rq36. In *IAA Planetary Defense Conference Proceedings*, volume 1, pages 1–8. International Academy of Astronautics, 2013.
- D Mohlmann. Cometary activity and nucleus modelling: a new approach. *Planet Space Science*, 44(6):541–546, 1996.
- L.V Moroz, A.V Fisenko, L.F Semjonova, C.M Pieters, and N.N Korotaeva. Optical effects of regolith processes on s-asteroids as simulated by laser shots on ordinary chondrite and other mafic materials. *Icarus*, 122(13):366–382, 1996.
- D Morrison. The spaceguard survey. In *Conference Proceedings NASA International Near Earth Object Detection Workshop*, 1992.
- D Morrison. The spaceguard survey: Report of the nasa international near-earth-object detection workshop. Technical report, NASA, 2007.
- D Morrison, C Chapman, and P Slovic. The impact hazard. In T Gehrels, editor, *Hazardous due to comets and asteroids*, pages 59–91. University of Arizona Press, 1994.
- D Morrison, A.W Harris, G Sommer, C.R Chapman, and A Carusi. Dealing with the impact hazard. In W.F Bottke, A Cellino, P Paolicchi, and R. P Binzel, editors, *Asteroids III*, pages 739–754. University of Arizona Press, 2004.
- T Moscicki, J Hoffman, and Z Szymanski. Laser ablated carbon plume: experiment and modelling. *NUKLEONIKA*, 57(2):283–286, 2012.

- M Mueller, M Delbo, J.L Hora, D.E Trilling, B Bhattacharya, W.F Bottke, S Chesley, J.P Emery, G Fazio, A.W Harris, A Mainzer, M Mommert, B Penprase, H.A Smith, T.A Spahr, J.A Stansberry, and C.A Thomas. ExploreNEOs iii physical characterisation of 65 potential spacecraft target asteroids. *The Astronomical Journal*, 141(109):1–9, 2011.
- T.G Muller, T Sekiguchi, M Kaasalainen, M Abe, and S Hasegawa. Itokawa: The power of ground-based mid-infrared observations. In *IAU Symposium Near Earth Objects, Our Celestial Neighbours: Opportunity and Risk*, volume 236, pages 261–266. International Astronomical Union, 2007.
- L.N Myrabo. Transatmospheric laser propulsion - final technical report. Prepared under contract No 2073803 for Lawrence Livermore Laboratory and the SDIO Laser Propulsion Program, 1989.
- L.N Myrabo. Ground and flight tests of a laser propelled vehicle. In *36th Aerospace Sciences Meeting & Exhibit*, pages 1–25. AIAA, 1998.
- L.N Myrabo. World recordflights of beam-riding rocket lightcraft: demonstration of disruptive propulsion technology. In *37th AIAA/ASME/SAE/ASEE Joint Propulsion Conference - AIAA Paper 2001-3798*, pages 1–25. AIAA/ASME/SAE/ASEE, 2001.
- H Nagahara, I Kushiro, H Mori, and B.O Mysen. Experimental vaporisation and condensation of olivine solid solution. *Nature*, 331:516–518, 1988.
- H Nagahara, I Kushiro, and B.O Mysen. Olivine at low pressures and its implications for the origin of chondrules. In *Lunar Planetary Science Conference Proceedings XXIII*, volume 1, pages 959–960. Lunar and Planetary Institute, 1992.
- H Nagahara, I Kushiro, and B.O Mysen. Evaporation of olivine: low pressure phase relations of the olivine system and its implications for the origin of chondritic components in the solar nebula. *Geochimica et Cosmochimica Acta*, 58:1951–1963, 1994.
- H Nagahara, N.T Kita, K Ozawa, and Y Morishita. Condensation of major elements during chondrule formation and its implications to the origin of chondrules. *Nature*, 331:516–518, 2009.
- A Navrotsky. Thermodynamic properties of minerals. In J Ahrens, editor, *Mineral Physics & Crystallography: a handbook of physical constants*, pages 18–28. American Geophysical Union, 1995.
- J.S Nelson, L Yow, L.H Liaw, L Macleay, and R.B Berns. Ablation of both methacrylate by a prototype mid-infrared er:yag laser. *Lasers in Surgery and Medicine*, 8:494–500, 1988.
- nLIGHT Press Release. nlight demonstrates 73% wall-plug efficiency, January 2006.
- R.C Nuss, R.L Fabian, R Sarkar, and C.A Puliafito. Infrared laser bone ablation. *Lasers in Surgery and Medicine*, 8:381–391, 1988.

- D O'Brien and R Greenberg. The collisional and dynamical evolution of the man-belt and near size distributions. *Icarus*, 178:179–212, 2005.
- M Ohkoshi, T Yoshitake, and K Tsushima. Dynamics of laser-ablated iron in nitrogen atmosphere. *Applied Physics Letter*, 64:3340–3342, 1994.
- J.D O'Keefe and T.J Ahrens. Shock melting and vaporisation of lunar rocks and minerals. In *Lunar Geophysics Conference*, volume 1, pages 1–7. Lunar Science Institute, 1971.
- J.R Olds, A.C Charania, and M.G Schaffer. Multiple mass drivers as an option for asteroid deflection missions. In *Planetary Defense Conference*, 2007.
- B O'Leary. Mining the apollo and amor asteroids. *Science*, 197(4301):363–366, 1977.
- B O'Leary, M.J Gaffey, D.J Ross, and R Salkeld. Retrieval of asteroidal materials, space resources and settlements. NASA SP-428 142-155, 1979.
- C.P Opeil, G.J Consolmagno, and D.T Britt. The thermal conductivity of meteorites: New measurement and analysis. *Icarus*, 208:449–454, 2010.
- S Ostro and J.D Giorgini. Radar reconnaissance of potentially hazardous asteroids and comets. In *Workshop on the Scientific Requirements for Hazardous Asteroids and Comets*, pages 1–2. Arlington, USA, 2002.
- B.R Pabani and K.A Pathak. CFD analysis of laser ablation for nanotube production a review. *International Journal of Engineering Research Applications*, 2:1204–1207, 2012.
- S.W Paek. A multi-functional paintball cloud for asteroid deflection. In *Conference Proceedings 63rd International Astronautical Congress*, volume 1, pages 1–7. International Astronautics Federation, 2012.
- A.V Pakhomov, M.S Thompson, W Swift, and D.A Gregory. Ablation laser propulsion: Specific impulse and thrust derived from force measurements. *AIAA*, 40(11): 2305–2311, 2002.
- A.V Pakhomov, M.S Thompson, and D.A Gregory. Ablative laser propulsion: A study of specific impulse, thrust and efficiency. In *AIP Conference Proceedings*, volume 664, pages 194–205. Institute of Physics, 2003.
- E Palomba, L Colangeli, P Palumbo, A Rotundi, J.M Perrin, and E Bussoletti. Performance of micro-balances for dust flux measurement. *Advances in Space Research*, 29(8):1155–1158, 2002.
- S-Y Park and D Mazanek. Mission functionality for deflecting earth-crossing asteroids/comets. In D Mazanek, C.M Roithmayr, J Antol, S-Y Park, R.H Koons, J.C Bremer, D.G Murphy, J.A Hoffman, R.R Kumar, H Seywald, L Kay-Bunnell, M.R Werner, M.A Hausman, and J.L Stokum, editors, *Comet/Asteroid Protection System: Preliminary Space-based System Concept and Study Results*, pages 121–147. NASA/TM-2005-213758, 2005a.
- S.Y Park and D.D Mazanek. Deflection of earth-crossing asteroids/comets using rendezvous spacecraft and laser ablation. *Astronautical Sciences*, 53:2–37, 2005b.

- S.Y Park and I.M Ross. Two-body optimisation for deflecting earth-crossing asteroids. *Guidance, Navigation and Control*, 22:415–420, 1999.
- J Pearson, J Oldson, and E Levin. Earth rings for planetary environment control. *Acta Astronautica*, 58:44–57, 2006.
- F.R Perez and J Martinez-Frias. Spectroscopy goes to mars. *SpectroscopyEurope*, 18(1): 18–21, 2006.
- C Perron and B Zanda. Meteorites: Sample of neos in the laboratory. *Comptes Rendus Physique*, 6:345–360, 2005.
- C.R Phipps. Laser deflection of neos. In *Proceedings of the Near-Earth-Object Interception Workshop*, pages 256–260. Los Alamos National Laboratory, 1992a.
- C.R Phipps. Laser deflection of the death asteroid. In *Proceedings of the IEEE/LEOS Conference*, pages 407–408. Boston, 1992b.
- C.R Phipps. Modification of earth-satellite orbits using medium-energy pulsed lasers. *SPIE - Gas Flow and Chemical Lasers*, 1810:577–581, 1992c.
- C.R Phipps. Dynamics of neo interception. Report of the NASA Near-Earth-Object Interception Workshop LA-12476-C, 1993.
- C.R Phipps. LISK-BROOM: A laser concept for clearing space debris. *Laser and Particle Beams*, 13:33–41, 1995a.
- C.R Phipps. A laser concept for clearing space junk. In *Laser Interaction and Related Plasma Phenomena*, pages 466–8. AIP Conference Proceedings, 1995b.
- C.R Phipps. Laser deflection of near-earth asteroids and comet nuclei. In *Proceedings of International Conference on Lasers 96*, pages 580–587. STS Press, McLean, VA, 1997.
- C.R Phipps. Requirements for laser acquisitions of neos. In *International Conference on Lasers '97*, pages 928–934. STS Press, 1998.
- C.R Phipps. Laser applications overview: The state of the art and the future trend in the united states. In *Focused on Laser Precision Microfabrication*, pages 11–19. RIKEN Review No 50, 2002.
- C.R Phipps. Will your children ride a laser beam into orbit? would you want them to? - realistic applications of ablative laser propulsion. In *Beamed Energy Propulsion: Third International Symposium on Beamed Energy Propulsion*, pages 1–19. American Institute of Physics, 2005.
- C.R Phipps. Can lasers play a role in planetary defence? In *AIP Conference Proceedings*, pages 502–508. International Symposium on High Power Laser Ablation, 2010.
- C.R Phipps. An alternate treatment of the vapor-plasma transition. *International Journal of Aerospace Innovations*, 3(1):45–50, 2011a.
- C.R Phipps. Clearing space debris with lasers. SPIE Newsroom, 2011b.

- C.R Phipps and R.W Dreyfus. The high laser irradiance regime: Laser ablation and plasma formation. In A Vertes, R Gibbels, and F Adams, editors, *Laser Ionization Mass Analysis*, pages 369–431. A Wiley-Interscience Publication John Wiley & Sons Inc, 1993.
- C.R Phipps and J Luke. Diode laser-driven microthrusters: A new departure for micropropulsion. *AIAA*, 40(2):310–318, 2002.
- C.R Phipps and J.R Luke. Advantages of a ns-pulse micro-laser plasma thruster. In *Beamed Energy Propulsion: APS Conference Proceedings*, pages 230–239. America Institute of Physics, 2003.
- C.R Phipps and J.R Luke. Laser space propulsion - applications at two extremes of laser power. In C.R Phipps, editor, *Laser Ablation and its Applications*, volume 129, pages 407–434. Springer Series of Optical Science, 2007.
- C.R Phipps and M.M Michaelis. Laser impulse space propulsion. *Laser and Particle Beams*, 12:23–54, 1994.
- C.R Phipps and M.M Michaelis. NEO-LISP deflecting near-earth objects using high average power, repetitively pulsed lasers. In *Laser Interaction and Matter Conference*, pages 383–387. Institute of Physics, 1995.
- C.R Phipps and S.J Sinko. Applying new laser interaction models to the orion problem. In *AIP Conference Proceedings*, pages 492–501. International Symposium on High Power Laser Ablation, 2010.
- C.R Phipps, T.P Turner, R.F Harrison, G.W York, W.Z Osborne, G.K Anderson, X.F Corlis, L.C Haynes, H.E Steele, K.C Spicochi, and T.R King. Impulse coupling to targets in vacuum by KrF, HF and Co2 single-pulse lasers. *Applied Physics*, 64(4): 1083–1096, 1988.
- C.R Phipps, G Albrecht, H Friedman, D Gavel, E.V George, J Murray, C Ho, W Priedhorsky, M.M Michaelis, and J.P Reilly. Orion: Clearing near-earth space debris using a 20-kw, 530-nm, earth-based, repetitively pulsed laser. *Laser and Particle Beams*, 14:1–44, 1996.
- C.R Phipps, J.P Reilly, and J.W Campbell. Optimum parameters for launching objects into low earth orbits. *Laser and Particle Beams*, 18:661–695, 2000.
- C.R Phipps, J Luke, T Lippert, M Hauer, and A Wokaun. Micropropulsion using a laser ablation jet. *Propulsion and Power*, 20:1000–1011, 2004a.
- C.R Phipps, J Luke, T Lippert, M Hauer, and A Wokaun. Micropropulsion using laser ablation. *Applied Physics A*, 79:1385–1389, 2004b.
- C.R Phipps, J Luke, D Funk, D Moore, J Glowina, and T Lippert. Laser impulse coupling at 130 fs. *Applied Surface Science*, 252:4838–4844, 2006.
- C.R Phipps, M Birkan, W Bohn, H-A Eckel, H Horisawa, T Lippert, M Michaelis, Y Rezunkov, A Sasoh, W Schall, and S Scharring and J Sinko. Review: Laser-ablation propulsion. *Propulsion and Power*, 25(4):609–637, 2010a.

- C.R Phipps, W Bohn, T Lippert, A Sasoh, W Schall, and J Sinko. A review of laser ablation propulsion. In *International Symposium on High Power Laser Ablation*, pages 710–722. American Institute of Physics, 2010b.
- C.R Phipps, K.L Baker, B Bradford, E.V George, S.B Libby, D.A Liedahl, B Marcovici, S.S Olivier, L.D Pleasance, J.P Reilly, A Rubenchik, D.N Strafford, and M.T Valley. Removing orbital debris with lasers. *Advances in Space Research*, 1:1–37, 2011.
- C.M Pieters and L.A McFadden. Meteorite and asteroid reflectance spectroscopy. *Annual Review Earth Science*, 33:457–97, 1994.
- G Plohli. Pulsed laser ablation. Seminar - Physics Department, Faculty of Mathematics and Physics, University of Ljubljana, 2005.
- P Pravec and A.W Harris. Fast and slow rotation of asteroids. *Icarus*, 148:12–20, 2000.
- P Pravec, A.W Harris, and T Michalowski. Asteroid rotations. In W.F Bottke, A Cellino, P Paolicchi, and R. P Binzel, editors, *Asteroids III*, pages 113–122. University of Arizona Press, 2002.
- P Pravec, A.W Harris, and B.D Warner. Nea rotations and binaries. In *IAU Symposium No 236*, pages 1–10. International Astronomical Union, 2006.
- S.D Price. The surface properties of asteroids. *Advances in Space Research*, 33:1548–1557, 2004.
- P Rahimi and C.A Ward. Kinetics of evaporation: Statical rate theory approach. *International Journal of Thermodynamics*, 8(1):1–14, 2005.
- G Ranc. Continuous vacuum sublimation of silica. *Vacuum*, 19(9):409–411, 1969.
- R Rantanen and T Gordon. On-orbit transport of molecular & particulate contaminants. In *Conference Proceeding of SPIE 2864*, pages 115–126, 1996.
- H Rath. Zarm drop tower bremem - user manual. *ZARM Drop Tower Operation*, 82:117–122, 1995.
- W.U Reimold, P.C Buchanan, D Ambrose, C Koeberl, I Franchi, C Lalkhan, L Schultz, L Franke, and G Heusser. Thuathe, a new h4/5 chondrite from lesotho: History of the fall, petrography and geochemistry. *Meteoritics & Planetary Science*, 39:1321–1341, 2004.
- J.L Remo. Asteroid/meteorite analogs and material properties. In *Near Earth Object Interception Workshop Proceedings*, 1993.
- J.L Remo. Classifying and modelling neo material properties and interactions. In T Gehrels, editor, *Hazardous due to comets and asteroids*, pages 551–596. University of Arizona Press, 1994.
- J.C Richard and L.N Myrabo. Analysis of laser-generated impulse in an airbreathing pulsed detonation engine: Part 1. In A Pakhomov and L Myrabo, editors, *Third International Beamed Energy Propulsion Symposium*, volume 766, pages 265–278. AIP Conference Proceedings, American Institute of Physics, 2005a.

- J.C Richard and L.N Myrabo. Analysis of laser-generated impulse in an airbreathing pulsed detonation engine: Part 2. In A Pakhomov and L Myrabo, editors, *Third International Beamed Energy Propulsion Symposium*, volume 766, pages 265–278. AIP Conference Proceedings, American Institute of Physics, 2005b.
- J.C Richard, C Morales, W.L Smith, and L.N Myrabo. Transatmospheric laser propulsion of a 100 mw class lightcraft technology demonstrator. In *AIAA/SAE/ASME/ASEE 24th Joint Propulsion Conference*, pages 564–575. AIAA/SAE/ASME/ASEE, 1988.
- J.C Richard, C Morales, W.L Smith, and L.N Myrabo. Earth to orbit laser launch simulations for a lightcraft technology demonstrator. In *AIP Conference Proceedings-830*, pages 564–575. American Institute of Physics, 2006.
- D.C Richardson, Z.M Leinhardt, H.J Melosh, W.F Bottke, and E Asphaug. Gravitational aggregates: Evidence and evolution. In W.F Bottke, A Cellino, P Paolicchi, and R. P Binzel, editors, *Asteroids III*, pages 501–515. University of Arizona Press, 2004.
- A.S Rivkin, E.S Howell, L.A Lebofsky, B.E Clark, and D.T Britt. The nature of m-class asteroids from 3- μ m observations. *Icarus*, 145:351–368, 2000.
- R.A Robbie, B.S Hemingway, and H Takei. Heat capacities and entropies of mg_2SiO_4 , mn_2SiO_4 and Co_2SiO_4 between 5 and 380 k. *American Mineralogist*, 67:470–482, 1982.
- U Rohner, J.A Whitby, and P.A Wurz. Miniature laser ablation time-of-flight mass spectrometer for in-situ planetary exploration. *Measurement, Science and Technology*, 14:2156–2194, 2003.
- F Rull, S Maurice, E Diaz, C Tato, and A Pacros. The raman laser spectrometer (RLS) on the exomars 2018 rover mission. In *42nd Lunar Planetary Science Conference*, pages 1–2. Lunar and Planetary Institute, 2011.
- C.T. Russell, C.A. Raymond, A. Coradini, H.Y. McSween, M.T. Zuber, A. Nathues, M.C De Sanctis, R. Jaumann, A.S. Konopliv, F. Preusker, S.W. Asmar, R. S. Park, R. Gaskell, H.U. Keller, S. Mottola, T. Roatsch, J.E.C. Scully, D.E. Smith, P. Tricarico, M.J. Toplis, U.R. Christensen, W. C. Feldman, D. J. Lawrence, T.J. McCoy, T.H. Prettyman, R.C. Reedy, M.E Sykes, and T. N. Titus. Dawn at vesta: Testing the protoplanetary paradigm. *Science*, 366(6082):684–686, 2012.
- J Russell, R Mink, W Boynton, D Lauretta, Ed Beshore, B Sutter, and B Bierhaus. OSIRIS-REx techniques applied to earth-crossing object deflection. In *IAA Planetary Defense Conference Proceedings*, volume 1, pages 1–8. International Academy of Astronautics, 2013.
- S.S Russell, L Folco, M.E Zolensky, R Jones, K Richter, J Zipfel, and J.N Grossman. The meteoritical bulletin no 88. *Meteoritics & Planetary Science*, 39:215–272, 2004.
- R.E Russo, X.L Mao, H.C Liu, J.H Yoo, and S.S Mao. Time-resolved plasma diagnostics and mass removal during single-pulse laser ablation. *Applied Physics A*, 69(1): 8887–894, 1999.

- R.E Russo, X Mao, H Liu, J Gonzalez, and S.S Mao. Laser ablation in analytical chemistry - a review. *Talanta*, 57:425–451, 2002.
- N Saks, A Harris, C Brown, M Chapuy, N Despre, J.L Cano, and G Bellei. Mission architectures and technologies to enable neoshield, a global approach to neo impact threat mitigation. In *63rd International Astronautical Congress*, pages 1–13. International Astronautics Federation, 2011.
- J.P Sanchez and C.R McInnes. Asteroid resource map for near-earth space. *Spacecraft and Rockets*, 48:153–165, 2011a.
- J.P Sanchez and C.R McInnes. On the ballistic capture of asteroids for resource utilisation. In *62nd International Astronautical Congress*, volume 1, pages 1–16. International Astronautics Federation, 2011b.
- J.P Sanchez and C.R McInnes. Assessment on the feasibility of future shepherding of asteroid resources. *Acta Astronautica*, 73:49–66, 2012.
- J.P Sanchez and C.R McInnes. Available asteroid resources in the earth’s neighborhood. In V Badescu, editor, *Asteroids: Prospective Energy and Material Resources*, pages 439–458. Springer Berlin Heidelberg, 2013.
- J.P Sanchez, C Colombo, M Vasile, and G Radice. Multicriteria comparison among several mitigation strategies for dangerous near earth objects. *Guidance, Control and Dynamics*, 23(1):121–142, 2009.
- J.P Sanchez, M Vasile, and G Radice. Consequence of asteroid fragmentation during impact hazard mitigation. *Guidance, Control and Dynamics*, 33(1):126–146, 2010.
- J.P Sanchez, D Garcia-Yarnoz, and C.R McInnes. Near-earth asteroid resource accessibility and future capture mission opportunities. In *Global Space Exploration Conference*, pages 1–15. AIAA, 2012.
- J.P Sanchez, D Garcia-Yarnoz, E.M Alessi, and C.R McInnes. Gravitational capture opportunities for asteroid retrieval missions. In *63st International Astronautical Congress*, volume 1, pages 1–15. International Astronautics Federation, 2013.
- A Sasoh. Laser-propelled ram accelerator. *Journal de Physique IV*, 10:41–47, 2000.
- A Sasoh. A laser-driver in-tube accelerator. *Review of Scientific Instruments*, 72: 1893–1898, 2001.
- A Sasoh. In-tube rocket propulsion using repetitive laser pulses. *Thermal Sciences*, 20: 201–204, 2011.
- A Sasoh, J.Y Choi, I.S Jeung, N Urabe, H Kleine, and K Takayama. Impulse enhancement of laser propulsion in tube. *Postepy Astronautyki*, 27:40–50, 2001.
- A Sasoh, N Urabe, and S Kim. Laser-driven in-tube accelerator operation using monoatomic gases. In *33rd Plasmadynamics and Laser Conference Proceedings*, pages 1–15. AIAA, 2002.

- A Sasoh, M Kister, N Urabe, and K Takayama. Laser-powered launch in tube. *Transactions of the Japan Society for Aeronautical and Space Sciences*, 46:52–54, 2003.
- A Sasoh, N Urabe, S Kim, and I.S Jeung. Impulse dependence on propellant condition in a laser-driver in-tube accelerator. *Transactions of the Japan Society for Aeronautical and Space Sciences*, 48:63–70, 2004.
- A Sasoh, S Suzuki, and A Matsuda. Wall-ablative, laser-driven in-tube accelerator. In *High-Power Laser ablation VII*, pages 1–15. Proceeding of SPIE 7005, 2008.
- A Sasoh, S Suzuki, and A Matsuda. Wall-propelled, in-tube propulsion with repetitive-pulse laser ablation. *Propulsion and power*, 25:540–542, 2009.
- W.O Schall. Orbital debris removal by laser radiation. *Acta Astronautica*, 24:343–351, 1991.
- W.O Schall. Removal of small space debris with orbiting lasers. SPIE 3343, 1998.
- W.O Schall, H.A Eckel, and W.L Bohn. Laser propulsion thrusters for space transportation. In C.R Phipps, editor, *Laser Ablation and its Applications*, volume 129, pages 435–454. Springer Series of Optical Science, 2007.
- D.J Scheeres and R.L Schweickart. The mechanics of moving asteroids. In *IAA Planetary Defense Conference Proceedings: Protecting Earth from Asteroids*, 2004.
- H.L Schick. A thermodynamic analysis of the high-temperature vaporization properties of silica. *Chemical Review*, 60(4):331–362, 1960.
- R.M Schmidt and K.A Holsapple. Theory and experiments on centrifuge cratering. *Journal of Geophysical Research*, 85:235–252, 1980.
- J Schou, S Amoruso, and J.G Lunney. Plume dynamics. In C.R Phipps, editor, *Laser Ablation and its Applications*, volume 129, pages 67–95. Springer Series of Optical Science, 2007.
- J.P Schwanethal, N McBride, and S.F Green. Detecting interplanetary and interstellar dust with the debie sensor. In *Proceedings of Asteroids, Comets and Meteors - ACM International Conference*, volume 1, pages 75–78. Technical University Berlin, Germany, 2002.
- J.P Schwanethal, N McBride, S.F Green, J.A.M McDonnell, and G Droidhagen. Analysis of impact data for the debie (debris in-orbit evaluator) sensor in polar low earth orbit. In *Symposium on Space Station Utilisation*, volume 1, pages 177–182. Proceedings for the Fourth European Conference on Space Debris, 2005.
- R Schweickart, C Chapman, D Durda, and P Hut. Threat mitigation: the gravity tractor. NESA NEO Workshop White Paper, 2006.
- RL Schweickart, ET Lu, P Hut, and C.R Chapman. The asteroid tugboat. *Scientific America*, 1:54–61, 2003.
- J.J Scialdone. Characterization of the outgassing of spacecraft materials. *SPIE - Shuttle Optical Environment*, 287:2–9, 1981.

- K Seiferlin, T Spohn, and J Benkhoff. Cometary ice texture and the thermal evolution of comets. *Advances in Space Research*, 15(10):35–38, 1995.
- B.P Shafer, M.D Garcia, R.A Managan, J.L Remo, C.E Rosenkilde, R.J Scammon, C.M Snell, and R.F Stellingwerf. Momentum coupling to neos. *Annals of the New York Academy of Sciences*, 882:552–565, 1997.
- M.A Shannon, X.L Mai, A Fernandez, W.T Chan, and R.E Russo. Laser ablation mass removal versus incident power density during solid sampling for inductively coupled plasma atomic emission spectroscopy. *Analytical Chemistry*, 67(24):4522–4529, 1995.
- V.L Sharpton and P.D Ward. Differential cretaceous/tertiary extinctions of nonmarine vertebrates; evidence from northeastern montana. In V.L Sharpton, editor, *Global Catastrophes in Earth History An Interdisciplinary Conference on Impacts, Volcanism and Mass Mortality*, pages 549–562. Geological Society of America, Special Paper 247, 1990.
- E Shoemaker, J Williams, E Helin, and R Wolfe. Earth-crossing asteroids: Orbital classes, collision rates with Earth and origins. In T Gehrels, editor, *Asteroids*, pages 253–282. University of Arizona Press, 1979.
- Y.V Shorov and H Rickman. A kinetic model of gas flow in a porous cometary mantle. *Planetary Science*, 43:1587–1594, 1995.
- A.E Siegman. *Lasers*. University Science Books, USA, 1990.
- J.E Sinko and C.R Phipps. Modeling co₂ laser ablation impulse of polymers in vapour and plasma regimes. *Applied Physics Letters*, 95:541–546, 2009.
- E Skoglov. Spin vector evolution for inner solar system asteroids. *Planetary and Space Science*, 47:11–22, 1999.
- Y.V Skorov, N.I Kolme, W.J Markiewicz, and H.U Keller. Mass and energy balance in the near-surface layers of a cometary nucleus. *Icarus*, 140:173–188, 1999.
- R.M Smith. Real-time control of polysilicon deposition in single wafer rapid thermal chemical vapour deposition furnaces. PhD Thesis North Carolina State University, 1998.
- Y.J Song, S.Y Park, and K.H Choi. Mission feasibility analysis on deflecting earth-crossing objects using a power limited laser ablating spacecraft. *Advanced in Space Research*, 45(1):123–143, 2009.
- J.N Spitale. Asteroid hazard mitigation using the yarkovsky effect. *Science*, 296(5565):77, 2002.
- T Spohn and J Benkhoff. Thermal history models for KOSI sublimation experiments. *Icarus*, 87:358–371, 1990.
- T.B Stewart, G.S Arnold, D.F Hall, and H.D Marten. Absolute rates of vacuum-ultraviolet photochemical deposition of organic films. *Physical Chemistry*, 93:2393–2400, 1989.

- C Stuck. The feasibility of shading the greenhouse with dust clouds at the stable lunar lagrange points. *Journal of the British Interplanetary Society*, 60:82–89, 2007.
- N Tarcea, T Frosch, P Rosh, M Hilchenback, T Stuffer, S Hofer, H Thiele, R Hochleitner, and J Popp. Raman spectrometer - a powerful tool for in-situ planetary science. *Space Science Review*, 135:1–4, 2007.
- P.A Taylor, E.S Howell, M.C Nolan, and A.A Thane. The shape and spin distribution of near-earth asteroids observed with the arcibo radar system. Asteroids, Comets and Meteors Meeting Abstracts No 6340, 2012.
- P.C Thomas, J Veverka, J.F Bell, B.E Clark, B Carcich, J Joseph, M Robinson, LA McFadden, M Malin, C.R Chapman, W Merline, and S Murchie. Mathilde:size, shape and geology. *Icarus*, 140:17–27, 1999.
- A.C Tribble. *Fundamentals of Contamination Control*. SPIE - international Society for Optics and Photonics, USA, 1961.
- Y Tsuda, M Yoshikawa, M Abe, H Minamino, and S Nakazawa. System design of hayabusa2 - asteroid sample return mission to 1999ju3. In *63st International Astronautical Congress*, pages 1–6. International Astronautics Federation, 2012.
- S Uchida, Y Shimada, K Hashimoto, M Yamaura, T Birou, and M Yoshida. Spot size limited carbon propellant characterisation for efficient high isp laser propulsion. In *AIP Conference Proceedings*, volume 766, pages 433–441. Institute of Physics, 2005.
- G.B Valsecchi, A Milani, G.F Gronchi, and S.R Chesley. Resonant returns to close approaches: Analytical theory. *Astronomy & Astrophysics*, 408:1179–1196, 2003.
- G.B Valsecchi, A Milani, G.F Gronchi, and S.R Chesley. Orbital debris-debris collision avoidance. *Advanced in Space Research*, 1:1179–2003, 2003.
- M Vasile and C Colombo. Optimal impact strategies for asteroid deflection. *Guidance, Control and Dynamics*, 31(4):858–872, 2008.
- M Vasile and C Maddock. On the deflection of asteroids with mirrors. *Celestial Mechanics and Dynamical Astronomy*, 107:265–284, 2010.
- M Vasile, C Maddock, G Radice, and C McInnes. Call for ideas: Neo encounter 2009 neo deflection through a multi-mirror system. Final Report, Ariadna Study Contract Number 21665/08/NL/CN, 2009a.
- M Vasile, C Maddock, and L Summerer. Conceptual design of a multi-mirror system for asteroid deflection. In *7th International Symposium on Space Technology and Science*, pages 1–5. sukuba, Japan, 2009b.
- M Vasile, C Maddock, and C Saunders. Orbital debris removal with solar concentrators. In *61st International Astronautical Congress*, pages 1–11. International Astronautics Federation, 2010a.
- M Vasile, I Watson, M Sorel, C Maddock, and A Gibbings. A light touch: Removing debris with solar light. Study Proposal Ariadan Study Reference No: AO/1-6411/10/NL/CBi, 2010b.

- M Vasile, A Gibbings, V Massimo, J-P Sanchez, D.G Yarnoz, S Eckersley, A Wayman, J Branco, D Burns, J-M Hopkins, C Colombo, and C McInnes. Light touch2: Effective solutions to asteroid manipulation. *SYSNova Challenge Analysis Final Report*, 1: 1–164, 2013a.
- M Vasile, M Vertriano, A Gibbings, D Yarnoz, J.P Cuartielles, C McInnes, D Burns, and J-M Hopkins. Light-touch2: A laser-based solution for the deflection, manipulation and exploitation of small asteroids. In *IAA Planetary Defense Conference Proceedings*, pages 1–16. International Academy of Astronautics, 2013b.
- M Vasile, A Gibbings, I Watson, and J-M Hopkins. Improved ablation model for asteroid deflection. *Acta Astronautica* <http://dx.doi.org/10.1016/j.actaastro.2014.01.033>, 2014.
- A Vertes, R Gijbels, and F Adams. *Laser Ionization Mass Analysis*. Wiley-International, USA, 1993.
- M Vertriano, J Branco, D.G Yarnoz, J Sanchez, and M Vasile. Deflecting small asteroids using laser ablation: Deep space navigation and asteroid orbit control for the lighttouch2 mission. In *AIAA Guidance, Navigation, and Control Conference*, pages 1–25. AIAA, 2013.
- J Veverka, P Thomas, A Harch, B Clark, J.F Bell, B Carcich, J Joseph, S Murchie, N Izenbergand C Chapman, W Merline M Malin, L McFadden, and M Robinson. Near encounter with asteroid 253 mathilde: Overview. *Icarus*, 140:3–16, 1999.
- F Vidal, T.W Johnston, S Laville, M Barthelemy, M Chaker, B Le-Drogoff, J Margot, and M Sabsabi. Critical-point phase separation in laser ablation of conductors. *Physical Review Letters*, 86(12):2573–2576, 2001.
- J.D Walker and S Chocron. Near-earth object deflection using conventional explosives. *International Journal of Impact Engineering*, 35:1473–1477, 2008.
- J.D Walker and S Chocron. Momentum enhancement in hypervelocity impact. *International Journal of Impact Engineering*, 38:1–7, 2011.
- A.D Wallace and S.A Wallace. Realistic performance specification for flight quartz crystal microbalance instruments for contamination measurements on a spacecraft. In *Thermophysics, Plasmadynamics and Laser Conference Proceedings*, volume 1, pages 1–9. American Institute of Aeronautics and Astronautics, 1988.
- J.T Walsh, T.J Flotte, and T.F Deutsch. Er:Yag laser ablation of tissue:effect of pulse duration and tissue type on thermal damage. *Lasers in Surgery and Medicine*, 9: 314–325, 1989.
- J Wang, D Davis, R Clayton, and A Hashimoto. Evaporation of single crystal forsterite: Evaporation kinetics, magnesium isotope fractionation, and implications of mass-dependent isotopic fractionation of a diffusion-controlled reservoir. *Geochimica et Cosmochimica Acta*, 63(6):653–966, 1999.
- P.S.P Wei, D.J Nelson, and R.B Hall. Laser-induced evaporation of solid surfaces. *Chemical Physics B*, 62(8):3050–3051, 1975.

- M.K Weisberg, T.J McCoy, and A.N Kro. Systematics and evaluation of meteorite classification. In D.S Lauretta and H.Y McSween, editors, *Meteorites and the Early Solar System II*, pages 19–52. University of Arizona Press, 2006.
- M Weksler and J Shwartz. Solar-pumped solid state lasers. *Quantum Electronics*, 24: 1222–1229, 1988.
- F.L Whipple. A comet model I the acceleration of comet encke. *Astrophysical*, 111(1): 375–394, 1950.
- F.L Whipple. *The Mystery of Comets*. Smithsonian Institution, Cambridge, USA, 1985.
- R.J Whiteley, D.J Tholen, and C.W Hergenrother. Lightcurve analysis of 4 new monolithic fast-rotating asteroids. *Icarus*, 157:139–154, 2002.
- M Wuest, G.G Managadze, and N.G Managadze. A combined raman/laser ablation mass spectrometer instrument for exploration of small solar system objects. *Advances in Space Research*, 39:477–481, 2007.
- T.K Xia and U Landman. Molecular evaporation and condensation of liquid n-alkane films. *Chemistry Physics*, 101(3):1587–1594, 1994.
- T Yabe and S Uchida. Laser propulsion. In C.R Phipps, editor, *Laser Ablation and its Applications*, volume 129, pages 455–471. Springer Series of Optical Science, 2007.
- T Yabe, C.R Phipps, K Aoki, M Yamaguchi, Y Ogata, M Shiho, G Inoue, M Onda, K Horioka, I Kajiwara, and K Yoshida. Laser-driven vehicles- from inner-space to outer-space. *Applied Physics A*, 77:243–249, 2003.
- M Yanagisawa and S Hasegawa. Momentum transfer in oblique impacts: Implications for asteroid rotations. *Icarus*, 146:270–288, 2000.
- D.G Yarnoz and J.P Sanchez. Opportunities for asteroid retrieval missions. In V Badescu, editor, *Asteroids: Prospective Energy and Material Resources*, pages 479–550. Springer Berlin Heidelberg, 2013.
- D.K Yeomans, J-P Barriot, D.W Dunham, R.W Farquhar, J.D Giorgini, C.E Helfrich, A.S Konopliv, J.V McAdams, J.K Miller, W.M Owen, D.J Scheeres, S.P Synnott, and B.G Williams. Estimating the mass of asteroid 253 mathilde from tracking data during the near flyby. *Science*, 278(5346):2106–2109, 2006.
- D.K Yeomans, S Baskaran, S.B Broschart, S.R Chelsley, P.W Chodas, and T.H Sweetser. Deflecting a hazardous near-earth object. In *IAA Planetary Defense Conference Proceedings: Protecting Earth from Asteroids*, 2009.
- J.H Yoo, S.H Jeong, and R.E Russo. Explosive change in crater properties during high power nanosecond laser ablation of silicon. *Applied Physics*, 88(1638):1–12, 2000.
- S.M Yoo, S.M Song, S.Y Park, and K.H Choi. Spacecraft formation flying for earth-crossing object deflections using a power limited laser ablation. *Advances in Space Research*, 12:1873–1889, 2009.
- D Zhang, J Wu, R Zhang, Z He, and F Zhang. Design and performance study of a new

- laser-electromagnetic coupling plasma thruster. In *63st International Astronautical Congress*, pages 1–6. International Astronautics Federation, 2012.
- N Zhang, W Wang, X Zhu, J Liu, K Xu, P Huang, J Zhao, R Li, and M Wang. Investigation of ultrashort pulse laser ablation of solid targets by measuring the ablation-generated momentum using a torsion pendulum. *Optics Express*, 19(9): 8870–8878, 2011a.
- N Zhang, L Xin, Z Mu-Lin, L Xiao-Xuau abd Z Zhi-Yuan, L Yu-Tong, and Z Jie. Laser propulsion with a high specific impulse using a thin film propellant. *Chinese Physics Letter B*, 20(8):1–4, 2011b.
- Z-Y Zheng, Z Jie, L Xin, H Zuo-Qiang, X Miao-Hua, W Zhao-Hua, and W Zhi-Yi. Effects of confined laser ablation on laser plasma propulsion. *Chinese Physics Letters*, 2:1725, 2005.
- F Zuaini, M Vasile, and A Gibbings. Evidence-based robust design of deflection actions for near earth objects. *Celestial Mechanics and Dynamical Astronomy*, 114 (1):107–136, 2012.

Manufacture of the Composite Sample

A1 Introduction

The highly porous composite sample was manufactured by mixing expanded perlite, fly ash, dry quartz sand and water [Housen and Holsapple, 2003]. It provided a homogeneously weak, dry material with very little cohesion. Expanded perlite provided the main source of porosity within the target material. It is formed from naturally occurring siliceous rock, which when heated to ~ 870 °C expands to form a highly porous, low mass aggregate. Fly ash was used as the main cementing agent. This ensured that the grains of expanded perlite and quartz sand did not separate. Quartz sand was used to fill the void spaces between the grains.

A2 Manufacturing Process

The target material was manufactured by mixing, by mass, 70 % dry quartz sand, 3 % expanded perlite, 10 % fly ash and 17 % water. It provided a sample with 45 % porosity [Housen, 2010]. The component parts are shown in Figure A.1.

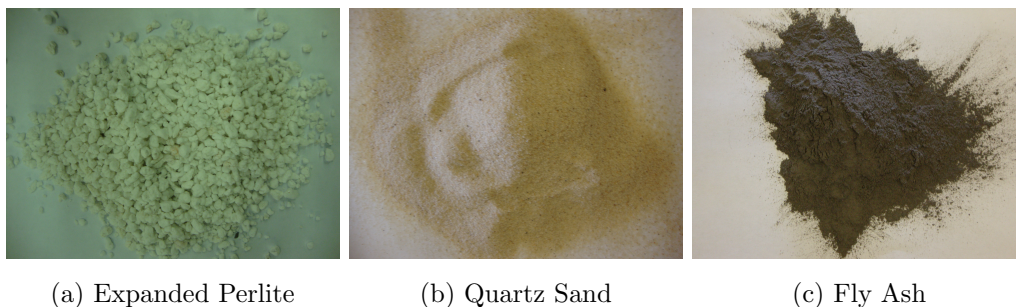


Figure A.1: Component Parts of the High Porous Composite Mixture

The dry particles were first measured and then mixed together. Water was then added. This avoided the clumping of particles and ensured an even blend within the mixture. Care was taken not to unduly compress the individual grains of expanded perlite. Once mixed, the mixture was placed into a number of small aluminium target containers and allowed to cure for five days at ambient temperature. The mixture was too weak to be free-standing. The surface of each target container was levelled with a screed. This

removed any excess waste. Curing enabled the particles to settle allowing for a chemical reaction (i.e bonding) to occur between all of the particles. This gave the target material minimal strength which prevented any material separation from occurring. Separation could have been caused by the handling, transportation and ongoing operations of the experiment.

Once cured the samples were then placed in an oven and baked-out at 90 °C for two days. This is the standard operating temperature for the bake-out of material; avoiding the loss of material and structure. Uniform heating enabled the volumetric removal of water. An aluminium target container was selected due to its high conductivity. It prevented the formation of any hot spots. During bake-out, each sample was periodically removed and their mass was measured. This was used to monitor the removal of water. After bake-out each sample was cooled. A long cooling time minimised the creation of any internal thermal stresses. This followed a pre-existing procedure that has been used successfully in a number of impact cratering experiments [Housen, 2004; Housen and Holsapple, 2003; Schmidt and Holsapple, 1980; Gibbings and Vasile, 2011].

A3 Note on Porosity

The measurement of porosity does not specify the form and size distribution of the pore space. It is assumed that the pore spaces are uniformly homogeneous and that the granulation of the target material is significantly smaller than the focus point of the laser beam. This ensured comparative assessment between the different targets. An inhomogeneous sample could have been created by varying the length-scale relationship between the spot size diameter of the laser beam and the target material's largest grain diameter. It would have resulted in the spatial variation of the target material's physical properties.

Tested Equipment and Proposed Methodologies

B1 Introduction

Throughout the design and development of the experiment platform, equipment, techniques and proposed methodologies were tested. These experiences have been documented in the hope that it will assist in the development of any future experimental campaigns and users of the vacuum chamber.

B2 Selection and Testing of the Target Material

In the design of the experiment the selection of the asteroid analogue target material was critical. Relative to the surface power density of the laser beam, and the chemical composition of the target material, it was uncertain whether or not a measurable ablation response could be achieved. Therefore each candidate target material had to be tried and tested on a trial-and-error basis. Testing was achieved through static and simple pendulum experiments. This is shown further in Figures B.1-B.6. Initially all samples were shaped into a small sphere with a diameter of approximately 3 cm. It provided a volumetrically similar shape that would ensure the same degree of surface curvature, assisting in the quantitative comparison. However only after testing was it determined that this was not the case. The surface curvature was too great. This was relative to the model's assumed parameters (for example, the spot providing two dimensional illumination) and the focal point of the laser beam. The focus of the laser beam also became overly sensitive to any inhomogeneous variation within the terrestrial target material. This varied on a case-by-case basis.

Advice on target material selection was given by Professor Martin Lee, School of Geographical and Earth Sciences, University of Glasgow. Initial candidates included: paraffin wax, carbon (representing an organic compound), pure and impure quartz sandstone (representing a S class asteroid), limestone (representing a C class asteroid), chalk, shale (representing a weak chondrite), granite (representing a strong chondrite), clay, white and black marble, olivine and a highly porous composite mixture (representing a rubble pile asteroid) [Shafer et al., 1997].



Figure B.1: Range of Tested Material



Figure B.2: Initial Limestone Ablation

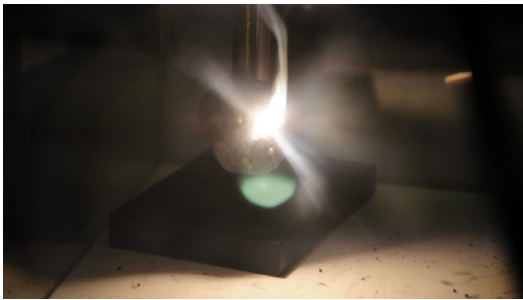


Figure B.3: Initial Sandstone Ablation

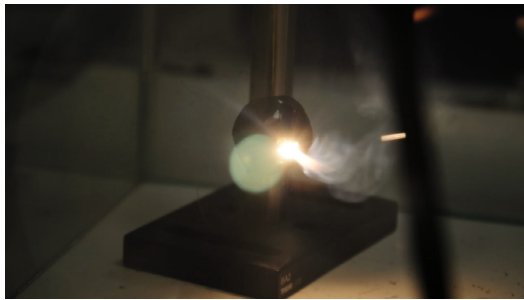


Figure B.4: Initial Shale Ablation



Figure B.5: Initial Marl Ablation

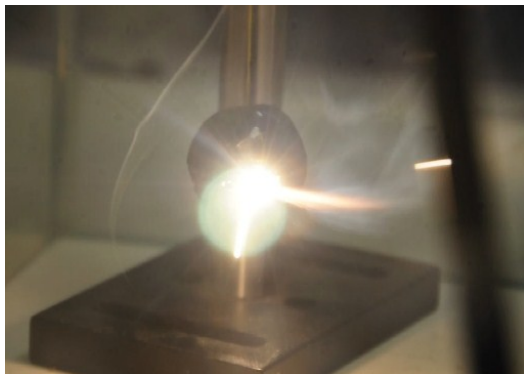


Figure B.6: Initial Shale Ablation

A torsion pendulum was also built. Shown in Figure B.7, this consisted of a balanced, horizontal bar that was hung from a central hook. The bar was free to rotate about its suspension point. At the far end of the bar the laser beam was used to ablate a given surface. This created a torque, which was measured by reflecting (off a highly polished section) a low power laser beam at the opposite end of the bar. The motion was tracked with a camera. Frame-by-frame analysis determined the maximum swing of the pendulum. This is proportional to the applied force. However, despite continued effort, with the available apparatus, this approach was found to be overly sensitive to the initial requirements. It was not investigated further.

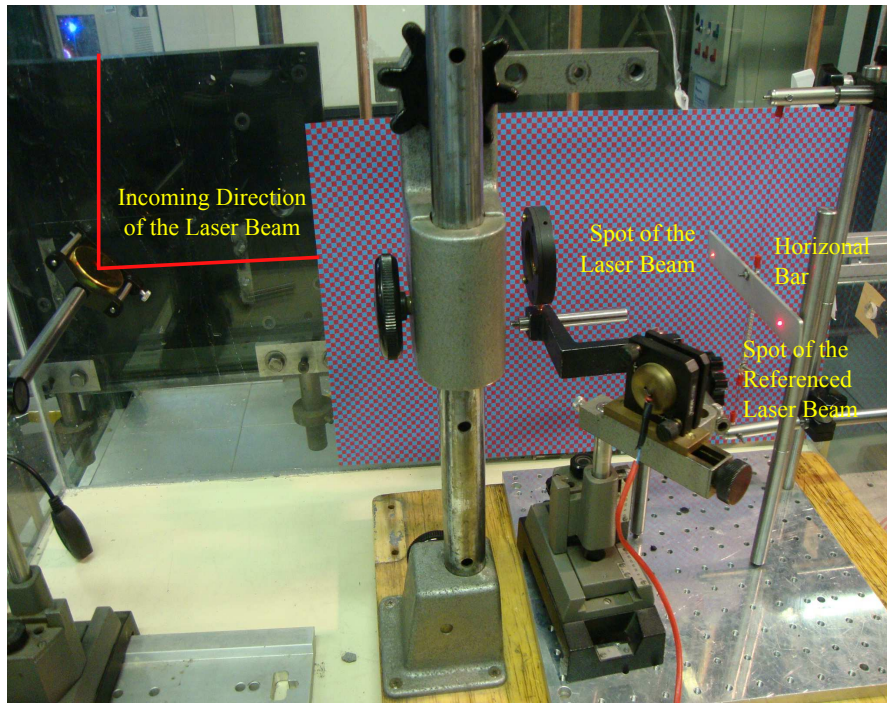


Figure B.7: Initial Development and Testing of a Torsion Pendulum

B3 Quality and Selection of the Collection Plates

During each experiment a number of standard, laboratory grade, microscope slides were used as collection plates. The central collection plate was also used to protect the main window of the vacuum chamber from the depositional effects of the ejecta plume. Each collection plate was initially manufactured from low grade silica. This was adequate for short duration ablation events that lasted less than one minute. However for extended periods of time the intense heating caused by the laser beam passing through the central collection plate caused the collection plate to crack and break. The central slide had to be upgraded. It was replaced with a microscope slide manufactured from a substrate of high quality fused silica (supplied by UQG Optics). This cost considerably more, but was necessary to the development of the experiment. Each collection plate had a low coefficient of thermal expansion. It was therefore highly resistant to the effects of thermal shock and a rapid variation to its thermal gradient. Qualification data states that each microscope slide can operate at temperatures over 1250 °C. Data was provided by UQG Optics.

B4 Ongoing Maintenance of the Experiment

The test chamber, the two pumps and the chiller needed constant maintenance and repair. After each experiment it was vital that the test chamber was wiped clean with an isopropyl alcohol solvent wipe. This prevented the accumulation of the ablated ejecta and general dirt degrading the system. The system was also checked thoroughly for any leaks. This was achieved by using the helium leak checker machine and by applying

a thin layer of vacuum grease to all seals and interfaces. The efficiency of the pumps was also monitored. Pump efficiency is affected by the cooling operations of the chiller, the sealing of the O-rings and the quality of the oil within the pumps (Ultra Grade 19 oil was used for the roughing pump and Santovac 5 for the diffusion pump). After prolonged activity, the oil within the roughing pump and the water level of the chiller needed to be topped-up. The chiller could also not be operational for extended periods of time (maximum limit of 8 hours). This therefore excluded any over-night pumping activities. The O-ring interface between the top of the diffusion pump and the bottom of the pumping line also needed ongoing care and attention. After continued operations it was found that the metal isolation valve between the two units was fouling the O-ring. A large gash was created around the rubber seal. Fouling can also be caused by the O-ring twisting or waste material becoming embedded across the sealing interface. It prevented the system from pumping down to base pressure. All seals need to have the same level of system integrity. To overcome this fault a metal spacer was manufactured. This allowed the isolation valve to be opened and closed freely, and more importantly, prevented any rubbing against the O-ring. It maximised the overall pumping efficiency of the system.

B5 Development of the Experimental Procedures

During the design, development and calibration of the experiment, several different experimental procedures were tested. Not all were successful techniques in producing meaningful results. This included:

- **The Use of Neutral Density Filters to Separate the Incandescent Light from the Formation of the Ablated Ejecta Plume.**

It was initially very difficult to optically separate and record the formation of the ejecta plume. The plume was hidden by the visible radiation emitted during the ablation process. This included stray light and laser light. It was thought that a neutral density filter mounted over the aperture of each camera could be used to attenuate the received light. It could also be used to prevent saturation of the camera's detector. Four different neutral density filters were tested. Each was pre-mounted with a diameter of 25 mm, but had a different optical density. The variation in optical density included: 0.6 (transmittance of 25 %), 0.5 (transmittance of 32 %), 0.4 (transmittance of 40 %) and 0.3 (transmittance of 50 %). The filters were supplied by Thorlabs Ltd. Each filter resulted in recording a small orb of light. It had little effect in improving the visualisation of the ejecta plume. Nor could the size of the solid particles be determined. Instead a thermal camera could be used.

- **The Use of Magnetic Levitation**

Magnetic levitation was tested as a method of re-creating the effects of microgravity. An irregular, composite target material could be created around a magnetic core. Stable magnetic levitation occurs when the magnetic force counter balances the

gravitational force. This has to be exact. It also restricts all linear forms of motion. This is due to the creation of a potential well. The target is only able to rotate. The direction of the ejecta plume is also restricted. This limits the ablation response and it is not representative of a freely-tumbling space-based body. It was therefore excluded from future investigation.

- **The Use of the Atomic Force Microscope.**

The Atomic Force Microscope at the School of Engineering, University of Glasgow was used in an attempt to measure the height and size distribution of the deposited ejecta. It was tried through colour analysis of the contaminated collection plates. However the available resolution was too fine to extract any worthwhile data. The SEM and optical microscopy were far more effective.

- **The Manufacture of the Highly Porous Composite Sample**

The manufacture of the highly porous, composite mixture was inherently messy and labour intensive. Dust from the expanded perlite was hard to control. A conscious effort had to be made to contain the mess and thoroughly clean the laboratory facilities after use [Gibbings et al., 2011a, 2010]. This should be noted for all future activities.

Between each manufactured sample, a small amount of scatter in the final porosity reading was observed. This was due to the unavoidable variation in the placement of the target material into the target container. Due care and attention was made to minimise this. The scatter was less than 5 %. This was deemed an acceptable level of tolerance.

The initial target containers (60·60·30 mm seamless tins) were too heavy for the electronic scales and had to be replaced. The low-strength, fragile nature of the porous sample also meant that it was impossible to attach a thermocouple onto the back of the sample. This was intended to measure the temperature related affects of ablation. A thermal camera could be used instead.

B6 Preliminary Development of Additional Experimental Techniques

During the experiment campaign, detailed and more inclusive procedures were developed. Although time limited their implementation, preliminary activities validated their initial proof-of-concept. Each proposed experiment has been documented. It is hoped that this will support any future investigations into the ablation process. This included:

- **Measuring the online mass flow rate of the ejecta plume**

Supplied by Mettler Toledo, a small and highly sensitive analytical mass balance can measure the continuous, in-situ (online) mass flow rate of the ablated ejecta plume. It is advantageous in increasing the sensitivity (and therefore decreasing the uncertainty) in the mass flow rate measurements [Fernandez et al., 1995]. Shown in

Figure B.8, preliminary testing of the WM25-SH analytical mass balance occurred under standard atmospheric conditions.

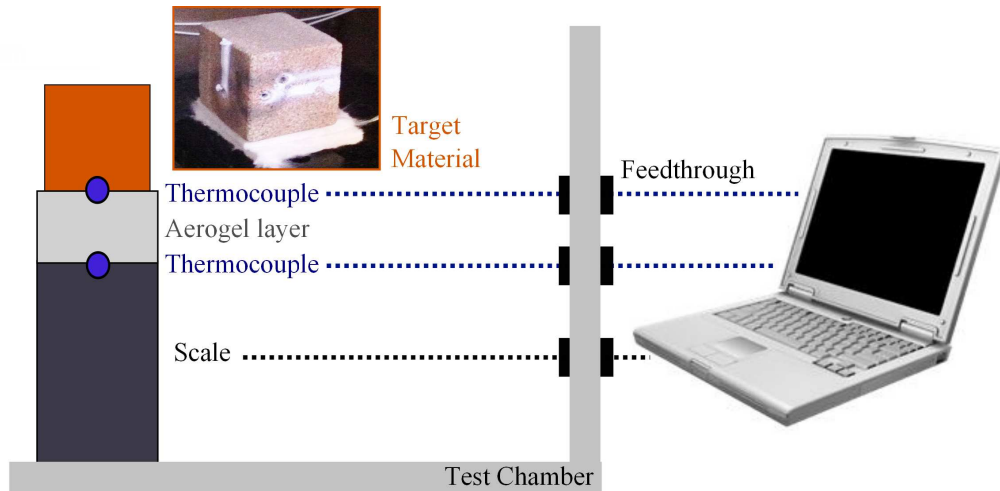


Figure B.8: Preliminary Testing of the WM25-SH Analytical Mass Balance

A small 18 g sample of either olivine or sandstone rock was positioned on top of the mass balance, between a 10 mm thick piece of aerogel foam (Pyrogel XT-E, supplied by Aspen Aerogels). The laser beam always illuminated the middle, central, flat face of the target material. Aerogel was used to thermally insulate the top of the weighing pan. It is a commercially available, low density and highly porous silicate structure, which provides high temperature insulation. The foot print of the aerogel was always slightly larger than the target material. Two thermocouples positioned across the scale-and-aerogel interface were used to monitor the temperature of the target material and the scale head. Local temperatures were not allowed to exceed 40 °C. This would have destroyed the electronic sensors in the scale head. The high ejection velocities prevented any of the ablated material from falling, hitting and depositing onto the weighing pan. The mass balance was also limited to a maximum sample mass of 21 g and a pan draft shield length of 2.5 cm. The system does however provide a readability reading of $1 \cdot 10^{-5}$ g. During the experiment, data was transferred through a hermetic sealed, electrical feedthrough. A RS232 series cable connected the data onto a laptop with an APW software link. Provided by Mettler Toledo, the APW software enabled the real-time monitoring, storage and analysis of the ablated sample mass. Analysis can be combined with data gained from the spectrometer, thermal camera and fast cameras.

Results from this experiment could also be combined with the orientation of the resultant thrust vector. A simple, ballistic or torsion pendulum could be used to measure the ablation generated momentum [Grun and Ripin, 1982; Zhang et al., 2011a; Zheng et al., 2005; Lenk and Witke, 1995; Lenk et al., 1996]. The recoil momentum of the ablation event causes the pendulum to swing [Lenk et al., 1997]. Video cameras can measure the maximum height of the pendulum swing, where the force and velocity can be measured [Zhang et al., 2011b].

- **Measuring the temperature profile of the ejecta plume & target material**

Supplied by the Institute of Photonics, University of Strathclyde, a FLIR thermal camera (SC700) can measure the spatial and temporal thermal distribution of the ejecta plume and the temperature gradient effects - thermal conductivity, distribution, emissivity and absorption - of the target material. Viewing access is achieved by mounting a small 60 mm diameter, 4 mm thick calcium fluoride (CaF_2) window into the main window of the vacuum chamber. Temperature gradients are expected to develop as the ejecta plume expands, acquiring a three dimensional character. Subsurface heating depends on the penetration depth of the laser energy, the ablation rates and heat conducting into the bulk of the target material.

- **Measuring the initial expansion, distribution and velocity of the ejecta plume**

Instead of track images, small time-delay gate analysis from a high speed camera can track the expansion, distribution and velocity of the ejecta plume. Initial velocity can also be correlated to particle size. Small particles will be ejected at higher velocities.

- **Measuring the temperature dependent effects of ejecta deposition**

Deposition of the ejecta plume is dependent on the mass flow rate of the ablated ejecta, the deposition time and the temperature profile of the exposed surface. To examine this further, a small flexible polyamide heater mounted onto the back of a collection plate was used to provide localised heating. Temperature intervals of 50, 100 and 150 °C can be easily achieved. These values are based on the expected operational limits of the laser (0-40 °C) and the thermal equilibrium temperature of the solar arrays (100 °C). At each interval the deposited density, height and absorptivity of the collected ejecta can be assessed. The deposition response would be compared to a nominal test sample (denoted by A in Figure B.9). The nominal sample would not experience an increase in surface temperature. Both collection plates would be positioned at a fixed radius from the spot, at a mirrored, symmetrical elevation (± 45 degs).

The polyamide heater needs to be controlled through a dedicated relay system (for example, an EZ-Zone PM controller). Power is supplied through an electrical feed-through and BNC connectors. A small thermocouple, positioned to touch the external surface of the collection plate provides a feedback control. It is used to increase, decrease or maintain the surface temperature of the collection plate. The temperature profile from the thermocouple is assumed to be uniform across the entire collection plate. A stiff connection between the heater and collection plate is maintained by two purpose-built clamps. Shown in Figure B.9, one is attached to the bottom and another one to the top of the collection plate. The use of a pressure sensitive adhesive was also investigated. This was thought to provide a thin, secure and semi-permanent bond. However in practice it was a very messy and permanent process. It was difficult to control the distribution and curing conditions of the adhesive. The adhesive would often spread onto the

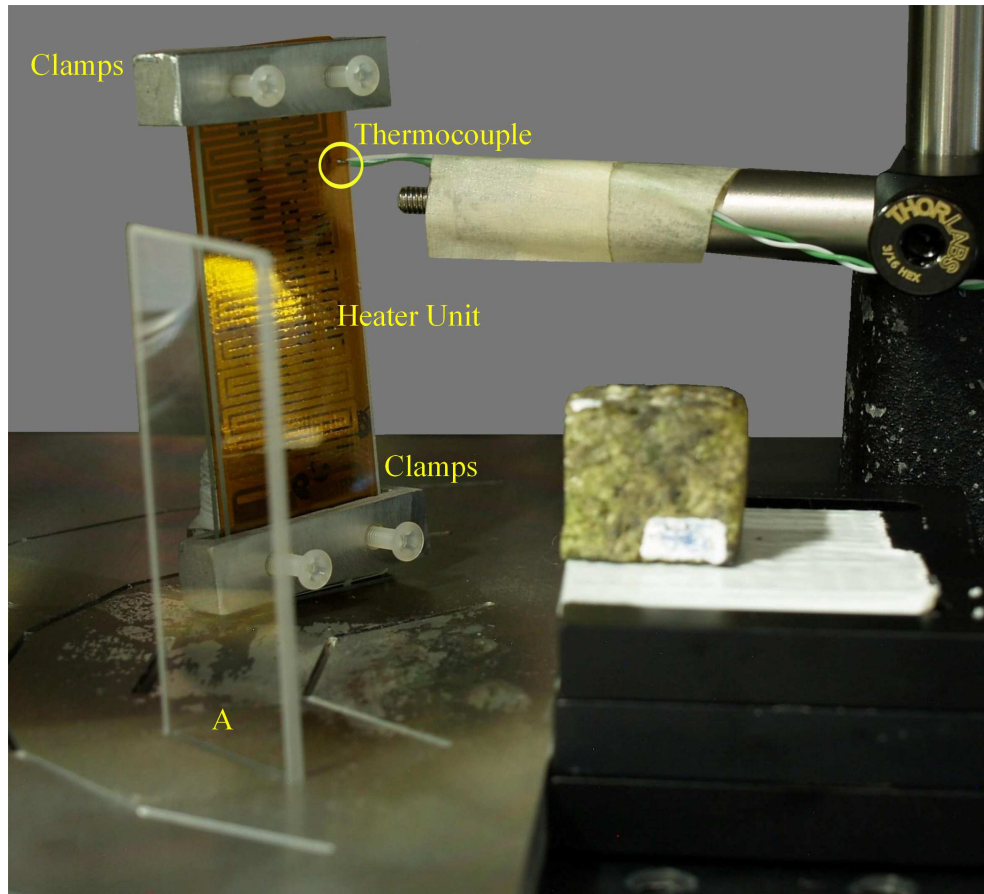


Figure B.9: Proposed Test Configuration

metal elements of the heater. This reduced the performance and reliability of the heater in providing a uniform heating load. The rapid heating and cooling of the collection plate must also be avoided. If not, the collection plate may crack. The heater, provided by Watlow Ltd, can provide a power density of 7.75 W/cm^2 and operate at a maximum temperature of $200 \text{ }^\circ\text{C}$.

- **Measuring the ablation response of more realistic and representative shape models**

The selection of target material can be improved by ablating a range of meteorite samples and including more realistic and representative shape models. Examples include an irregular potato shape, samples with a layer of surface regolith and highly porous structures. Currently, open ended questions include: 1) How does the ablation response vary between a dense, porous and inhomogeneous composite material? - Are there any differences between a monolithic structure, fractured shard and rubble pile body?, 2) How does the variation in shape model, surface roughness and rotation affect the ablation event? - Does this create any elongation of the surface spot?, 4) What are the effects of ablation on a three dimensional tumbling body? - Does this significantly alter the asteroid's rotational velocity and orientation? How does this affect the surface power density?

To answer these questions, the samples could also be mounted onto a simple, ballistic or torsion pendulum. A pendulum can measure the ablation generated

momentum that causes the pendulum to swing [Grun and Ripin, 1982; Zhang et al., 2011a; Zheng et al., 2005; Lenk and Witke, 1995; Lenk et al., 1996]. Video cameras can measure the maximum height of the swing, where the force and velocity can be directly measured. It will enable the orientation of the resultant thrust vector to be derived. For an improved shape model, the dimensions of the asteroid can be estimated by using an ellipsoidal shape model. This is further defined in Figure B.10, where a_I , b_I and c_I are the three radii along the orthogonal axis [Delbo et al., 2007]. d_A is the estimated diameter based on the asteroid's observed magnitude.

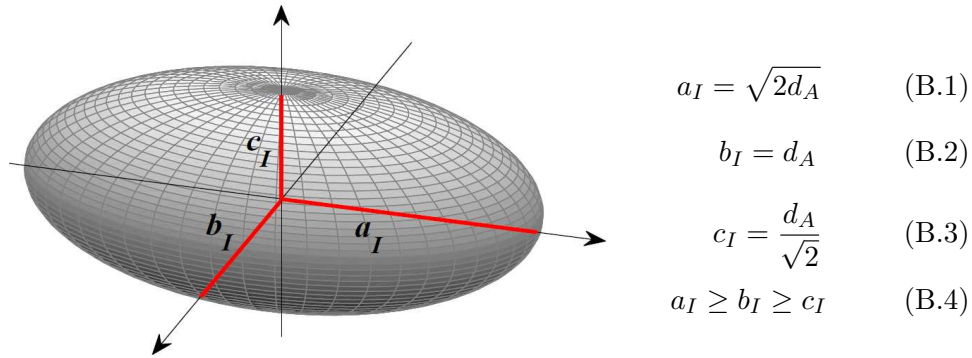


Figure B.10: Ellipsoidal Shape Model

Meteorites Bensor, Allende and Thauthe were also pre-selected as analogues of an S, C and M class asteroids respectively. Each sample is classified further in Table B.1. Samples were sourced from MeteoriteMarket.com. This is an approved and official supplier of the International Meteorite Collection Association. A certificate of authenticity was supplied. Each sample comes from a witness fall (this is very rare for a carbonaceous chondrite meteorite) and has experienced negligible levels of terrestrial weathering [Gattacceca et al., 2003; Russell et al., 2004; Reimold et al., 2004]. They do however have a dark fusion crust. This is shown in Figure B.11, where a small one centimetre cube is used for scale.

Meteorite	Type	Material
Bensor	Ordinary chondrite (LL6)	Olivine, pyroxenes, feldspar, iron, nickel, troilite and chromite [Russell et al., 2004; Lee et al., 2006].
Allende	Carbonaceous chondrite (CV3)	Carbon and microscopic diamonds.
Thauthe	Ordinary chondrite (H4/5)	High iron content, including olivine, iron-nickel and troilite [Reimold et al., 2004].

Table B.1: Classification of the Pre-selected Meteorites

A fusion crust is formed as the meteorite passes through the Earth's atmosphere. Intense heating melts the outermost portion of the meteorite, forming a thin

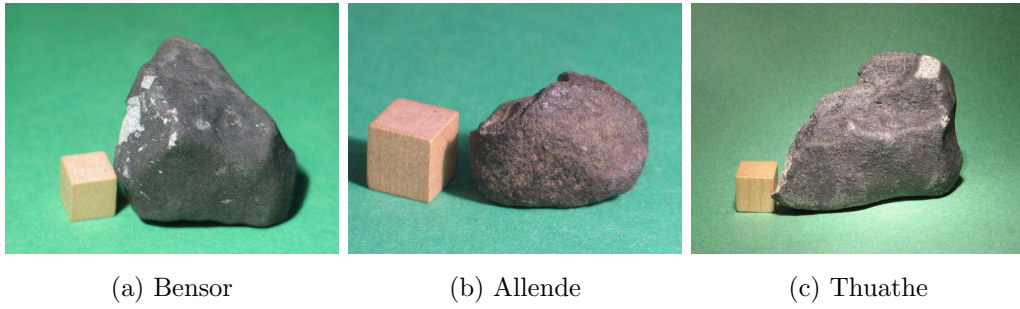


Figure B.11: Photos of the Pre-selected Meteorites

(0.1-0.2 mm) layer of contaminated material [Reimold et al., 2004; Lee et al., 2006]. The interior of the meteorite is unaffected. The fusion crust must therefore be removed. Ablation has to occur on the surface of the meteorite. Reported in Lee et al. [2006], removal can be achieved by either cutting away the affected area with a diamond blade or mechanically breaking the sample to produce smaller subsamples.

Health and Safety of Operating the Laser

Lasers produce electromagnetic radiation that is located in the ultra-violet, visible and infra-red spectrum. Hazard classes based on their power level have been defined. Given in Table C.1, this is the amount of energy emitted by the laser that is accessible to the user.

Laser Class	Hazard Level
1	Safe
1M	Safe if not viewed through magnifying optics
2	Safe for short exposure
2M	Safe for short exposure, if not viewed through magnifying optics
2R	Hazardous to eyes, for direct exposure longer than 0.25 seconds
3B	Hazardous for eyes, for direct and diffused exposure
4	Hazardous to eyes and skins, can constitute a fire hazard

Table C.1: Hazard Classes for Laser Beams

The LIMO laser is a class 4 laser. It can cause serious burns, wounds (particularly eye injury), accidental fire and electrocution. To reduce this risk, the following precautions were taken:

1. Appropriate signage was used throughout. A laser hazard label was fixed onto the laser housing.
2. All operators were trained, qualified and familiar with the risks related to the use of the laser. The operators defined and followed a set of clear experiment procedures. The laser was never left on in an unoccupied room.
3. Protective goggles were provided and readily available. Goggles were worn throughout the experiment campaign. It avoided accidental contact with the laser beam. The goggles were compliant with EU regulation and the wavelength of the laser beam.
4. The laser was mounted on an optical table with the laser beam travelling in the

horizontal plane. The laser beam was always lower than eye level. The set-up was designed to minimise the possibility of any direct and scattered radiation from entering the eye.

5. The track of the laser beam was always known and contained. This included any possible reflecting surfaces. The laser light was prevented from leaving the optical table.
6. All testing, alignment and calibration activities were performed at minimal power. An infrared viewer and card was always used to locate the laser beam. No hand (or other part of the body) was placed in the path of the laser beam.
7. Equipment inside the vacuum chamber was compatible with the laser beam. Non flammable material was used. This avoided the risk of fire and toxic smoke.
8. The chiller for the laser was always operational (when the laser was on) and functioning efficiently. Water was always contained and kept away from the electric connections.

Operations of the LIMO Fibre-Coupled Diode Laser

D1 Turn-on Procedure

Do not proceed unless you have been trained by David Burns or John-Mark Hopkins - any problems, issues **call 0141 548 4120 immediately**.

1. Wear the appropriate laser safety glasses. Warn others in the laboratory that you are about to turn the laser on. Check the optical bench for anything that should be removed.
2. Check that the diode is shorted at switch.
3. Turn on the chiller
4. Set the chiller temperature to 15 °C - check that the temperature is reached
5. Check that the flow rate is at least 5 litres/minute
6. Check that the current knob on the diode driver is fully turned down and that the voltage knob is fully turned up
7. Ensure that the travel short (small lead) on the diode is removed
8. Turn on the diode power supply (black knob)
9. Turn the key to the ON position, the RSD LED should go OFF
10. Push the driver ON/OFF button, the DCF LED should go ON
11. Open the short and switch
12. Dial up the current on diode the driver (threshold ~ 7.1 A) to a **maximum of 36.5 A**. Use 36 A for all experiments

D2 Turn-off Procedure

1. Dial down the current on the diode driver
2. Short the diode at switch
3. Push the driver ON/OFF button, the DCF LED should go OFF

4. Turn the key to the OFF position, the RSD LED should go ON
5. Turn off the driver (black knob) - wait, it will switch off!
6. Wait for the diode temperature to stabilise
7. Turn off the chiller
8. Replace the travel short for long periods of inactivity

Revised JMH 30th August 2012

Images of the Optical Bench

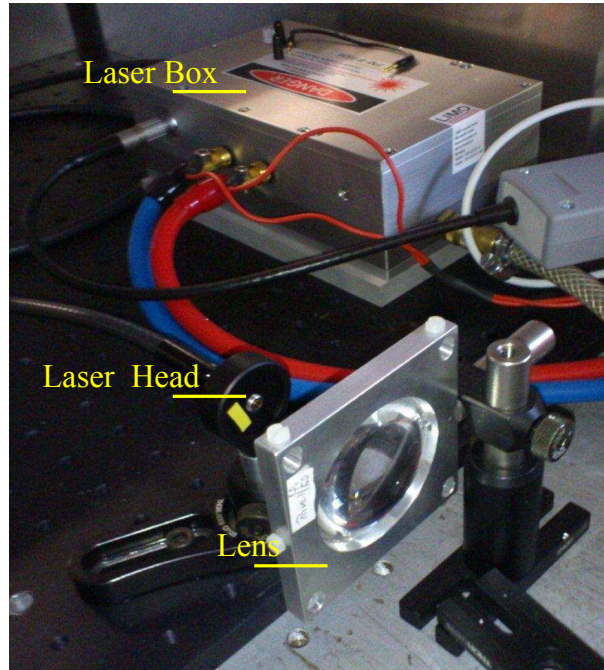


Figure E.1: Laser Head

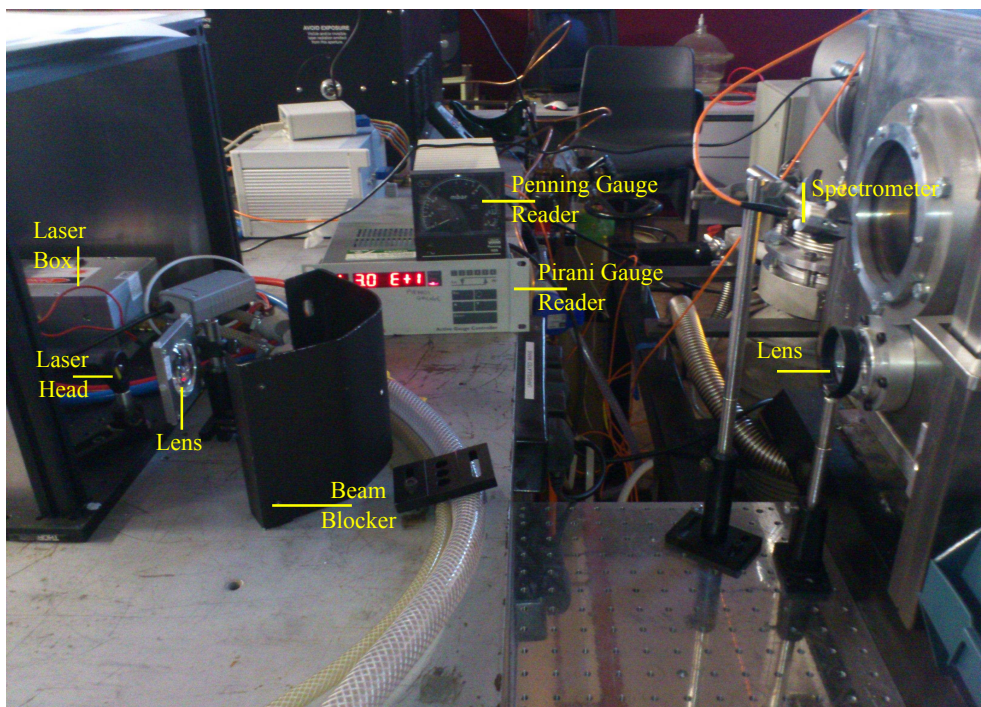


Figure E.2: Optical Bench

Holder for the Collection Plates

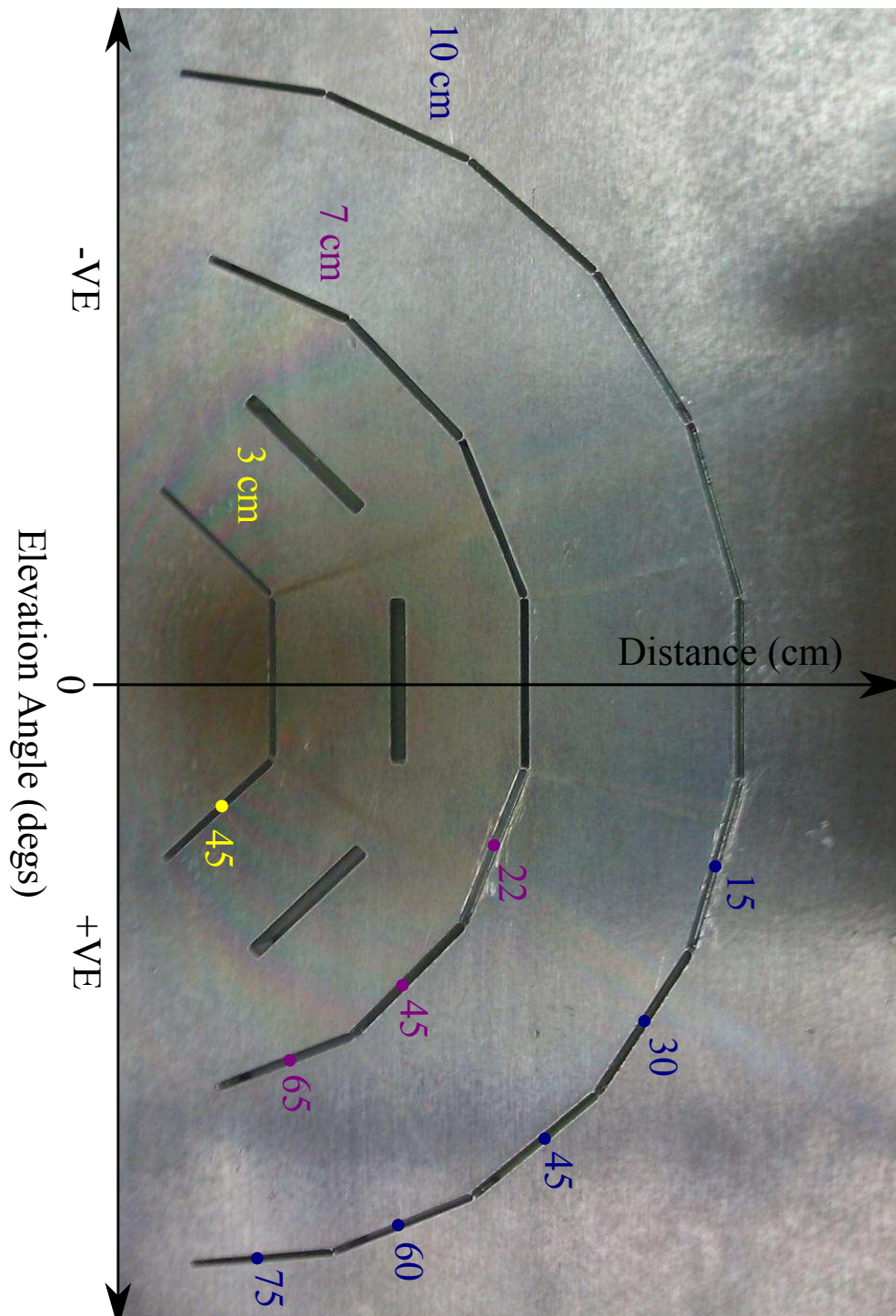


Figure F.1: Orientation of the Collection Plate Holder

SEM Analysis of the Pre-ablated Olivine Sample

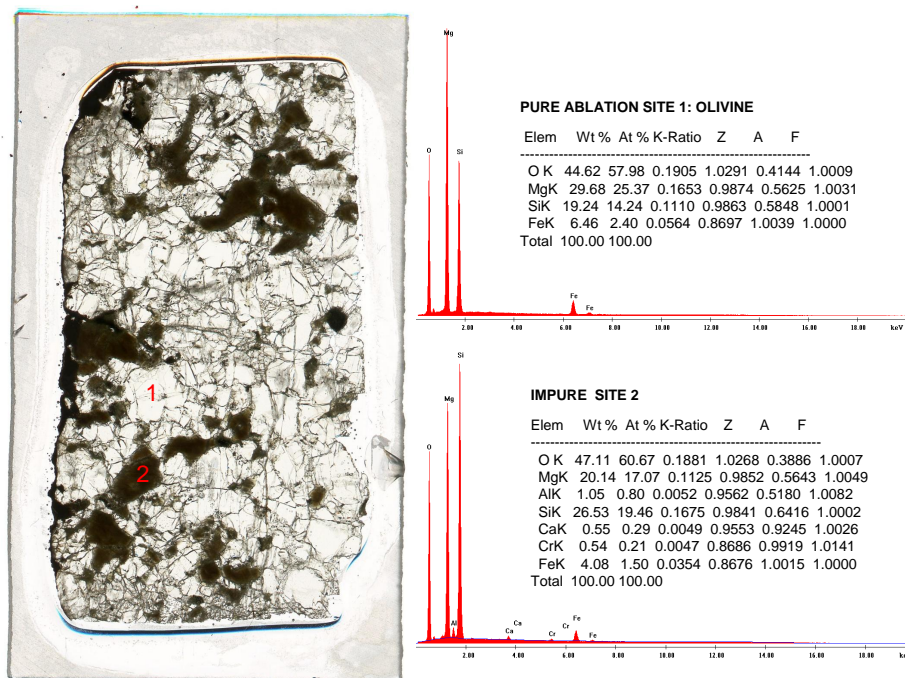


Figure G.1: Elemental Analysis of the Olivine Target Material

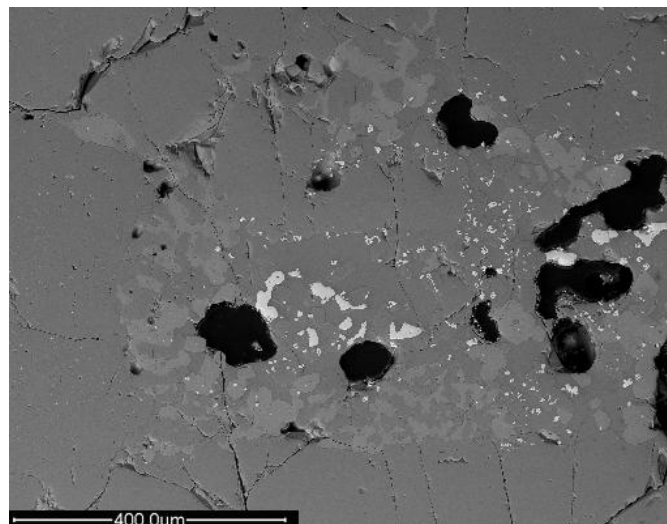


Figure G.2: Rock Sample for Compositional Analysis

The brighter the colour the more abundant the element is.

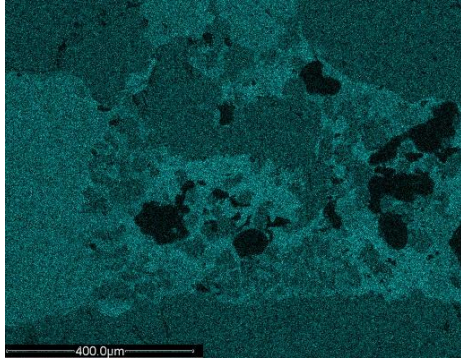


Figure G.3: Presence of Silicon

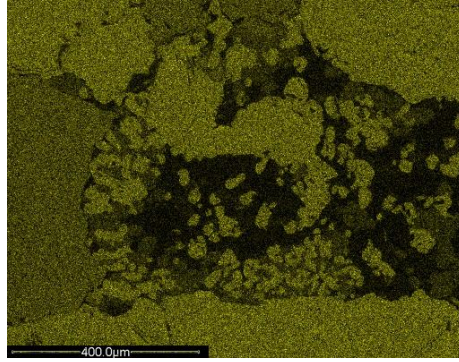


Figure G.4: Presence of Magnesium

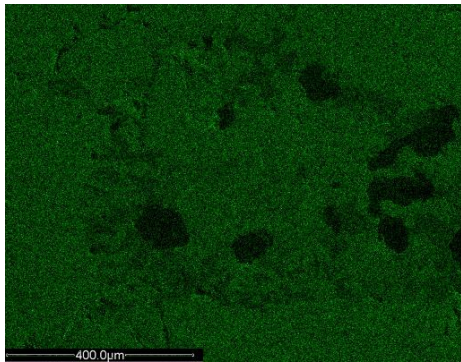


Figure G.5: Presence of Oxygen

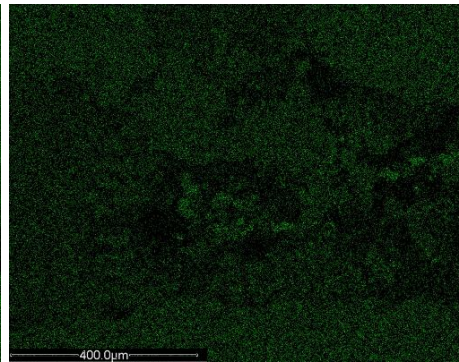


Figure G.6: Presence of Iron

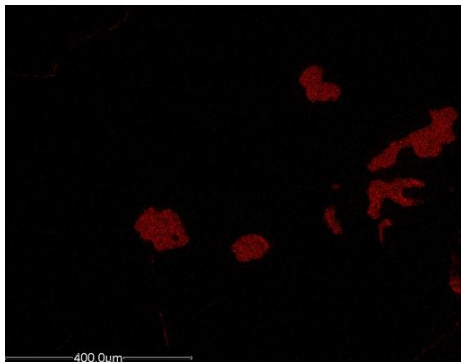


Figure G.7: Presence of Carbon

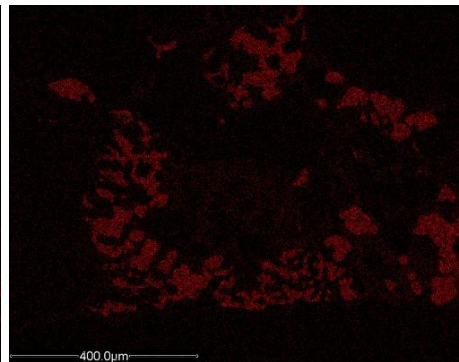


Figure G.8: Presence of Calcium

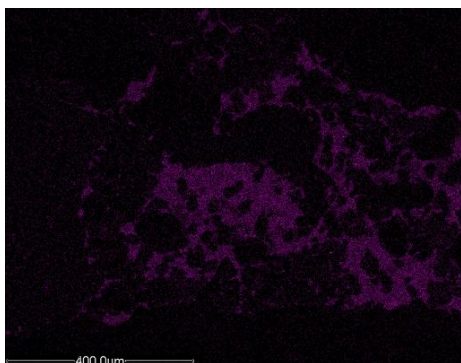


Figure G.9: Presence of Aluminium

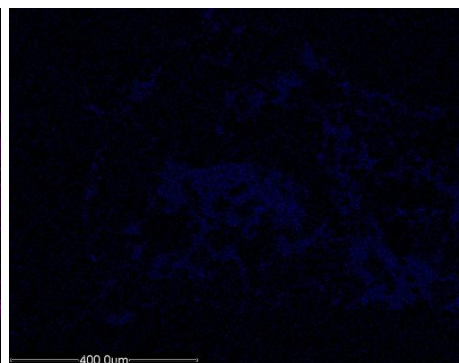


Figure G.10: Presence of Sodium

SEM Analysis of the Recrystallised Ablation Rim

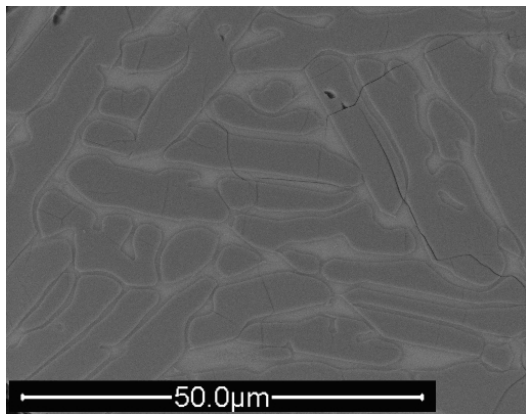


Figure H.1: Assessed Section

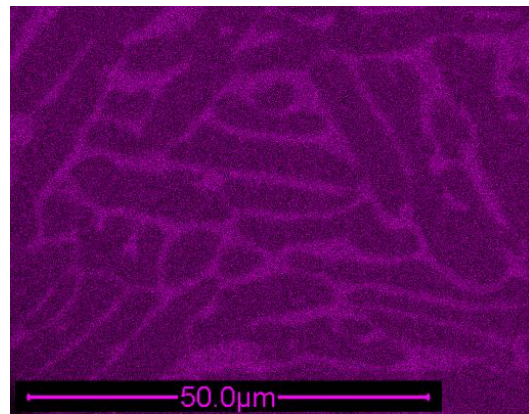


Figure H.2: Recrystallised Silicon

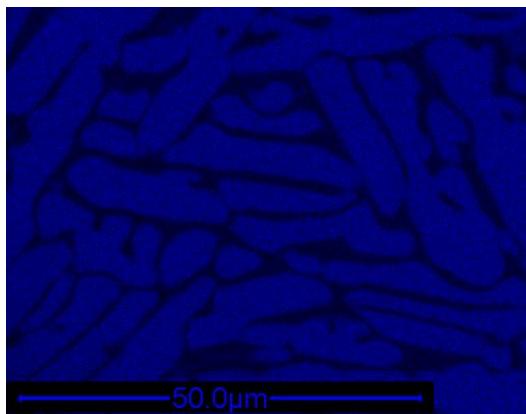


Figure H.3: Recrystallised Magnesium

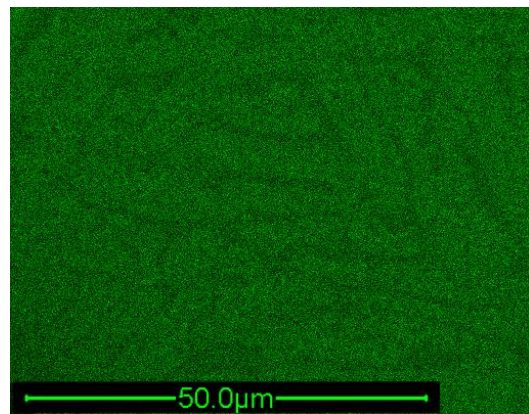


Figure H.4: Recrystallised Oxygen

The brighter the colour the more abundant the element is. The magnesium rich surface indicated the preference of ablating the fayalite component of the olivine target material. The observed heterogeneity suggests that the surface diffusion was not fast enough to homogenise the surface.

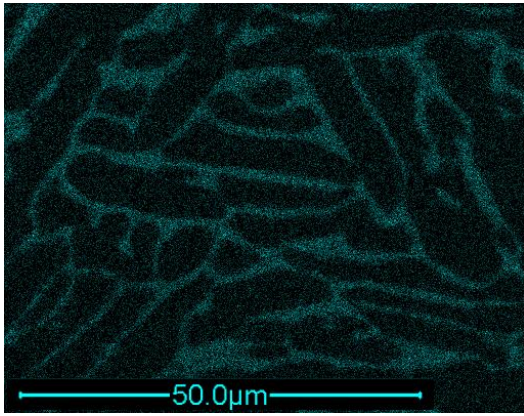


Figure H.5: Recrystallised Calcium

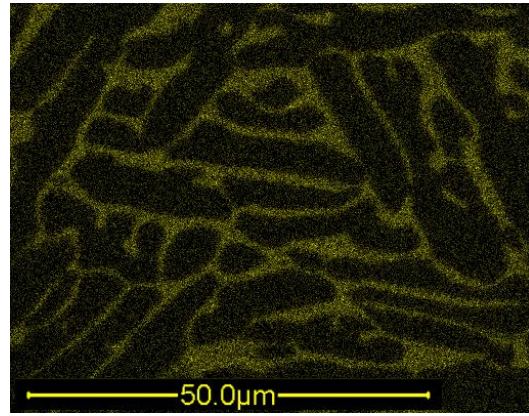


Figure H.6: Recrystallised Aluminium

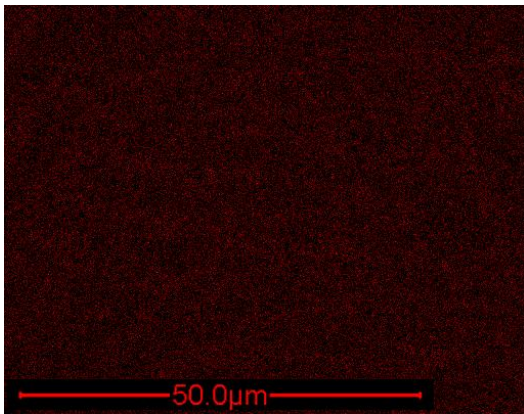


Figure H.7: Recrystallised Iron

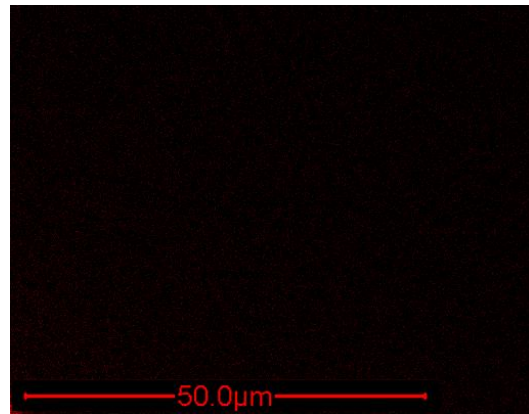


Figure H.8: Recrystallised Carbon

Error Analysis

For increased confidence in the experimental results, each test was repeated three times. Error bar analysis was also used to assess whether or not an additional experiment needed to be performed and repeated. An example of this analysis is presented in Figure I.1. It was produced using Standard Error of the Mean (SE).

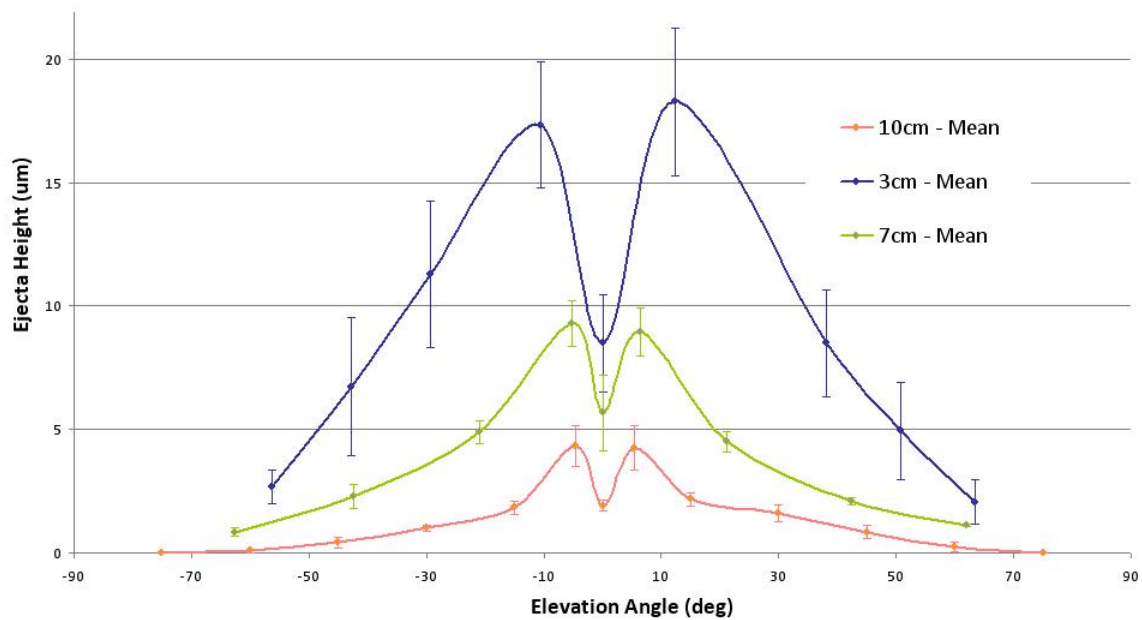


Figure I.1: Error Bar Analysis

Where:

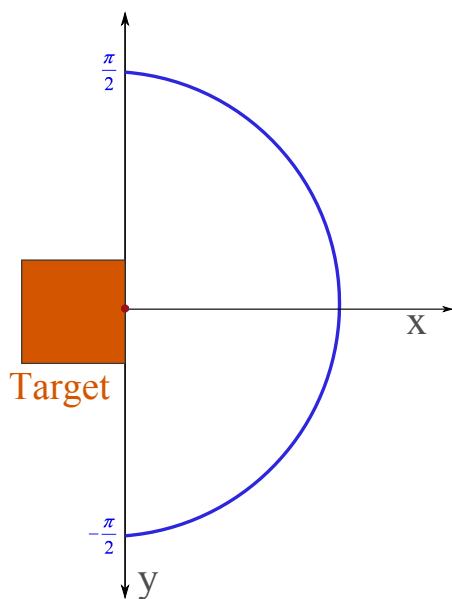
$$SE = \frac{SD}{\sqrt{n}} \quad (I.1)$$

SD is the standard deviation. It is given by:

$$SD = \sqrt{\frac{1}{n-1} \sum_{i=1}^n (x_i - \bar{x})^2} \quad (I.2)$$

n is the number of values in the sample population, (x_1, x_2, \dots, x_n) are the measured values of the sample and \bar{x} is the mean of those values.

Scatter Factor



$$\lambda = \int_{-\frac{\pi}{2}}^{\frac{\pi}{2}} \frac{\cos\theta}{\pi} d\theta \quad (\text{J.1})$$

$$\lambda = \frac{1}{\pi} \int_{-\frac{\pi}{2}}^{\frac{\pi}{2}} \cos\theta d\theta \quad (\text{J.2})$$

$$\lambda = \frac{1}{\pi} [\sin\theta]_{-\frac{\pi}{2}}^{\frac{\pi}{2}} \quad (\text{J.3})$$

$$\lambda = \frac{1}{\pi} \left[\left(\sin \frac{\pi}{2} \right) - \left(\sin - \frac{\pi}{2} \right) \right] \quad (\text{J.4})$$

$$\lambda = \frac{1}{\pi} [1 - (-1)] \quad (\text{J.5})$$

$$\lambda = \frac{2}{\pi} \quad (\text{J.6})$$

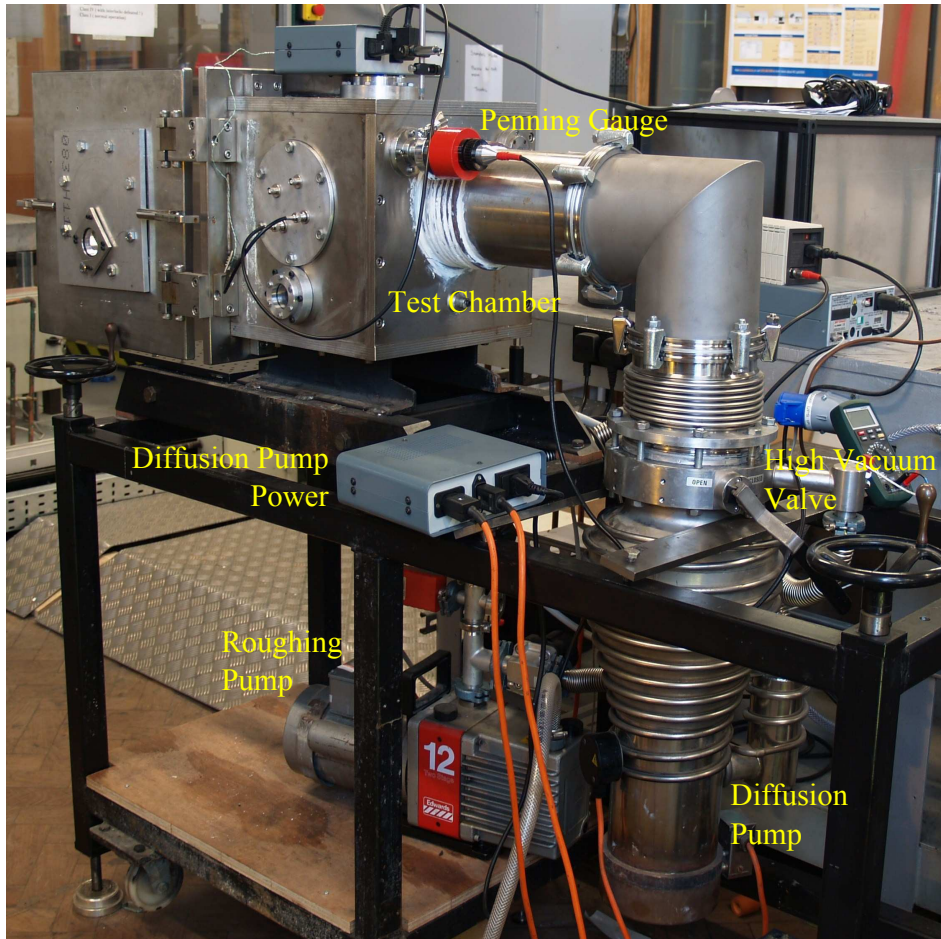
Figure J.1: Definition of the Scatter Factor

Roughing and Diffusion Pump

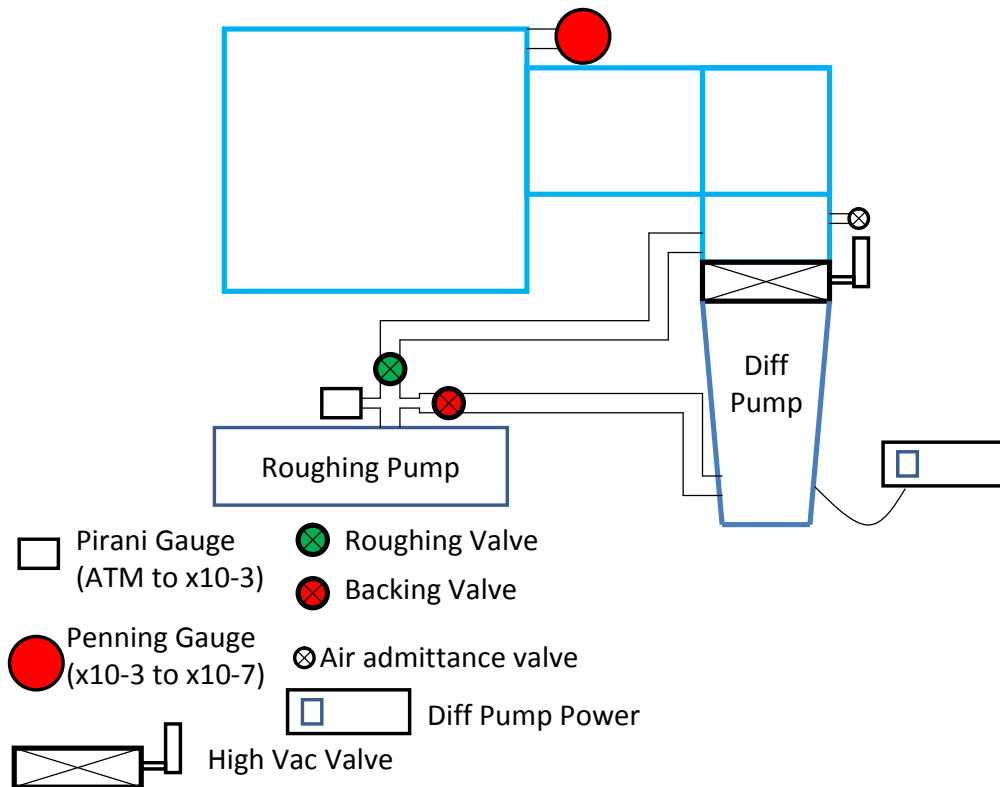
With a maximum pumping time of four hours, the combined operation of the roughing and diffusion pump system can provide a minimum based pressure of $2 \cdot 10^{-5}$ mbar. The roughing pump was first used to remove (rough) the majority of the air molecules from the test chamber. This provided a back-down pressure and an outlet exhaust pressure below $1 \cdot 10^{-2}$ mbar. It was low enough to ensure the safe and continued operations of the diffusion pump. Diffusion pumps cannot operate directly from standard atmospheric pressure, nor can they be directly discharged into an atmosphere. The roughing pump must therefore be used to back-down the pressure inside the diffusion pump's main chamber. The pump-down operating procedures is given in Appendix L. Figure K.1 outlines a schematic of the entire system, including the location of all the back-end pumping equipment.

A diffusion pump is a stainless steel chamber. Shown in Figure K.2 it contains a number of vertically stacked, cone-shaped, jet assemblies. At the base of the chamber there is a pool of high quality, low vapour pressure oil. An electric heater is mounted at the base of the chamber, below the pool. The heater is used to vaporise the pool of oil, which is then forced upwards through the central columns of the jet assembly. They then strike an umbrella and are expelled downwards, through the nozzle of each jet stack. Each vaporised molecule exits with a high velocity and travels downwards, between the jet assemblies and the chamber wall. They then collide with any air molecules still present within the diffusion pump's main chamber or collide and condense onto the cooled outer shell of the diffusion pump. Collision is caused by thermal motion. This compresses the air molecules, forcing them towards the base of the chamber. The condensed material is recovered, running down the inside of the pump, and is re-directed back to the pool of oil. By the time that the vaporised-oil-oxygen mixture reaches the pool of oil it has cooled enough to release the trapped air molecules. It is then available to be re-vaporised into another cycle through the jet stack. The process is repeated in a continuous loop. The accumulation of gaseous air molecules increases the pressure at the base of the diffusion pump. These molecules are removed by the continual discharge operations of the roughing pump. It creates a high vacuum, low pressure environment in the upper portion of the test chamber.

The test chamber and the diffusion pump are connected by a bellow. The outside of the diffusion pump is surrounded by coils of copper pipe work. Water is used as a coolant. A 2 kW chiller (supplied by Betta Tech Controls), operating at 20 °C, was used to continuously pass chilled water through the coils. Water was passed at a minimum



(a) Laboratory Arrangement of the Test Chamber and Pumps



(b) Schematic of the Test Chamber and Pumps

Figure K.1: Configuration of the Test Chamber, Roughing Pump and Diffusion Pump

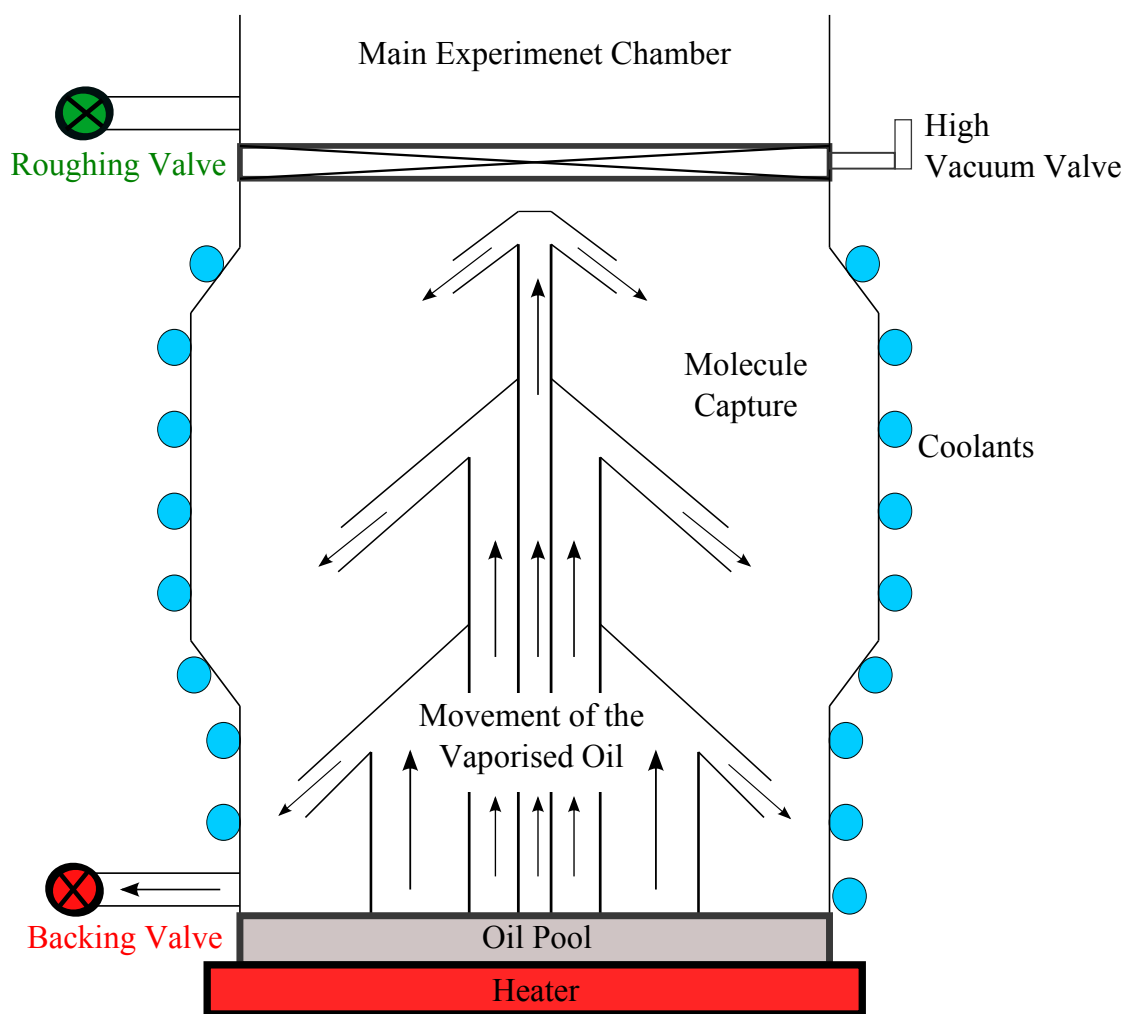


Figure K.2: Cross Sectional View of the Diffusion Pump and Cooling System

level of 115 litres/hour. Coolant is needed to cool the diffusion pump, preventing any thermal runaway effects. It also extends the lifetime operations of the pump. Vaporisation temperatures at the base of the chamber vary from 190-280 °C. The system automatically switches-off once the temperature exceeds 280 °C.

Diffusion pumps are driven by convection. It provides a simple and stable pumping design that does not create any vibrations or noise. It is also relatively inexpensive to operate and maintain. This increases the system's durability and reliability.

Throughout the pumping process the inlet and outlet temperature of the pipe work and the mass flow rate of the water coolant were constantly monitored. The temperature of the outlet was not allowed to exceed 30 °C. The system trips at 35 °C. Care was also taken to maintain the internal quality of the pipe work. Pipes can become clogged and corrode with time. The performance of the diffusion pump can also be enhanced with the selection of a high quality oil. This will minimise the need for maintenance. Key criteria include low toxicity, flammability, chemical inertness, level of reactivity and cost. The oil needs to be stable, perform over an extended period of time with little or no degradation and have a low vapour pressure. When heated to its operational temperature the oil should never be exposed to the local atmosphere. If so, the oil will burn, decompose and diffuse throughout the system. The oil will have to be replaced and the system

thoroughly cleaned. Polyphenyl ether (Santovac 5, supplied by Edwards Vacuum) was selected for its exceptional thermal and chemical stability. The performance of the diffusion pump is also susceptible to changes in local humidity and temperature.

The performance of the vacuum chamber will also be affected by the outgassing of particles and the cleanliness of the test chamber and equipment. Outgassing is caused by the desorption, diffusion and decomposition of any light volatile chemical [Tribble, 1961]. Diffusion is the major component of molecular contamination. Loose molecules acquire enough thermal energy to overcome the surface forces and evaporate into the local environment [Tribble, 1961]. Desorption is the release of surface molecules held by electrical-chemical forces. It is dependent on the specific binding energies, the surface temperature and the surface area. Decomposition is the division of a chemical compound into two or simpler substances, which may then outgas through either desorption or diffusion.

The release of these molecules represents a permanent source of unwanted contamination. This reduces the quality of the chamber pressure, increases the time taken to reach high vacuum conditions and degrades the sensitivity of the experiment set-up. To alleviate this effect all internally mounted equipment and the target material were pre-baked. This occurred prior to any experiment. Each piece of equipment was cleaned with an isopropyl alcohol solvent wipe and heated overnight at 90 °C in a small convection oven. Care was taken to ensure that all of the equipment was pre-conditioned in the same manner. Pre-baking was used to accelerate the outgassing phenomenon; effectively de-gassing all component parts. This minimises the quantity of the outgassed products as it reduces the bulk concentration of loose, volatile molecules. A coarse filter, with a small mesh size was also placed at the back of the main chamber. This covered the outlet of the diffusion pump. It was used as a preventative action against the larger products of ablation.

The cleanliness of the test chamber was maintained by cleaning all internal surfaces, seals and equipment with an isopropyl alcohol solvent wipe. This was the most obvious cleaning solution. It is effective at removing both molecular and particular contamination [Tribble, 1961]. Solvent wiping occurred before and after each experiment. All optical surfaces were cleaned with lens paper coated in methanol. The chemical properties of the solvent dislodges and removes any contaminated, dirty material [Tribble, 1961]. Surfaces were wiped clean until, under visual inspection, the wipe appeared clean. Then an extra test wipe was used to verify the surface cleanliness [Tribble, 1961]. Disposable, surgical, unpowdered gloves were also worn throughout.

Operating Procedures - Vacuum Chamber and Pump

L1 Starting Up

1. Check the water levels in the chiller.
2. Turn on the chiller (3-phase switch in the wall box) with the black mission switch.
3. Switch on the power for the rotary roughing pump and the pirani gauge.
4. Make sure that the pump is achieving at least $1 \cdot 10^{-2}$ mbar on the pirani gauge.
5. Open the backing valve until the pressure goes below $1 \cdot 10^{-1}$ mbar on the pirani gauge.
6. Close the backing valve and open the roughing valve.
7. Once the pressure is below $1 \cdot 10^{-1}$ mbar on the pirani gauge, close the roughing valve, open the backing valve and switch on (green light will come on) the power to the diffusion pump. *The majority of the air molecules in the test chamber have now been removed by the roughing pump.*
8. Switch on the penning gauge and open the high vacuum valve (between the test chamber and diffusion pump).

The diffusion pump will take about 20-30 minutes to heat-up. It will then take just over an hour to reach base pressure, providing that you have a clean system which was kept under vacuum. The chamber of the diffusion pump must always be at a lower pressure than the test chamber. **Never have the high vacuum valve and the roughing valve open at the same time.**

L2 Venting the System to Atmosphere

1. Close the high vacuum valve.
2. Open the air admittance valve.
3. Undo the clamps on the door.

A break in the vacuum makes it possible to insert and remove items from the test chamber.

L3 Pumping the System from Atmosphere

1. Load the sample into the test chamber. Clean the door seal with an isopropyl alcohol solvent wipe.
2. Clamp the door closed and close the air admittance valve.
3. Close the backing valve and open the roughing valve.
4. Once the pressure is below $1 \cdot 10^{-1}$ mbar, close the roughing valve and open the backing valve.
5. Open the high vacuum valve and wait for approximately 1 hour for base pressure to be reached.

L4 Shutting Down

1. Close the high vacuum valve.
2. Switch off the power to the diffusion pump.
3. Switch off the penning gauge.
4. After 30 minutes, close the backing valve. *The diffusion pump must have cooled before the roughing pump and chiller are turned off.*
5. Switch off all remaining power supplies.
6. Switch off the chiller.

When the diffusion pump is not in use, or left idle for long periods of time, it should always be kept under vacuum conditions. If possible the test chamber should be back filled with nitrogen or argon. Any exposure to a local, humid atmosphere will increase the pump-down time.

Catastrophic failure of the diffusion pump can be caused by the back streaming of the pumping fluid. Hot vaporised oil can enter and condense in the test chamber. This can be caused by exceeding the discharge pressure of the roughing pump, by exceeding the maximum through capacity and by using an incorrect start-up/shut-down procedure. It is therefore critical that the system operations are always adhered to.